A Comprehensive Study of Phase Change Materials (PCMs) for Building Walls Applications

BY

Yuan Fang

Submitted to the graduate degree program in Civil Engineering and the Graduate Faculty of the University of Kansas in partial fulfillment of the requirements for the degree of Doctor of Philosophy

Committee:

_____
Mario A. Medina, Ph.D., P.E., Chairperson

_____
Carl E. Kurt, Ph.D., P.E.

_____
Bryan C. Young, Ph.D., P.E.

_____
Edward F. Peltier, Ph.D.

_____
Bedru Yimer, Ph.D.

Date defended:_____

The Dissertation Committee for Yuan Fang certifies
that this is the approved version of the following dissertation:

A Comprehensive Study of Phase Change Materials (PCMs)
for Building Walls Applications

Committee:

_____
Mario A. Medina, Ph.D., P.E., Chairperson

_____
Carl E. Kurt, Ph.D., P.E.

_____
Bryan C. Young, Ph.D., P.E.

_____
Edward F. Peltier, Ph.D.

_____
Bedru Yimer, Ph.D.

Date approved: _____

Abstract

Air conditioning energy consumption in summer represents a challenge in many areas with hot and humid climates. When incorporated into the walls of light-weight residential and commercial buildings, phase change materials (PCMs) can increase the effective thermal mass of the walls, shift part of the space cooling loads to off-peak hours when less cooling is needed, and lower the peak space cooling load of the buildings.

In this dissertation, the working environment of the PCMs (i.e., the temperatures within the wall) was studied from summer field experimental temperature data. Results of Differential Scanning Calorimeter (DSC) tests, performed on pure PCMs, PCM/cellulose mixtures, and "aged" PCM samples, used to better understand PCMs' thermal behavior, the effects of mixing them with cellulose insulation, and the impact that ambient air had on samples when these were exposed, are presented. The results of the mass change experiments, carried out to investigate PCMs' mass changes when these were exposed to ambient air, under room temperature and under high temperature conditions, are summarized.

The performance of PCM-enhanced walls was evaluated under full weather conditions and in a laboratory setting. The PCM was integrated into test walls using two methods, namely, direct mixing of the PCMs with cellulose insulation and macro-encapsulation. Information on the test setups, experimental approach, and results are presented. The heat transfer process in PCM-enhanced walls was analyzed for different situations. A detailed explanation of how PCMs reduce the peak heat

flux through PCM-enhanced wall is presented. A new method for integrating the PCM into building walls, referred to as “layer method,” was proposed to overcome some of shortcomings of previous PCM integrating methods. A detailed analysis of this method is also presented.

A DSC test method and its detailed steps, used to study the performance of PCMs when these would cycle from partially-melted states, are introduced. Based on these DSC data, a modified phase change heat transfer model, for a paraffin-based PCM, was developed. The model was implemented via a FORTRN program.

Based on the developed model, numerical simulations were run. The simulation results were compared with experimental data to validate the model. To investigate the influence of various variables on the performance of the PCM-enhanced building walls, a parametric study was conducted using the validated heat transfer model.

The performance of the PCM-enhanced wall in several U.S. climate zones was studied. The simulation results for the representative cities showed that a 7 mm (0.28 in) thick PCM layer placed at (3/16)L from the wallboard would produce large peak reductions for most climate zones. For the cities located in places with hot climates, such as Phoenix, AZ, the PCM layer would need to be moved towards the colder side of the wall. For all the climate zones, the PCM-enhanced wall retrofitted with the proposed layer method could lower the peak space cooling load through the walls by about 50%.

Acknowledgements

I would like to express my sincere gratitude to my advisor Dr. Mario A. Medina for his invaluable guidance in the past four years.

I would like to thank my committee members, Dr. Carl E. Kurt, Dr. Bryan C. Young, Dr. Edward F. Peltier and Dr. Bedru Yimer for their help.

I would like to thank the support from CEAE department, especially Laboratories Director Mr. Jim Weaver. And I would like to acknowledge the contribution of the National Science Foundation for funding this research under Grant #0533362.

I will never forget the help from my friend, research partner Angie Evers and my friends at KU, Jie Huang, Xianping Li, Wanbo Liu, Eric Li, Xiaoming Yang, Fei Lu, Oliver and Mashud. We had such a wonderful time together.

I would like to thank my parents, Hongyi and Yirong, for their 120% support in my life. I look forward to spending more time with you now that I have finished my Ph.D. study.

Yuan Fang

Table of Content

List of Figures

List of Tables

Nomenclature

A	area, m^2, ft^2
c	specific heat, J/(kg·K), (Btu/lb·^{o}F)
C_p'	effective heat capacity, J/(kg·K), (Btu/lb·^{o}F)
f	the liquid fraction
h_f	forced convective heat transfer coefficient, W/(m^2·K), Btu/(ft^2 hr ^{o}F)
h_n	natural convective heat transfer coefficient, W/(m^2·K), Btu/(ft^2 hr ^{o}F)
k	thermal conductivity, W/(m·K), Btu/(ft·hr·^{o}F)
L_{st}	standard meridian for the local time zone, ^{o}
L_{loc}	local longitude, ^{o}
P	vapor pressure, cmHg, inHg
q	Heat flux transferred into the indoor environment, W/m^2, Btu/(ft^2·hr)
t	temperature, ^{o}C, ^{o}F
T_s	phase change temperature, ^{o}C, ^{o}F
T_{in}	indoor air temperature, ^{o}C, ^{o}F
T_{liquid}	the upper-limit of the phase change temperature range, ^{o}C, ^{o}F
T_{solid}	the lower-limit of the phase change temperature range, ^{o}C, ^{o}F
T_{surf}	exterior wall surface temperature, ^{o}C, ^{o}F
T_{air}	the outdoor air temperature, ^{o}C, ^{o}F
R_f	surface Roughness Multiplier
V	wind speed, m/s, ft/s
β	slope, ^{o}
ρ	density, kg/m^3, lbm/ft^3

θ angle of incidence, ^{o}

ϕ local latitude, ^{o}

γ surface azimuth angle, ^{o}

ω hour angle, ^{o}

δ declination, ^{o}

Δh the heat of fusion, kJ/kg, Btu/lbm

Δx distance between the phase change interface, m, ft

ΔX x direction mesh size, m, ft

ΔY y direction mesh size, m, ft

$\Delta \tau$ time step, s

Chapter I

Introduction

1.1 Background

The United States uses about 15 times more energy per person than a typical developing country and ranks seventh in energy consumption per-capita in the World (EIA, 2005). Furthermore, most of the energy used in the U.S. is derived from fossil fuels. U.S. energy-related carbon dioxide emissions by fossil fuels alone was 4,985 million metric tons (5495 million short tons) in 1990; a value that rose to 5,877 million tons (6478 million short tons) in 2005 (EIA, 2006).

In most regions of the United States, energy use by air conditioning devices tops the list of electricity consumption in buildings during the summer. In fact, the percent of Americans with central air-conditioning has increased over the past couple of decades. Household electricity consumption resulting from the use of air conditioning alone was estimated to be about 183 billion kWh (624.4 MMBtu) for year 2001 (the most recent data available), which represented about 16% of the total annual consumption (EIA, 2002).

The space cooling loads of light-frame residential and commercial buildings reach their peaks at about the same time. This adds a large peak demand on the electric grid, especially in populated areas, which raises three main problems:

1) New electricity generation capacities are needed to meet the peak demand;

2) More energy is used to generate the peak electricity because, for economic reason, relatively low efficient natural gas turbines are usually used to generate the peak hour electricity;

3) Extra stress is placed on the electricity transmission and distribution system.

The current state of energy supply and demand in the country and the projected growth in residential and commercial buildings in the near future create the necessity to reduce energy consumption and to formulate ways to manage electricity peak loads from air conditioning.

There are several ways to approach this problem with "demand-side management." Shifting part of the peak load to off-peak time by adding building thermal mass is a promising one. However as promising as this approach may be, when common building materials are used, large masses of these materials are required. Phase change materials (PCMs), on the other hand, can absorb large amounts of heat during the phase change process without being so massive. For example, Benard et al. (1985) found that for the same thermal performance, a wall outfitted with phase change materials would only need about one-twelfth of the weight of a concrete wall. When PCMs are placed in building walls, they absorb a major part of the heat transferred from hot outside environment in the daytime and release the absorbed heat during the night and early morning hours. As a result, part of the peak space-cooling load is reduced and shifted to off-peak hours.

For real applications, PCMs should be able to work in daily cycles, which means the PCM melted in the daytime should solidify at night and/or during early morning hours and then be ready for the next melting process. However, relative narrow phase change temperature ranges bring some challenges to this application. For example, because the temperature change in the insulation has its only fixed characteristics, if the location or the concentration of the PCMs within the insulation is not optimized, the PCM will not perform as expected. Some problems will come up, for example, the PCMs would melt very rapidly that the load shifting effect would not be significant. Or, it may be that the night and/or early morning temperatures of the environment surrounding the walls might be higher than the solidification temperature of the PCM, in which case the PCM would not solidify.

Therefore, in addition to the phase change temperature, other properties and/or design parameters of the PCMs, such as the heat of fusion, the way PCMs are incorporated into the insulation system, and how much PCM is placed in the insulation will also affect the performance of PCM-enhanced wall. Thus, it is necessary to thoroughly understand how different factors, including those mentioned above and others, such as climate, would affect the PCM-enhanced wall's performance.

1.2 Literature review

1.2.1 Introduction to phase change materials

Phase Change Materials (PCMs) are substances that release and absorb large amounts of heat during the phase change process, for example, from liquid to solid or

from gas to liquid. For PCM applications in buildings, which operate in relatively low temperatures, around the ambient air temperatures, only solid-liquid and solid-solid phase change materials are of interest. Liquid-gas phase change materials would be impractical because of the large volume changes that would be required of the PCMs during the phase change processes.

Phase Change Materials (PCMs) can be generally divided into three categories: organic, inorganic, and mixtures. A schematic of the PCM classification is shown in Figure 1.1. Among them, hydrated salts and paraffin are the two most commonly used PCMs in building applications.

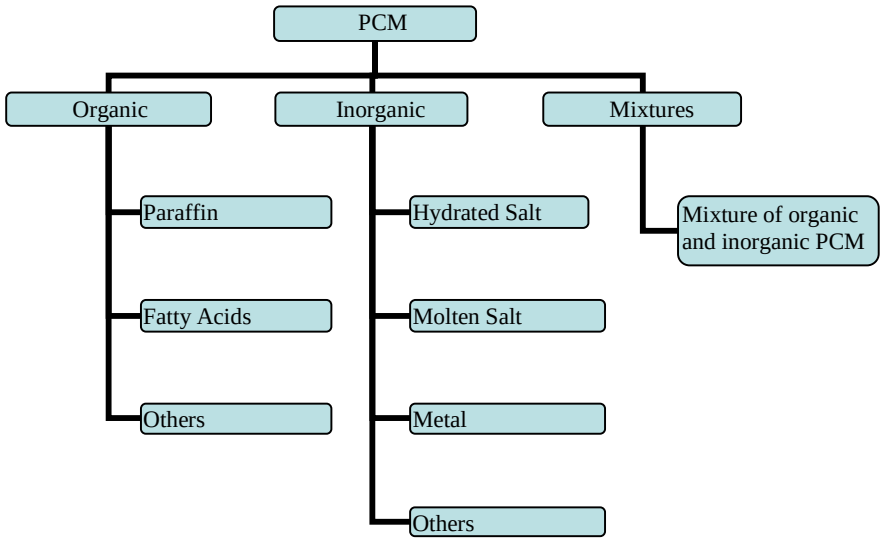

Figure 1.1 PCM classifications

1.2.1.1 Hydrated salt PCMs

Hydrated salt PCMs are formed by anhydrous salts and a few fixed number of water molecules, which are usually called “water of crystallization.” Their melting

temperatures can be from several degrees Celsius to over one hundreds of degrees. The properties of some hydrate salts are shown in Table 1.1 (Telkes, 1980).

Table 1.1 Properties of hydrated salts

Compound	H_2O change	Melting point $^oC/^oF$	Specific gravity
$Ba(OH)_2$	8-0	78/172.4	2.18
$CaCl_2$	6-2	29.5/85.1	1.68
$Ca(NO_3)_2$	4-2	42.6/108.7	1.82
$Cd(NO_3)_2$	4-3	59.5/139.1	2.45
$Co(NO_3)_2$	6-4	57/134.6	1.87
CoSO4	7-1	96/204.8	1.95
$Cu(NO_3)_2$	6-4	24/75.2	2.07
$FeCl_3$	6-0	37/98.6	-
$LiNO_3$	3-0	30/86.0	-
$Mg(NO_3)_2$	6-4	90/194.0	1.46
$MgSO_4$	7-1	48/118.4	1.64
$MgCl_2$	6-4	117/242.6	1.56
$MnCl_2$	4-2	58/136.4	2.01
$Mn(NO_3)_2$	3-2	35.5/95.9	-
$Mn(NO_3)_2$	6-4	26/78.8	1.82
$NaC_2H_3O_2$	3-0	58/136.4	1.45
NaOH	1-0	64/147.2	-
Na_2CO_3	10-1	34/93.2	1.44
Na_2CrO_4	10-4	20/68.0	1.48
Na_2HPO_4	12-2	36.5/97.7	1.52
Na_3PO_4	12-2	70/158.0	1.64
Na_2SO_4	10-0	32.4/90.3	1.46
$Ni(NO_3)_2$	6-4	57/134.6	2.05
$Zn(NO_3)_2$	6-4	36.4/97.5	2.07

Hydrated salt PCMs normally have high conductivity, high density and large latent heats of fusion, which make them suitable for thermal storage applications. Unlike organic PCM, hydrated salts are not flammable. They, however, are corrosive

to most metallic materials. According to the handling instructions from PCM Energy P. Ltd, a manufacturer of hydrated salt PCMs, only containers made of aluminum, lined with plastic or stainless steel, are recommended for use as PCM holding containers. Another drawback of hydrated salts is that these are hygroscopic (i.e., they will absorb moisture when exposed to, say, ambient air).

1.2.1.2 Paraffin PCMs

Paraffins are straight-chain or branched saturated organic compounds with the composition C_nH_{2n+2}. Paraffin can be obtained from crude oil, coal and other organic materials like wood, lignite, bituminous shale, fish tallow, etc. With increasing average molecular weight, the melting point of paraffins rises. For example, the melting points of $C_6H_{14,}$, $C_{10}H_{22,}$ $C_{30}H_{62,}$ and $C_{40}H_{82}$ are 95.4 ^oC(-139.2 ^oF), 29.7 ^oC(-21.5^oF), 65.4^oC(149.7^oF), and 81.5^oC(178.7^oF), respectively (Freund et la., 1982).

Paraffins are nontoxic, noncorrosive, and stable. However, paraffins have relatively lower thermal storage capacity (when compared to hydrated salts), which is the result of their lower density and lower latent heat of fusion. Another of the drawbacks of paraffins is their flammability. Therefore, fire retardant formulation should be used.

1.2.2 Mathematical solutions to the phase change heat transfer problem

1.2.2.1 Exact solutions

In the 1860s, Franz Neumann presented the exact solution for a semi-infinite phase change problem with first type boundary condition (Yao and Prusa, 1989). El-

Genk and Cronenberg (1979) provided a solution for heat transfer across a liquid phase at phase change temperature using second type boundary conditions. For the third type boundary condition, no exact solution is yet available. In general, the key requirements for a possible solution of heat transfer in substances undergoing phase change are 1) unbounded domain, 2) constant thermo physical properties, and 3) constant temperature boundary conditions driving the phase change process (Yao and Prusa, 1989).

1.2.2.2 Approximate solutions

The integration method is an approximate method for the solution of phase change problems. The basic principle behind the integration method is related to fixing the formats of all the variables, usually through the use of second order polynomials. After this step, the coefficients in the assumed format can be determined directly from the boundary conditions. Goodman (1964) solved several phase change problems, including problems with first, second, and third type boundary conditions for semi-infinite bodies.

As a powerful tool to solve nonlinear problems, the perturbation method is another approximate method that can be used to solve phase change heat transfer problems. The basic idea of the perturbation method is that the differential equations that govern the physical aspects of the problem are cast into dimensionless form as the first step. Then, the one variable with of smallest magnitude is chosen to be the perturbation quantity, ϵ. Usually, the choice of ϵ is based on the understanding of the problem or experience. Then, the rest of the variables are expanded in terms of ϵ. For

this, boundary conditions are used to obtain the constants used in the expansion (Aziz and Na, 1984). This method has been successfully used to solve phase change problems with simple geometries, like one-dimensional planar slabs (Charach et al., 1987) and cylinders (Song, 1981).

1.2.2.3 Numerical methods (finite difference and finite element)

All the exact solutions and analytical methods are limited to some specific types of problems, which also involve simple boundary conditions, such as simple shapes of the PCM, uniform temperature boundary and uniform initial conditions. In real applications, the computational domain and/or the boundary conditions are too complicated for these analytical methods.

Nowadays the use of numerical methods has become the preferred approach of solving phase change heat transfer problems. Finite difference and finite element methods provide accurate solutions to the heat transfer problem with phase change (Arampatzis and Assimacopoulos, 1998, Stetiu and Feustel, 1998, Giangi et al., 1999, and Heim and Clarke, 2004).

1.2.3 PCM models used in numerical simulation

Phase change problems can be expressed using three equations: one energy equation for the solid region, one energy equation for the liquid region, and a heat balance equation for the interface. Of the PCM models that have been developed to

solve the phase change problem, the most commonly used ones are the enthalpy method and the apparent (effective) heat capacity method.

1.2.3.1 Enthalpy method

If it is assumed that the enthalpy in the energy equation is composed of sensible and latent parts, the sensible enthalpy is calculated by

$$h_s = h_{ref} + \int_{t_{ref}}^{t} C_p(t)dt \qquad (1\text{-}1)$$

The latent part, h_l, is calculated by

$$h_l = \Delta h \times f \qquad (1\text{-}2)$$

where,

Δh = the heat of fusion, kJ/kg, (Btu/lbm)

f = the liquid fraction.

The liquid fraction, f, is the fraction of the melted PCM in the total PCM. In this case, f = 0 if the temperature is below the solidification temperature (no liquid in the PCM), and f = 1 if the temperature of the PCM is above the melting temperature (no solid in the PCM). If the temperature is between the melting and the solidification temperatures, then

$$f = \frac{T - T_{solid}}{T_{liquid} - T_{solid}} \quad \text{(liquid and solid coexist in the PCM)} \qquad (1\text{-}3)$$

where,

T = Temperature of the PCM, ^{o}C, ^{o}F

T_{liquid} = the upper-limit of the phase change temperature range, ^{o}C, ^{o}F

T_{solid} = the lower-limit of the phase change temperature range, ^{o}C, ^{o}F.

Then instead of temperature, the enthalpy, $H = h_s + h_l$, is cast into the following equation

$$\frac{\partial}{\partial t}(\rho H) + \nabla \cdot (\rho \bar{V} H) = \nabla \cdot (k \nabla T) + S \qquad (1\text{-}4)$$

In Equation 1-4, $\bar{V}$ is the speed vector of the liquid phase. Note that if only conduction is considered, the term containing $\bar{V}$ disappears. S is the internal heat source term. ρ and k represent the density and conductivity, respectively. For a phase change problem that involves convection, the enthalpy-porosity method can be used (Voller and Prakash, 1987, Giangi et al., 1999, and Casella and Giangi, 2001).

1.2.3.2 Apparent (Effective) heat capacity method

Carslaw and Jaeger (1959) suggested that an additional value could be added to the specific heat during the phase change process to simulate the delayed effect of the phase change on the heat transfer process. If it is assumed that the potential heat is evenly released throughout the whole phase change process, the following set of equations can be written

$$C_p' = \frac{\Delta h}{T_{liquid} - T_{solid}} + C \quad \text{if } T_{solid} \le T \le T_{liquid} \tag{1-5}$$

and $C_p' = C$ if $T < T_{solid}$ or $T > T_{liquid}$ (1-6)

where,

C_p' = effective heat capacity, J/(kg·K), Btu/(lbm·^{o}F)

C = real specific heat of PCM, J/(kg·K), Btu/(lbm·^{o}F).

In this fashion, only one energy equation is needed. Other relationships between the effective heat capacity and temperature are used. Heim and Clarke (2004) assumed a linear relationship, while Darkwa et al. (2006) expressed the effective heat capacity in a Gaussian format.

Compared to the enthalpy method, this method is more straightforward and generally more efficient in terms of computing time (Yao and Prusa, 1989). For this reason, in recent research and especially in the simulation of real applications, the apparent heat capacity method is more popular than the enthalpy method (Petrie et al., 1995, Stetiu and Feustel, 1998, and Heim and Clarke, 2004). One drawback of the apparent heat capacity method is that the latent heat might be "jumped" during the calculations. This is particular of cases involving PCMs with a narrow phase change temperature range in which a large time step in the finite differences is used. In other words, the temperature of the node "jumps" past the phase change range in one time step and the latent heat is ignored in the calculation. Pham (1985) presented a method that would prevent this "jumping" from happening.

1.2.4 Current study: PCMs' applications in buildings

PCMs have been utilized in many industries, for example, aerospace, pharmaceutical, automotive and the sports industries, to name a few. Building researchers have also made significant efforts to explore how PCM technology can be used in buildings.

Because PCMs would be in the liquid state when melted, it is necessary to encapsulate it. Macroencapsulation and microencapsulation are often used. In macroencapsulation, also referred to as large volume containment in some references (Cabeza et al., 2007), leakage of the PCM from a container could potentially be a life long problem. In addition, the installation of such containers would require extra labor. Furthermore, the heat transfer across the container is poor when PCMs are undergoing the solidification process (Schossig et al., 2005).

Microencapsulation refers to the packaging of micronized material in the form of capsules, which range in size from 1μm to about 300μm. Microencapsulation can 1) reduce the reactivity of the PCM with the outside environment, 2) increase the heat transfer area, and 3) permit the PCM to withstand the volume change when phase change occurs (Schossig et al., 2005). Hawlader et al. (2003) used the coacervation and spray drying methods to microencapsulate the paraffin, which resulted in the PCM microcapsules having a high-energy storage and release capacities. The latent thermal storage capacity depends on the ratio of coating to paraffin.

Salyer and Sircar (1990) proposed four other ways of incorporating the PCM into the building materials. These are:

1. Direct imbibing of melted PCM into the open spaces in the porous materials.

2. Containment of PCM by swelling it into a matrix of cross linked high-density polyethylene pellets or sheets.

3. Mixtures of PCMs with uncrossed linked high-density polyethylene.

4. Mixtures of PCMs with hydrophobic silica to form a dry powder.

Various thermal storage-building materials have been developed and tested experimentally and via numerical simulation. Some examples are reviewed below.

1.2.4.1 Wallboards

Wallboards are treated by directly impregnating them in melted PCM (Feldman et al., 1991, Scalat et al., 1996, and Heim and Clarke, 2004). The microencapsulation method mentioned above has also been used in wallboards (Schossig et al., 2005). All these showed positive results regarding temperature fluctuations in the wall surfaces, peak heat flux reductions and peak heat flux shifting. According to Feldman et al. (1991), the water absorption ability of PCM boards is only one-third of that of a standard board. Because of the high water resistance, in some situations, condensation could become a problem.

Oak Ridge National Laboratory (ORNL) conducted aging tests of the imbibed boards by setting some samples at 38 ^{o}C (100.4 ^{o}F) for three months. In these tests, no mass loss or “pooling” were observed. A sample was run to 200 melt/freeze cycles where differential scanning calorimeter (DSC) tests showed no significant changes in the storage properties of the boards (Kedl and Stovall, 1989).

Stetiu and Feustel (1998) used a finite difference program called RADCOOL to study PCM wallboard's performance in an office building in California. They concluded that when the nighttime temperature was above 18 ^{o}C (64.4 ^{o}F), some other discharge (heat rejection from the PCM) system would be needed other than ventilation for the solidification process of the PCM to be completed.

Heim and Clarke (2004) used the effective heat capacity method to simulate a passive solar building. The simulation results showed that PCM-wallboards designed for passive heating worked properly under spring-autumn weather condition. For summer cooling season, a wider analysis was recommended.

Other than the thermal storage performance, Scalat et al. (1996) tested the Volatile Organic Compounds (VOCs) concentration level when a PCM (fatty acid esters) wallboard was installed. The results were all under ASHRAE (American Society of Heating, Refrigerating, and Air-conditioning Engineers) standard limits; that is, indoor air quality (IAQ) would not be affected by the PCM in this case, but VOC problems should be a considered if organic PCMs are used.

1.2.4.2 Concrete panels and blocks

Cabeza et al. (2007) mixed microencapsulated PCM into concrete panels. From field test, the results demonstrated a real opportunity in energy saving. According to this research, the presence of the PCM would affect the mechanical strength of the concrete. Therefore, the concrete blocks or concrete panels should be tested to make sure they have enough strength for building applications.

1.2.4.3 Multilayered walls

Ismail and Castro (1997) placed a layer of PCM in the middle of a brick wall and ceiling system. Experimental results showed that the PCM could maintain the indoor temperature very close to the established comfort limits. Numerical simulation results agreed with the experimental results.

1.2.4.4 Insulation systems

Petrie et al. (1995) tested the performance of hydrated calcium chloride dispersed in perlite and contained within watertight test cells. From test results, the cells that had a PCM/perlite ratio of 2:1, by weight, reduced the peak heat flux by 42%. The peak heat flux in the PCM/perlite test cells was delayed by four hours. The 6:1 ratio cells produced a 79% peak heat flux reduction. The effective heat capacity method was used to simulate the thermal behavior of the mixtures of perlite and phase change material.

ORNL conducted research on PCM-enhanced cellulose insulation (Kośny et al., 2008). A paraffin PCM was first microencapsulated using acrylic polymer shells with a diameter between 2 and 20 micrometers. Then, the newly created spheres were added to the insulation. The performance of the mixture was tested in a dynamic hot-box. For the first five-hour ramp period, the PCM-enhanced cellulose material reduced the total heat transfer rate through the wall by over 40% when compared to a control wall with the same insulation. The mixed insulation samples passed the smoldering combustion tests (ASTM C1149). The conductivity of the mixture did not change significantly when compared to the results of the control insulation system.

Zhang et al. (2005) performed field tests of pipe-encapsulated paraffin-based PCM wall insulation systems. The performance of these systems was tested using two side-by-side houses of identical construction under full weather conditions. Results indicated that the peaks of the space cooling load were reduced by 8.6% and 10.8% for PCM concentrations of 10% and 20%, respectively. The concentration of PCM was based on the weight of the interior wallboard layer of the wall. The pipe-encapsulated hydrated salt PCM was also tested using the same testing houses (Medina and Stewart, 2008). The results showed that the PCM offered the potential to reduce the peak heat transfer rate through the walls by 27%. It was also found that the interior wall surface temperatures fluctuations could both be reduced by 2.6 ^{o}F.

Medina et al. (2008) and Medina and Zhu (2008) studied the performance of PCMs in structural insulated panel (SIP) outfitted with PCM encapsulated in pipes using two side-by-side test houses (Medina et al., 2008) and a dynamic wall simulator (Medina and Zhu, 2008). This research concluded that SIPs could benefit from the presence of PCMs. Copper pipes were the recommended container and a horizontal pipe arrangement performed better than the vertical pipe arrangement.

1.3 Research objectives

The overall objective of this research was to find a practical method by which PCMs can be incorporated into the wall insulation of residential buildings to reduce the peak space cooling load in the summer.

To achieve this goal, the main tasks of this research were:

1. To study the working environment of the PCMs (i.e., the temperatures within the wall) and the properties of the PCMs.

2. To obtain detailed information about the phase change process, especially the phase change process starting from partially-melted states.

3. To directly verify the potential to reduce peak cooling loads via experimental research using side-by-side test houses under full weather conditions and a dynamic wall simulator under controlled laboratory conditions.

4. To develop a robust phase change heat transfer model.

5. To investigate the principle of the peak heat flux reductions and to determine a practical method of incorporating the PCM into the wall systems.

6. To conduct parametric studies and to predict the performance of PCM-enhanced wall systems in different climate zones using numerical simulation.

A schematic of the research framework is shown in Figure 1.2.

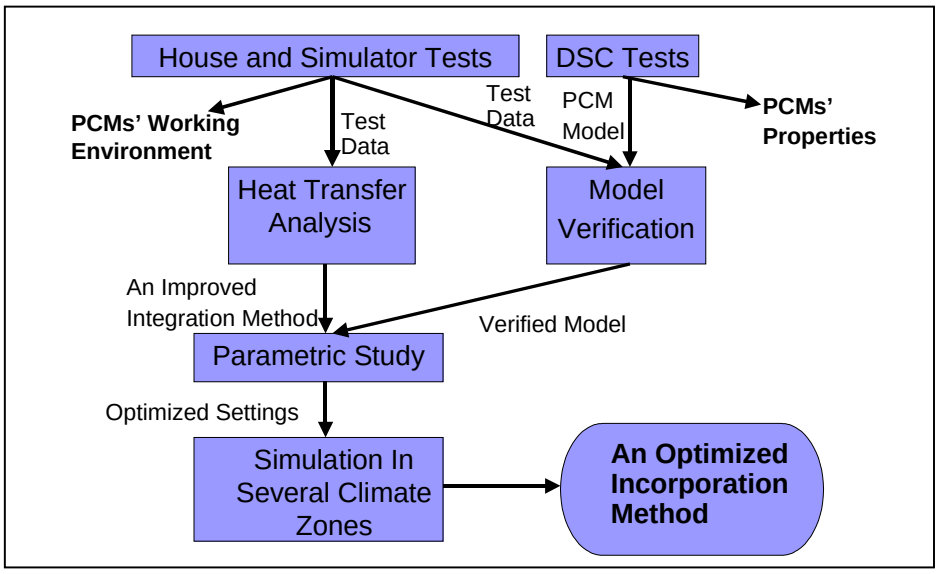

Figure 1.2 Research framework

Chapter II

Study of the PCMs' Working Environment and Properties of Various PCMs

The working environment of the PCMs (i.e., the temperatures within the wall) and the properties of the PCMs themselves are two factors that are critical for the successful application of PCMs in building walls. In this chapter, temperature data from summer field experiments were studied to find wall surface temperature change ranges and typical wall temperature values under which PCM would normally work in real applications. The temperature distribution and the daily temperature change in different locations within a wall, for a typical hot day, were studied using numerical methods where field experimental data were used as boundary conditions. Results of Differential Scanning Calorimeter (DSC) tests, performed on pure PCMs, PCM/cellulose mixtures, and "aged" PCM samples, used to better understand PCMs' thermal behavior, the effects of mixing them with cellulose insulation, and the impact that ambient air had on samples when these were exposed are presented. The results of the mass change tests, carried out to investigate PCMs' mass changes when these were exposed to ambient air under room temperature and under high temperature conditions are summarized. Recommendations for application of PCMs in real application are provided.

2.1 Study of temperatures within residential building walls

2.1.1 Test setup

Field experiments were performed using two small-scale test houses located on West Campus of the University of Kansas in Lawrence, Kansas, U.S.. The test houses were 1.83 m by 1.83 m by 1.52 m (6 ft by 6 ft by 5 ft high) and were built using typical residential house frame wall construction practices. The test houses and their cooling system are shown in Figure 2.1. The internal structure of the wall, showing the structural stud framing and siding, is shown in Figure 2.2. Both houses were air-conditioned using fan coil units. A small refrigeration chiller produced cold water that was used for space conditioning. Zhang (2004) provided more detailed information about the system.

Figure 2.1 Test houses and cooling system

Figure 2.2 Internal structure of test house walls

Type T thermocouples were installed to measure the exterior wall surface temperatures, indoor wall surface temperatures and indoor air temperatures. Heat flux meters were installed on the interior side of each wall to monitor the heat transfer rates per unit area through the walls. The thermocouple and heat flux meter used in the experiments are shown in Figure 2.3. Six heat flux meters were installed on the west wall, two were on east wall, four on the south wall, and four on the north wall. The data from the sensors on each wall were averaged and used in the analyses. The different number of sensors per wall responds to the features found in each wall. For example, a significant portion of the east wall was used by the fan coil unit. The south wall had a window. Part of the north wall was a removable door. The west wall did not have any of the mentioned features, and therefore, there was more space for sensors.

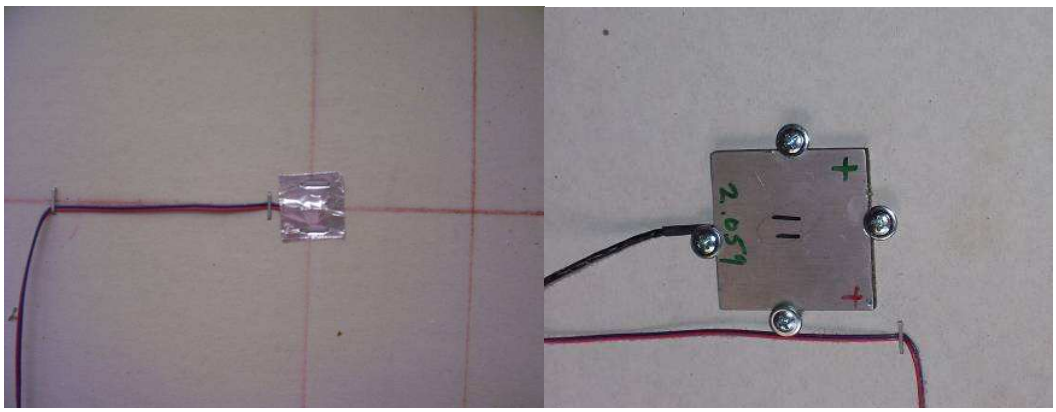

Figure 2.3 Types of thermocouple and heat flux meter used in the experiments

A data logger and a computer were housed in a small wooden shed, as shown in Figure 2.4. The data collection system collected the data at an interval of 10 seconds, which were later averaged hourly or every half hour.

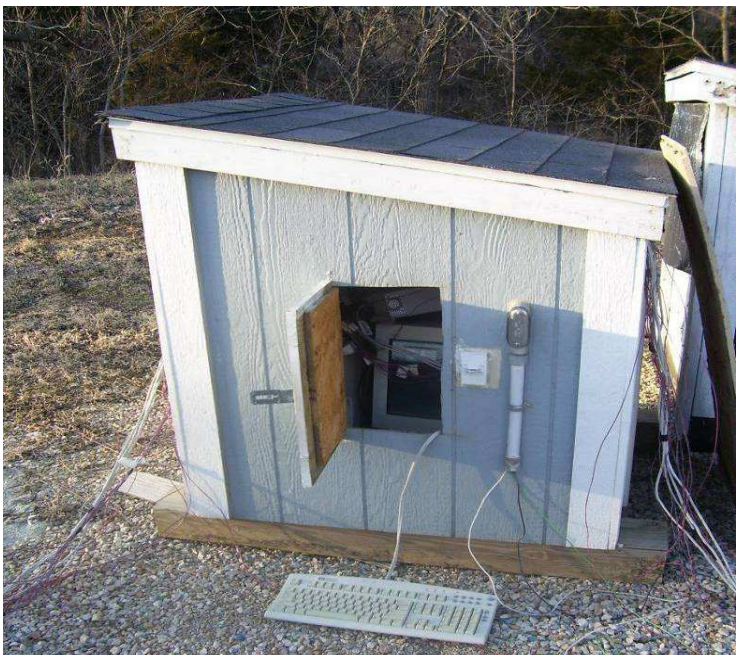

Figure 2.4 Wooden shed housing the data logger and computer used in the field experiments

2.1.2 Analysis of summer data

Experiments were run all year long; however, because the focus of this research was on the peak space cooling load reduction and load shifting, only summer data (July and August) are discussed in this chapter. The distribution of the daily maximum/minimum outdoor air temperatures and the exterior wall surface temperatures, based on data collected over a two-year period, are shown in Figures 2.5 through 2.7. From Figure 2.5, it was found that in 40% of days, the maximum outdoor air temperature was 35 ^{o}C (95 ^{o}F) or higher, while nights were relatively cool. Eighty-eight percent of days had a minimum temperature of 23 ^{o}C (73.4 ^{o}F) or lower.

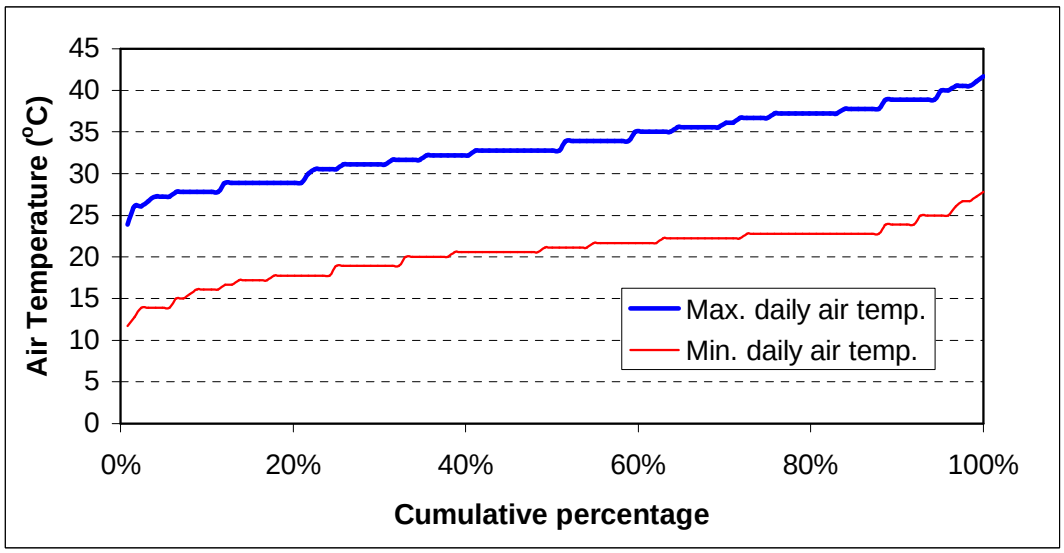

Figure 2.5 Cumulative percentages illustrating the distribution of daily maximum and minimum outdoor air temperatures

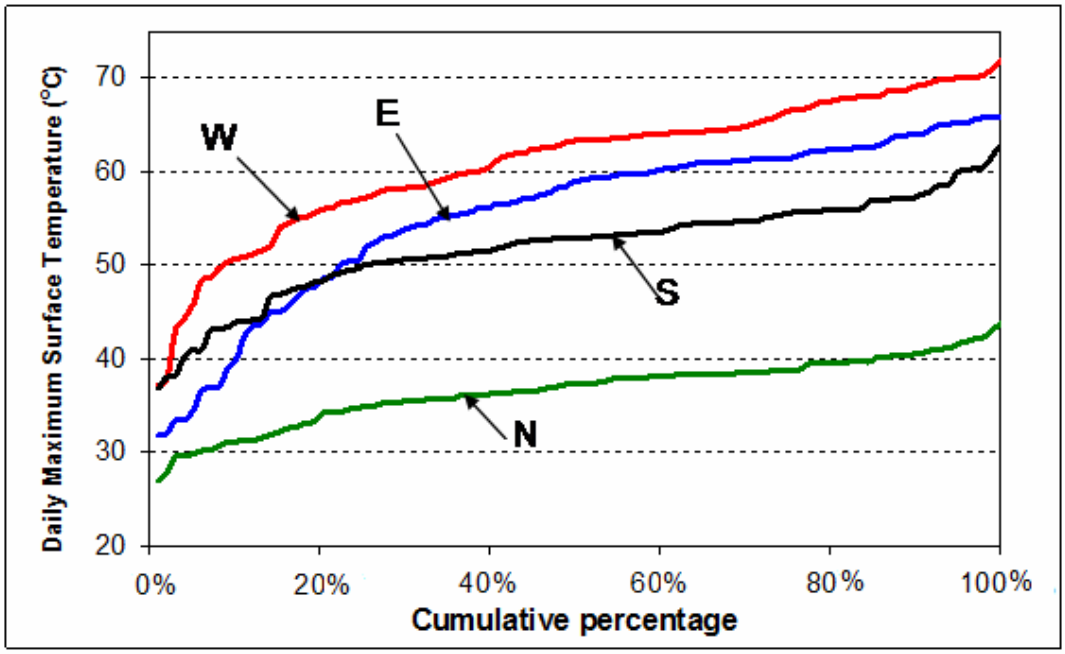

Figure 2.6 Cumulative percentages illustrating the distribution of daily maximum exterior wall surface temperatures

As depicted in Figure 2.6, the west wall had the highest maximum wall surface temperature while the north wall always had the lowest temperature. These temperatures were driven by the amount of solar radiation incident on the walls. Also under different weather conditions the maximum exterior wall temperature varied significantly during the summer. This was true for all the walls. For example, the highest maximum temperature of the west wall reached 71.9 ^{o}C (161.4 ^{o}F), while the minimum value was 37.1 ^{o}C (98.8 ^{o}F). This is important in the current analysis because this means that the requirements for the PCM (e.g., melting temperature) could differ in the same season. Because hot days were of more interest in this research, those temperatures that were higher than 80% of all the data points were chosen as the typical exterior wall temperatures for later study. For example, for the

east wall the selected maximum exterior wall surface temperature was 62.3 ^{o}C (144.1 ^{o}F); for the west wall it was 67.8 ^{o}C (154.0 ^{o}F); for the south wall it was 55.9 ^{o}C (132.6 ^{o}F); and for the north wall it was 39.5 ^{o}C (103.1 ^{o}F).

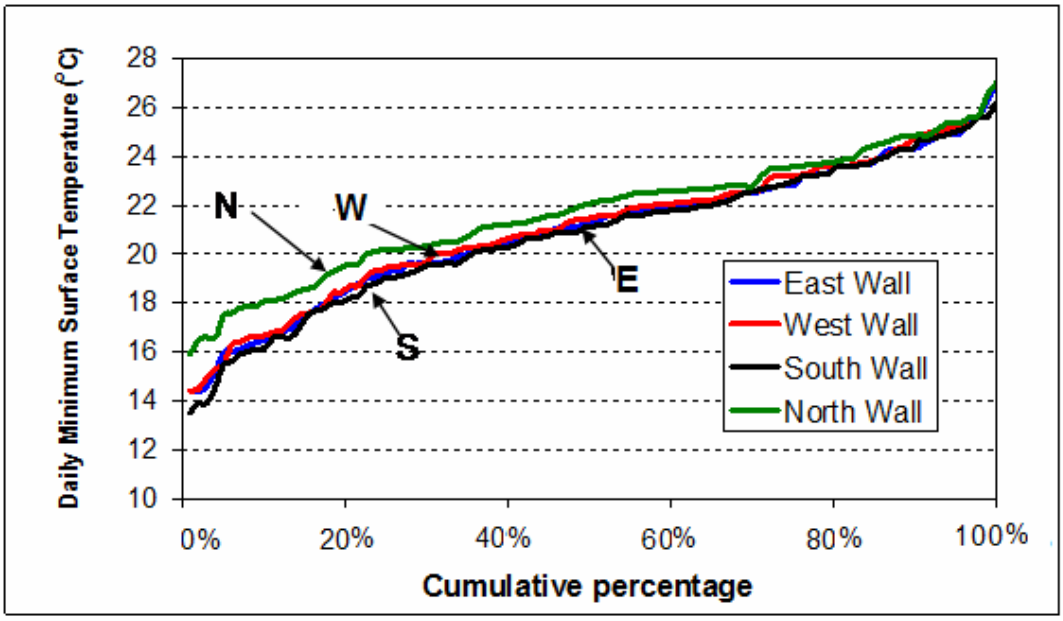

Figure 2.7 Cumulative percentages illustrating the distribution of daily minimum exterior wall surface temperatures

Unlike the maximum temperature, in the absence of solar radiation at night and early mornings, the minimum exterior wall surface temperatures for the four walls were very close to each other. The difference of the four walls, as shown in Figure 2.7, might come from the difference in the radiation exchange with the surrounding environment and the sky. Therefore, the west wall's minimum temperature data, which were always in between the highest and the lowest, were chosen for analysis. Figure 2.8 shows the distribution of daily maximum and the corresponding daily minimum temperatures for the exterior surface of the west wall.

The figure shows that on the top 20% of hot days the minimum exterior wall surface temperatures were mostly above 20 ^{o}C (68 ^{o}F). Because higher minimum temperatures at night would make it more difficult for the PCM to solidify, it was safe to assume that the typical minimum exterior wall temperature for the four walls would be about 23.6 ^{o}C (74.5 ^{o}F), which was higher than 80% of the data points in Figure 2.7.

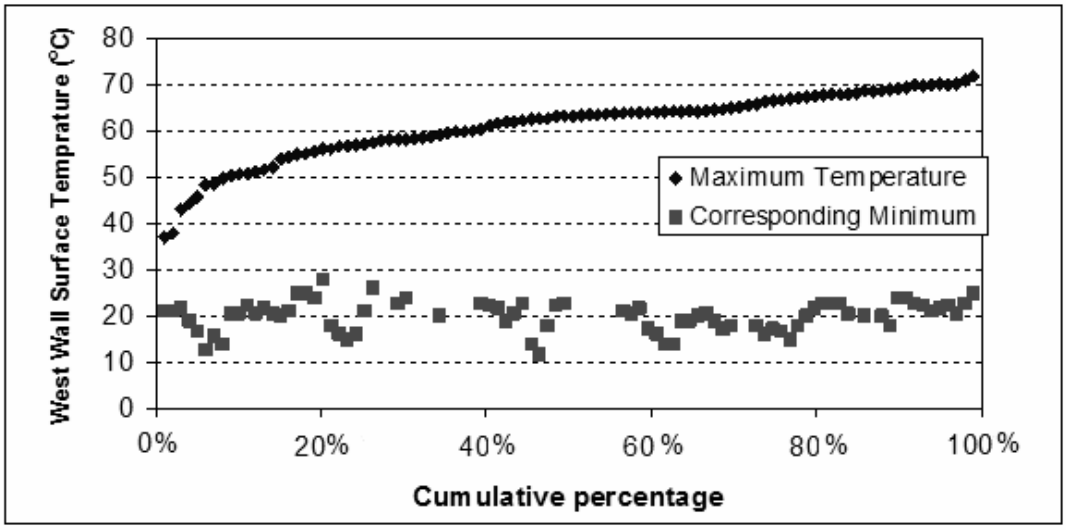

Figure 2.8 Cumulative percentages illustrating the distribution of daily maximum and corresponding minimum temperatures for the exterior surface of the west wall

2.1.3 Study of temperature change in one typical day

The temperature data for one typical summer day (in July) and its two neighboring days, one before and one after, were chosen for a detailed study. The outdoor air temperatures and the exterior wall surface temperatures for the four facing walls are shown in Figures 2.9 and 2.10:

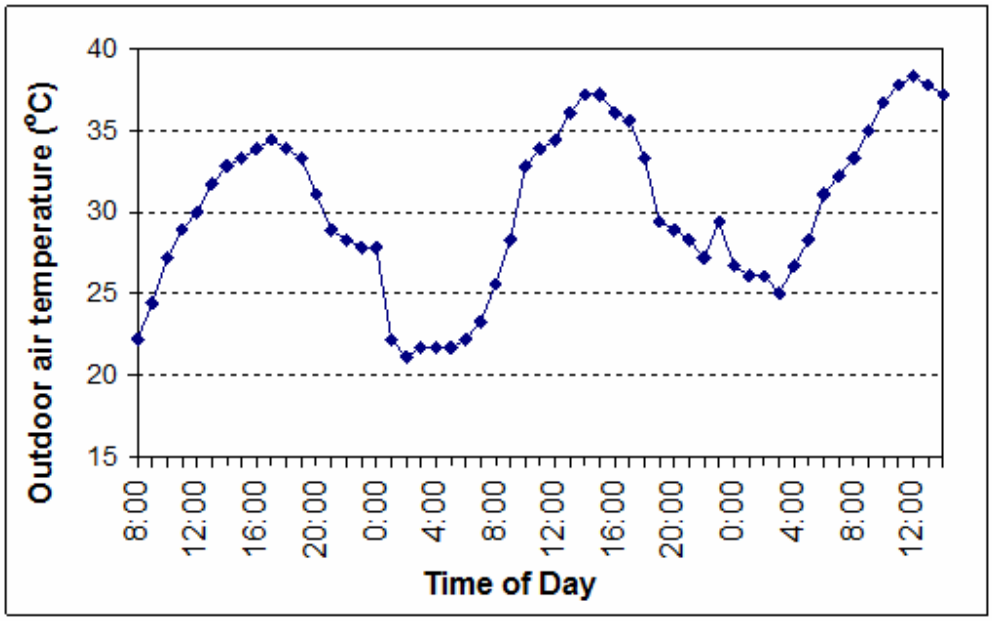

Figure 2.9 Outdoor air temperatures

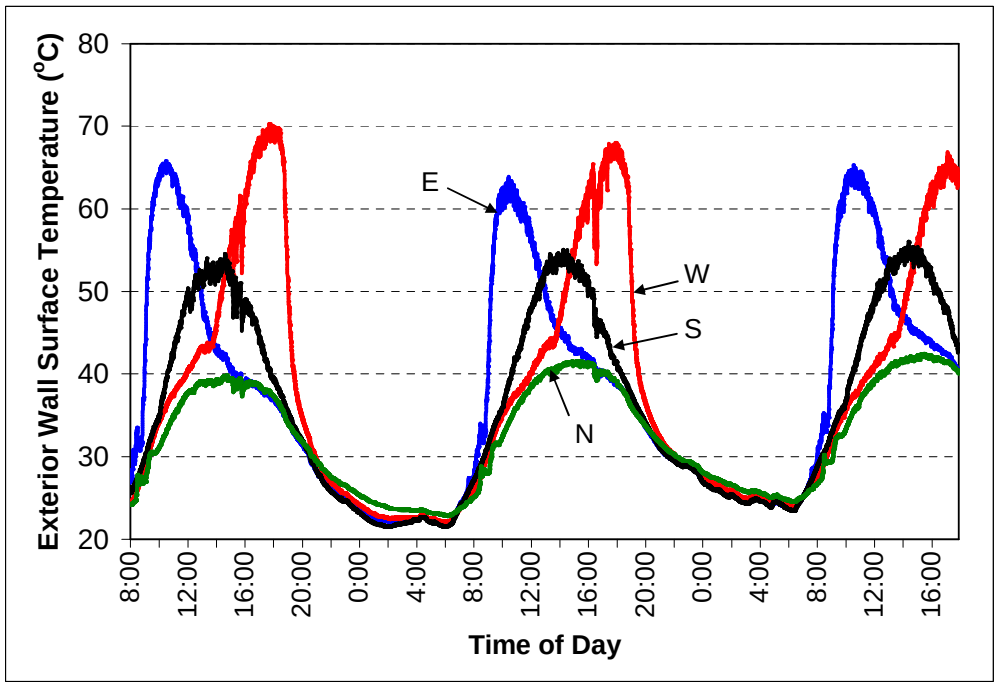

Figure 2.10 Exterior wall surface temperatures

From Figure 2.10, the peak temperature of the west wall occurred in late afternoon (about 6:00 PM) and for the east wall it occurred in the morning (about 10:30 AM). The south and north wall temperature peak hours were in between those of the east and west wall (between 2:30 to 3:00 PM). For the second day in the Figure 2.10, the peak temperatures for the east, west, south and north wall were 63.8 ^{o}C (146.8 ^{o}F), 67.9 ^{o}C (154.2 ^{o}F), 55.1 ^{o}C (131.2 ^{o}F), and 41.5 ^{o}C (106.7 ^{o}F), respectively. The lowest temperatures for the four walls were close to each other, and for the west wall the minimum temperature was 23.9 ^{o}C (75.02 ^{o}F).

In addition to the magnitude of temperatures, both maximum and minimum, the temperature change rate was important to the phase change and overall heat transfer processes. The change rate of the exterior wall surface temperature calculated from 15-minute data intervals is shown in Figure 2.11. It was found that the temperature change rate was less than 0.25 ^{o}C/min (0.45 ^{o}F/min) for most of the day. The maximum change rates were 0.81 ^{o}C/min (1.46 ^{o}F/min) for the east wall and 0.67 ^{o}C/min (1.21 ^{o}F/min) for the west wall, respectively, during times when the radiation incident on the walls varied significantly (e.g., sunrise for the east wall and sunset for the west wall). Furthermore, the further the location was towards the inside of the wall, the lower the temperature change rate was. Unlike previous PCM research, which involved and/or assumed sudden boundary temperature changes, the slow temperature boundary change should be accounted for in PCM modeling in the present research.

PCMs change phase over a temperature range. When the temperature change rate is high, the process is mainly "thermally controlled" (i.e., the process is mainly controlled by the heat transfer and the influence of the PCM phase change properties is limited). The manner in which the heat is absorbed or released over the temperature range does not affect the phase change process significantly. When the temperature change is low, it takes longer for the temperature to go over the whole phase change temperature range. That is, in the melting process, part of the PCM will change phase first while the rest would remain solid and "waiting" until the temperature reaches a value high enough for the PCM to complete the melting process. In this case, the properties of the PCM determine how much PCM will melt at certain temperature and how much heat will be absorbed at a certain time in the phase change process. The process in this case is "property controlled."

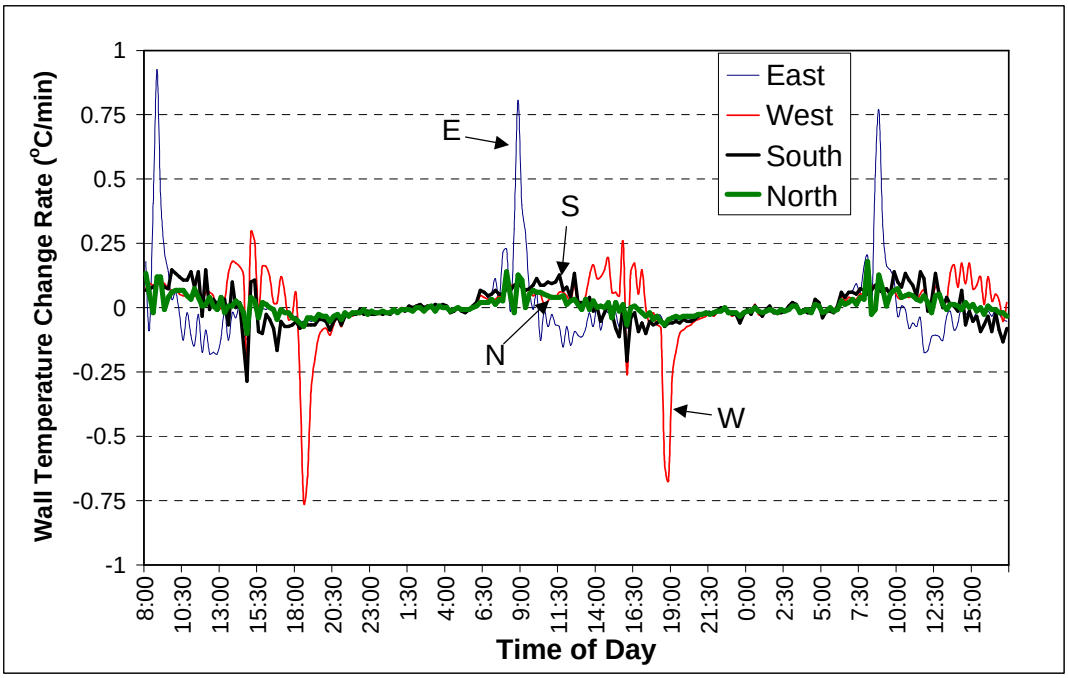

Figure 2.11 Temperature change rate in the four exterior wall surfaces

2.1.4 Temperature distribution within the insulation

Because different locations within the insulation will have different temperature changes, it was necessary to find out the temperature change for different locations within the insulation. The PCM, when added to the insulation, would change the temperature field in the insulation during the phase change process. It is difficult to predict the temperature distribution in advance unless calculations, either analytical or numerical, are made for each individual case. However, the temperature distribution for the case without PCM could provide a starting point for predicting the temperature distribution in the PCM case.

Because the wall cavity was small and the thermocouples themselves would influence the heat conduction in the insulation, it was not easy to keep the

thermocouples in place after installing the insulation and still make accurate measurement of the temperatures at various locations inside the insulation. As mentioned in literature review, using finite difference method to solve the heat conduction equation has proved practical and accurate. Therefore, a computer program was written in FORTRAN to investigate the temperature distribution using the above typical day wall temperature data as boundary conditions. A backward difference (in time) and central difference (in space) scheme was used to discretize the heat transfer equation. A tri-diagonal matrix algorithm (TDMA) was used to solve the algebraic equations. The layers of the wall and their properties are shown in Table 2.1.

Table 2.1 Wall layers and their properties (2005 ASHRAE handbook: Fundamentals)

	Conductivity (W/(m^{o}C))/(Btu/hr·ft·^{o}F)	Density (kg/m^3))/(lbm/ft^3)	Specific heat (kJ/kg^{o}C) /(Btu/lbm·^{o}F)
9.5 mm (3/8 in) siding	0.16/0.092	884/55.2	1.22/0.29
12.7 mm (1/2 in) OSB	0.13/0.075	650/40.6	1.21//0.29
88.9 mm (3.5 in) cellulose insulation	0.04/0.23	48/3	1.38/0.33
12.7 mm (1/2 in) gypsum board	0.16/0.092	800/49.9	1.09/0.26

The hourly temperature distributions in the insulation for the west wall are shown in Figure 2.12 (8:00 to 19:00) and Figure 2.13 (20:00 to 7:00). In these figures for most of the day, except for hours 20:00 and 21:00, the temperature distribution was almost linear. This was the result of the small density of the insulation and the slow temperature change rate. The hours 20:00 and 21:00 represent the two hours after sunset during which the exterior wall surface temperature dropped rapidly. For

the other three walls, the following was found from the simulated results. Except for the hours 9:00 and 10:00, the temperature distribution in the east wall was almost all linear. For the north and south walls, the temperature distribution was almost linear the entire day. Therefore, to simplify the calculation of heat transfer in the insulation, the specific heat of the insulation could be neglected without introducing significant errors.

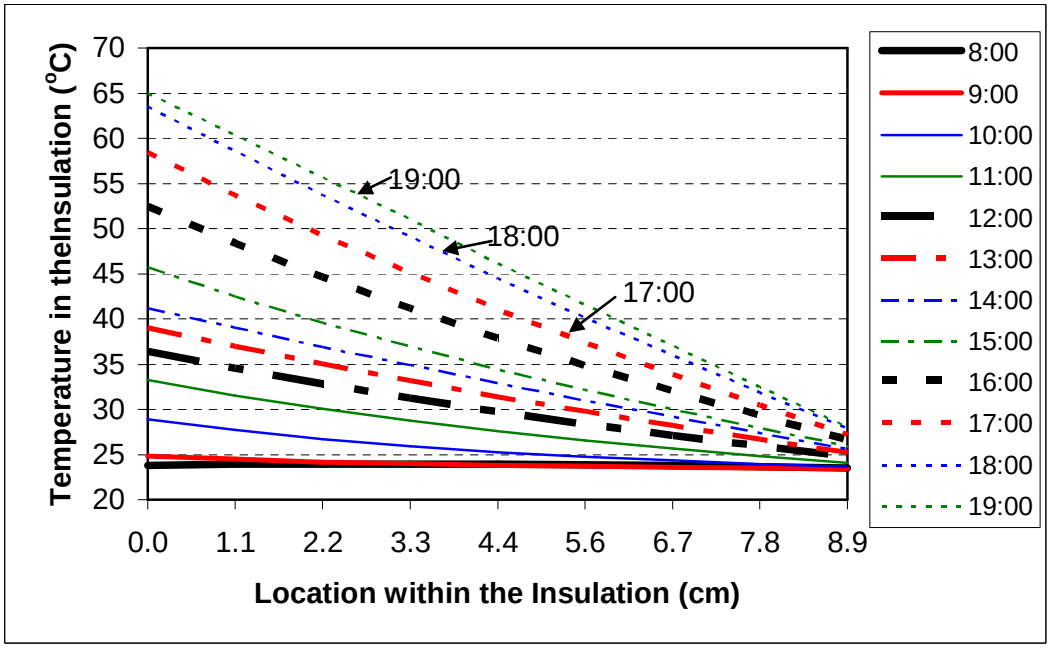

Figure 2.12 West wall hourly temperature profile in a day (8:00-19:00)

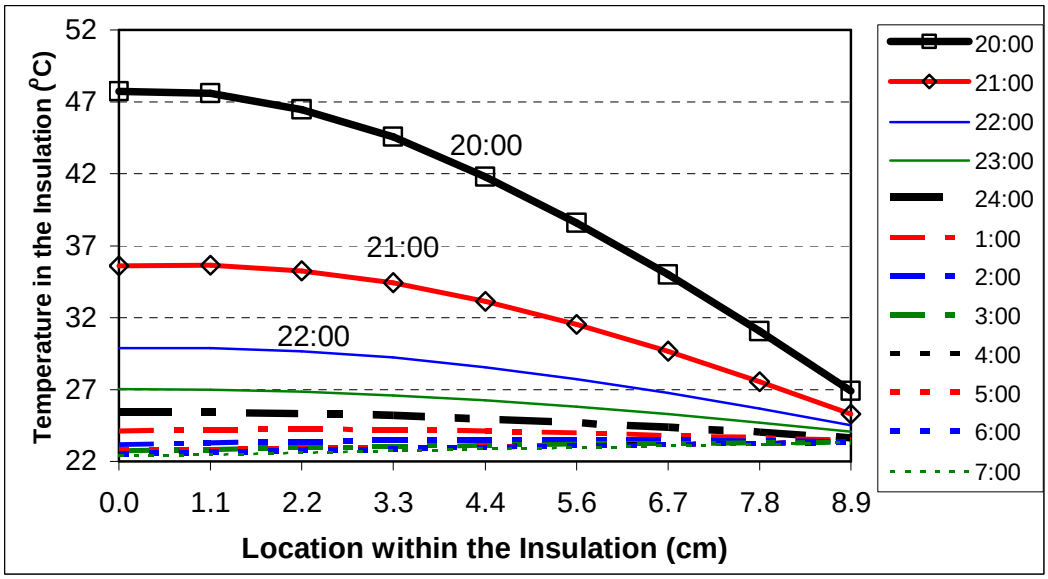

Figure 2.13 West wall hourly temperature profile in a day (20:00-7:00)

Nine different locations were evenly distributed along the insulation, which were labeled “P1” to “P9” (Point 1 to Point 9) from outside to inside as shown in Figure 2.14. The temperature changes for the four walls are shown in Figures 2.15 through 2.18.

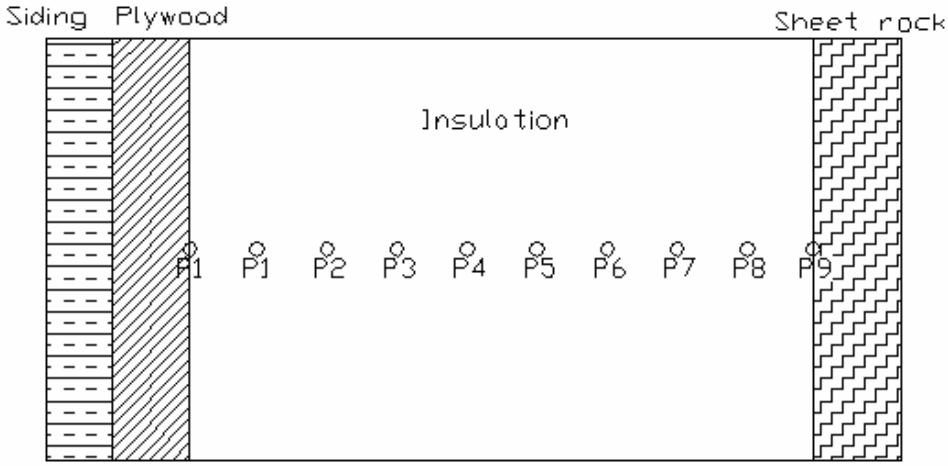

Figure 2.14 Locations of the temperature points within the wall

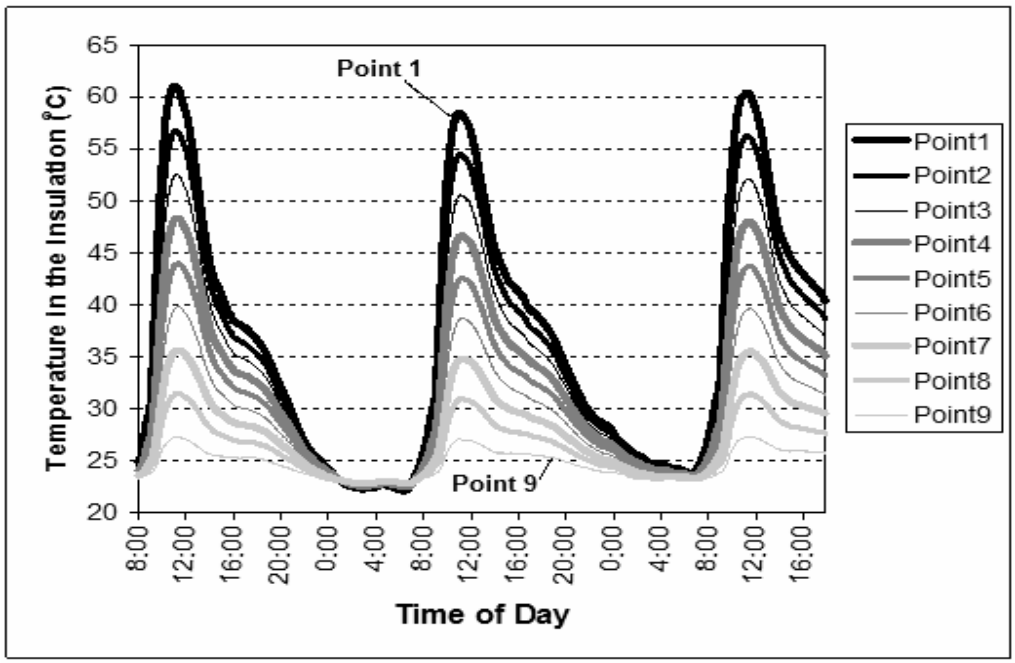

Figure 2.15 Temperature changes in different locations within east wall

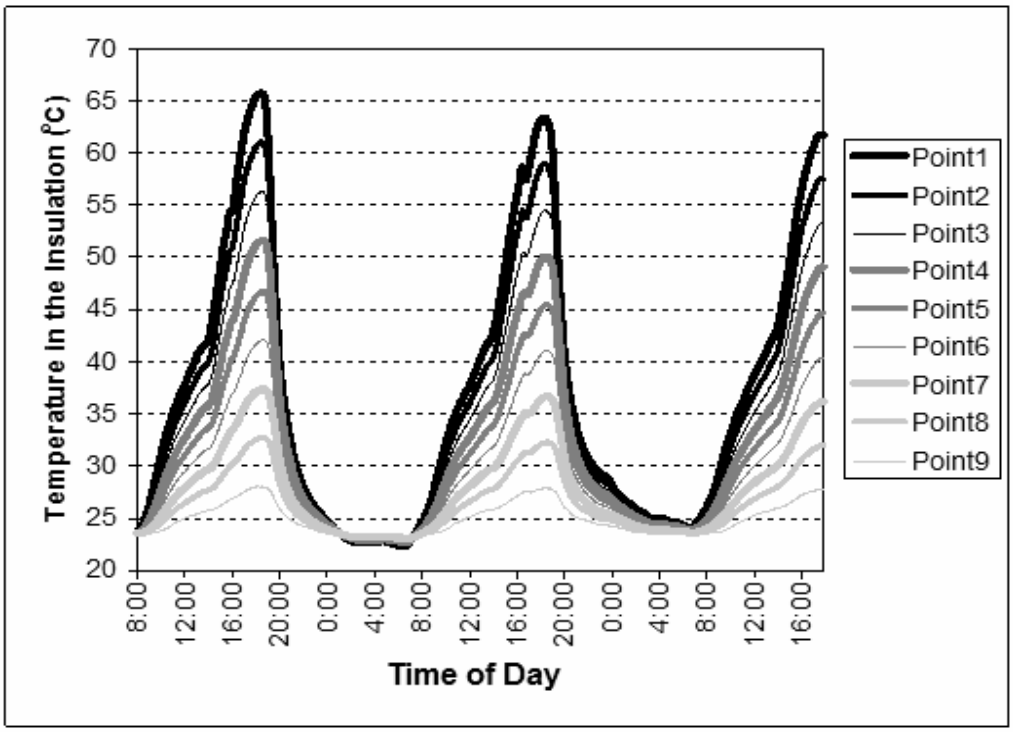

Figure 2.16 Temperature changes in different locations within west wall

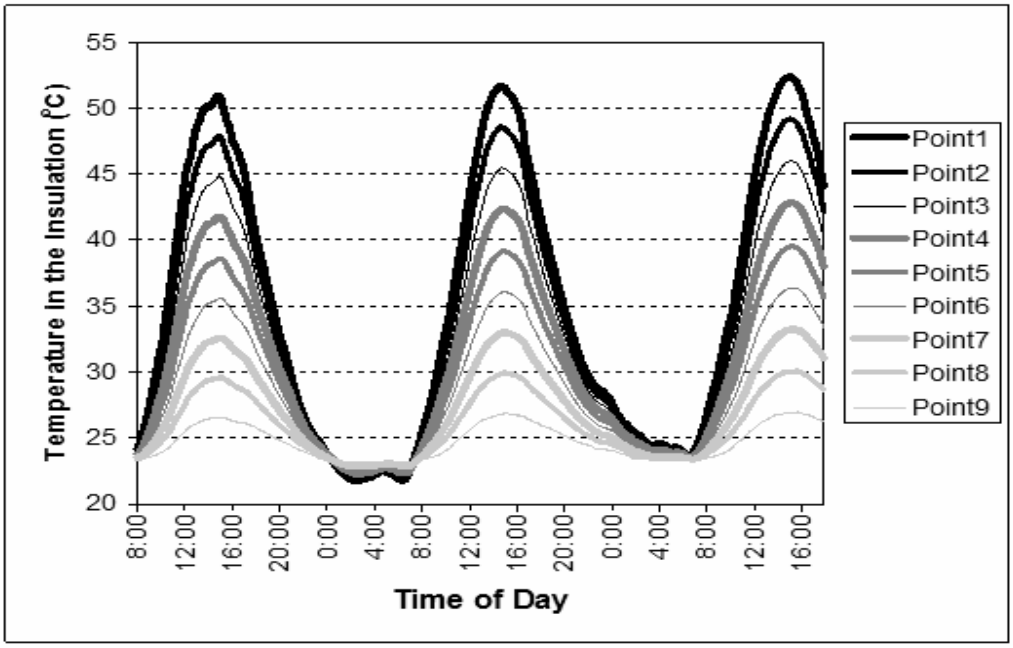

Figure 2.17 Temperature changes in different locations within south wall

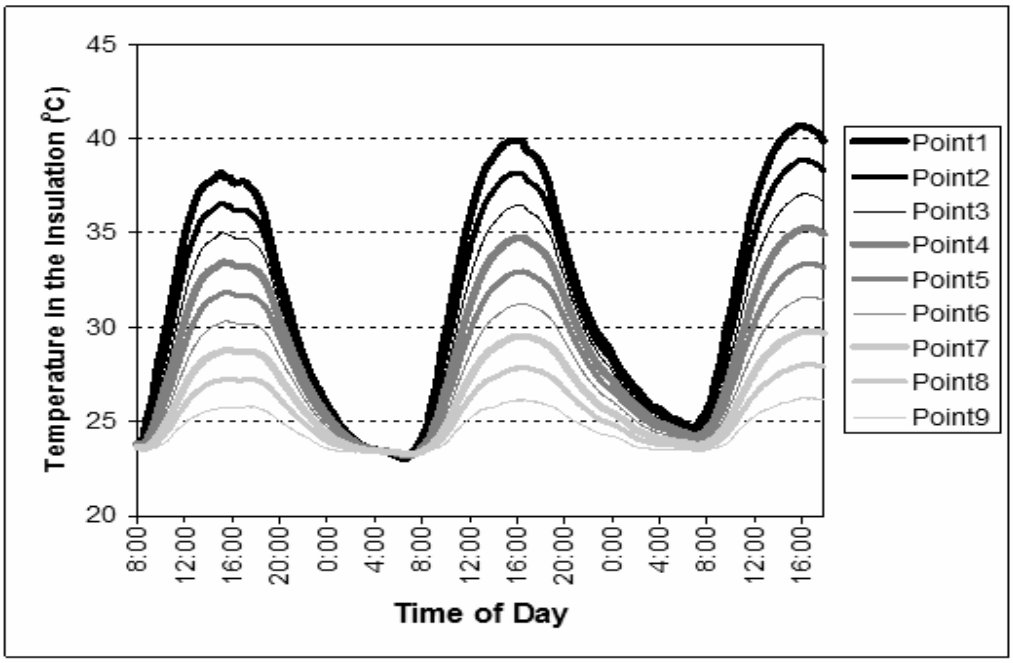

Figure 2.18 Temperature changes in different locations within north wall

As depicted in the graphs of Figures 2.15 through 2.18, for the outermost point (Point 1), the daily temperature change range was the largest, which meant it could tolerate a wider range of PCMs. Towards the inside of the wall, the daily temperature change range became smaller, and therefore, this factor would limit the choices of PCMs.

From the figures above, if the solidification point of PCM were assumed to be 26 ^{o}C (78.8 ^{o}F), then the PCM would most like solidify on a typical day because most of the locations within the insulation would experience this temperature, and other temperatures somewhat below 26 ^{o}C(78.8 ^{o}F), for at least some time during the day. Closer to the inside, this temperature, and temperatures somewhat below this temperature, would be experienced for longer periods of time. Thus, the PCM located closer to the inside was more likely to complete the solidification or at least get close to a complete solidification state.

PCMs melt and solidify over a temperature range. If the working temperatures around the PCM do not cover the whole phase change temperature range, the PCMs will have part of the latent thermal storage capacity "unused," but the PCM could still absorb and release certain percentages of the total latent heat of fusion, as will be shown in later DSC studies.

2.2 Phase change materials used in this research

Four types of commercial PCM products available were chosen as the potential PCMs for building application:

1) Calcium-chloride hexahydrate, which was sold under the trade name TH29 by PCM Energy P. Ltd, Bombay, India.

2) Octadecane paraffin, which was sold under the trade name RT27 by Rubitherm GmbH, Berlin, Germany.

3) Hydrated salt and paraffin mixture, which was sold under the trade name SP25 by Rubitherm GmbH, Berlin, Germany.

4) Paraffin contained in a SiO_2 substructure, which was sold under the trade name PX27 by Rubitherm GmbH, Berlin, Germany

The four PCMs are shown in Figures 2.19 through 2.23. Their property data, as provided by their manufacturers, are shown in Table 2.2.

Table 2.2 Manufacturer properties data of selected PCMs (Rubitherm GmbH and PCM Energy P. Ltd.)

	Approximate melting point ($^oC/^oF$)	Approximate solidification point ($^oC/^oF$)	Latent heat of fusion (kJ/kg, Btu/lbm)	Density (kg/m^3, lbm/ft^3)	Conductivity ($W/(m^oC)$, $Btu/(ft\cdot hr\cdot^oF)$)
Hydrated salt TH29	29/84.2	*	182.4/78.5	1500/93.6	*
Paraffin RT27	28/82.4	26/78.8	147/63.2	870/750,54.3/46.8 (solid/liquid)	0.2/0.12
Paraffin and hydrated salt mixture SP25	26/78.8	25/77	142.5/61.3	1380/86.2	0.6/0.35
Paraffin SiO_2 powder PX27	28/82.4	*	88/37.9	640/40	0.1/0.06

* Data not provided by the manufacturers

Figure 2.19 Picture of hydrated salt PCM at room conditions (24 ^{o}C/75.2 ^{o}F)

Figure 2.20 Picture of paraffin PCM at room conditions (24 ^{o}C/75.2 ^{o}F)

Figure 2.21 Picture of paraffin and hydrate salt mixture PCM at room conditions (24 ^{o}C/75.2 ^{o}F)

Figure 2.22 Picture of paraffin-SiO_2 powder at room conditions (24 ^{o}C/75.2 ^{o}F)

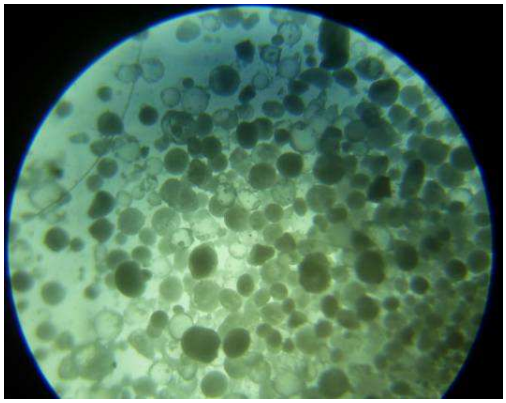

Figure 2.23 Picture of paraffin-SiO_2 powder under 40X microscope

The properties and characteristics of paraffin and hydrated salt PCMs were summarized in the Chapter 1. From observations, the paraffin and hydrated salt mixture (SP25) was found to be close to hydrated salt in appearance. For the paraffin-SiO_2 powder (PX27), paraffin was contained within a hydrophilic silica powder substructure. By observation under a 40X microscope, it was found that the substructure held the paraffin well. Even when the surrounding temperatures were above 40 ^{o}C (104 ^{o}F), no liquid paraffin leaked out and the powder remained in the

same shape. The latent heat of fusion per unit mass of PX27 was lower compared to pure paraffin because the hydrophilic Silica would not change phase at the aforementioned room temperature ranges. Like paraffin PCMs, PX27 are nontoxic, noncorrosive, chemical inert, but flammable.

2.3 PCMs Differential Scanning Calorimeter (DSC) tests

When mixed with cellulose or exposed to the air, some changes may occur to the properties of the PCMs. To investigate this, DSC (Differential Scanning Calorimeter) tests were performed. The DSC is instrumental in helping obtain phase change related properties, such as melting point, solidification point, and latent heat of fusion. A TA Instrument Model 2920 DSC, as shown in Figure 2.24, was used. Dry N_2 gas was connected to the purge gas and vacuum gas ports of the machine at a rate of 50 ml/min. Before testing, the testing cell was cleaned according to the recommendations outlined in the User's Manual. Baseline and cell constant calibrations were run. To prevent the PCM sample from contacting the air, aluminum hermetic pans were used to contain the samples. All the DSC tests were run at 1 ^{o}C/min (1.8 ^{o}F/min) heating or cooling rates.

Figure 2.24 DSC testing system

2.3.1 Hydrated salt based PCM (TH29)

The melting DSC curves for pure hydrated salt, the mixture of hydrated salt with cellulose, with a mass ratio of salt to cellulose of 2.04 to 1, and hydrated salt sample placed in an open container for 14 days are shown in Figures 2.25 through 2.27.

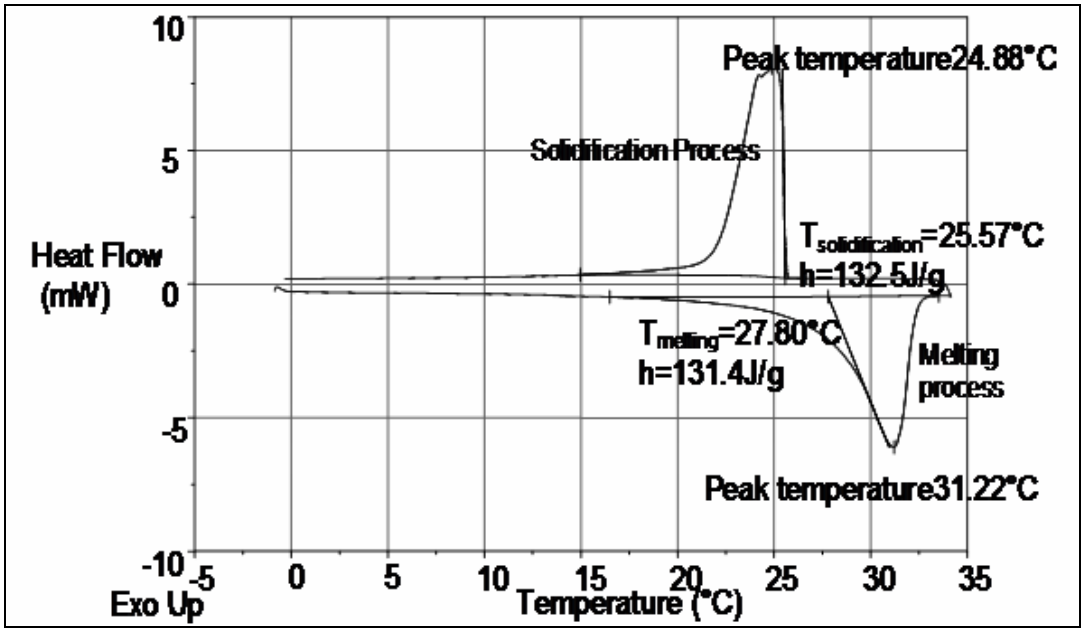

Figure 2.25 DSC curve of pure hydrated salt

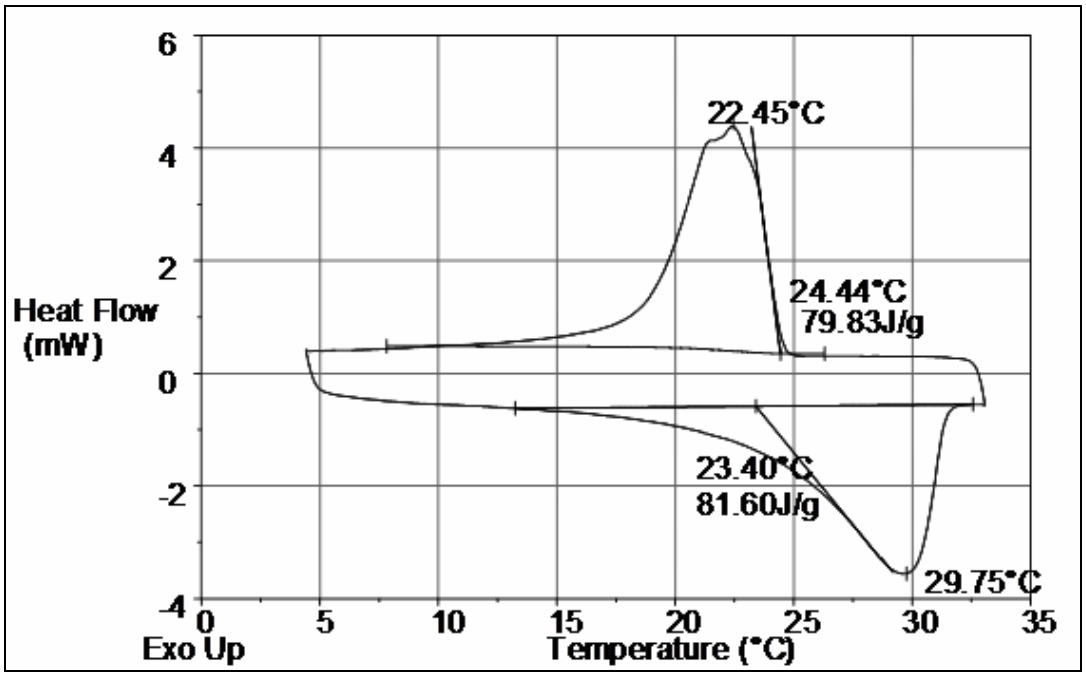

Figure 2.26 DSC curve of hydrated salt cellulose mixture

When mixed with cellulose, the onset point (i.e., usually defined as the melting point) of the salt changed from 27.8 ^{o}C to 23.4 ^{o}C (82.0 ^{o}F to 74.1 ^{o}F) and the solidification point changed from 25.6 ^{o}C to 24.4 ^{o}C (78.1 ^{o}F to 75.9 ^{o}F). Also, the temperature range of phase change (the width of the peak) became broader for the mixture. But because of the inherent problems in the DSC testing as presented in Chapter 5, the above changes in phase change temperature might result from the increase in sample mass and the loose structure of the insulation, which made a larger time delay between the heat flow and temperature signals. More tests, based on the heat of fusion, are needed to get a solid conclusion about the melting/solidification temperature change after mixing hydrated salt with cellulose insulation.

The latent heat of fusion was reduced for the mixture of hydrated salt and cellulose when compared to that of the pure hydrated salt, which was most likely the result of the mass added by the cellulose. If one assumed that the cellulose did not change the properties of hydrated salt and the latent heat of fusion of the pure hydrated salt from Figure 2.25 was used, the latent heat of fusion of the hydrated salt and cellulose mixture would be 88.9 J/g [132.5 x 2.04/(2.04+1)] (38.25 Btu/lbm). The experimental results were 81.6 J/g (35.11 Btu/lbm). The difference of 8.2% might come from the method used to integrate the area under the curve, an error in weighting, and/or an error from the DSC tests. Or, it could be that some moisture was absorbed by the salt in the process of mixing the cellulose with the insulation, which would lower the latent heat of fusion. Therefore, the cellulose would not significantly

affect the latent heat of fusion of the hydrated salt in the mixture with cellulose. The property change at different concentration level needs further study.

As stated above, hydrated salt is hygroscopic. After the sample was placed in the open air for 14 days, moisture was absorbed and the mass of the sample changed from 17.98 mg to 29.24 mg. The latent heat of fusion dropped from 131.4 J/g to 1.2 J/g (56.53 Btu/lbm to 0.52 Btu/lbm), as shown in Figure 2.27. That is, the hydrated salt lost most of its thermal storage capacity.

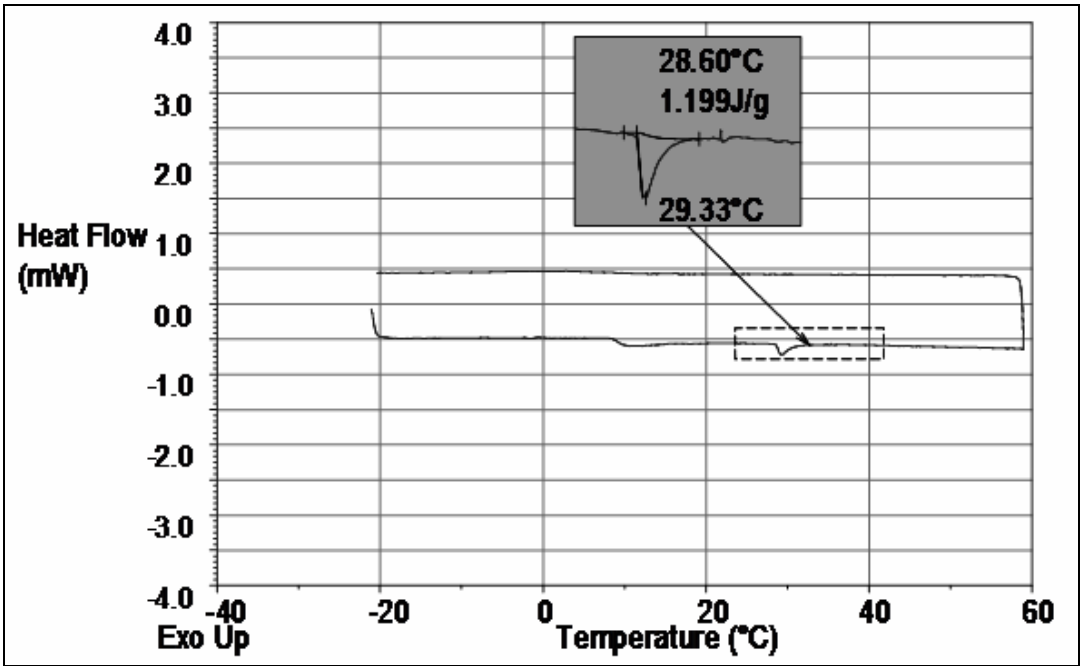

Figure 2.27 DSC curve of the hydrated salt after absorbing moisture

2.3.2 Paraffin based PCM (RT27)

DSC tests were also performed to investigate property changes of paraffin based PCM when mixed with cellulose, with a mass ratio of paraffin to cellulose of 0.7 to 1, and exposed to the air. Results are shown in Figures 2.28 through 2.30.

From the figures, it can be seen that when mixed with cellulose, the melting curve of the pure paraffin did not change significantly and that the solidification curve was broadened. Also, the solidification point did not change significantly. For the same reason as the hydrated salt test, more tests based on the heat of fusion are needed to get a solid conclusion about the temperature change after mixing paraffin with cellulose insulation.

Compared with pure PCM, the latent heat of fusion of the mixture with cellulose decreased from 137.5 J/g to 60.45 J/g, which was the result of the mass of the cellulose added. Assuming that the cellulose did not change the properties of the paraffin and the latent heat of fusion of the pure paraffin from Figure 2.28 was used, the latent heat of fusion of the paraffin and cellulose mixture should be 56.83 J/g [137.5 x 0.7/(0.7+1)], 24.45 Btu/lbm. The test result was 60.45 J/g (26.0 Btu/lbm). The difference of 6.37% may also come from the same sources listed above. Therefore, the cellulose would not affect the latent heat of fusion of the paraffin in the mixture with cellulose much.

By comparing the DSC curves in Figures 2.28 and 2.30, the “aged” paraffin, which consisted of the paraffin placed in the open air for one year, had higher melting and solidification points and larger latent heat of fusion. The difference might come from the change in the composition of paraffin after oxidation. Again, tests based on the heat of fusion are needed to get a solid conclusion about the temperature change. Furthermore, as this is only one of the “aged” samples, more studies should be done for samples with different aging time and under different temperatures.

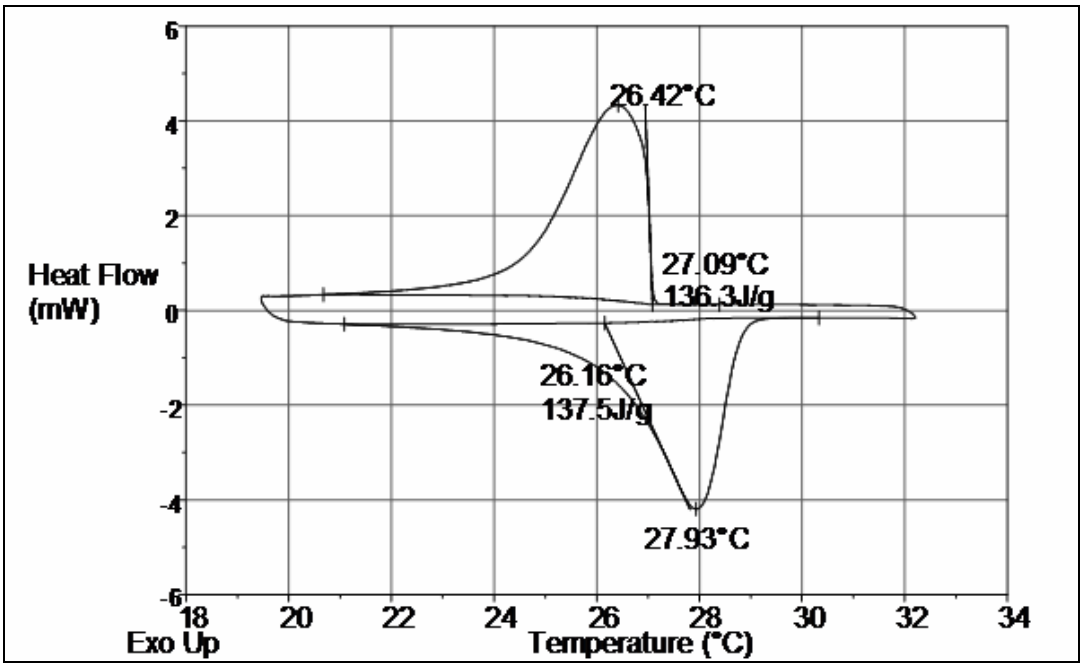

Figure 2.28 DSC curve of pure paraffin

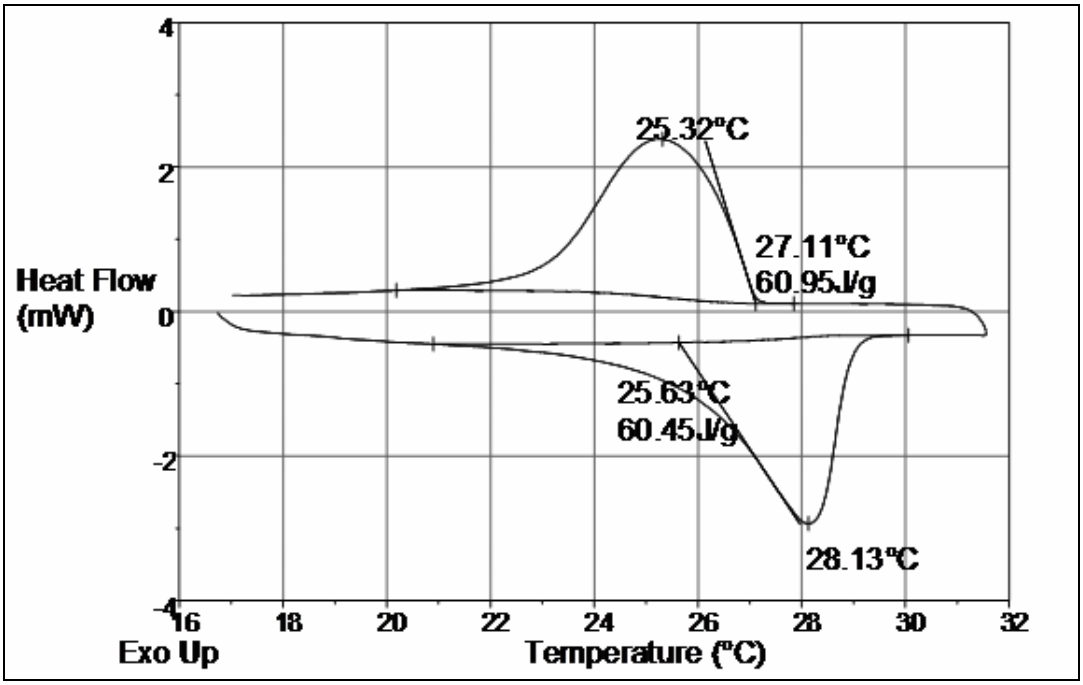

Figure 2.29 DSC curve of paraffin cellulose mixture

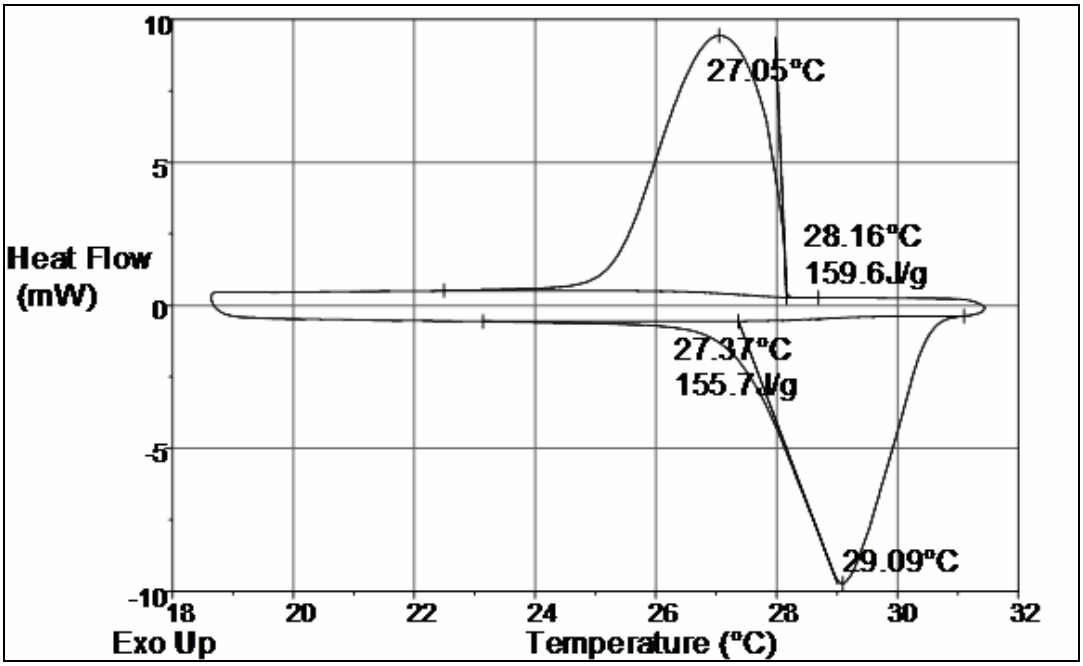

Figure 2.30 DSC curve of the "aged" paraffin

2.3.3 Paraffin and hydrated salt mixture PCM (SP25)

DSC tests were performed to investigate the property change of the paraffin-hydrated salt mixture (SP25) as a result of the mixing with insulation and moisture absorption. In the DSC test, correct solidification process results were not available because of supercooling. Because the mass of the sample was small (usually 5-10 mg), the mixture PCM formed a thin film at the bottom of the sample pan. The hydrated salt crystals had smaller chance to grow and as a result supercooling took place. This meant that PCM did not solidify until its temperature reached ten to twenty degrees below its freezing point. The solidification process began at different temperatures for the various cycles that were run as a result of surrounding disturbances. The melting processes' starting temperature remained the same.

Therefore, only the melting process was studied. Results are shown in Figures 2.31 through 2.33.

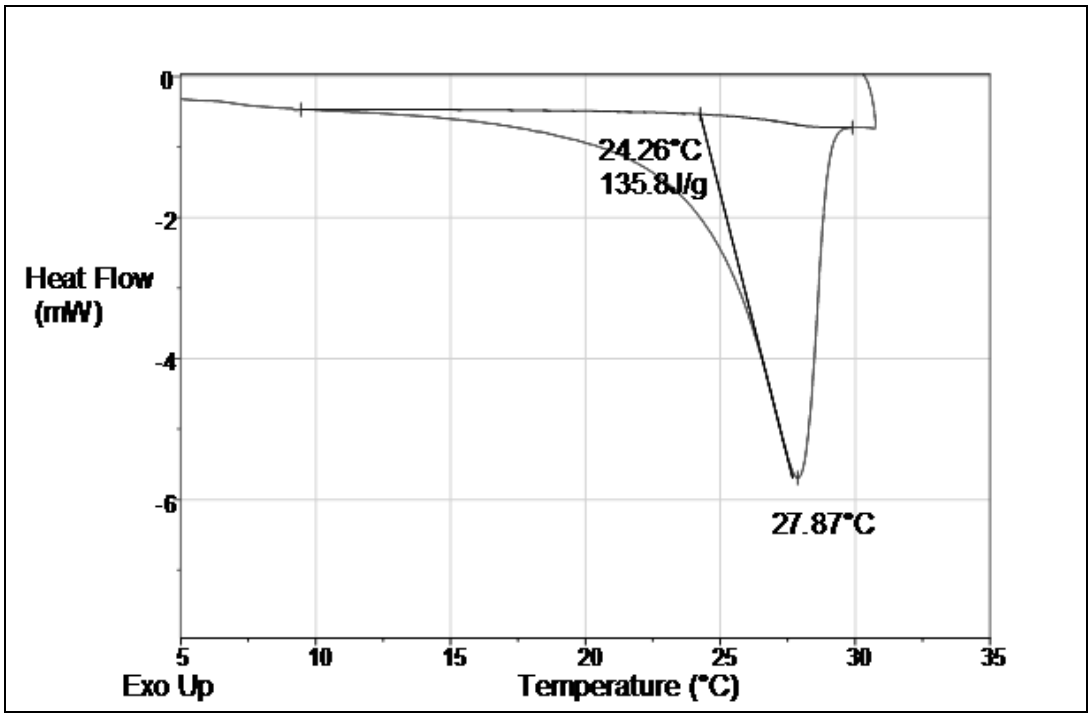

Figure 2.31 Melting curve of paraffin and hydrated salt mixture

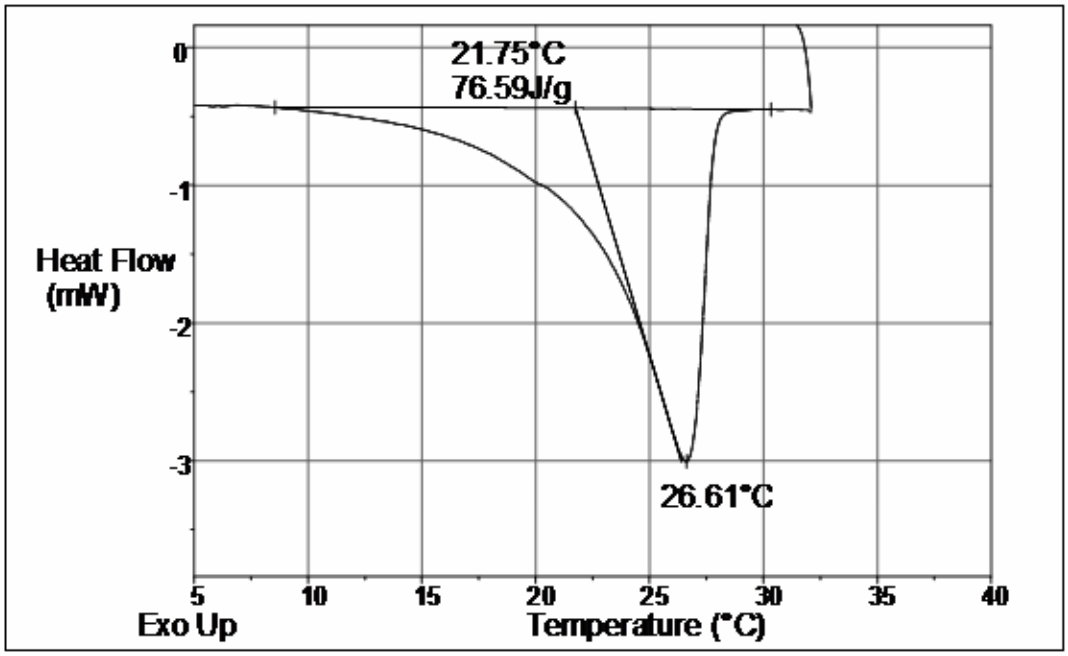

Figure 2.32 Melting curve of paraffin and hydrated salt mixture and cellulose

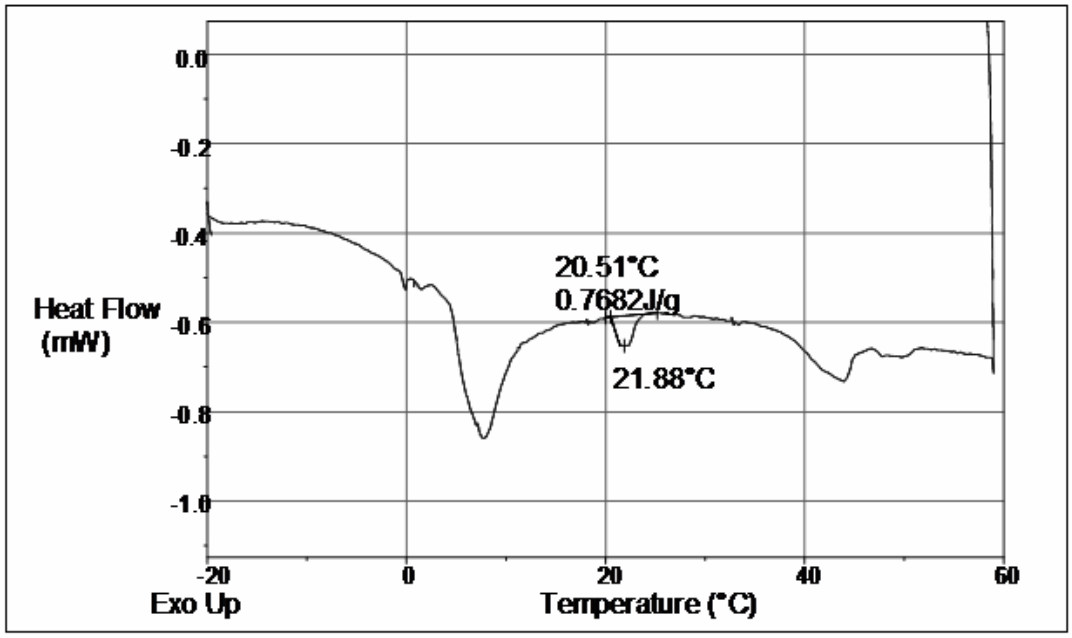

Figure 2.33 Melting curve of the residual paraffin and hydrated salt mixture

When this PCM was mixed with cellulose, with a mass ratio of PCM and cellulose of 1.64 to 1, the onset point (i.e., the melting point) changed from 25.08 ^{o}C to 21.75 ^{o}C (77.14 ^{o}F to 71.15 ^{o}F). Also, the temperature range of phase change (the width of the peak) became broader for the mixture, which was similar to the response of the pure hydrated salt case. For the same reason, more tests based on the heat of fusion are needed to get a solid conclusion about the temperature change after mixing.

The latent heat of fusion of the cellulose mixture was lower than that of the pure PCM, which was the result of the mass of cellulose added. Assuming the cellulose did not change the properties of hydrated salt and the latent heat of fusion of the pure SP25 from Figure 2.31 was used, the latent heat of fusion of the SP25 and cellulose mixture should be 84.36 J/g [135.8 x 1.64/(1.64+1)], (36.29 Btu/lbm). The test result was 76.59 J/g (32.95 Btu/lbm). The difference was 9.2%, which may come from the same sources listed above. The cellulose would not significantly affect the latent heat of fusion of the SP25 in the mixture with cellulose.

As shown in Figure 2.33, similar to hydrated salt, when moisture was absorbed (the mass of the sample changed from 15.9 mg to 24.98 mg), only a small peak of 0.77 J/g (0.33 Btu/lbm) in the range of 20 ^{o}C-30 ^{o}C (68 ^{o}F-86 ^{o}F) was observed. The paraffin-hydrated salt mixture (SP25) lost most of its thermal storage ability. Thus, SP25's performance was very similar to that of the hydrated salt (TH29).

2.3.4 Paraffin-SiO_2 powder PCM (PX27)

As shown in Figure 2.34, the powder was trapped between the cellulose fibers and remained intact. Therefore, the property of the PCM would not change by its mixing with cellulose. DSC tests were performed to investigate the properties of new PCM and “aged” PCM that was exposed to air for a long time. The results are shown in Figures 2.35 and 2.36. Similar to the results of paraffin, the “aged” PCM had higher melting and solidification points. But the latent heat of fusion was lower for the “aged” PCM. This can be explained by the lower ratio of effective PCM to the inert hydrophilic silica after the oxidation mass loss.

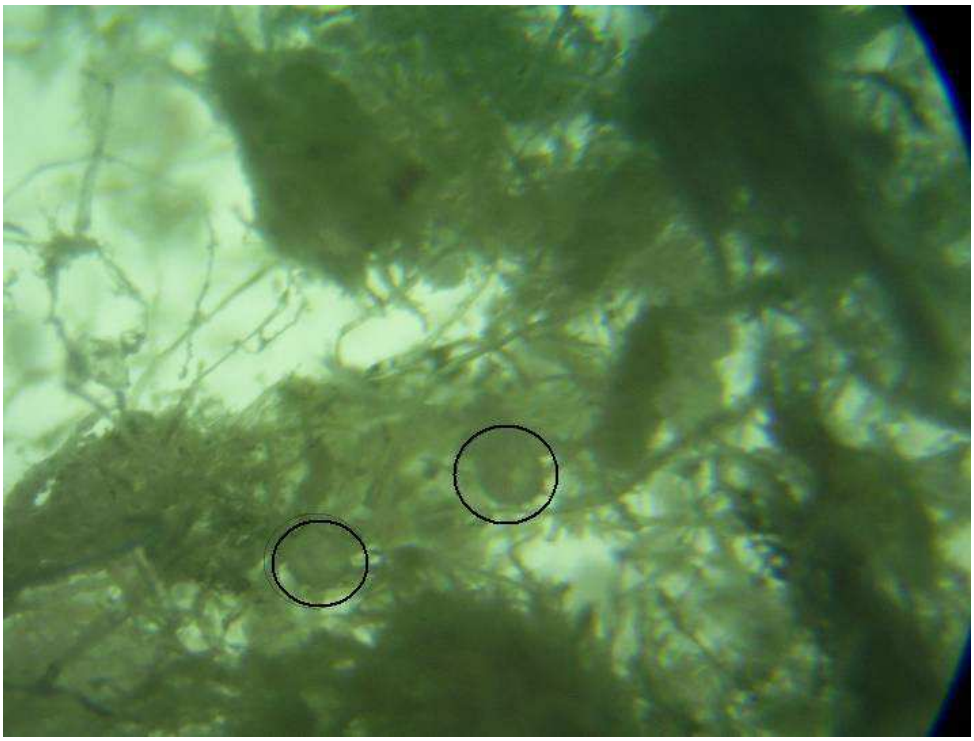

Figure 2.34 PCM powder trapped between insulation fibers

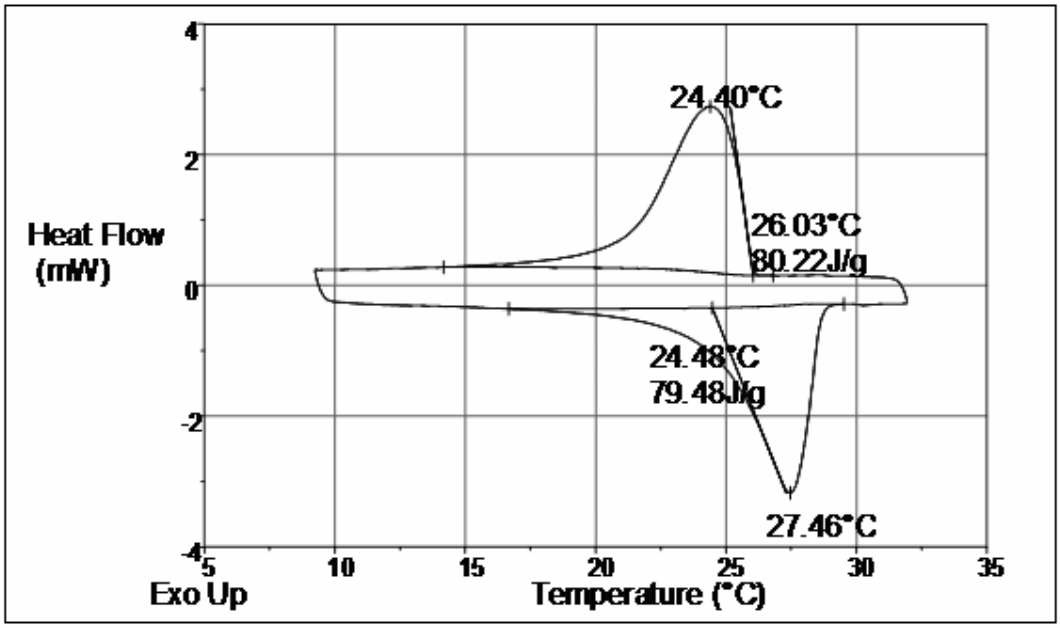

Figure 2.35 DSC curve of Paraffin-SiO_2 powder

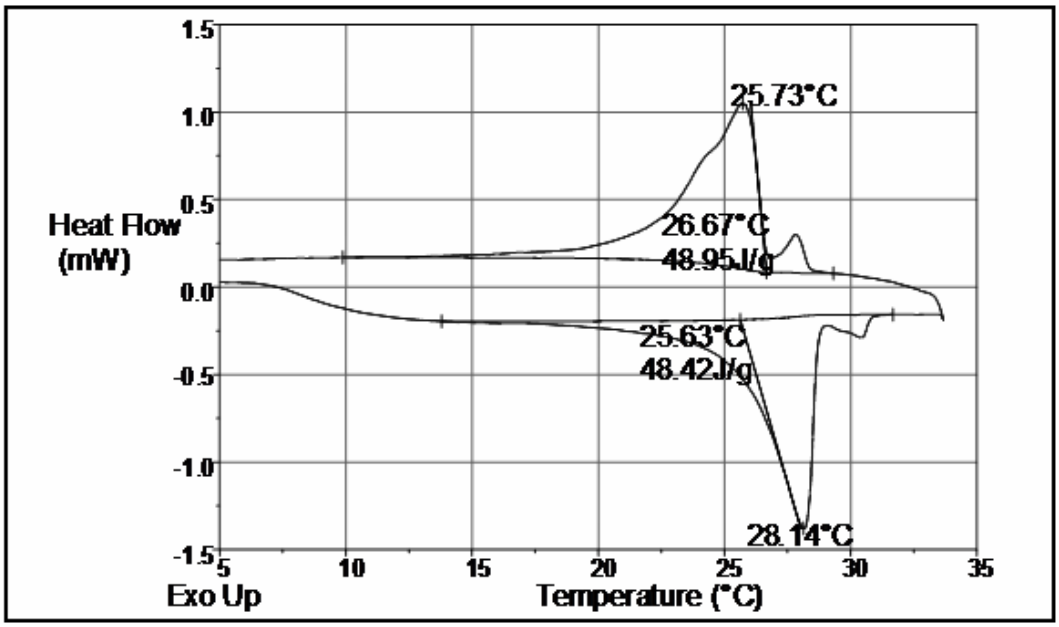

Figure 2.36 DSC curve of "aged" Paraffin-SiO_2 powder

2.4 Mass changes of PCMs exposed to air

The oxygen and moisture in the air can diffuse through the walls of a building and be carried through infiltration across cracks. When oxygen and moisture come in contact with the PCM, the properties of PCMs would change, as discussed above. A sample mass test was conducted to investigate the mass change of PCM samples when in contact with air. Different types of PCMs were placed in small metal pans (about 5 mm in diameter) with holes punched in the cover of the pan to let the PCM come in contact with the air. An empty reference pan was also weighted to eliminate the possible error from dust and scale calibration.

2.4.1 Hydrated salt PCM (TH29) and paraffin-hydrated salt mixture PCM (SP25)

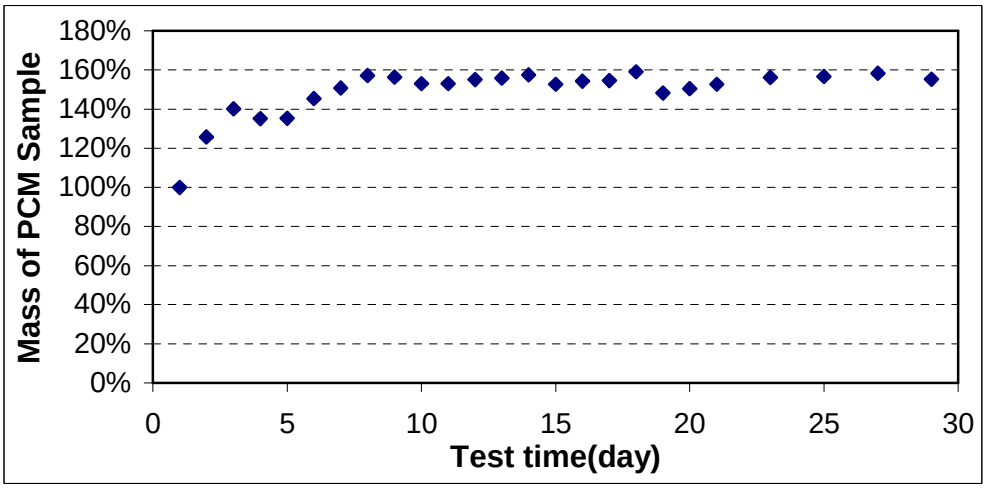

Figure 2.37 Mass change of pure hydrated salt (TH29) exposed to air at room temperature (24 ^{o}C/75.2 ^{o}F)

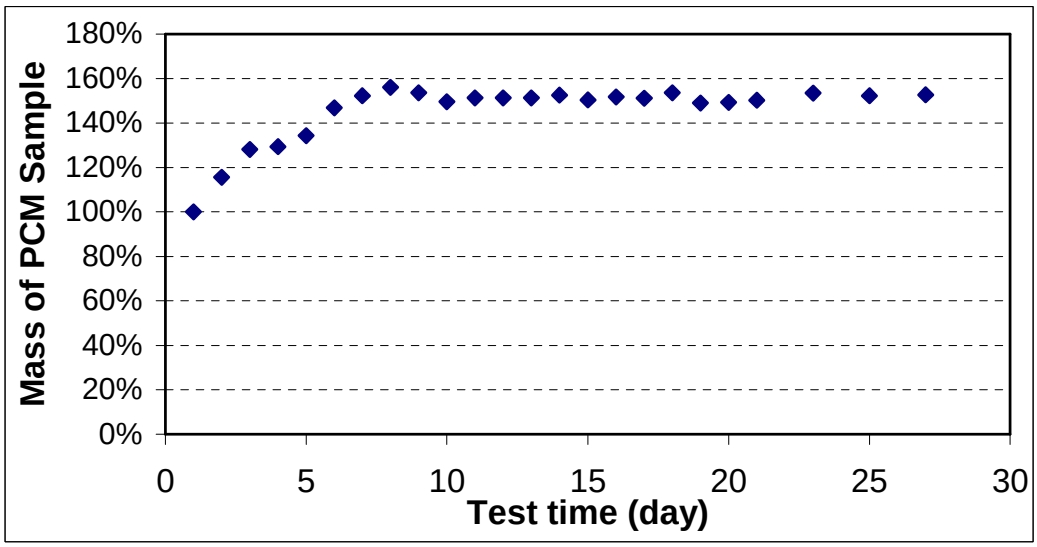

Figure 2.38 Mass change of pure paraffin-hydrated salt mixture (SP25) exposed to air at room temperature (24 ^{o}C/75.2 ^{o}F)

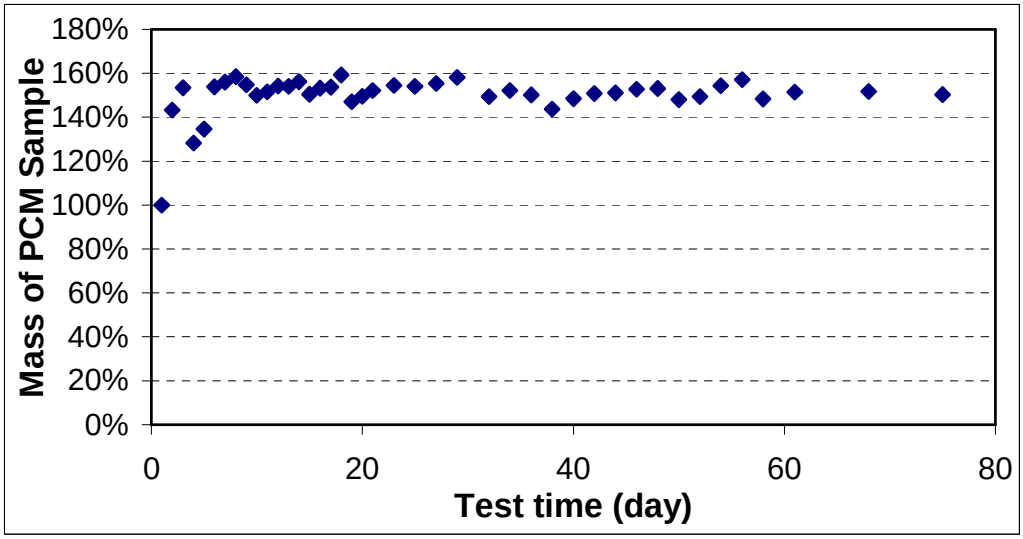

Figure 2.39 Mass change of hydrated salt (TH29) in TH29 cellulose mixture exposed to air at room temperature (24 ^{o}C/75.2 ^{o}F)

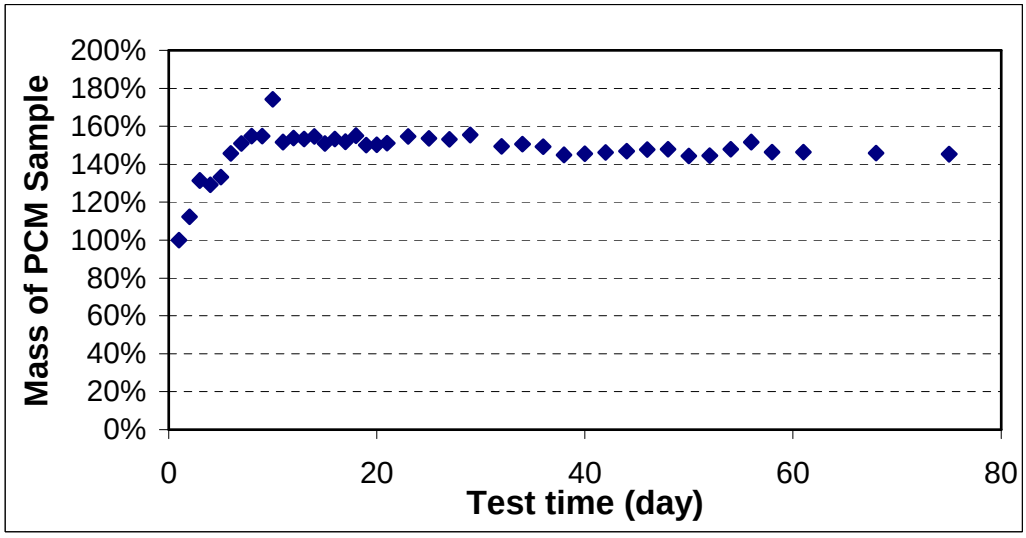

Figure 2.40 Mass change of paraffin and hydrated salt mixture (SP25) in SP25 cellulose mixture exposed to air at room temperature (24 ^{o}C/75.2 ^{o}F)

As depicted in the figures, the mass of both types of PCMs first increased with time and then remained stable. The PCM mass of both the hydrated salt based PCMs either in pure state or mixed with insulation increased by about 50%, which meant about 50% of initial weight's moisture was absorbed. Some of the solution even came out of the sample pan because of increased volume as shown in Figure 2.41.

Figure 2.41 Overflow of hydrated salt (TH29) exposed to air at room temperature (24 ^{o}C/75.2 ^{o}F)

It took about eight days for the mass of those hydrated salt-based PCM to reach the steady state. This time may vary with different environment temperatures and ventilation conditions. Combined with the DSC results shown in Figures 2.27 and 2.33, it was found that hydrated salt and the paraffin-hydrated salt mixture would absorb moisture and lose their ability to store heat very quickly when exposed to the air. Mixing these types of PCMs with cellulose insulation would not change this fact. Unless sealed with some other moisture insulating substance, it is inevitable that the hydrated salt based PCMs will become a salt solution and stop performing after a short time.

2.4.2 Paraffin PCM (RT27)

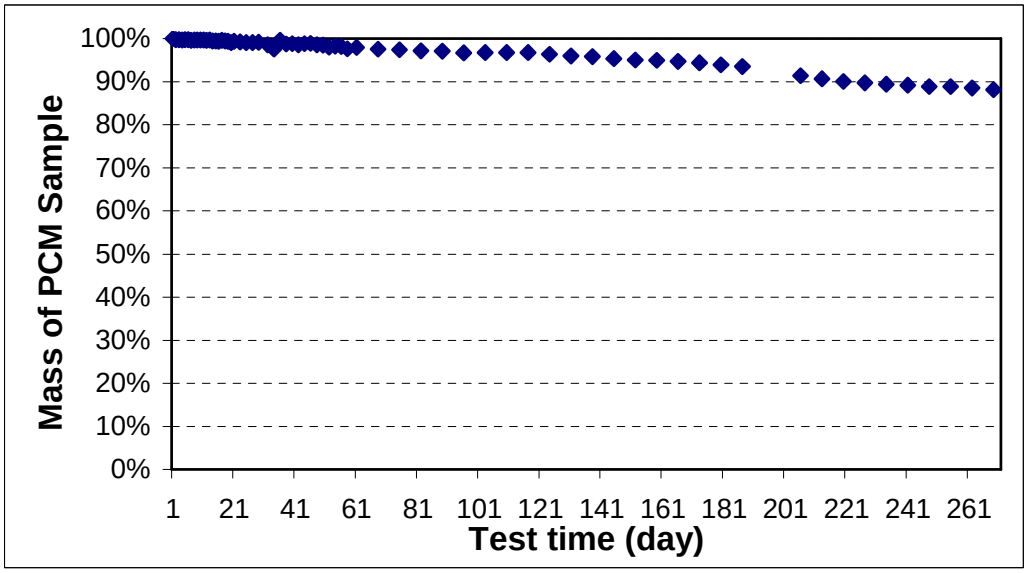

Figure 2.42 Mass change of pure paraffin (RT27) exposed to air at room temperature (24 ^{o}C/75.2 ^{o}F)

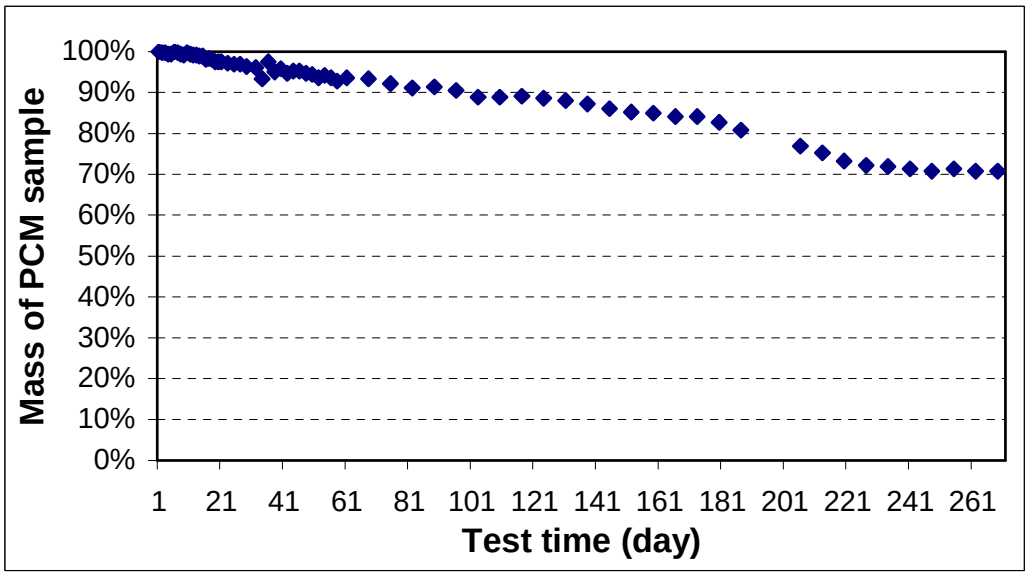

Figure 2.43 Mass change of paraffin (RT27) in paraffin cellulose mixture exposed to air at room temperature (24 ^{o}C/75.2 ^{o}F)

From Figures 2.42 and 2.43, it is evident that the paraffin lost some mass over time. In this case, the sample lost 12% of its initial mass for pure paraffin and 30% for the mixture with insulation in a total of 269 days. The difference may come from the difference in area exposed to the air. When the paraffin is mixed with insulation, it is dispersed between the cellulose fibers that have larger surface areas. Though paraffin usually is assumed to be stable, the mass loss may still be caused by the slow oxidation process. From (Feud et al., 1982), the oxidation process becomes significant only at temperatures between 80 ^{o}C and 100 ^{o}C (176 ^{o}F and 212 ^{o}F). The oxidation problem for paraffin is also mentioned in (Kissock et al., 1998). Another possible cause for the mass loss is evaporation. For octadecane with a melting point

of 28 ^{o}C (82.4 ^{o}F), the vapor pressure can be calculated by (Bradley and Shellard, 1949):

$$\log_{10} P = -\frac{7995}{T} + 21.831 \text{ (for solid 15-25 } ^{o}\text{C,(59-77}^{o}\text{F))} \quad \text{(2-1);}$$

$$\log_{10} P = -\frac{4730}{T} + 11.036 \text{ (for liquid 30-40 } ^{o}\text{C,(86-104}^{o}\text{F))} \quad \text{(2-2)}$$

In which P is in cmHg and T in K.

From the above equations, the vapor pressure at 20 ^{o}C (68 ^{o}F) is 3.5x10^{-6} cmHg (1.4 x10^{-6} inHg) and the vapor pressure at 40 ^{o}C (104 ^{o}F) is 8.4x10^{-5} cmHg (3.3 x10^{-5} inHg). Compared with water (1.754 cmHg (0.96 inHg) for 20 ^{o}C (68 ^{o}F) and 5.53 cmHg (2.2 inHg) for 40 ^{o}C (104 ^{o}F)), the vapor pressure of paraffin is so low that the evaporation can be neglected. Therefore, oxidation was the cause for the mass change of paraffin.

To explore the influence of temperature on the oxidation process, another set of paraffin sample pans were set in a heated environment of 40 ^{o}C (104 ^{o}F). The mass changes are shown in Figures 2.44 and 2.45.

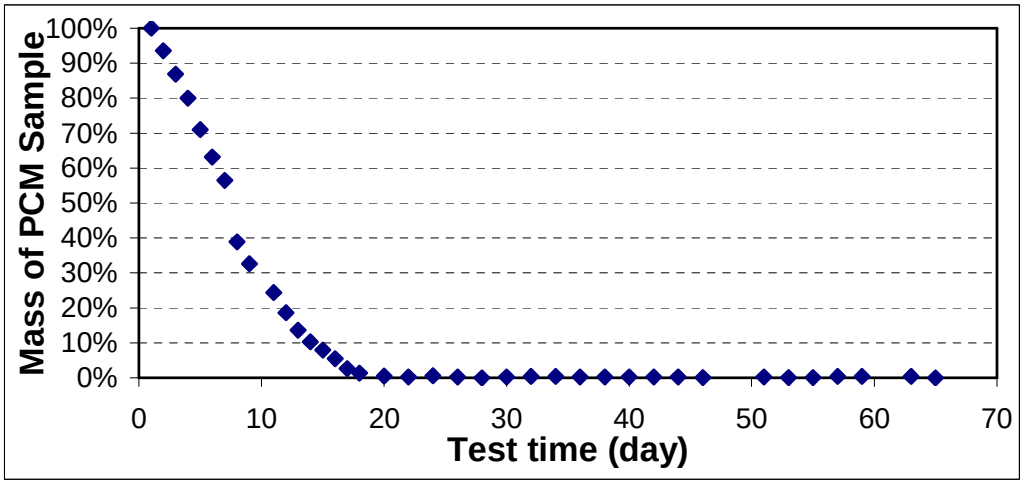

Figure 2.44 Mass change of pure paraffin (RT27) exposed to air at a temperature of 40 ^{o}C/104 ^{o}F

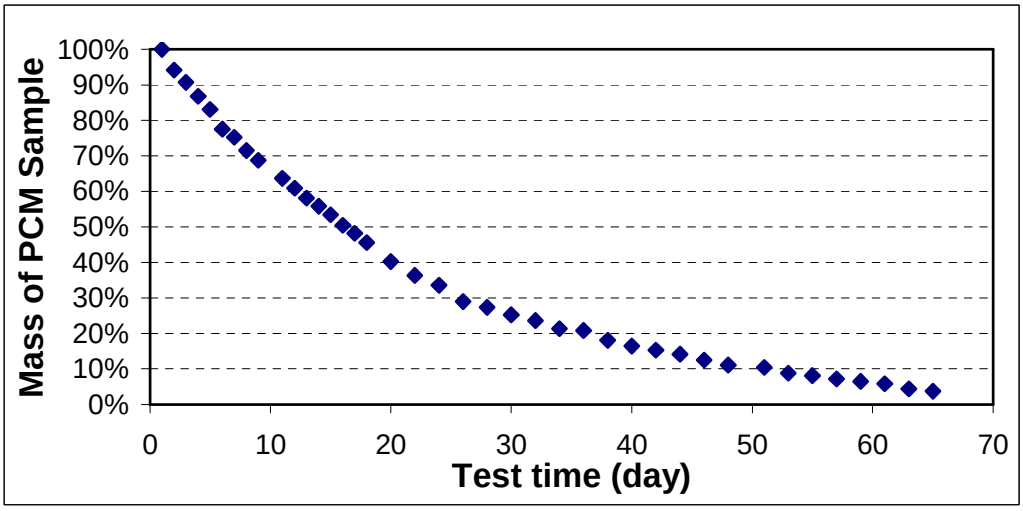

Figure 2.45 Mass change of paraffin (RT27) in the paraffin cellulose mixture exposed to air at a temperature of 40 ^{o}C/104 ^{o}F

Under a high temperature, the pure paraffin sample almost completely disappeared in about 20 days. When mixed with insulation, the oxidation process was slower. This could be because the fibers blocked some of the air. After two months,

the PCM was almost all consumed. Compared with the results at room temperature, it was evident that the oxidation process occurred slower at room temperature. The reaction speed increased with the increase in temperature. From the analysis in the previous section, for the east, west and south wall, almost half of the insulation reached 40 ^{o}C (104 ^{o}F) or higher. Therefore, oxidation would become a problem for these applications as well.

Unlike the sample pan test, there is no significant air movement in the building walls; therefore, the oxidation process would be slower. Another mass change test, with a paraffin and insulation mass ratio of 1.3:1, was performed to investigate this problem. The paraffin and insulation mixture were placed in a 4 cm (1.5 in) layer in a plastic bucket and covered with OSB board to simulate the conditions in a building wall, as shown in Figure 2.46. Air could only reach the PCM by diffusion through the OSB or the small gap along the perimeter. Like the small sample pan test, the test mixture was placed in a 40 ^{o}C (104 ^{o}F) environment. The mass change of the paraffin in the sample is shown in Figure 2.47. From the data available, it was found that the mass loss rate was about six times slower than that of the test shown in Figure 2.45. However, for the real applications in which PCMs are expected to be installed for years, oxidation would become a potential problem. Thus, like hydrated salt-based PCMs, some kind of coating or encapsulation around or over the PCM would be necessary for long-term applications.

Figure 2.46 Paraffin cellulose mixture placed in the test bucket

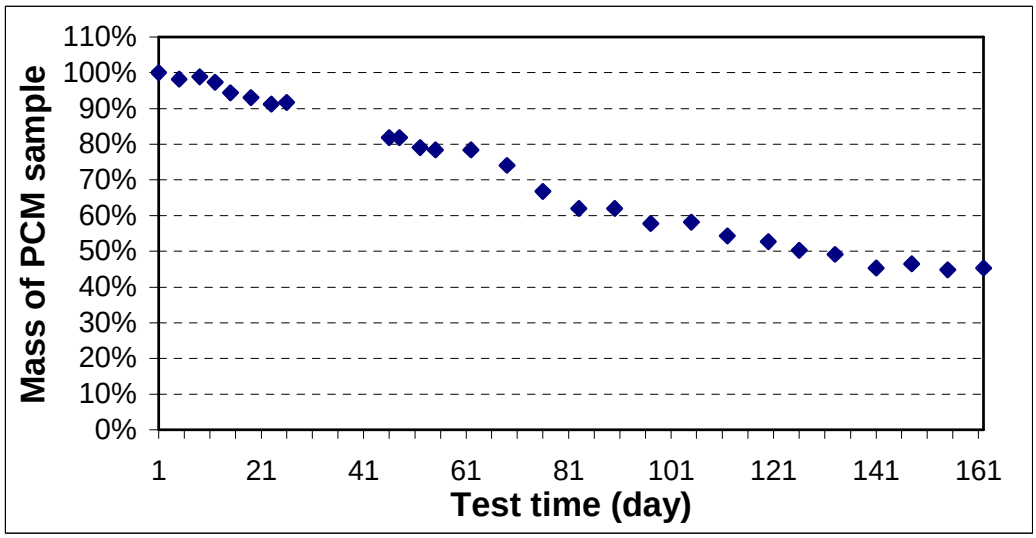

Figure 2.47 Mass change of paraffin (RT27) in the paraffin cellulose mixture exposed to air at a temperature of 40 ^{o}C/104 ^{o}F ("bucket" test)

2.4.3 Paraffin powder (PX27)

From Figures 2.48 and 2.49, like paraffin, the paraffin powder would lose mass over time when exposed. In the experiments, the sample lost 2% of its initial mass for pure state and 23% for a sample mixed with insulation in about 269 days. The cause of the difference was similar to that of the pure paraffin as listed above.

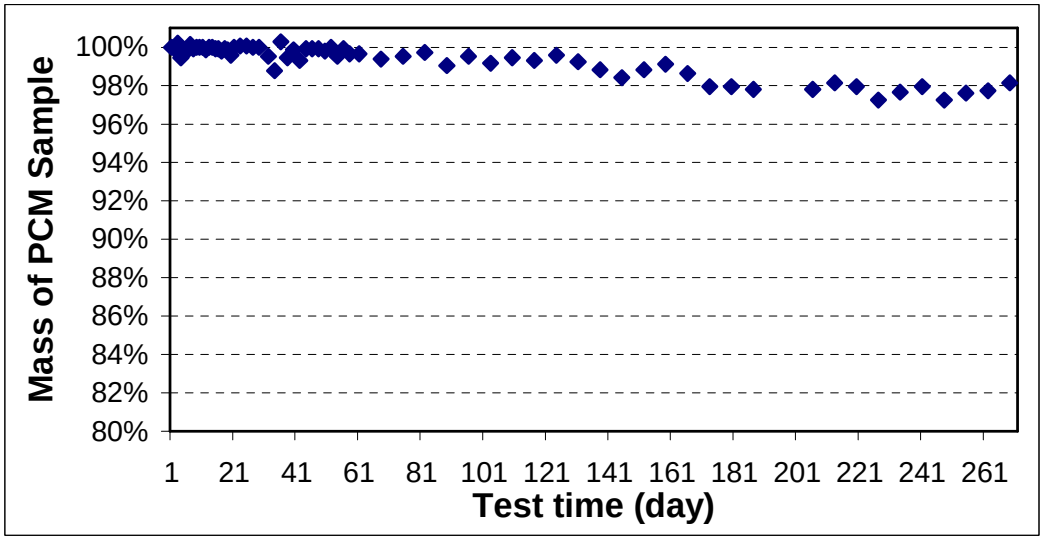

Figure 2.48 Mass change of pure paraffin powder (PX27) exposed to air at room temperature (24 ^{o}C/75.2 ^{o}F)

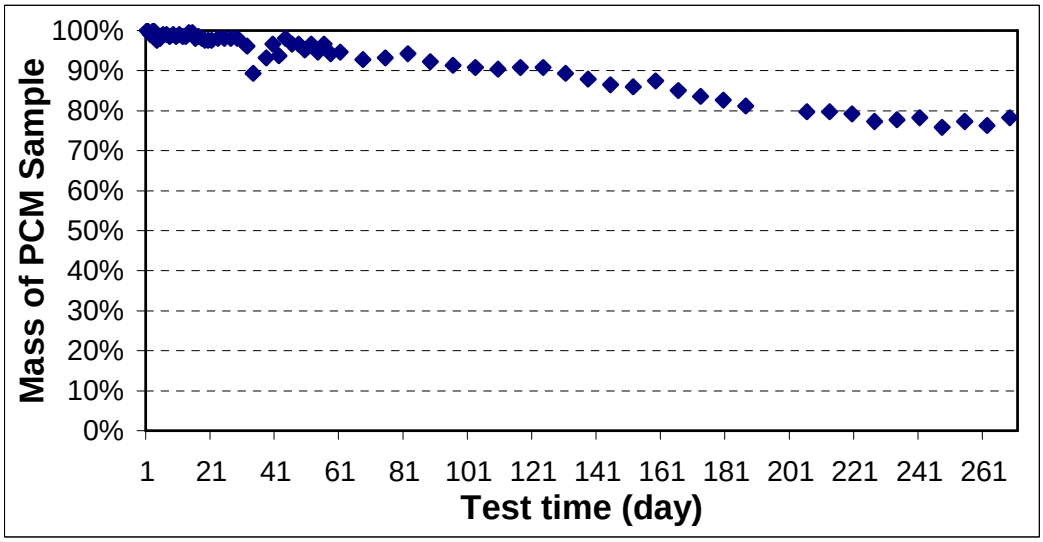

Figure 2.49 Mass change of paraffin powder (PX27) in the mixture with cellulose exposed to air at room temperature (24 ^{o}C/75.2 ^{o}F)

Compared with pure paraffin, the oxidation process was slower, which might be the result of the protection of the SiO_2. High temperature (40^{o}C) tests were also performed. Results are shown in Figures 2.50 and 2.51.

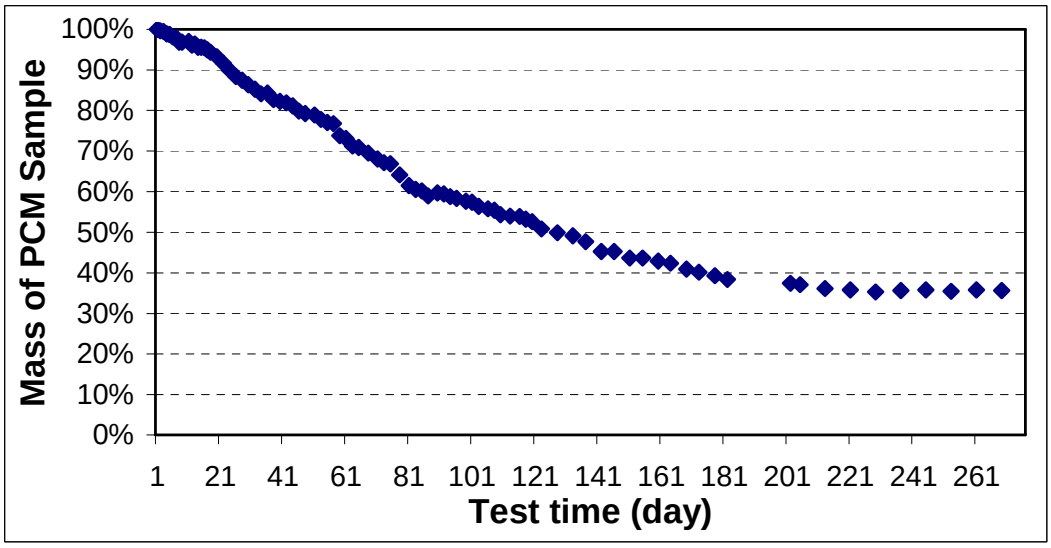

Figure 2.50 Mass change of pure paraffin powder (PX27) exposed to air at a high temperature of 40 ^{o}C/104 ^{o}F

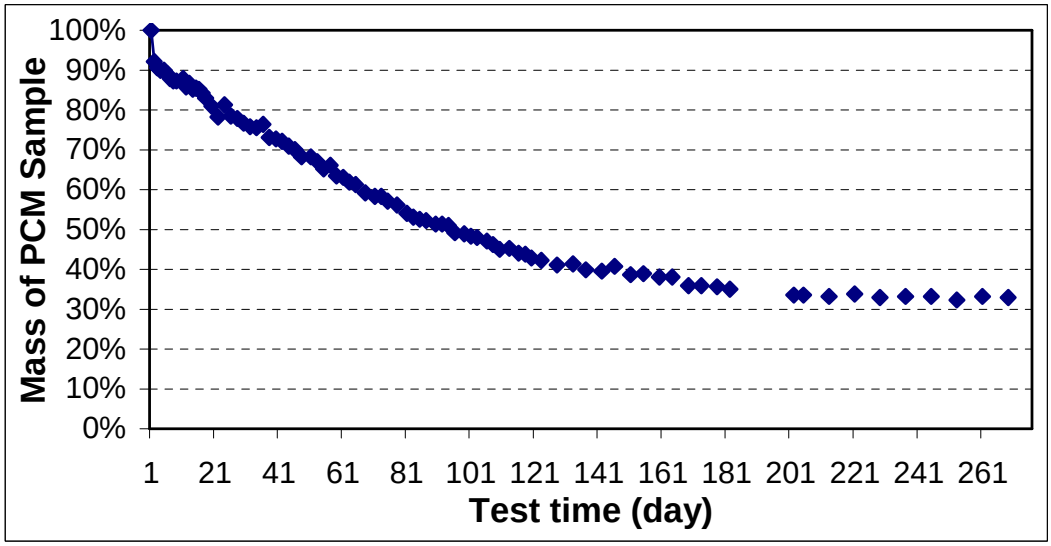

Figure 2.51 Mass change of paraffin powder (PX27) in the mixture with cellulose exposed to air at a high temperature of 40 ^{o}C/104 ^{o}F

Like the paraffin, at higher temperatures, the paraffin powder lost its mass at a higher rate. The mass stopped decreasing after 200 days. The remaining mass was very likely to be the SiO_2, which was about 32-35% of the initial paraffin powder mass. However, compared with that of the pure paraffin, the oxidation rate was three times slower because of the SiO_2 substructure.

A similar mass change test as described in the previous section was performed to investigate the performance of paraffin powder insulation in building wall. The mass ratio of paraffin powder to insulation was 1.3:1. The powder mass change is shown in Figure 2.52. If the mass percentage of SiO_2 in paraffin powder was assumed to be 35% as discussed above, the mass change of paraffin in the paraffin powder cellulose mixture is shown in Figure 2.53. From the trend, the mixture lost about 40% of its initial paraffin in 320 days. If it was assumed that the insulation would stay at hot temperatures for 12 hours in a day for five months in a year, it will take about four years for the mixture to lose approximately 40% of the PCM. Although paraffin powder performed relatively better compared with the other three types of PCMs, some kind of coating would still be necessary for long-term applications.

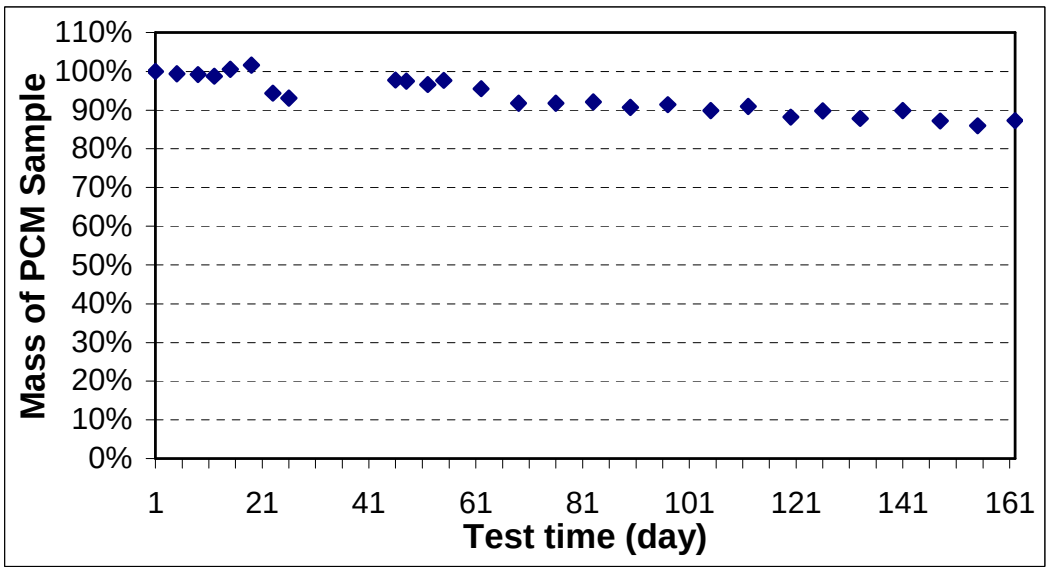

Figure 2.52 Mass change of paraffin powder (PX27) in the mixture with cellulose exposed to air at a high temperature of 40 ^{o}C/104 ^{o}F ("bucket" test)

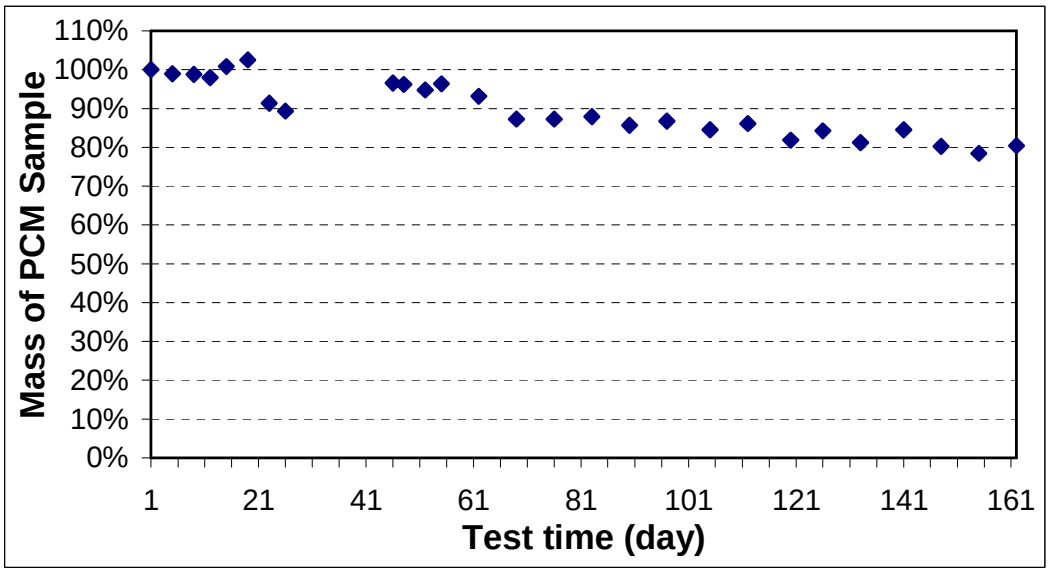

Figure 2.53 Mass change of paraffin in paraffin powder (PX27) cellulose mixture exposed to air at a high temperature of 40 ^{o}C/104 ^{o}F ("bucket" test)

2.5 Summary

From the experimental data, the local typical maximum exterior wall surface temperature could be assumed to be 62.3 ^{o}C (144.1 ^{o}F) for the east facing wall, 67.8 ^{o}C (154.0 ^{o}F) for the west wall, 55.9 ^{o}C (132.6 ^{o}F) for the south wall, and 39.5 ^{o}C (103.1 ^{o}F) for the north wall. The typical minimum exterior wall surface temperature for the four walls could be assumed to be 23.6 ^{o}C (74.5 ^{o}F). The temperature change rate for the insulation was low. The influence of PCMs' properties on the phase change process could not be neglected and should be incorporated into the PCM heat transfer modeling.

From the numerical simulation results using experimental temperature data as boundary conditions, it was found that the specific heat of the insulation could be neglected in heat transfer calculation because of its low density and slow temperature change rate. Based on the analysis of the temperature within the insulation, it was found that the outermost point had the largest daily temperature change range. The PCM located close to the inside was more likely to complete the solidification process or get close to a complete process

From DSC tests, the mixing of the PCMs and cellulose insulation did not change the heat of fusion of the PCMs in the mixure much. The mixture still showed a capacity to absorb and release heat during the phase change process.

From the mass change tests, hydrated salt-based PCMs (both pure hydrated salt and hydrated salt and paraffin mixture) absorbed moisture at about 50% of their weight and lost their heat storage capability in a short time (about eight days in the

tests). Some moisture insulating substance would be needed to completely seal the PCM; otherwise, they would not be suitable for use in direct mixing with cellulose insulation.

Paraffin would lose mass by oxidation when exposed to air. For low temperatures, this process was slow. For high temperatures (40 ^{o}C, 104 ^{o}F), the process would proceed at a faster rate. The pure paraffin sample almost completely disappeared in about 20 days. Like the hydrated salt based PCM, paraffin would not be suitable to be directly mixed with insulation unless some airtight coating or encapsulation was developed to prevent oxidization.

Like paraffin, paraffin SiO_2 powder lost mass under both low and high temperatures. Because of the SiO_2 substructure, the oxidation rate was lower than that for pure paraffin. From the test results, it was estimated that the paraffin powder will lose approximately 40% of its working paraffin in about four years when placed in building walls. although paraffin powder performed relatively better when compared with the other three types of PCMs, some kind of coating or encapsulation would still needed for long-term applications.

Chapter III

Experimental Study of the Application of PCMs in Building Walls

The performance of PCM-enhanced walls was evaluated under full weather conditions and in a laboratory setting. The PCM was integrated into the experimental walls using two methods, namely, via direct mixing of the PCMs with cellulose insulation and via macro-encapsulation (pipe encapsulation). Information on the test setups, experimental approach, and results are presented.

3.1 PCM-enhanced wall testing - Direct mixing method

3.1.1 Preparation of the PCM-enhanced insulation via direct mixing

Before mixing it with the cellulose insulation (a type of wall insulation made from recycled paper products) the paraffin-based PCM (RT27) was melted in a water bath. Once melted, it was sprayed into the cellulose insulation where it was evenly mixed by hand. This process is shown in Figure 3.1. After mixing, the PCM-insulation mixture was blown into the wall cavities of the test house. For easy comparison with previous research, the PCM concentration used was defined as the percentage of the weight of the gypsum wallboard. For the 5.08 cm x 10.16 cm (2 in x 4 in) stud frame wall, the 30% of the weight of the gypsum board (the concentration used in this research) was equivalent to 70% of the weight of the cellulose insulation in the wall cavity.

Figure 3.1 Spraying and mixing the PCM with cellulose insulation

3.1.2 Calibration (Null) tests

A calibration test was performed to set the baseline in relation to temperatures and heat transfer between both test houses before the retrofit and to eliminate any possible future experimental errors from the test system. For the calibration test, the same plain cellulose insulation was installed in both test houses. The thermal performance of the two houses, that is, the heat fluxes across the walls, interior/exterior wall surface temperatures, and indoor air temperatures were monitored, recorded, stored, and analyzed. It was found that these pre-retrofit data were very similar, almost identical, for both houses. One example of heat flux data for the west walls of both houses is shown in Figure 3.2. The corresponding exterior and interior surface temperatures of the west walls are shown in Figure 3.3. From both figures, it was inferred that the thermal responses of the two houses were nearly

identical prior to adding the PCM-enhanced insulation to one of the test houses. Any differences in temperatures and/or heat fluxes in later tests would be the result of adding the PCM.

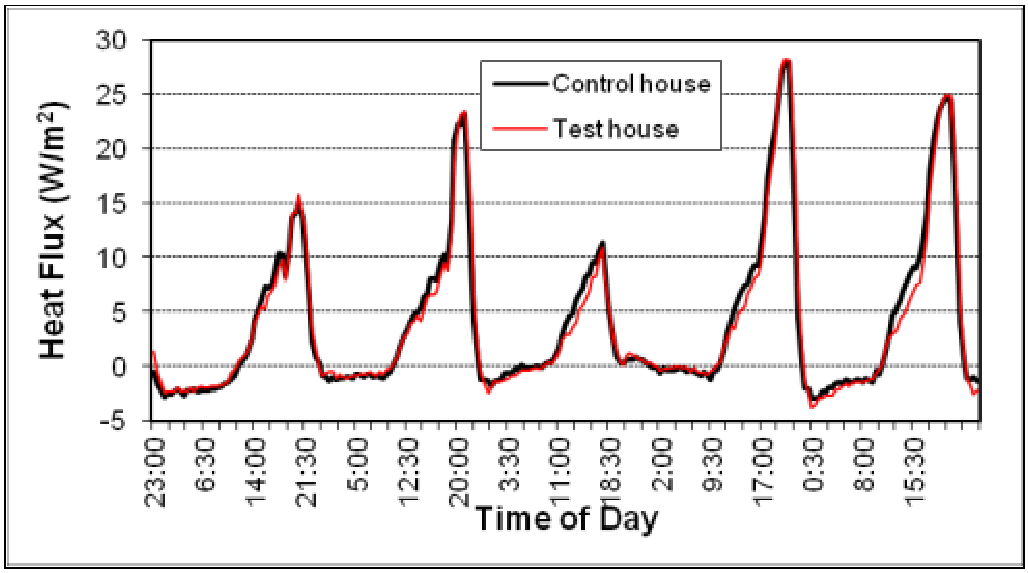

Figure 3.2 Heat fluxes across the west walls (calibration test)

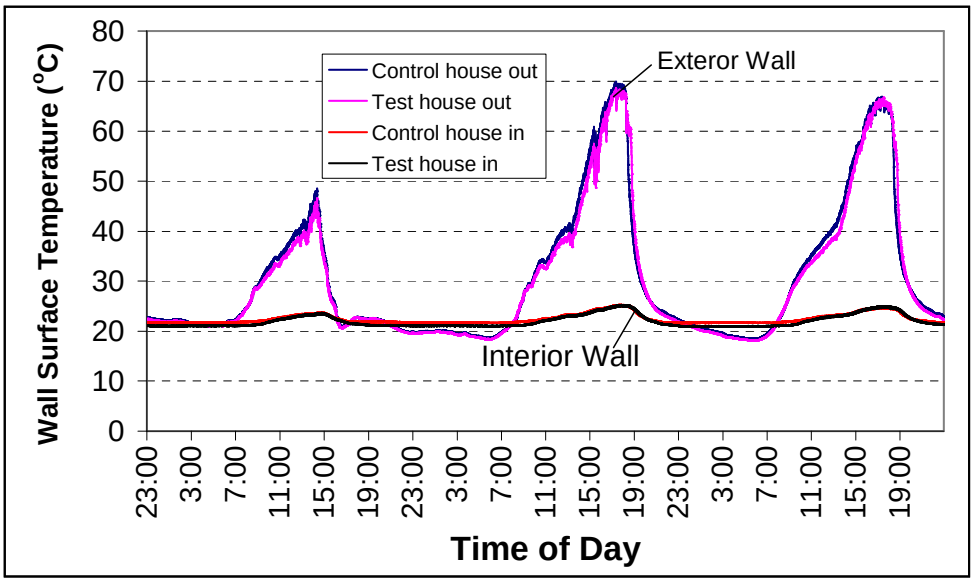

Figure 3.3 Exterior and interior surface temperatures of the west walls (Calibration Test)

3.1.3 Experimental results

3.1.3.1 Results for individual walls

In the analyses that follow, the house that was retrofitted with the PCM-enhanced insulation was referred to as the "test house" and the walls to as "PCM walls" or "PCM-enhanced wall." The house that remained with the standard (plain) cellulose insulation was referred to as the "control house" and the walls as "control walls" or "standard walls." Because the focus of this research was the space cooling load reduction and load shift (in time), only summer data (July and August) were studied. The parameters that were monitored were the heat fluxes and the interior and exterior surface temperatures of each wall. These data were collected every 10 seconds, but were averaged for every half hour. This averaging minimized effects caused by sudden changes in wind speed, passing clouds, and/or indoor temperature fluctuations produced by the cooling system's "on/off" cycles. Samples of the wall heat flux data are presented in Figures 3.4 through 3.7. The outdoor air temperature corresponding to the testing time presented in Figures 3.4 through 3.7 is shown in Figure 3.8.

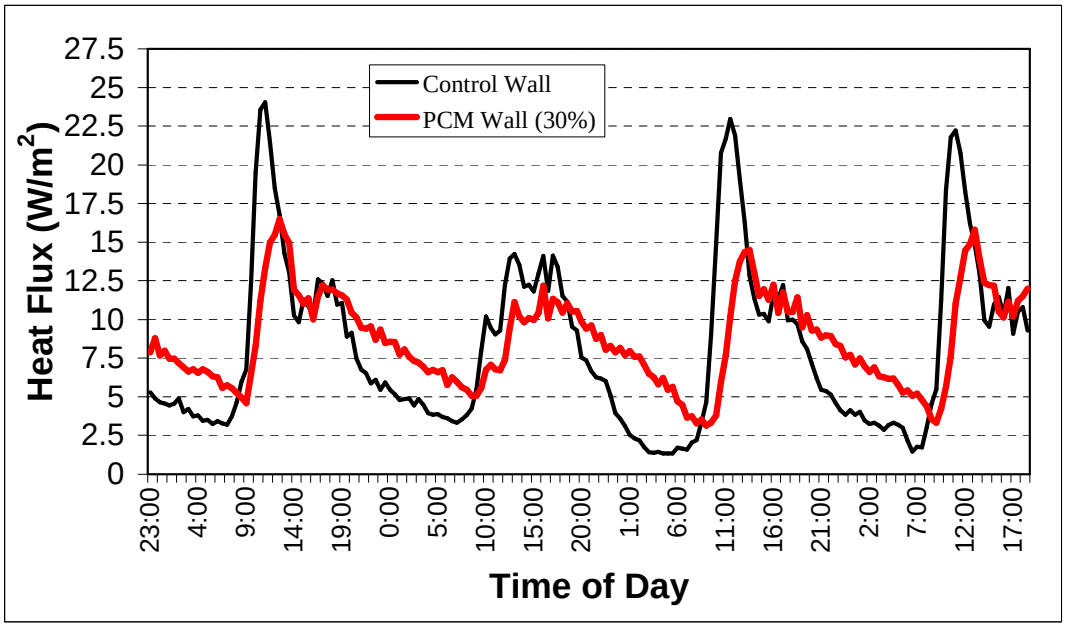

Figure 3.4 Heat fluxes across the east walls (30% PCM concentration tests)

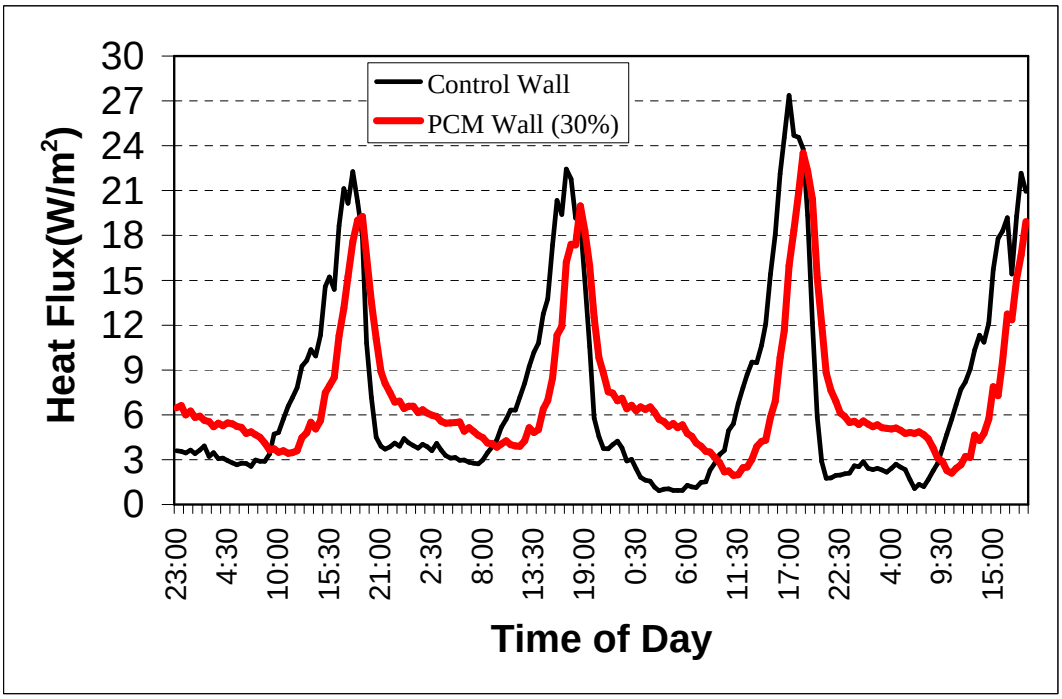

Figure 3.5 Heat fluxes across the west walls (30% PCM concentration tests)

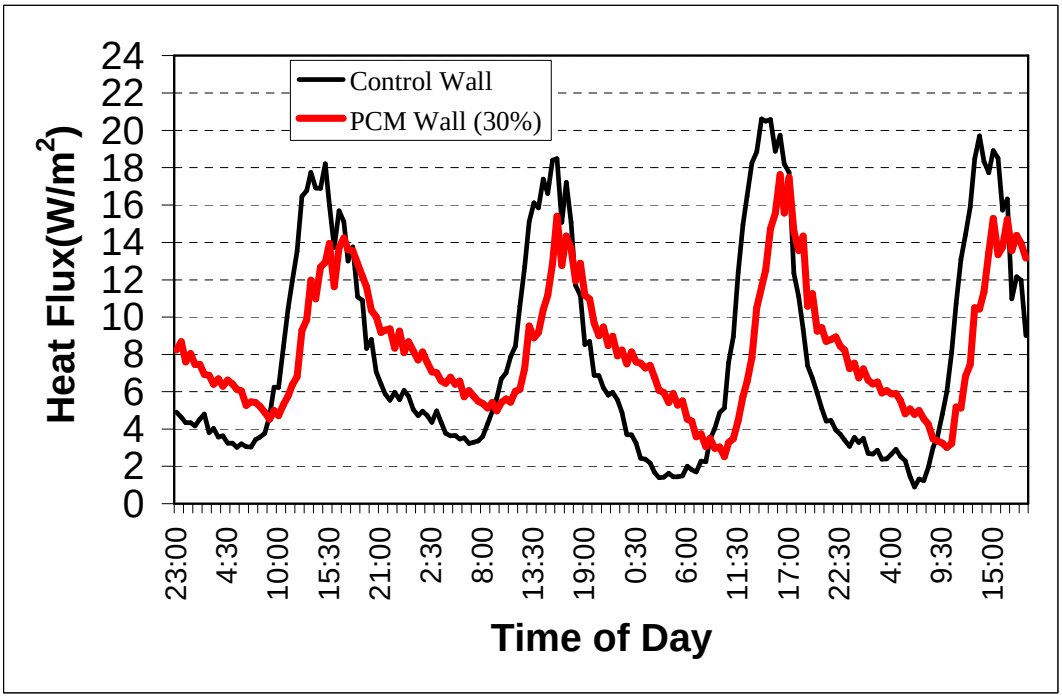

Figure 3.6 Heat fluxes across the south walls (30% PCM concentration tests)

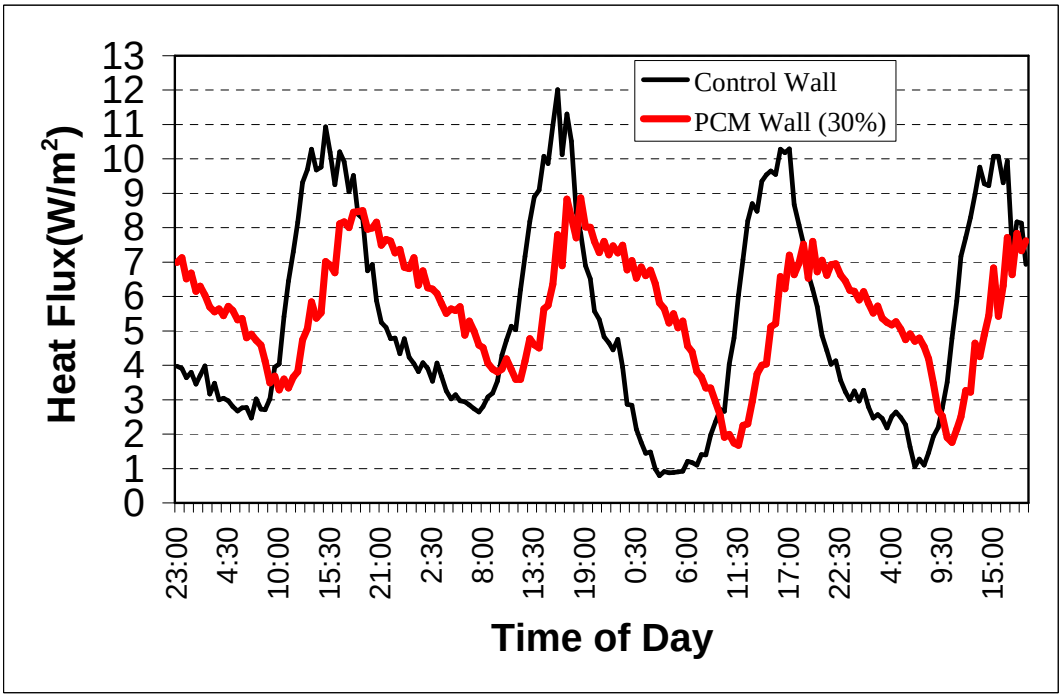

Figure 3.7 Heat fluxes across the north walls (30% PCM concentration tests)

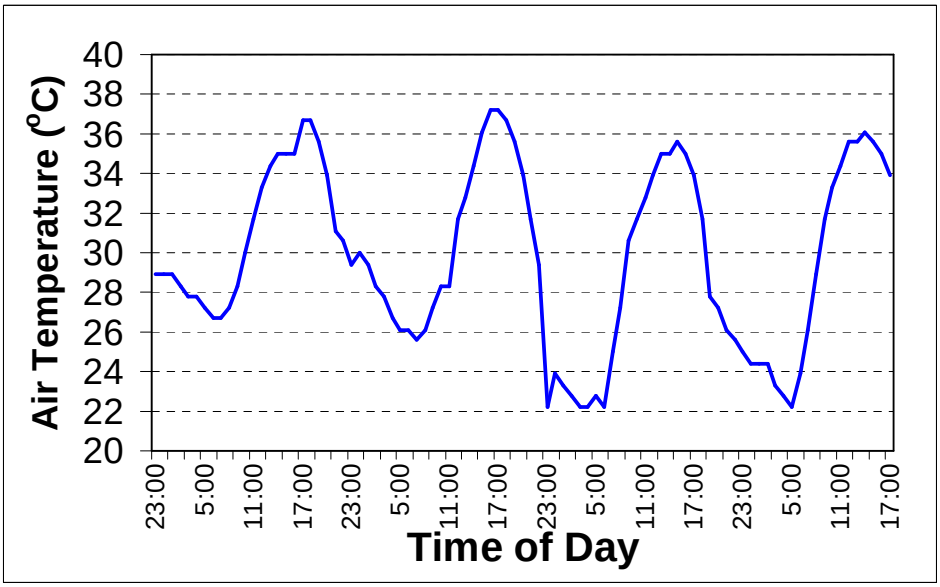

Figure 3.8 Outdoor air temperature corresponding to the data of Figures 3.4 through 3.7

The results showed that, for all four walls, the peak hour for the heat flux across the PCM walls were a few hours behind those of the control walls, thus proving the concept of space cooling load shifting. The peak heat flux values for the four PCM-enhanced walls were reduced by different percentages. It was found that the east and north walls had larger peak heat flux reductions while the west and south walls had relatively smaller reductions. As depicted in the graphs of Figures 3.4 through 3.7 the heat fluxes of the PCM-enhanced walls were lower than those of the control walls before reaching their corresponding peaks and larger after the peaks had occurred, which showed that part of the space cooling load was shifted to the later time of the day.

In addition, it was found that the areas under the heat flux curves of both the PCM walls and control walls were about the same. What this means is that PCMs reduced the peak heat fluxes, but on a daily basis, the PCM-enhanced insulation would not necessarily reduce the total heat transferred across the walls because the reductions produced by the melting process in the daytime would be cancelled out by increases in heat fluxes produced by the solidification process at night.

Under different weather conditions, different peak heat flux reductions were observed. More experimental data showing the daily heat flux peak reduction for the four walls are shown in Tables 3.1 through 3.4, in which q1 represents the peak heat flux of the control wall and q2 is the peak heat flux value of the 30% concentration PCM-enhanced wall. Days with relatively low wall surface temperatures (cold days) were eliminated because they were not representative of typical summer condition.

Table 3.1 Heat flux peak reductions (East wall)

Date	q1(W/m^2)	q2(W/m^2)	(q1-q2)/q1
27-Jul	24.3	20.51	15.60%
28-Jul	20.55	11.18	45.60%
1-Aug	20.16	10.46	48.10%
3-Aug	19.98	11.87	40.60%
4-Aug	21.86	13.88	36.50%
5-Aug	21.98	14.21	35.40%
6-Aug	23.06	13.76	40.30%
7-Aug	24.05	16.49	31.40%
9-Aug	22.96	14.5	36.90%
10-Aug	22.22	15.79	28.90%
13-Aug	22.66	14.34	36.70%
14-Aug	26.06	17.11	34.40%
15-Aug	26.23	17.97	31.50%
16-Aug	24.1	14.27	40.80%
17-Aug	15.86	10.26	35.30%
20-Aug	23.06	11.75	49.00%
21-Aug	23.41	16.28	30.50%

22-Aug	18.69	10.7	42.80%
23-Aug	17.49	11.03	36.90%
25-Aug	22.55	11.56	48.70%
26-Aug	19.05	8.43	55.80%
Avg.	21.92	13.64	38.20%

Table 3.2 Heat flux peak reductions (West wall)

Date	q1(W/m^2)	q2(W/m^2)	(q1-q2)/q1
2-Aug	15.32	9.56	37.60%
3-Aug	19.88	14.93	24.90%
4-Aug	18.01	14.86	17.50%
5-Aug	17	12.96	23.80%
6-Aug	20.11	18.38	8.60%
7-Aug	22.27	19.27	13.50%
8-Aug	22.44	19.97	11.00%
9-Aug	27.38	23.51	14.10%
13-Aug	24.61	21.35	13.20%
14-Aug	25.68	22.94	10.70%
15-Aug	24.68	22.41	9.20%
16-Aug	22.95	15.55	32.20%
17-Aug	20.44	13.84	32.30%
19-Aug	17.16	11.17	34.90%
20-Aug	20.15	15.65	22.30%
21-Aug	17.82	13.33	25.20%
23-Aug	18.31	12.28	32.90%
25-Aug	25.22	17.87	29.10%
26-Aug	18.52	9.39	49.30%
Avg.	20.95	16.28	23.30%

Table 3.3 Heat flux peak reductions (South wall)

Date	q1(W/m^2)	q2(W/m^2)	(q1-q2)/q1
28-Jul	15.65	12.37	21.00%
1-Aug	16.94	13.53	20.10%
2-Aug	17.07	10.65	37.60%
3-Aug	17.1	13.12	23.30%
4-Aug	16.58	12.51	24.60%
5-Aug	16.81	13.62	19.00%
6-Aug	18.59	14.7	21.00%
7-Aug	18.2	14.23	21.80%
8-Aug	18.47	15.39	16.70%
9-Aug	20.6	17.63	14.45%
10-Aug	19.7	15.27	22.50%

13-Aug	22.02	20.46	7.10%
14-Aug	22.6	22.09	2.30%
15-Aug	23.05	22.7	1.50%
16-Aug	22.04	21.19	3.90%
17-Aug	18.42	15.21	17.40%
19-Aug	16.82	10.46	37.80%
20-Aug	22.77	13.58	40.40%
21-Aug	21.53	16.04	25.50%
25-Aug	15.2	13.55	10.80%
26-Aug	15.25	12.11	20.60%
Avg.	18.83	15.26	19.50%

Table 3.4 Heat flux peak reductions (North wall)

Date	q1(W/m^2)	q2(W/m^2)	(q1-q2)/q1
28-Jul	8.48	6.26	26.20%
1-Aug	9.66	6.26	35.20%
2-Aug	8.69	5.29	39.10%
3-Aug	9.14	6.41	29.90%
4-Aug	9.1	6.58	27.70%
5-Aug	9.71	7.37	24.10%
6-Aug	11.36	8.74	23.00%
7-Aug	10.93	8.49	22.30%
8-Aug	12.02	8.87	26.20%
9-Aug	10.3	7.61	26.10%
13-Aug	11.69	9.78	16.30%
14-Aug	13.39	10.57	21.00%
15-Aug	13.5	10.67	20.90%
16-Aug	13.31	9.85	26.00%
17-Aug	9.51	6.51	31.50%
19-Aug	8.19	5.62	31.40%
20-Aug	11.71	7.32	37.50%
21-Aug	11.12	8.34	25.00%
23-Aug	8.44	6.41	24.00%
26-Aug	8.97	4.95	44.90%
Avg.	10.46	7.6	27.90%

From the tables above, it was found that, as expected, weather conditions would affect the performance of the PCM-enhanced walls. For example, on average,

relatively cool days, which had lower peak heat fluxes for the control walls, produced larger heat flux peak reductions.

Another finding was that not only the peak heat flux values would influence the percent reductions in heat fluxes as stated above, but also the way in which the temperature changed in the day would affect the performance of the PCM-enhanced insulation. For example, a closer observation of the heat transfer across the west walls during August 15 and August 25 revealed that although the peak heat fluxes of the control wall were close, the reduction of August 15 was larger than the reduction observed on August 25. As shown in Figures 3.9 and 3.10, the heat flux curve for August 15 was narrow and steep, which meant the exterior wall surface temperature increased at a fast rate. The temperature increased very rapidly that the less PCM mixed in the insulation melt before the peak time, compared with the day when wall temperature increased slowly (August 25). As a result, a larger peak reduction was produced.

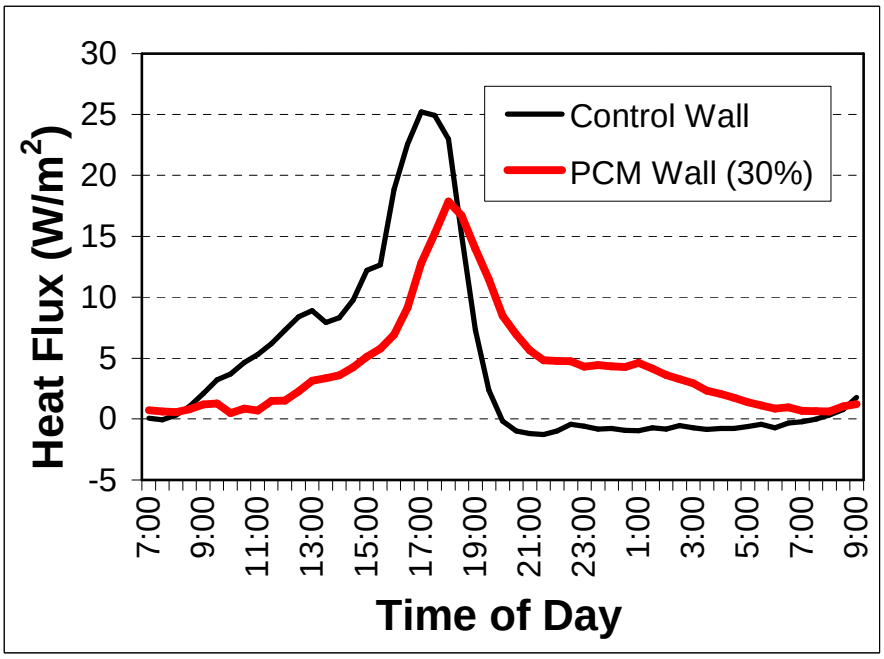

Figure 3.9 Heat flux typical of a day in which the wall temperature increased rapidly (August 15)

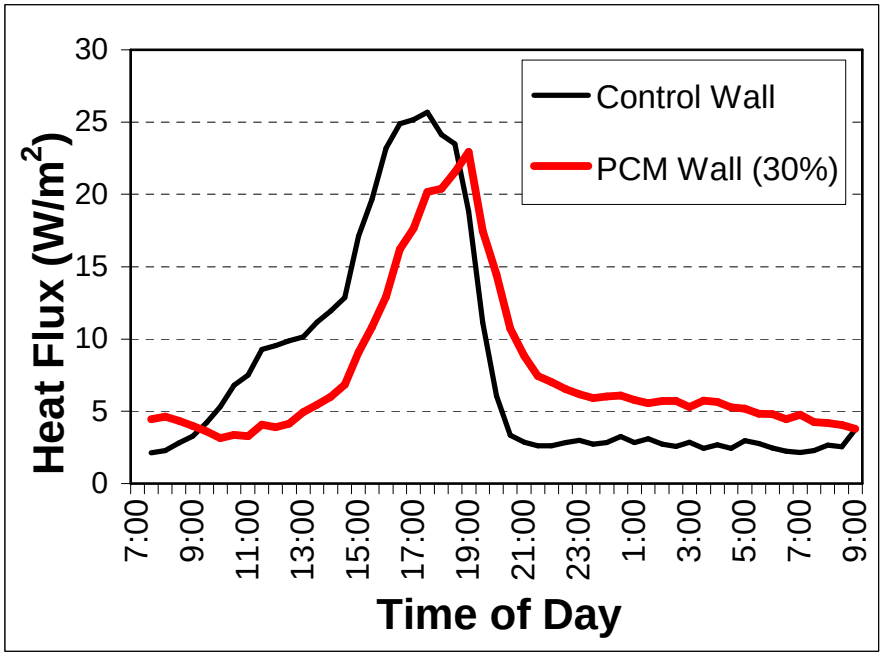

Figure 3.10 Heat flux typical of a day in which the wall temperature increased slowly (August 25)

3.1.3.2 Combined results: all walls considered

If the radiation heat transfer between the internal surfaces of the walls in the room were neglected, the sum of the heat fluxes of the four walls would represent the total space cooling load through the walls. Because the shape and orientation plans of U.S. residential houses vary, it is difficult to estimate the weights of each wall when summing up their total heat transferred into the conditioned space. In this research, the house was assumed to be a cubic box (i.e., the weighs for the four walls were the same). The sum of the heat fluxes of all four walls during the days used above is shown in Figure 3.11.

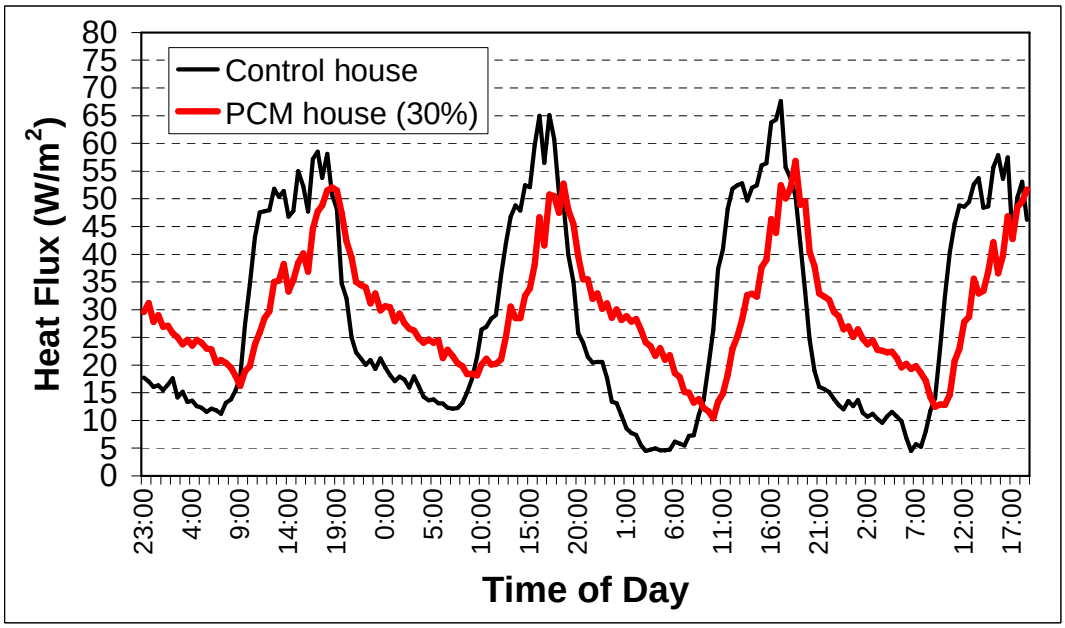

Figure 3.11 Sum of all heat fluxes across all walls (30% PCM concentration tests)

Although it was shown in Figures 3.4 through 3.7 and in Tables 3.1 through 3.4 that the peak heat fluxes for the individual walls were reduced by the application

of the PCM-enhanced insulation. The reduction of the sum of the heat flux peaks was lower than the average of the heat flux reductions observed on each wall. Take the third day in the Figure 3.11 for example. For each individual wall on this day the reductions were 36.9% for the east wall; 14.1% for the west wall; 14.5% for the south wall; and 26.1% for the north wall. The average heat flux reduction would be 22.9%; however, the reduction of the sum was 18.7%. This happened because the peak heat fluxes for the various walls occurred at different times in the day. This is illustrated in Figures 3.12 through 3.15. For east, south, and north wall, though the peak heat flux was reduced individually, at the moment when the sum of the all heat fluxes reached its peak ("new peak" in the figures), the heat flux values of these three walls were about the same or even slightly higher than those of the control walls. For the 30% concentration PCM-enhanced insulation, it was found that only the PCM-enhanced insulation installed in the west wall affected the peak reduction in a significant manner.

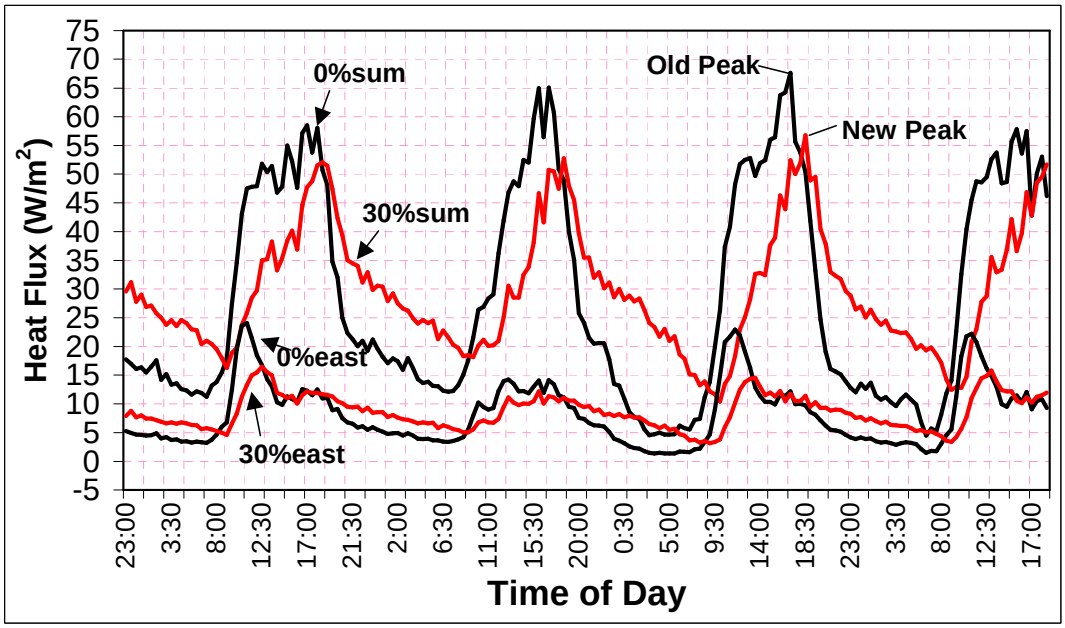

Figure 3.12 Comparison of individual wall heat fluxes with the sum of all heat fluxes (East wall – 30% concentration tests)

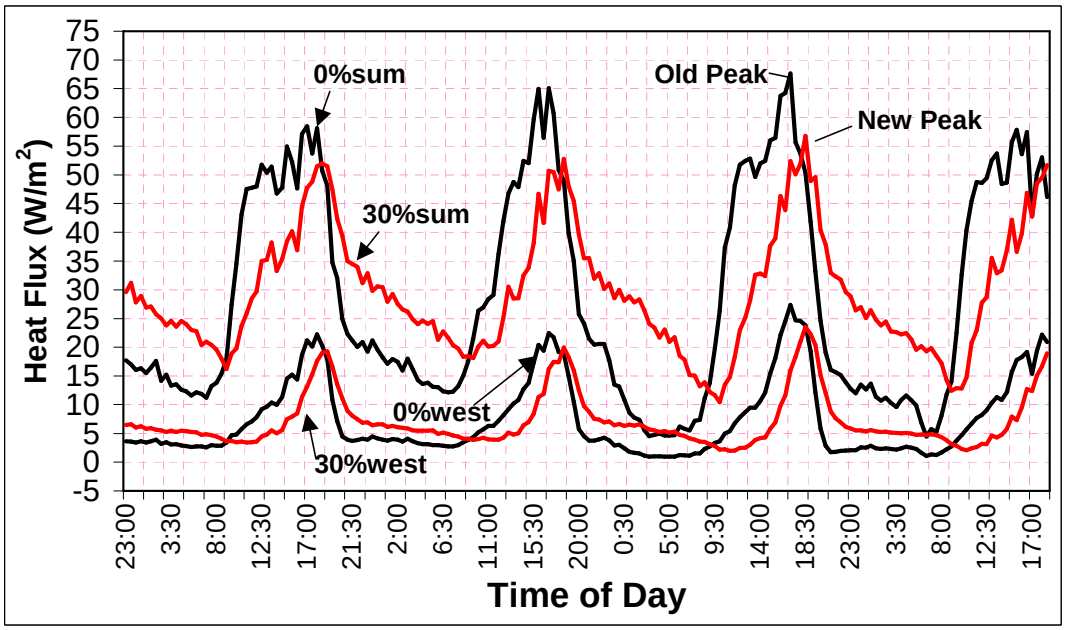

Figure 3.13 Comparison of individual wall heat fluxes with the sum of all heat fluxes (West wall – 30% concentration tests)

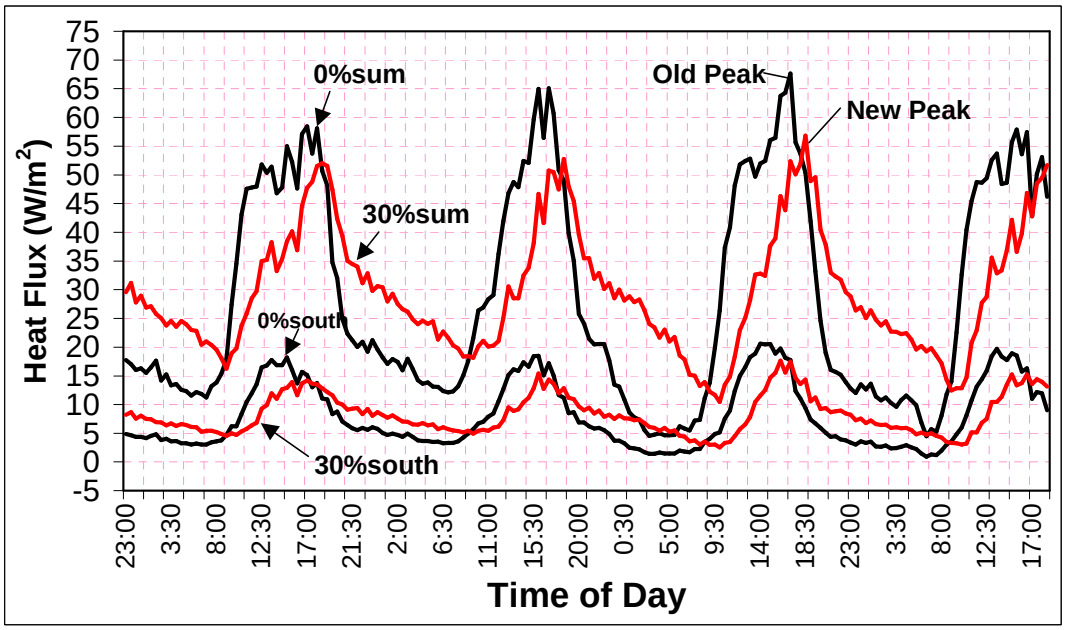

Figure 3.14 Comparison of individual wall heat fluxes with the sum of all the heat fluxes (South wall – 30% concentration)

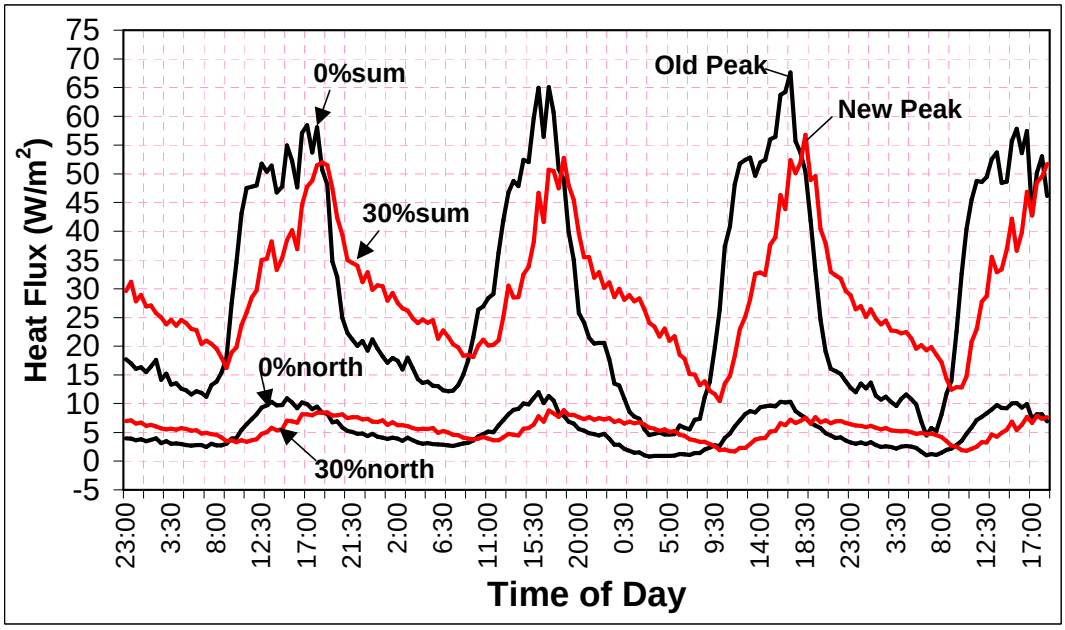

Figure 3.15 Comparison of individual wall heat fluxes with the sum of all the heat fluxes (North wall – 30% concentration)

Table 3.5 presents the sum of all heat fluxes for the same days in Tables 3.1 through 3.4. With 30% concentration paraffin, on average, the peak of combined peak heat flux was lowered by 20.87%. Thus, the PCM-enhanced insulation could lower the peak of the space cooling load through walls for residential buildings. Similar to the three days discussed above, cooler days tended to have larger reductions.

Table 3.5 Peak heat flux reductions (Sum of all walls)

Date	q1(W/m^2)	q2(W/m^2)	(q1-q2)/q1
2-Aug	52.23	31.19	40.30%
4-Aug	49.92	40.52	18.80%
5-Aug	54.36	43.32	20.30%
6-Aug	60.11	49.62	17.50%
7-Aug	58.47	52.02	13.70%
9-Aug	65.09	52.76	18.70%
13-Aug	67.27	60.76	9.70%
14-Aug	73.82	63.36	14.20%
15-Aug	73.34	64.55	12.00%
16-Aug	74.44	60.95	18.10%
17-Aug	59.12	45.02	23.80%
20-Aug	63	46.03	26.90%
21-Aug	58.82	47.43	19.40%
26-Aug	53.4	32.68	38.80%
Avg.	60.8	48.12	20.90%

3.1.4 Recommendations on the placement of PCM-enhanced insulation in individual walls

3.1.4.1 West wall

The heat fluxes across the west wall were higher than those for the other walls in the afternoons when the peak of the sum of the heat fluxes across the walls occurred. That is, the west walls heat fluxes were dominant in the peak of the sum.

Therefore, to get a large reduction in the peak wall space cooling load, the west wall's peak heat flux should be reduced as much as possible.

3.1.4.2 East, south and north walls

From the field experimental data, it was found that at 30% PCM concentration, the PCM-enhanced insulation did not contribute significantly to the reduction of the combined peak heat flux. Thus, it appears that PCM-enhanced insulation should not be applied to these three walls. However, if high concentration of PCM could be used and the PCM were placed in an optimized manner, the PCM in these walls could contribute to the reduction of the combined peak heat flux. Further study through numerical simulation is needed to get a definitive answer.

3.2 Dynamic wall simulator experiments – Macro-encapsulation method

3.2.1 Test setup

The dynamic wall simulator used in this research is shown in Figure 3.16. The simulator was located in an air-conditioned room, in which the indoor room air temperature was kept relatively constant. Inside the simulator, six 200-W light bulbs were used as the heat source to simulate solar radiation. Thus, the inside of the simulator represented the hot outside environment while the air-conditioned room simulated the cool indoor space. The four vertical 5.08 cm x 10.16 cm (2 in x 4 in) frame wall panels were installed "inside out."

By different combinations, two sets of timers and dimmers created wall

surface temperature changes that were close to those produced in the outer surface of walls under full weather conditions. Three fans were installed inside the simulator to stir the air and reduce stratification effects. A hole was cut at the bottom of the simulator and an exhaust fan was installed over the hole to exhaust hot air when a quick temperature drop was required.

Similar to the field tests, type T thermocouples were installed to measure wall surface temperatures, indoor air temperatures, and the temperatures around the PCM encapsulation pipes. Thermocouples were shielded with aluminum tape to eliminate the effects of radiation on the temperature measurement. Four heat flux meters were installed on each of the four walls to monitor the heat fluxes across the walls. A data logger and a computer collected the data at an interval of 10 seconds.

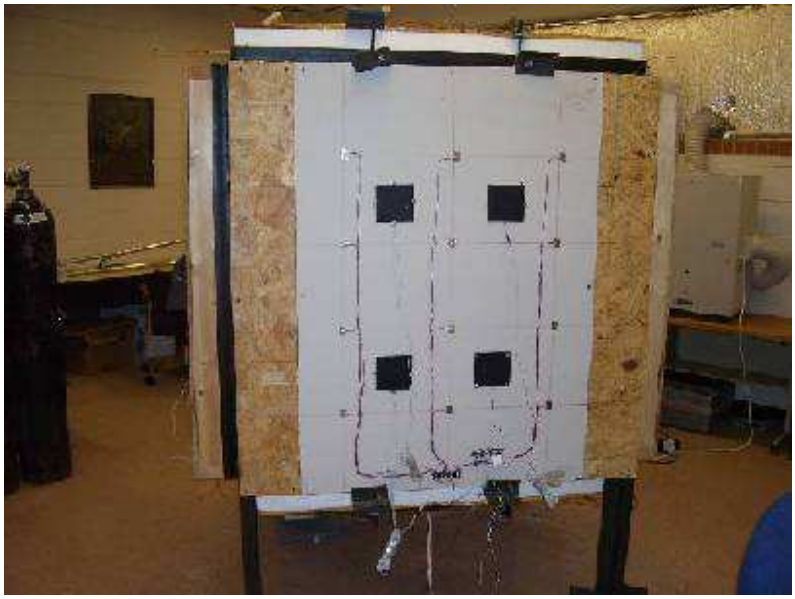

Figure 3.16 Dynamic wall simulator

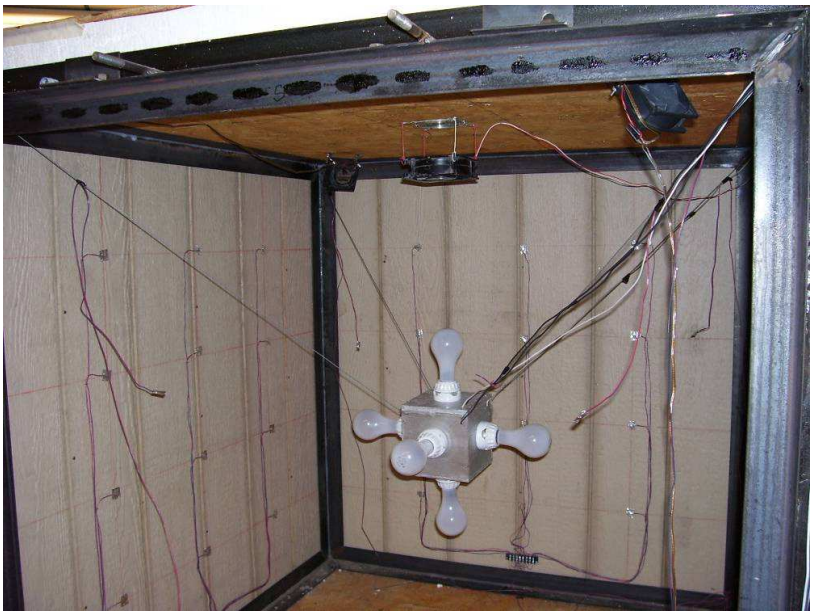

Figure 3.17 Interior of the dynamic wall simulator

Figure 3.18 Air mixing fan inside the simulator

Figure 3.19 Timer and dimmer combination

Figure 3.20 Data logger

3.2.2 Temperature control in the simulator

As discussed in Section 3.1.4, the west wall contributed the most to the peak heat flux reduction. For this reason, the daily temperature changes of the west wall were used to program the simulator controls for these experiments. After observing the shape of the temperature curves from the experimental tests under full weather

conditions, it was found that the temperature of west wall increased gradually in the morning. Then, after the noon hour, the temperature increased at a faster rate because of the direct solar radiation on this wall. After sunset, the wall surface temperature decreased rapidly. Thus, three timers and two dimmers were installed to control the two sets of lights and the exhaust fan in the simulator.

For the simulator tests, one timer first turned on the lights to create the slow temperature increase. This period lasted 6.5 hours. Then the second timer turned on to add more heating. As a result, the temperature curve became steep. This period lasted 4.5 hours. Afterwards, all the lights were turned off and the exhaust fan was turned on by the third timer to lower the temperature inside the simulator. The cooling down period lasted 13 hours. Different daily temperature curves could be created by adjusting the input power via the two dimmers.

As shown in Figures 3.21 to 3.23, the wall surface temperature curves created by the simulator were close to those from the field tests. Thus, the simulator could successfully create a boundary condition that was close to the one under the real weather conditions.

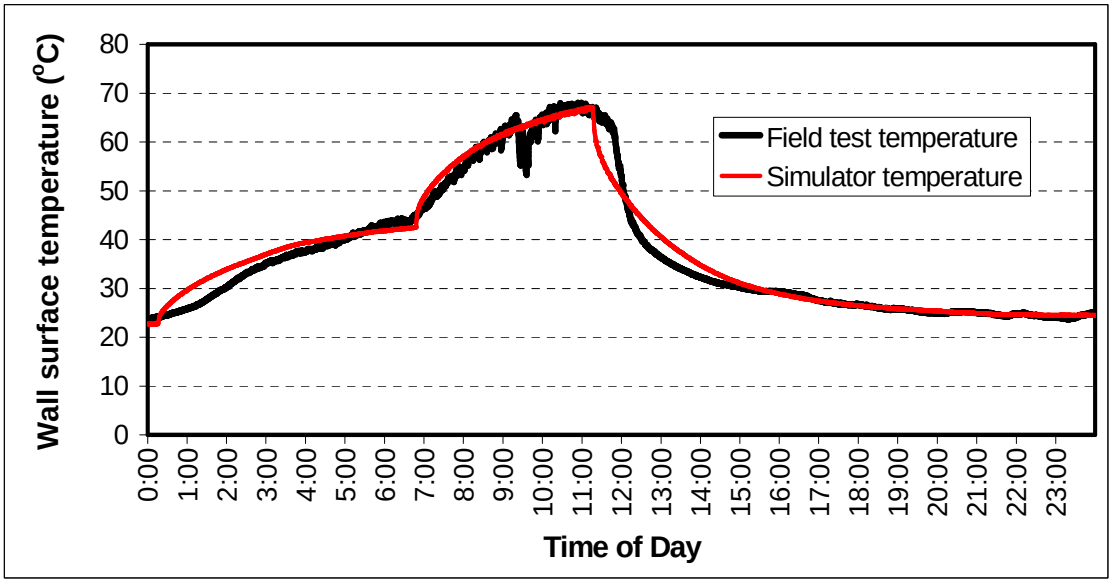

Figure 3.21 Comparison of the wall surface temperature curve created by the simulator with the one from field tests (maximum wall temperature of 69 °C /156.2°F)

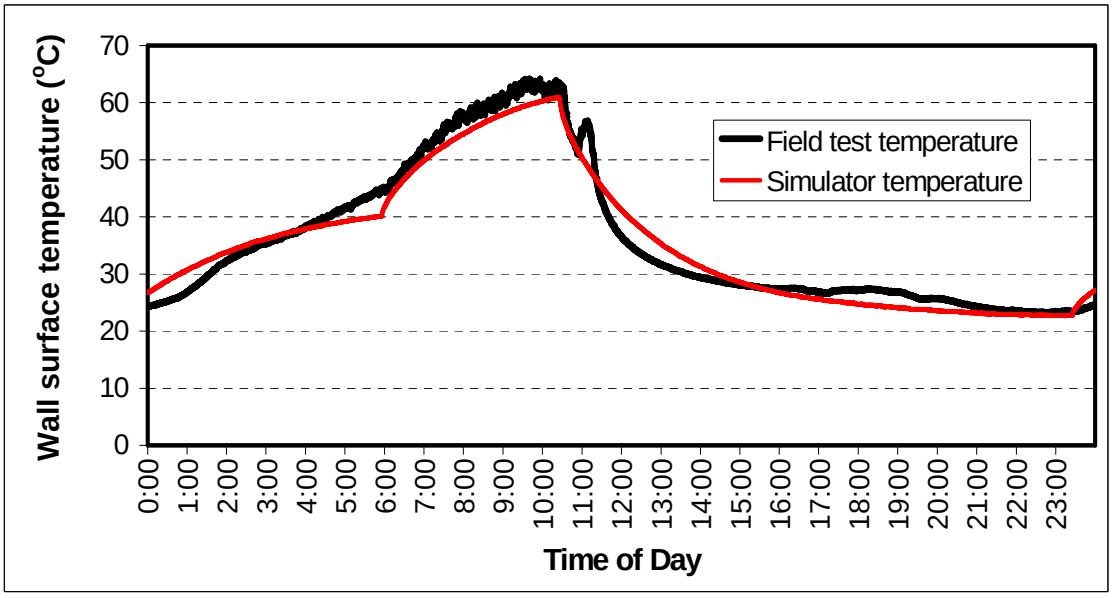

Figure 3.22 Comparison of the wall surface temperature curve created by the simulator with the one from field tests (maximum wall temperature of 61 °C/141.8°F)

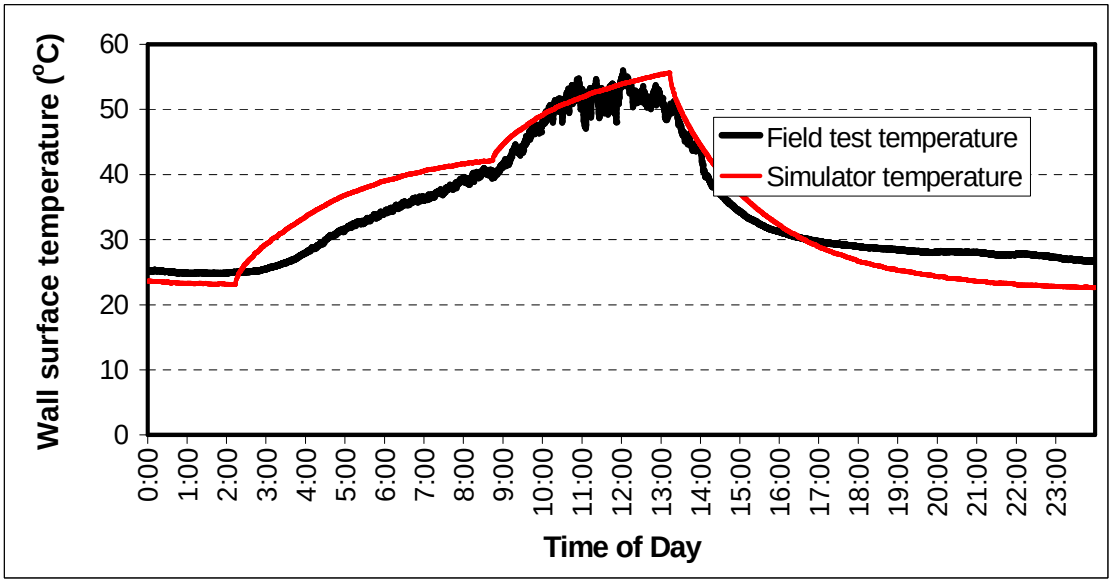

Figure 3.23 Comparison of the wall surface temperature curve created by the simulator with the one from field tests (maximum wall temperature of 55°C/131°F)

3.2.3 Installation of PCM-encapsulation pipes

The paraffin-based PCM used in this part of the research was n-Octadecane, sold under the trade name of RT27. This PCM was first melted and then poured into capped type M copper pipes. The two ends of each pipe were sealed using copper caps and plumbing glue. Wood frames were used to attach the pipes in the wall cavity. This is shown in Figures 3.24 through 3.27. Small pipes (1.27 cm, 1/2 in diameter) were placed 5.08 cm (2 in) apart and large pipes (1.9 cm, 3/4 in diameter) were placed 9.4 cm (3.7 in) apart from each other. If the PCM concentration was defined as the percentage of the weight of the gypsum board, the concentration for the tests using 1.27 cm (1/2 in) diameter pipes was 24.8% and the concentration for the tests using 1.9 cm (3/4 in) diameter pipes was 25.6%

When the PCM pipes were placed in the middle of the wall cavity and two layers of fiberglass batt insulation with a thermal resistance value of 1.94 $m^2 \cdot K/W$ (11 $hr \cdot ft^2 \cdot R/Btu$) were installed over and beneath the pipes, the tests were referred to as "middle depth" tests. When the PCM pipes were place next to the wallboard which was close to the cool environment, and the two layers of insulation were placed over the pipes, the tests were referred to as "next to wallboard" test.

Figure 3.24 Wall assembly used in the "middle depth" tests

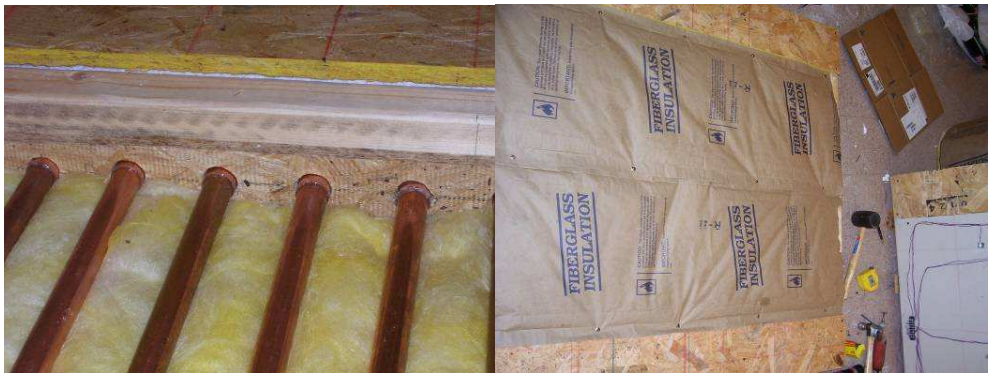

Figure 3.25 Close up view of the wall assembly used in the “middle depth” tests

Figure 3.26 Wall assembly used in the “next to wallboard” tests (1.27 cm,1/2 in diameter pipes)

Figure 3.27 Wall assembly used in the “next to wallboard” tests (1.9 cm, 3/4 in diameter pipes)

3.2.4 Results and analysis

3.2.4.1 “Calibration” test

Because of the pipes, the insulation was compressed to some extent compared with the case without pipes. As a result, the thermal resistance value of the insulation might have changed. In the calibration test, the inside surface of the wall panel (the hot side) was heated to a high temperature of around 70^{o}C (158^{o}F) until the system reached steady state. Under steady state the phase change process would not affect the heat transfer. The comparison of the heat fluxes between the control wall panel (the wall panel in which plain insulation was installed), and the PCM-enhanced wall panels is shown in Figure 3.28. As shown, at steady state the heat fluxes for the “middle depth” configuration were very close to the heat fluxes across the control

wall panel. That is, the thermal resistance (R-value) of the insulation did not change with the installation of the small 1.27 cm (1/2 in) pipes.

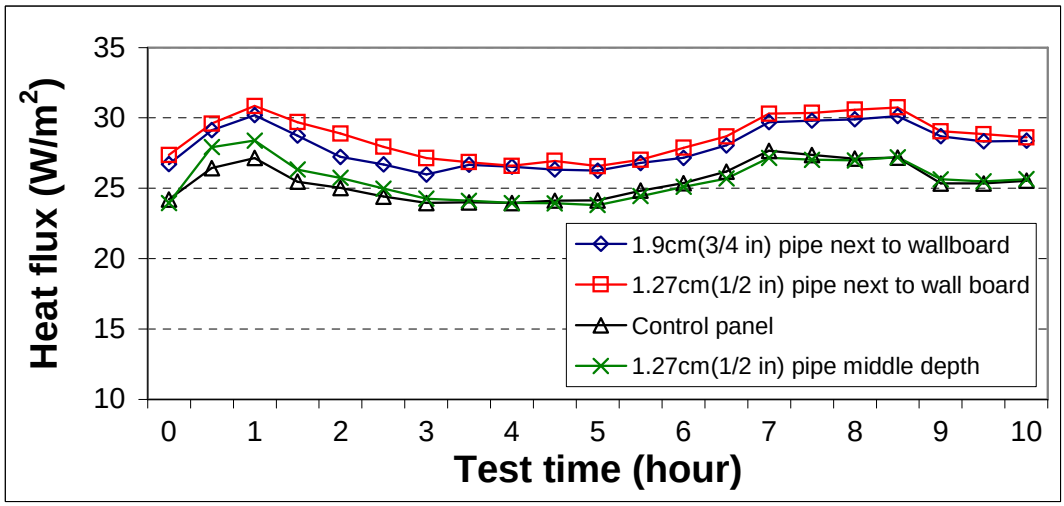

Figure 3.28 Heat fluxes across walls panels in the dynamic wall simulator (Calibration)

For the “next to wallboard” configuration, the heat fluxes of the 1.9 cm (3/4 in) and 1.27 cm (1/2 in) pipe tests were close to each other and approximately 10% higher than those of the control panel. This happened because in the “next to wallboard” configuration the insulation did not wrap around the pipes as well as in the “middle depth” configuration, which in turn created an air space between the insulation and the wallboard. This is illustrated in Figure 3.29.

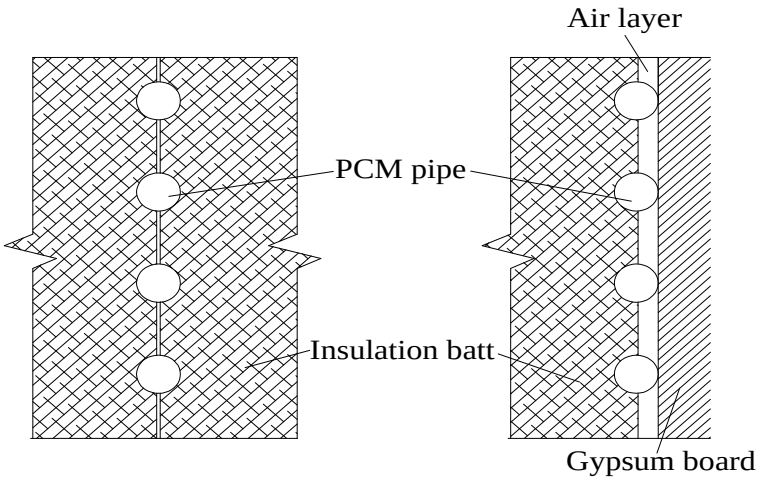

Figure 3.29 Schematic of the "Middle Depth" configuration (left) and "Next to Wallboard" configuration (right)

3.2.4.2 Experiments using the "middle depth" configuration

The heat flux peak reductions for different wall surface temperature curves (different weather conditions) are shown in Figures 3.30 through 3.33. In the figure captions, the temperatures in parenthesis indicate the maximum wall surface temperatures corresponding to the temperature curves in Figures 3.21 through 3.23.

From the figures, it was found that in all tests PCM-wall's peak heat fluxes were lower than those of the control walls and the peak hours were shifted by a few hours. As depicted in the graphs, the first day of testing always produced a large peak heat flux reductions, while the peak reductions of the rest testing days were much smaller. This could be explained by that, during the first day of testing, the PCM melted from a completely solidified state, while in the rest of the testing days, the PCM melting process started from partially melted states, which meant less latent thermal storage capacity. That was because the pipes were located in the middle of

the insulation, the thermal resistance between the PCM and the conditioned cool environment was large; therefore, the solidification process was slow and the PCM in the pipes was not able to completely solidify or recovere most of its latent thermal storage capacity during the cool down period. As a result, at the beginning of the next day, the PCM started melting from a partially-melted state, which resulted in a smaller heat flux peak reduction.

It was also found that the tests with lower maximum surface temperatures produced larger heat flux peak reductions than those with higher temperatures. This is the case because, at low temperatures, the PCM solidification problem was not as severe as those in the tests in which the surface temperatures were high.

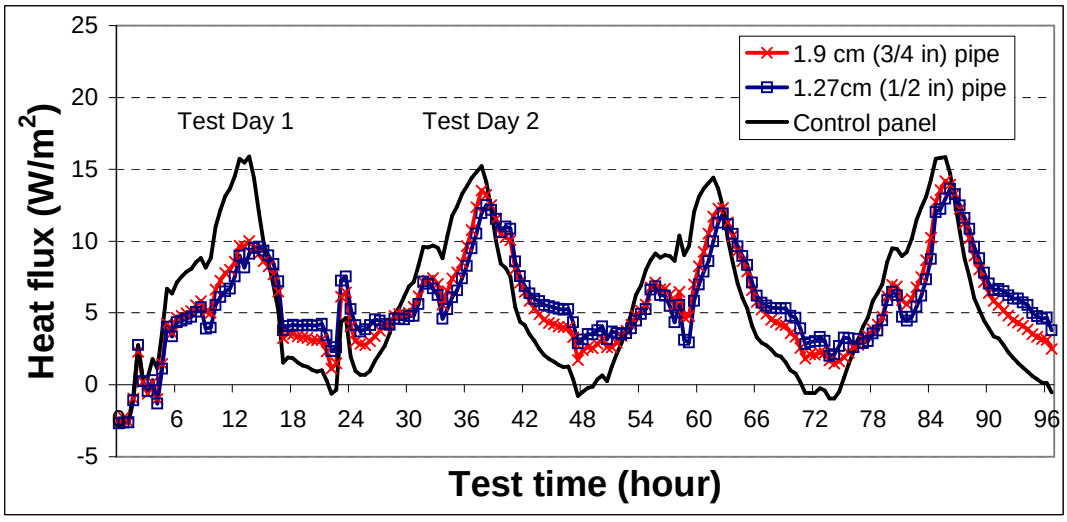

Figure 3.30 Heat fluxes across the wall panels in the dynamic wall simulator (maximum wall temperature of 55 ^{o}C/131 ^{o}F)

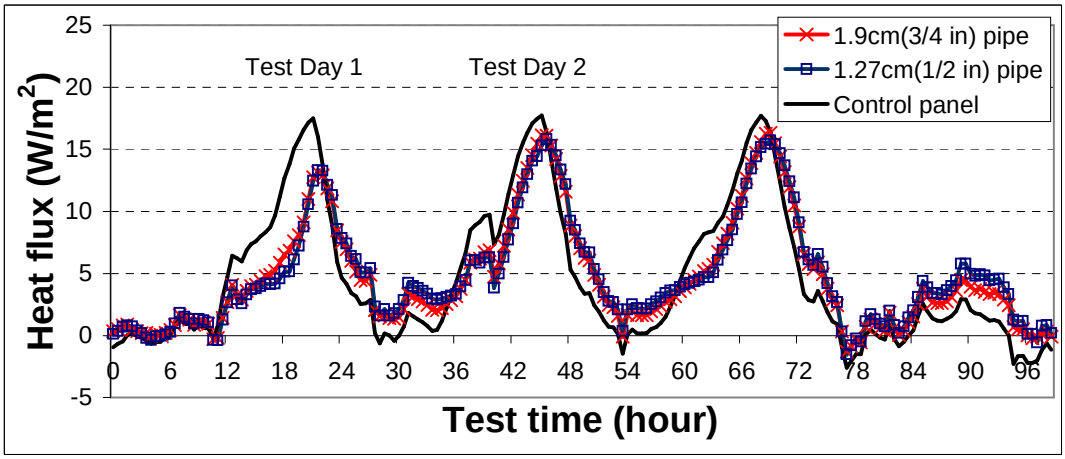

Figure 3.31 Heat fluxes across the wall panels in the dynamic wall simulator (maximum wall temperature of 61 ^{o}C/141.8 ^{o}F)

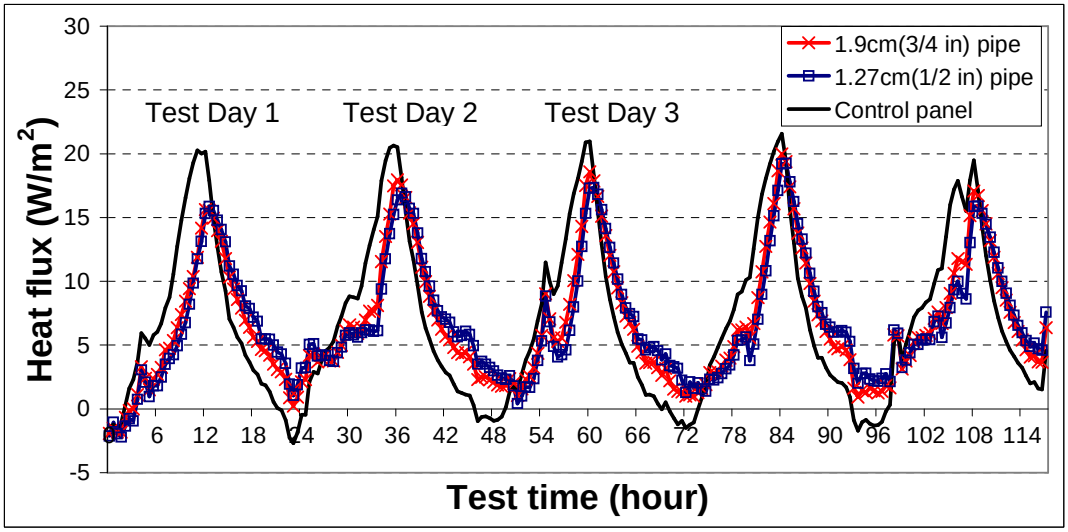

Figure 3.32 Heat fluxes across the wall panels in the dynamic wall simulator (maximum wall temperature of 65 ^{o}C/149 ^{o}F)

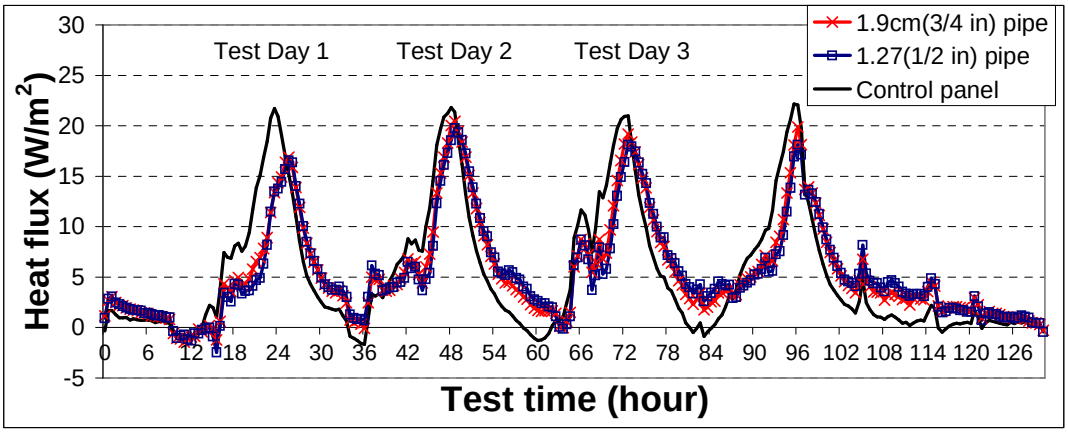

Figure 3.33 Heat fluxes across the wall panels in the dynamic wall simulator (maximum wall temperature of 69 ^{o}C/156.2 ^{o}F)

The temperature at one point on the pipe, as illustrated in Figure 3.34, was monitored. The temperatures of this single point corresponding to the tests of Figures 3.30 to 3.33 are presented in Figures 3.35 through 3.38.

As shown in these figures, the peak temperatures for the first day of each test were lower when compared with those of the rest days. This explains why the peak heat fluxes for the first day in the previous graphs were lower.

When the heating period stopped, the temperature decreased. However, from the figures, it was found that when the pipe surface temperatures dropped to about 26 - 27 ^{o}C (78.8 - 80.6 ^{o}F), the temperature curves became flat, which meant the temperature of the PCM pipe was kept relatively constant as a result of the solidification process. As mentioned above, because of the large thermal resistances between the PCM and the colder conditioned space, the solidification process was too slow to be completed during the cool down period. In the graphs, it can be observed that the temperatures of the PCM did not drop below 25 ^{o}C (77 ^{o}F) before rising

again, which meant the PCM did not completely solidify at the end of the cool down period.

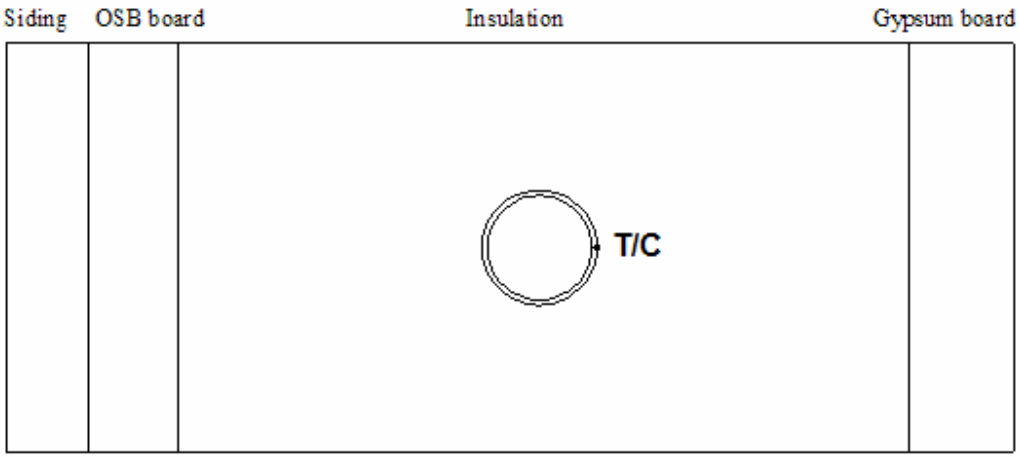

Figure 3.34 Location of the thermocouple used to monitor the encapsulating pipe temperature ("middle depth" configuration)

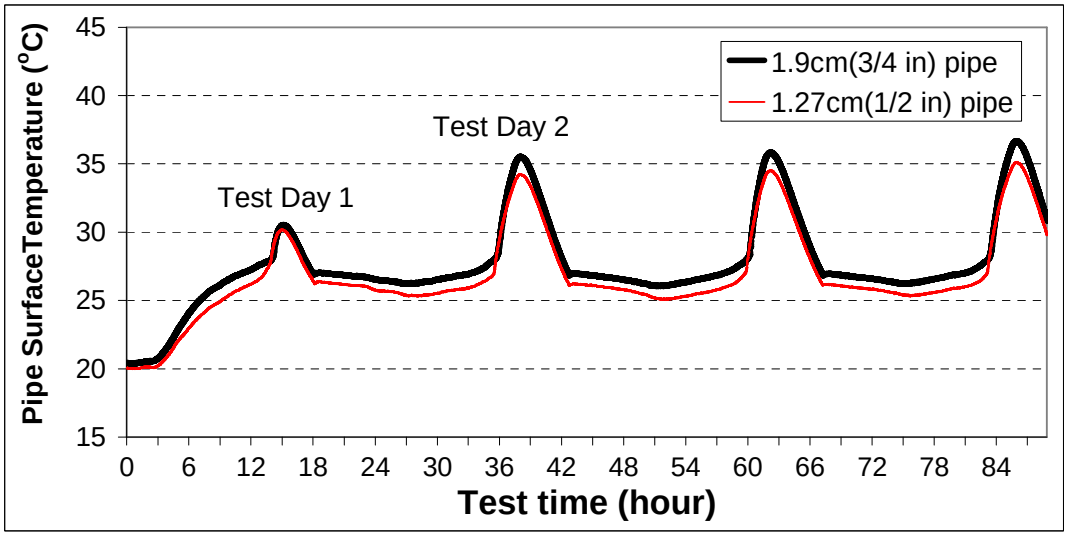

Figure 3.35 Surface temperature of the encapsulating pipes (maximum wall temperature of 55 °C/131 °F)

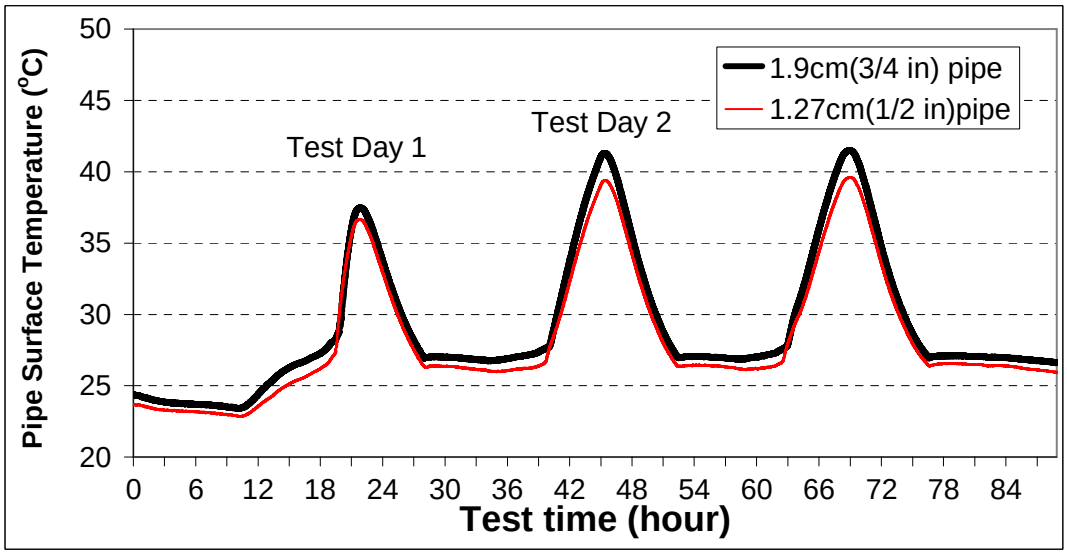

Figure 3.36 Surface temperature of the encapsulating pipes (maximum wall temperature of 61 °C/141.8 °F)

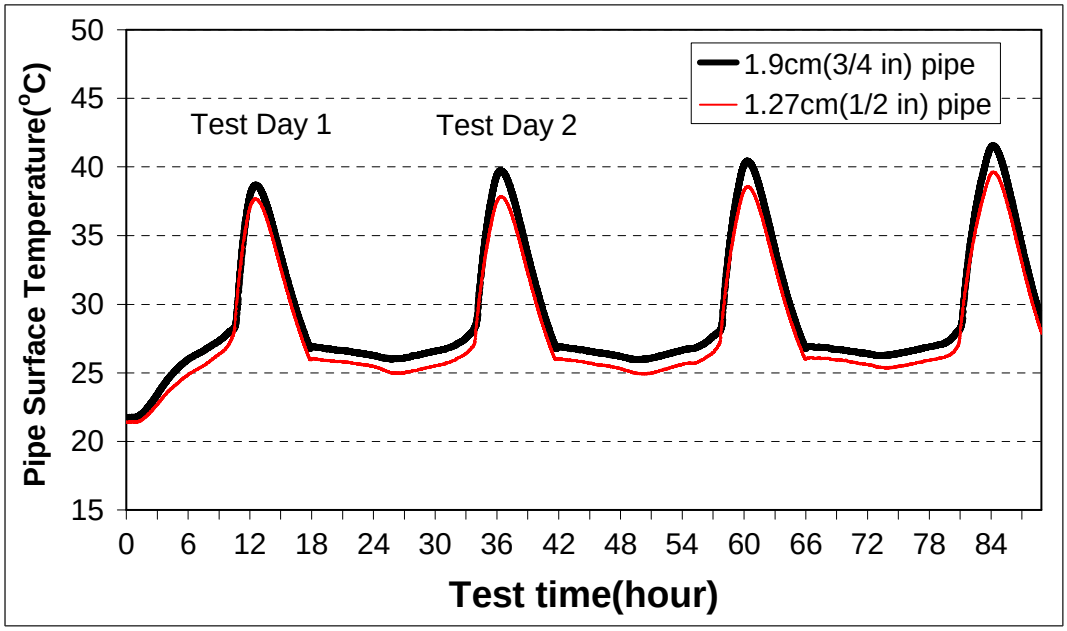

Figure 3.37 Surface temperature of the encapsulating pipes (maximum wall temperature of 65 °C/149 °F)

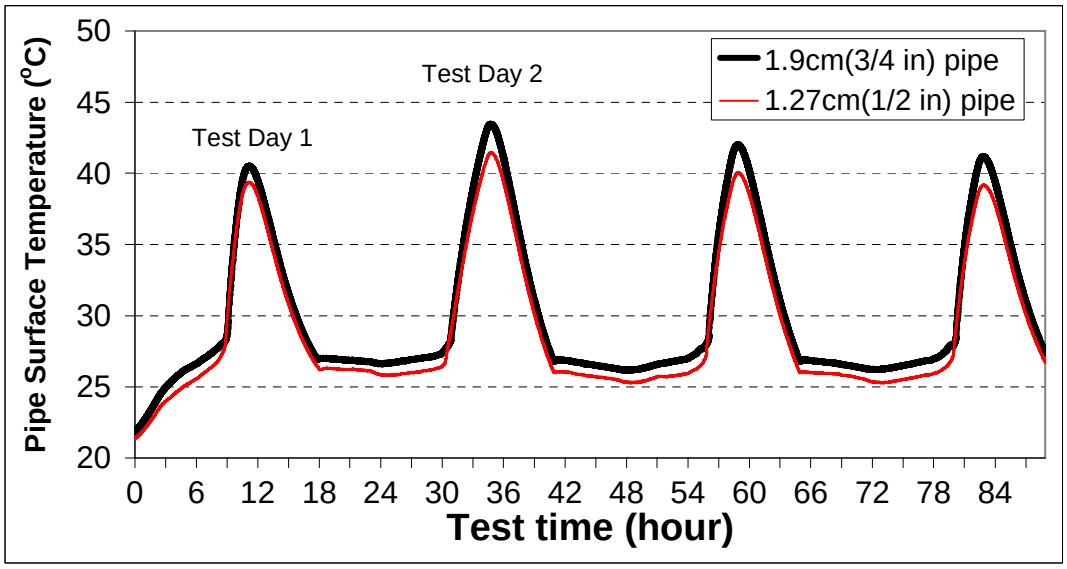

Figure 3.38 Surface temperature of the encapsulating pipes (maximum wall temperature of 69 ^{o}C/156.2 ^{o}F)

Another set of tests was conducted to further investigate the solidification process under a maximum wall temperature of 65 ^{o}C (149 ^{o}F). This temperature was chosen because it was close to the typical value that was observed in field tests. In these tests, the cooling down period was extended first by four hours, and later by eight hours, while the melting period was kept the same. The results are shown in Figures 3.39 through 3.42. As shown, with longer solidification times, the peak heat flux reductions did not change significantly. The surface temperature of the pipe still did not drop below 25 ^{o}C (77 ^{o}F). This was also the case when the cooling down period was extended by eight hours. Thus, it was concluded that the "middle depth" configuration was not an ideal position to install the PCM encapsulating pipes because of the difficulty in solidification, especially during hot days.

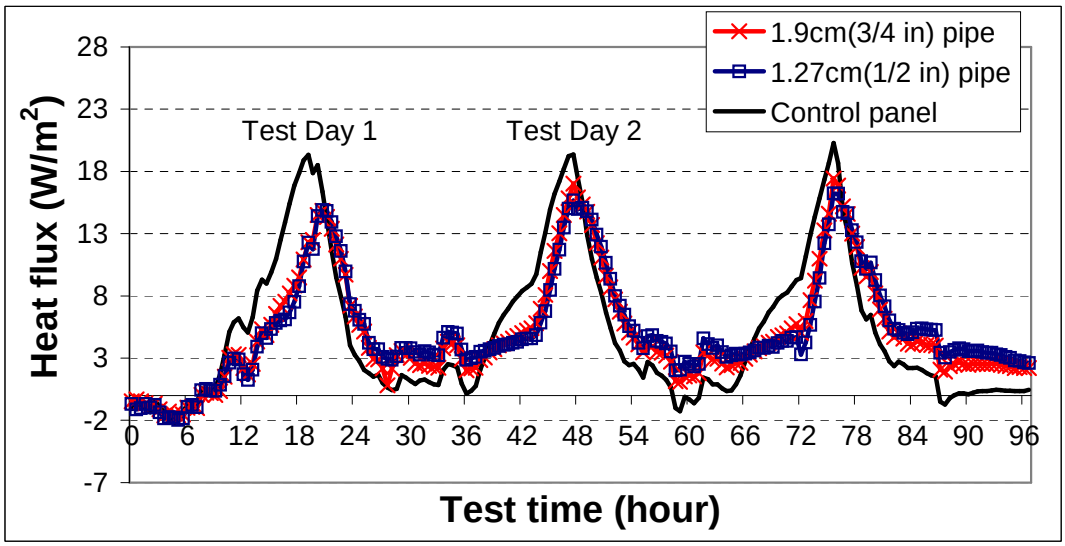

Figure 3.39 Heat fluxes across the wall panels in the dynamic wall simulator (maximum wall temperature of 65 ^{o}C/149 ^{o}F, with 4h extension)

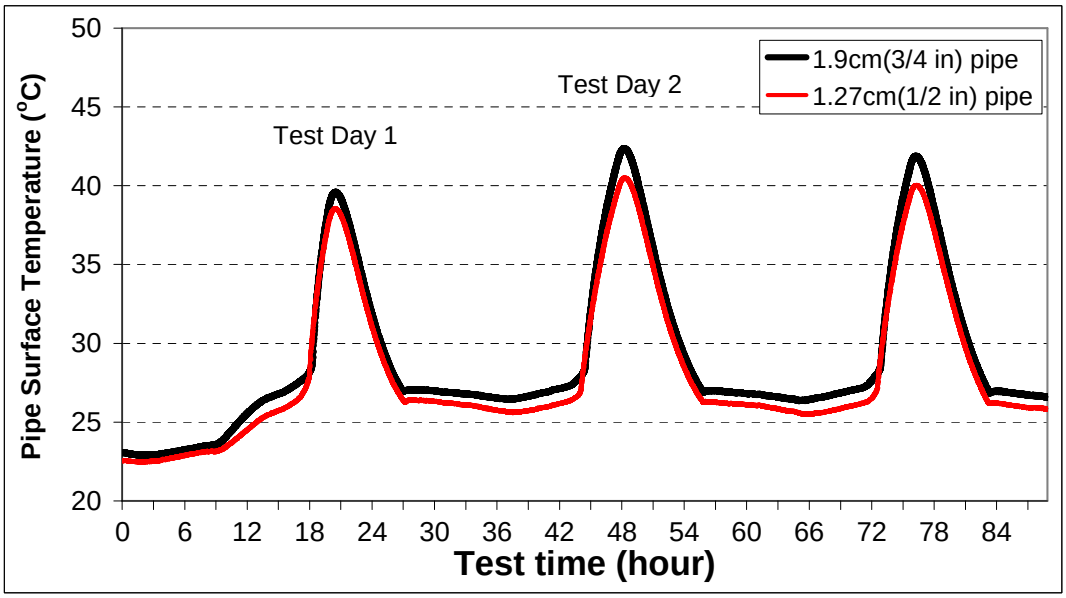

Figure 3.40 Surface temperature of the encapsulating pipes (maximum wall temperature of 65 ^{o}C/149 ^{o}F, with 4h extension)

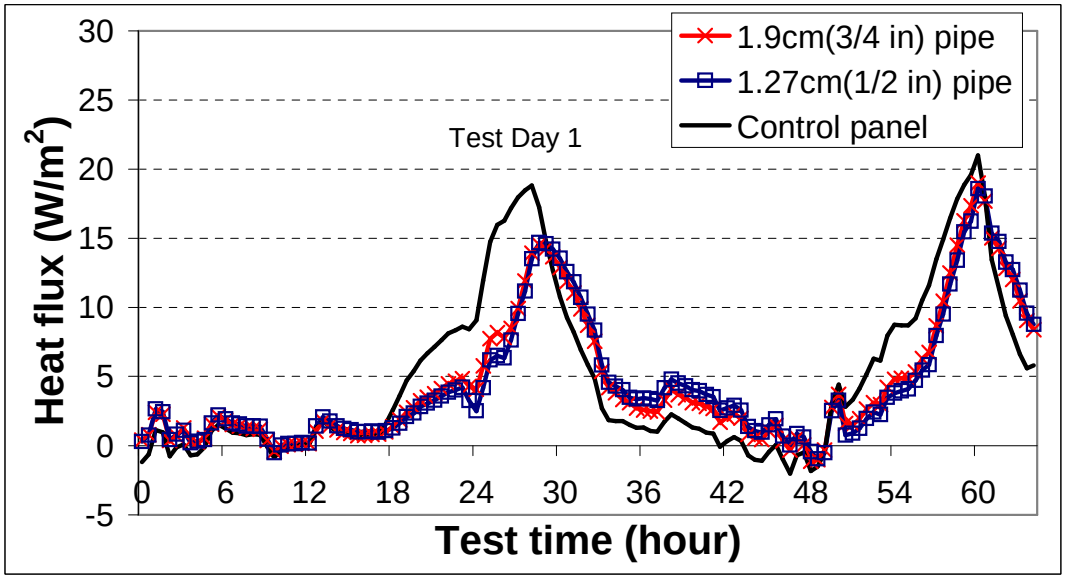

Figure 3.41 Heat fluxes across the wall panels in the dynamic wall simulator (maximum wall temperature of 65 ^{o}C/149 ^{o}F, with 8h extension)

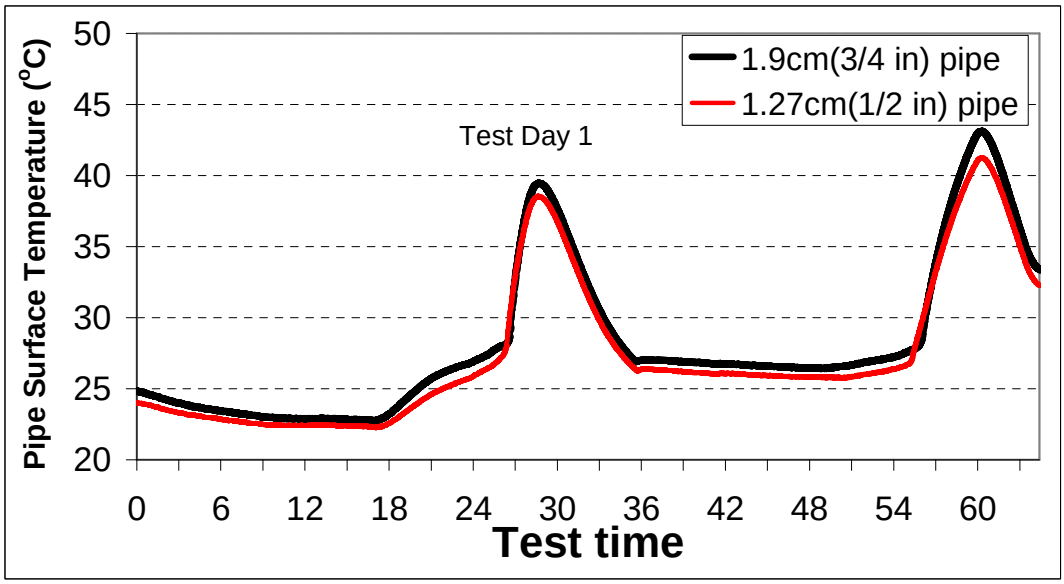

Figure 3.42 Surface temperature of the encapsulating pipes (maximum wall temperature of 65 ^{o}C/149 ^{o}F, with 8h extension)

3.2.4.3 Experiments using the “next to wallboard” configuration

Figure 3.43 depicts the “next to wallboard” configuration. Heat flux peak reductions for experiments using the “next to wallboard” configuration for different wall surface temperature curves are shown in Figures 3.44 through 3.46.

Unlike the “middle depth” configuration tests, the peak reductions in heat flux for the first day of the experiments were not much different from those of the rest of the days. That was because the pipes were closer to the indoor conditioned environment, which made the thermal resistance for the solidification process, R_{inside} in Figure 3.43, significantly smaller than in the previous configuration. Thus, in the “next to wallboard” test, the solidification of the PCM was no longer a problem. The peak heat flux reduction depended only on the melting process. It was also found that, contrary to the “middle depth” configuration, higher surface wall temperature tests yielded larger heat flux peak reductions in the “next to wallboard” configuration.

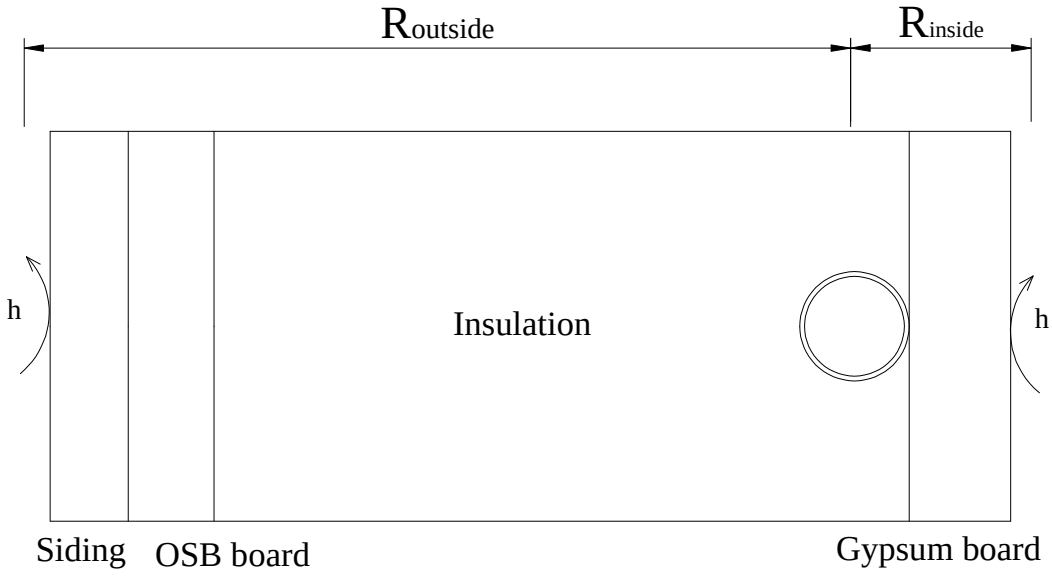

Figure 3.43 Schematic of the "Next to Wallboard" configuration

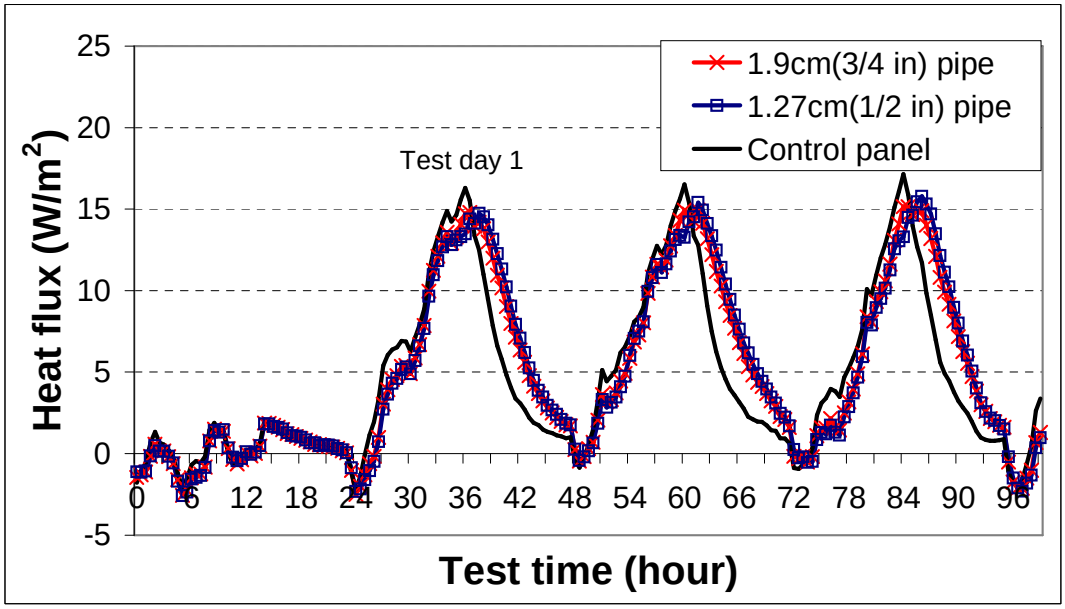

Figure 3.44 Heat fluxes across the wall panels in the dynamic wall simulator (maximum wall temperature of 58 ^{o}C(136.4 ^{o}F))

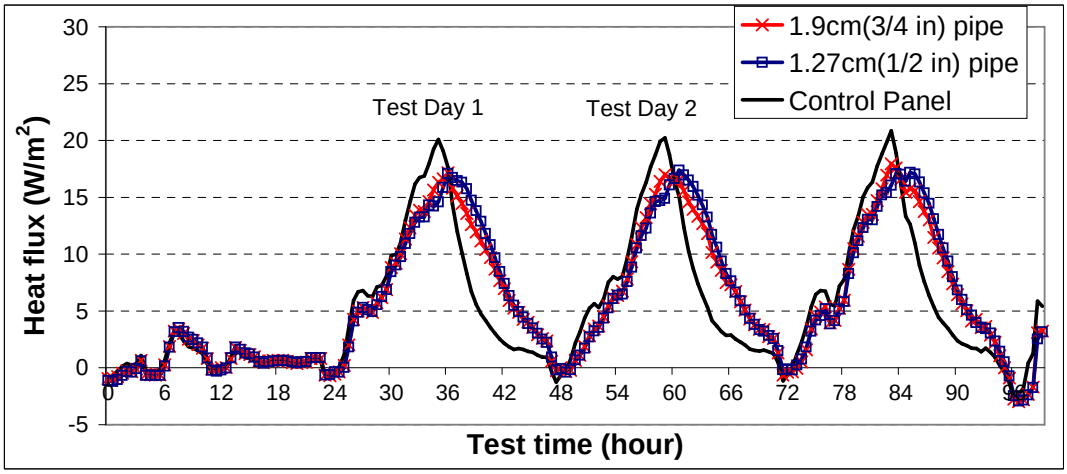

Figure 3.45 Heat fluxes across the wall panels in the dynamic wall simulator (maximum wall temperature of 65 ^{o}C(149 ^{o}F))

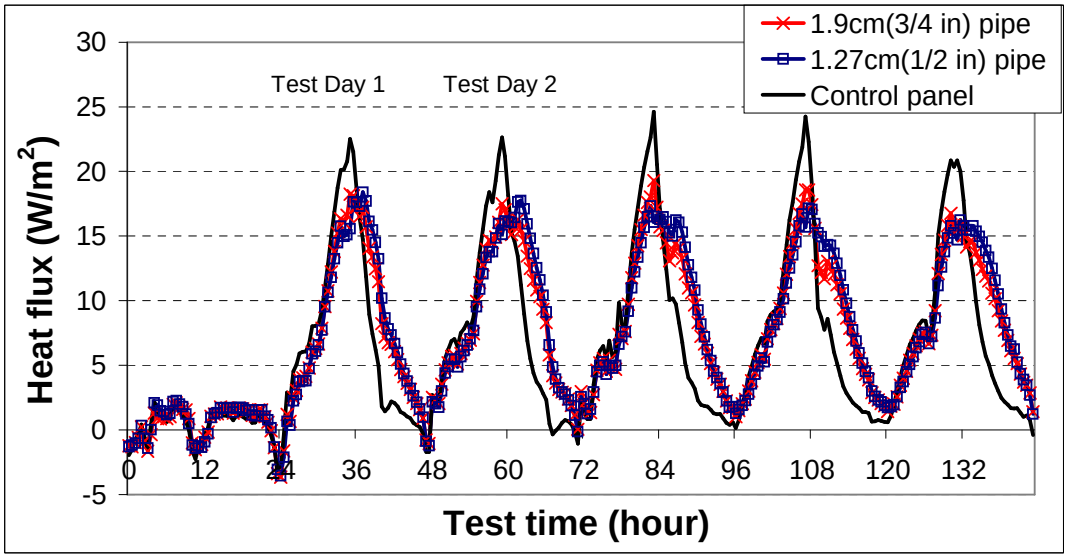

Figure 3.46 Heat fluxes across the wall panels in the dynamic wall simulator (maximum wall temperature of 70 ^{o}C(158 ^{o}F))

The temperatures at the four points around the pipe, as illustrated in Figure 3.47, were monitored. The data are shown in Figures 3.48 through 3.53. The temperatures at the different locations were close. That was because of the small size

of the pipe and the high conductivity of the copper. It was also observed that, for all the tests, the temperatures around the pipe did not get high enough. This could be explained by the fact that the pipes were too close to the cold side. Even though the temperatures of the pipes were relatively low, the heat fluxes were almost of the same values as those recorded using the "middle depth" configuration because the heat resistance between the pipe and the indoor environment was smaller.

For different tests, with the maximum wall temperatures increasing from 58^{o}C to 70^{o}C (131-158 ^{o}F), the PCM pipe's highest temperatures increased accordingly, which meant more of the thermal storage capacity of the PCM was used. That was why the tests under the higher maximum wall temperature yielded larger heat flux peak reductions. But even in the 70^{o}C test, the highest temperature of the pipe was still below the peak temperature range of the R27 PCM (27-27.5^{o}C, 80.6-81.5^{o}F). Thus, under this configuration, most of the latent heat of fusion was not used, which explained why large peak reductions could not be produced. Thus, the "next to wallboard" configuration did not represent an ideal location for the encapsulating pipes.

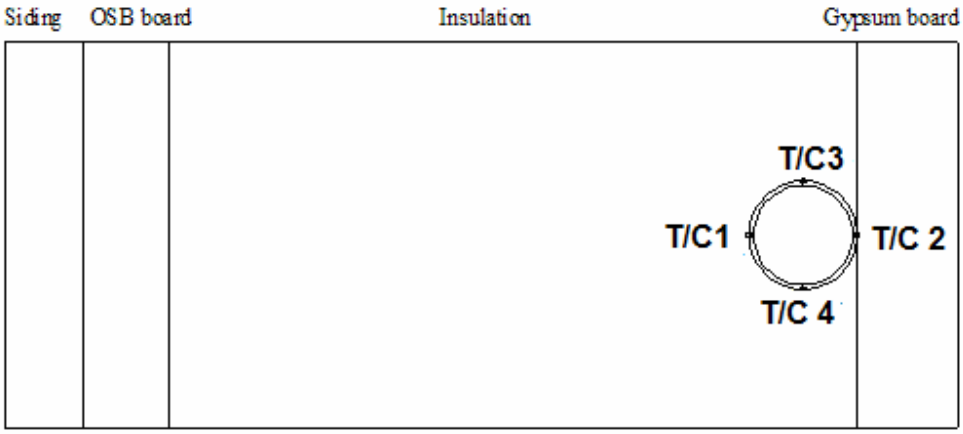

Figure 3.47 Location of the thermocouples used to monitor the encapsulating pipe temperature ("next to wallboard" configuration)

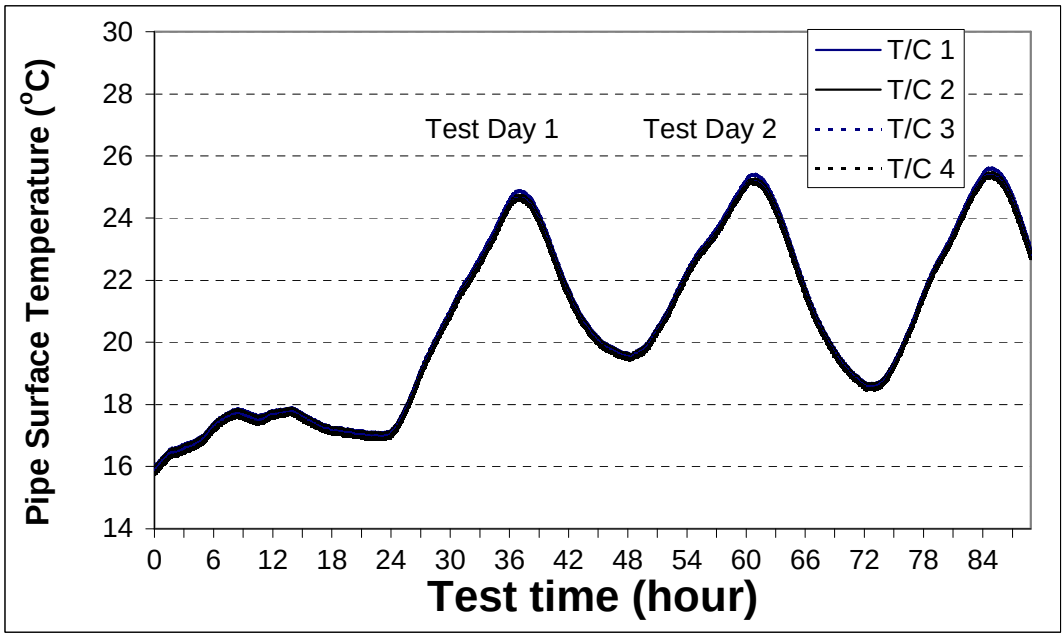

Figure 3.48 Surface temperature of the encapsulating pipes (maximum wall temperature of 58 °C/131 °F, 1.9 cm (3/4 in) pipe)

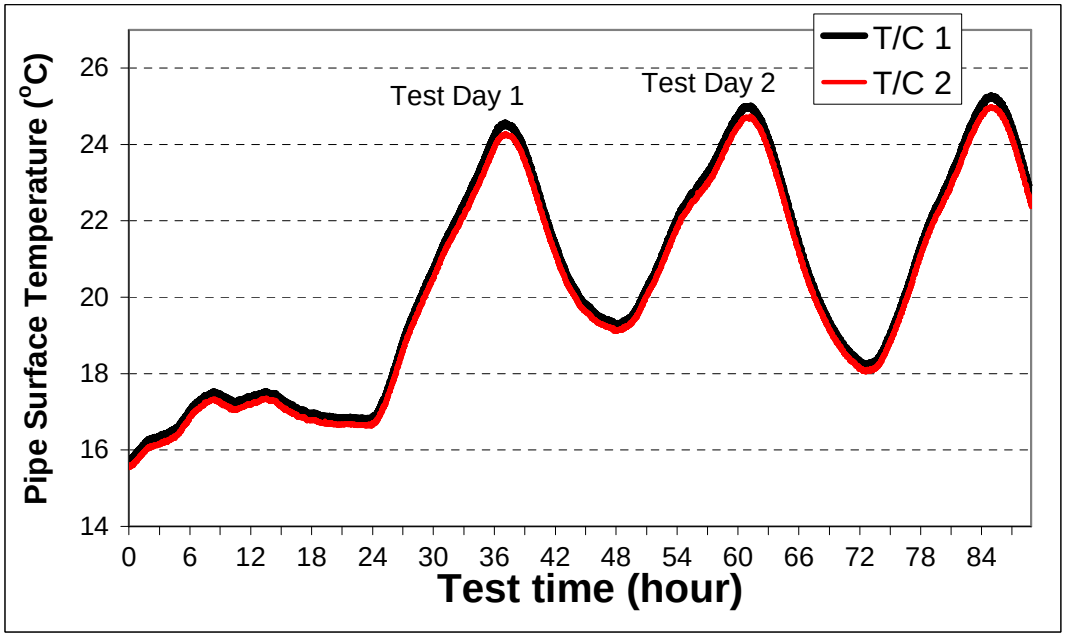

Figure 3.49 Surface temperature of the encapsulating pipes (maximum wall temperature of 58 °C/131 °F, 1.27 cm (1/2 in) pipe)

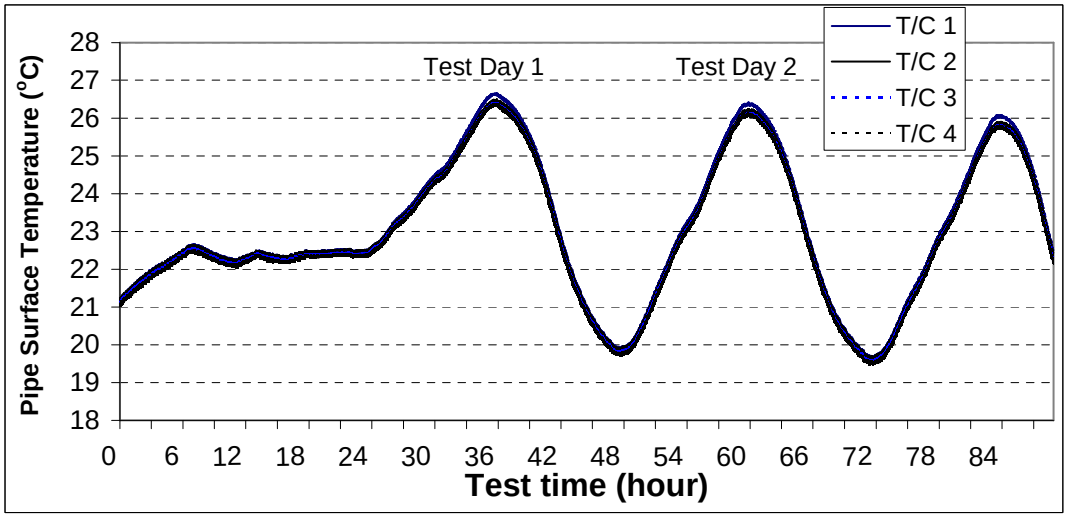

Figure 3.50 Surface temperature of the encapsulating pipes (maximum wall temperature of 65 °C/149 °F, 1.9 cm (3/4 in) pipe)

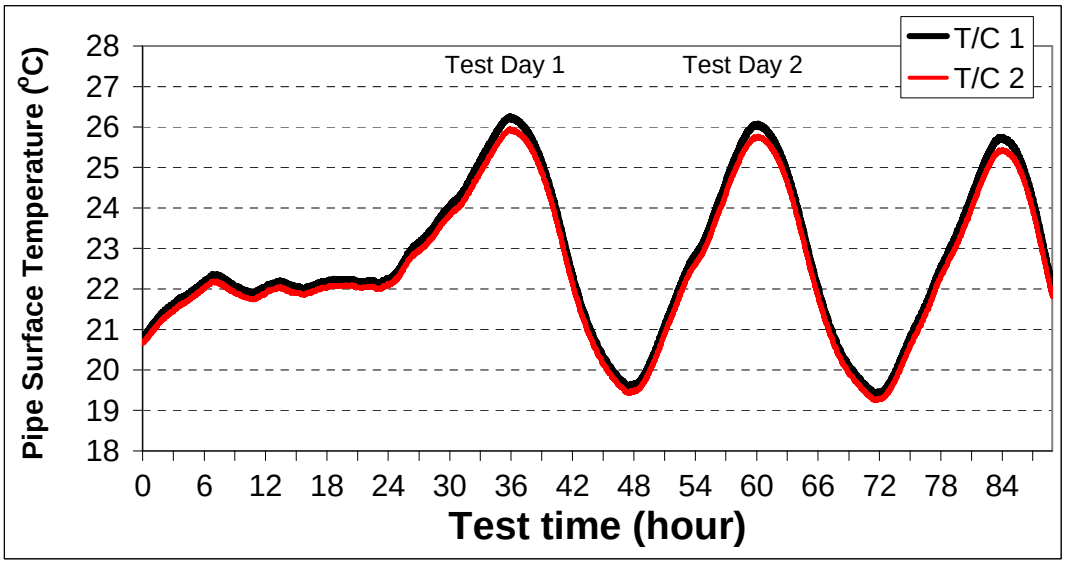

Figure 3.51 Surface temperature of the encapsulating pipes (maximum wall temperature of 65 °C/149 °F, 1.27 cm (1/2 in) pipe)

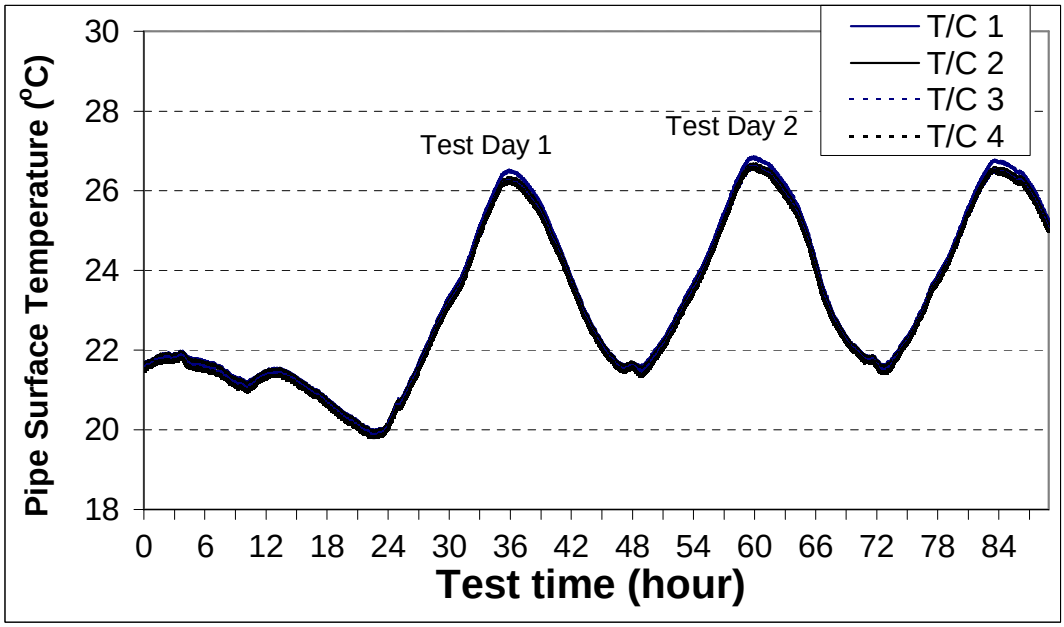

Figure 3.52 Surface temperature of the encapsulating pipes (maximum wall temperature of 70 °C/158 °F, 1.9 cm (3/4 in) pipe)

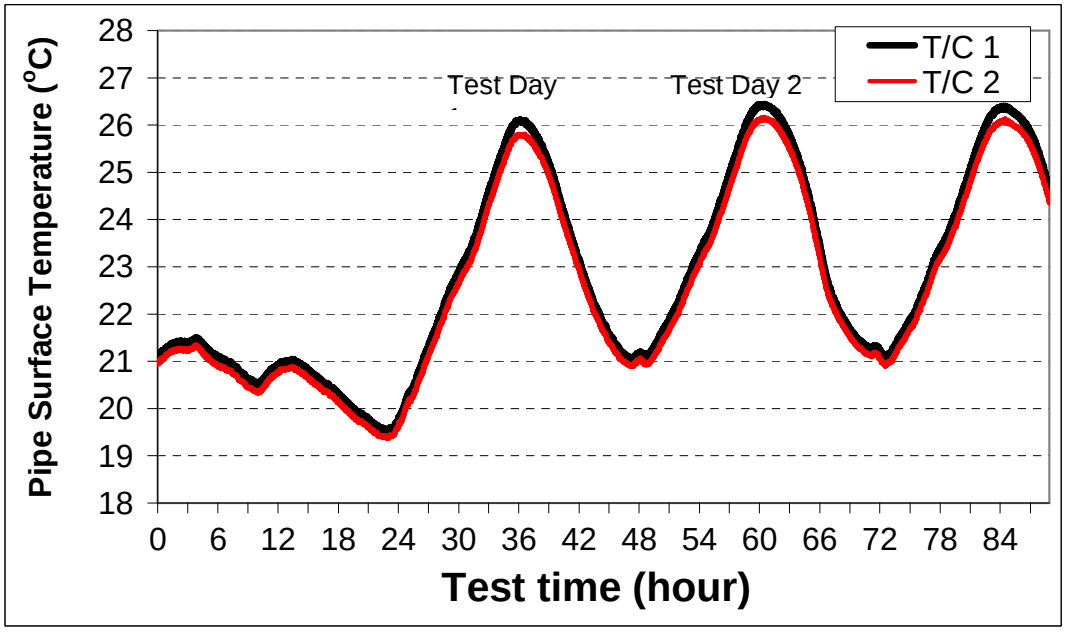

Figure 3.53 Surface temperature of the encapsulating pipes (maximum wall temperature of 70 °C/158 °F, 1.27 cm (1/2 in) pipe)

3.2.4.4 Discussion: Optimized pipe location

From the analysis above the optimized location of the PCM encapsulating pipes should be somewhere between the above two locations, namely, in the middle of the wall and next to the wallboard. For the solidification process, the thermal resistance between the pipe and indoor environment should not be too high for the PCM to solidify. It is equally important that the thermal resistance should not be too low as to make the temperatures around the PCM pipes too low for the PCMs to melt (i.e., the latent thermal storage capacity is not used). In Chapter 6, numerical simulations were used to find the optimal location for the PCM in PCM-enhanced insulation.

3.3 Summary

From the experimental results using a 30% PCM concentration in the PCM-enhanced cellulose insulation (direct mixing), it was found that the PCM could lower and shift the peak heat fluxes. On average, for the east wall, the absolute peak heat flux was reduced by 38.5%; for the west wall, the reduction was 22.3%; for the south wall, the reduction was 19.0%; and for the north wall, the reduction was 27.4%. The PCM-enhanced insulation only reduced the peak heat fluxes, but on a daily basis, the use of PCM-enhanced insulation would not reduce the daily space cooling load because the reductions produced by the melting process in the daytime would be cancelled out by increases in heat fluxes produced by the solidification process at night and early morning hours.

Assuming the weights of the four walls were the same, on average, the absolute sum of the peak heat fluxes could be reduced by 20.9%, which was lower than the sum of the heat flux reductions of the four walls. From a detailed analysis, it was found that this happened because the various walls peaked at different times during the day. For 30% PCM concentration, the east, south and north walls did not contribute to the peak heat flux reduction. Based on this, the west wall should be the wall where the PCM-enhanced insulation should be installed to lower the peak heat fluxes as low as possible. When higher concentrations of PCM are used, the PCM in the east, south and north walls may help in reducing the total heat flux peak. Further study through numerical simulation is needed to get a definitive answer.

From experiments using the dynamic wall simulator, it was found that for the "middle depth" configuration, the PCM would not solidify enough in the cool down period to yield a large peak heat flux reduction. While for the "next to wallboard" configuration, the latent thermal storage capacity of the PCM could not be fully used because the temperature around the PCM pipe was too low. A large peak heat flux reduction could not be achieved either. An optimal location for the PCM may exist between the location of the encapsulating pipes in the "middle depth" and "next to wallboard" locations, which could to be evaluated using numerical methods.

Chapter IV

Analysis of the Heat Transfer Process and Peak Reduction Principal of the PCM-wall

In this chapter, a new PCM incorporating method was proposed as an improvement of the macro-encapsulation (pipe) method. The new method is thought to overcome the problems associated with previous PCM incorporating methods, namely the imbibing method, macro-encapsulation method and direct mixing method, and make the process of integrating PCM into wall systems more practical. The heat transfer process across the walls enhanced with PCM was analyzed for different situations. The peak reduction principal of the PCM-wall was revealed. The results are presented in this chapter.

4.1 A new incorporating method

For the macro-encapsulation method using metal pipes ("Pipe test" in Chapter 3), the heat transferred into the indoor environment, during summer days, can be divided into two parts. One is the heat transfer between the outside hot environment and the indoor cool environment through the path between the PCM pipes (Q1) and the other is the heat transfer between the PCM pipes and the indoor cool environment (Q2), as illustrated in Figure 4.1.

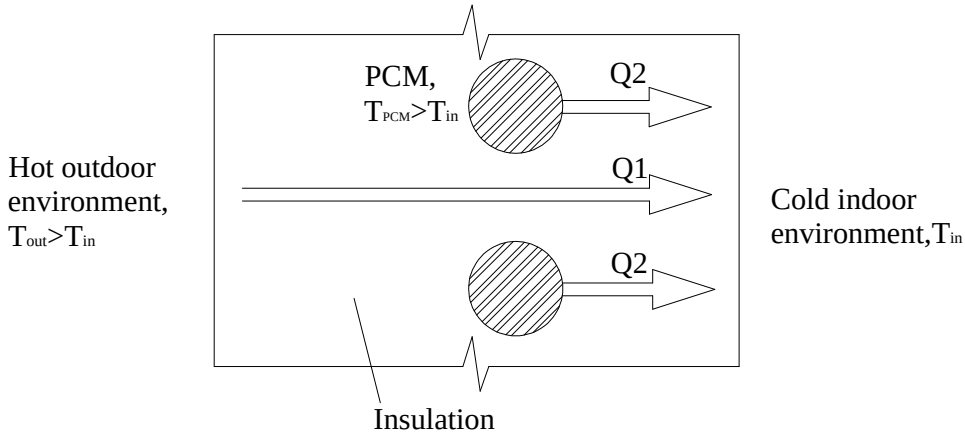

Figure 4.1 Illustration of the heat transfer in the wall with PCM pipes

The overall heat transfer across the PCM-enhanced wall includes the superposition of the heat transfer across the path that includes only plain insulation and that of the path where there is insulation and PCM pipes. Because the reduction in peak heat flux is only related to the path that contains PCM pipes, it is advantageous to reduce the vertical distance between pipes. That is, a continuous section where the pipes are placed next to one another with no insulation spaces in between, as illustrated in Figure 4.2, would be optimum.

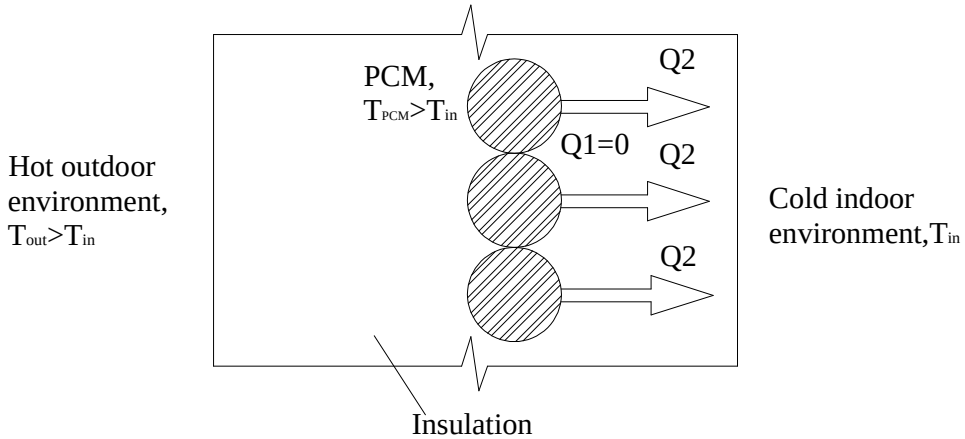

Figure 4.2 Illustration of the heat transfer in the wall with PCM pipes (optimum situation)

Based on this, a new PCM integration method can be proposed. This method is herein referred to as "PCM layer method" and it is illustrated in Figure 4.3. Under this method, the PCM would be hermetically sealed and held in place between two thin polymer sheets ("sandwiched") into small "packages" in a grid-like structure, surrounded by long narrow sections, of the same polymer sheets, where a number of perforations would be placed to allow for moisture transfer. This method represents an improvement over the imbibing, macro-encapsulation, and direct mixing methods. It should be preferred over the wall board imbibing method because the layer method allows moisture transfer and because the PCM is encapsulated so that it would not come in contact with coatings, wall finishes, and or people. It is more practical than having to install individual pipes as is the case with the macro-encapsulation method, and it is superior to the direct mixing method in regards to the oxidation problems (paraffin) or hygroscopic problems (hydrated salts) experienced by the PCMs under direct mixing with the insulation.

Simulation results presented in Chapter 6 indicate that only a thin PCM layer is needed to produce large reductions in peak heat fluxes. The PCM layer can be installed in retrofit applications or be sandwiched between two fiberglass insulation layers during the manufacture process. The final product would still be flexible enough for rolling or folding. As a result, the PCM-insulation can be packaged and installed like ordinary fiberglass insulation. Therefore, the PCM layer method would be more promising in acceptance than the pipe method and the mixing method.

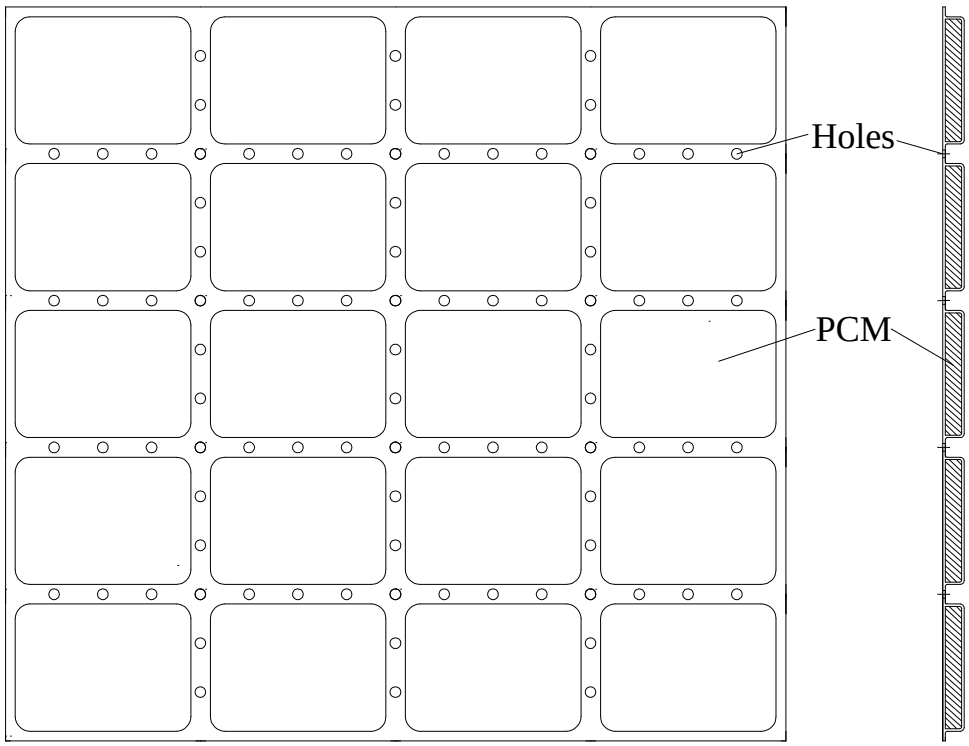

Figure 4.3 Illustration of the “PCM layer” method

4.2 Analysis of the heat flux transferred into the indoor environment

Because the layer method was an “improvement” of the macro-encapsulation method, the heat transfer processes of the two methods were similar. Thus, only the layer method and the mixing method were considered in the heat transfer analysis.

On the other hand, the PCM-enhanced insulation in the mixing method can be viewed as a new type of phase change material that has low conductivity and low density, which makes its latent thermal storage capacity several times smaller than that of the pure PCM. In the mixing method, however, the “new PCM” (i.e., the PCM-enhanced insulation) is distributed all over the wall cavity instead of in a single layer as the case with the layer method. In that sense, the two methods, the layer

method and the mixing method, are similar where the mixing method is taken as one special case of the PCM layer method. So are their phase change and heat transfer processes.

To simplify the problem, the following assumptions were made in the analysis:

1. It was assumed the PCM changed phase at a single temperature point instead of a temperature range.
2. The melting and solidification temperatures were assumed to be the same.
3. The specific heat of the insulation was neglected. This was possible because of the low density of the insulation and low temperature change rate in the insulation.
4. For the mixing case (i.e., PCM and insulation mixture) the conductivity of the PCM-enhanced insulation (both the insulation mixed with liquid PCM or solid PCM) was the same as that of the plain insulation.
5. The properties of the PCM-enhanced insulation were assumed to be homogeneous.
6. The heat transfer was assumed to be one-dimensional.
7. The indoor room temperature was assumed to be constant.

For both layer method and mixing method, the heat flux across the internal side of the wall and into the indoor environment, when there was phase change process occurring, was calculated by:

$$q = \frac{T_s - T_{in}}{\frac{\Delta x}{K} + R} \tag{4-1}$$

Where,

T_s = phase change temperature (^oC, ^oF)

T_{in} = indoor air temperature (^oC, ^oF)

K = thermal conductivity of the insulation (W/mK, Btu/hr ft ^oR)

Δx = distance between the phase change interface (i.e., the interface of solid and liquid PCM) and the wallboard (m, ft)

R = thermal resistance of the wallboard and indoor air film (K/W, hr-^oR/Btu)

When the indoor temperature was assumed to be 24 ^oC (75.2 ^oF) and the properties of the building materials were those as listed in Table 2.1 in Chapter 2, the heat fluxes into the indoor environment as a function of the solid-liquid phase change interface, when using two PCMs with melting temperatures of 27 ^oC (80.6 ^oF) and 30 ^oC (86 ^oF) respectively, was calculated and the results are shown in Figure 4.4.

From Equation 4-1 and Figure 4.4, it was found that when Δx became smaller, that is, as the PCM's phase change interface got closer to the wallboard (the cold environment), the heat flux q increased dramatically. Through the last 10% of the thickness of the insulation, the heat flux doubled its value. Thus, in order to get a large peak heat flux reduction, distance between the phase change interface and the

wallboard, Δx, should not be too small (i.e., the phase change interface should not get too close to the inside surface of the wall).

From Equation 4-1 and Figure 4.4, it was also found that a few degree of increase in the phase change temperature (3 ^{o}C /5.4 ^{o}F of increase in Figure 4.4) would increase the heat flux value significantly, when one assumed the phase change interfaces for both cases (walls with 24 ^{o}C/80.6 ^{o}F and 27 ^{o}C/86 ^{o}F phase change temperature PCMs) were at the same location in the wall. As a result, a smaller peak reduction was expected for the PCM wall with higher phase change temperature PCM. The above findings are true for both layer method and mixing method.

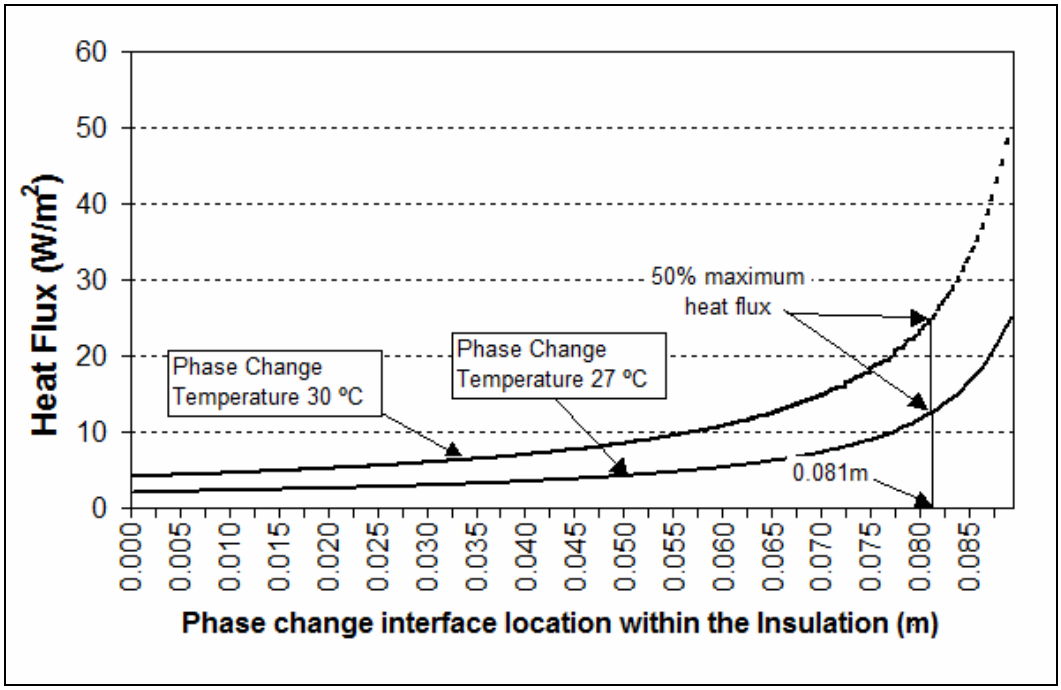

Figure 4.4 Heat Flux for two PCMs with different phase change interface locations in the insulation

4.3 Case study of the heat transfer in PCM-enhanced wall – Infinite thin PCM layer - Stationary phase change interface

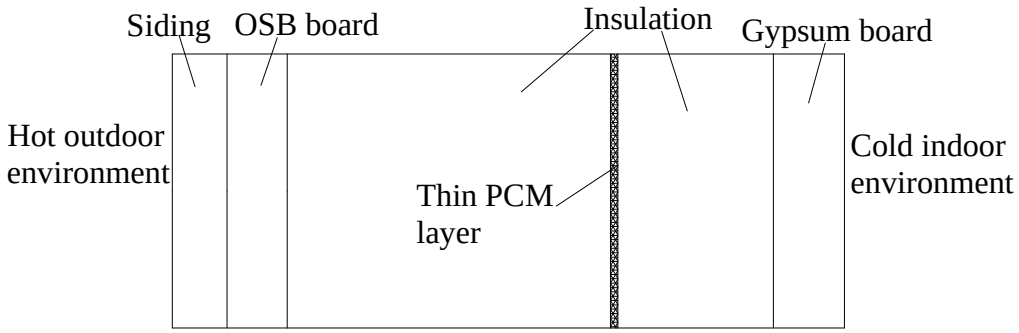

Figure 4.5 Profile of the wall with thin PCM layer

A simplified extreme situation was first studied. As illustrated in Figure 4.5, the PCM was assumed to be distributed in an infinitive thin layer in the insulation and the latent heat of fusion was assumed to be infinitive. As a result, the PCM was always in the phase change process and the temperature in the PCM layer was constant all the time. The temperature difference between the phase change interface and the inside environment would not change, nor would the heat flux through the interior wall according to Equation 4-1. Under this case scenario, the heat flux curve for the PCM-enhanced wall was a horizontal line (i.e. a constant value line) as shown in Figure 4.6. The heat flux value only depended on the phase change temperature and PCM layer's position. For a certain type of PCM, the heat flux value for each position could be easily calculated from Equation 4-1, when k, Δt and Δx were all known.

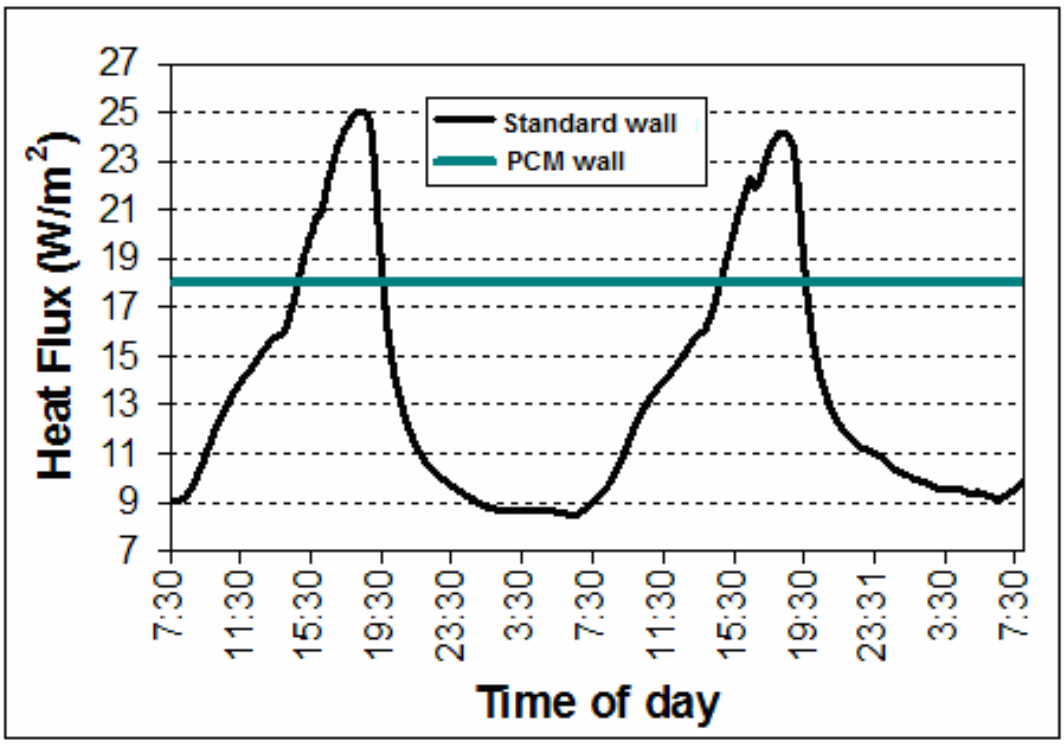

Figure 4.6 Heat flux across walls showing a standard wall with plain insulation and a PCM-enhanced wall (PCM assumed with an infinite heat of fusion)

On the other hand, when the heat of fusion was not infinite, there was a possibility that the PCM would completely melt or solidify in the melting or solidification process. When the PCM completely melted and the phase change process no longer had any influence on the heat transfer in the wall, the temperature in the PCM layer would increase and the heat flux transferred into the indoor environment, q in Equation 4-1, would become the same as that of the standard wall until the beginning of the solidification process. This analogy would also be true for the solidification process. The heat flux curve for the case when the heat of fusion was not infinite is illustrated in Figure 4.7.

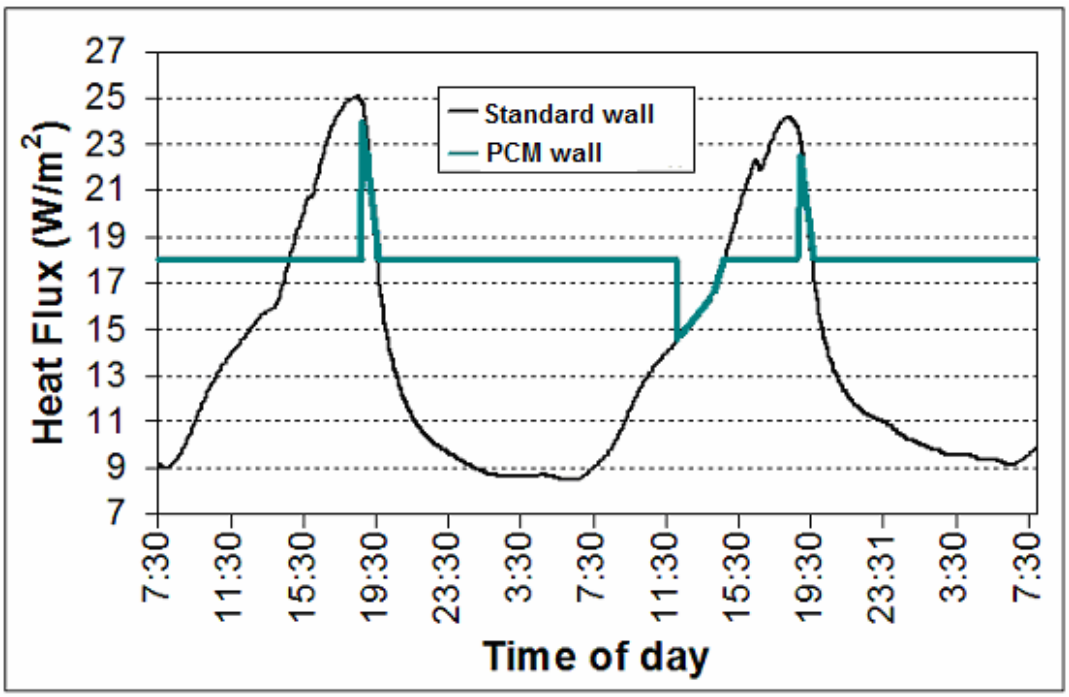

Figure 4.7 Heat flux across walls showing a standard wall with plain insulation and a PCM-enhanced wall (PCM assumed with a finite heat of fusion)

When the phase change process was assumed to occur over a temperature range rather than a single point, the heat flux curve was not a flat line like in the previous two cases. In this case, the curve would gradually rise and drop during the phase change process, as illustrated in Figure 4.8. The shape of the rising or dropping curves depended on many factors, like the properties of the PCM, the position of the PCM layer and temperature boundary conditions.

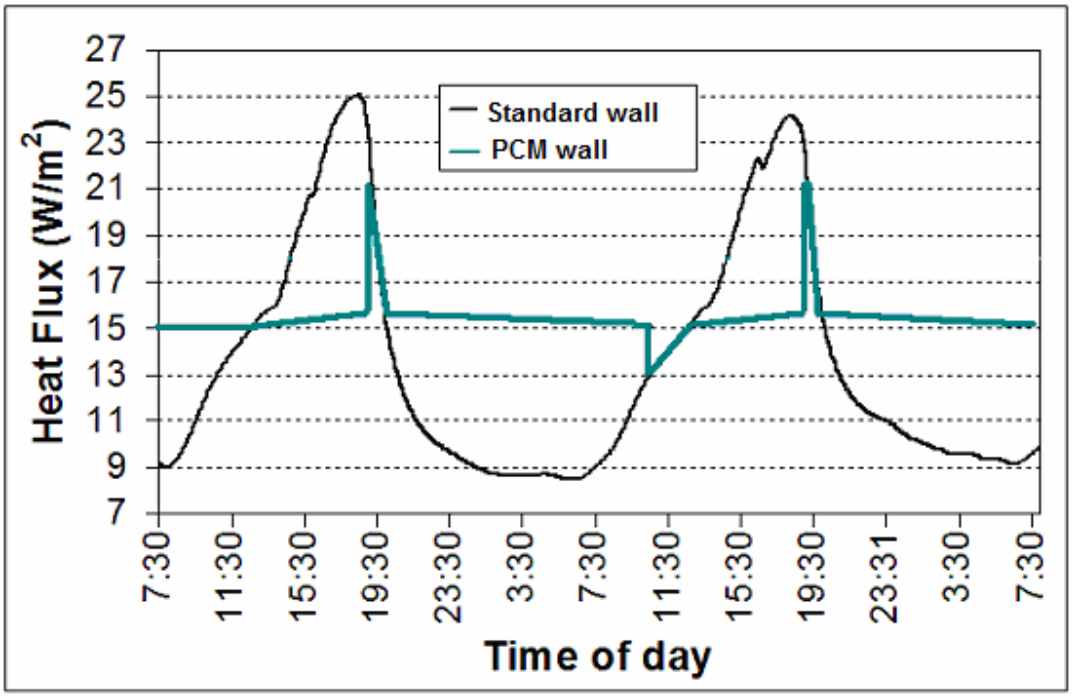

Figure 4.8 Heat flux across walls showing a standard wall with plain insulation and a PCM-enhanced wall (phase change process was assumed to take place over a temperature range)

In the above three cases, because the phase change interfaces were stationary, the temperature in the PCM layer became the only variable in Equation 4-1. As long as that temperature was kept within the phase change temperature range (i.e., the melting process didn't complete in the day time), the heat flux curve of the PCM-wall would remain relatively flat and a large peak reduction would be produced.

4.4 Case study of the heat transfer in PCM -enhanced wall - Mixing method – Moving phase change interface

The case in which the PCM was mixed evenly with the insulation and when the latent heat of fusion was finite was considered. As mentioned in section 4.2, the

PCM-enhanced insulation in the mixing method can be viewed as a new type of phase change material that is distributed all over the wall cavity. Unlike the cases presented in Section 4.3, the interface of the solid and liquid “new insulation PCM” in this case would move towards the inside surface of the wall (cold side) when the PCM melted and would move towards the outside surface of the wall (hot side) in the solidification process, which made the heat transfer and phase change process more complex.

4.4.1 Temperature profile change in the PCM-enhanced insulation during phase change

The temperature profiles within the PCM-enhanced insulation during phase change are shown in Figure 4.9, in which the indoor environment temperature, $T_{in,}$ and the temperature in the phase change interface, Ts, remained constant and the outside hot environment temperature, T_{out}, increased and decreased with time. In this figure, the dash lines represent the temperature profile of the plain insulation and the solid lines represent the temperature profile of the PCM-enhanced insulation.

In the figure, the slope of the temperature profile indicates the value of the heat flux through that location. The slope of the melted liquid PCM, which was close to the hot outside environment, indicated the heat flux transferred from outside environment to the wall. While the slope of the unmelted solid PCM, which was close to the cool indoor environment, indicated the heat flux transferred from the wall into the indoor environment. As shown, during the melting process, the slope of the melted liquid PCM was steeper than that of the unmelted solid PCM. The sum of two heat fluxes was positive, which meant PCM in the solid-liquid interface was

absorbing heat. After some time, the slopes of solid and liquid portions became equal. At this point, the phase change interface would stop moving. This is the case because no heat was being absorbed or released by the PCM. Also, at this point, the distance between the solid-liquid phase change interface and the wallboard, Δx in Equation 4-1, reached its minimum and, as a result, the interior wall heat flux (the slope of the solid PCM curve) would reach its maximum value. When the outside temperature (T_{out}) continued decreasing, the slope of the melted liquid PCM part would become less steeper than that of the solid PCM part. As a result, instead of absorbing, the PCM had begun to release heat and the phase change interface was moving towards the outside.

By comparing the curves in Figure 4.9, it was also found that the slope of the solid part (close to the cold environment) during melting was always less steep than that for the plain insulation. This meant that the heat flux transferred into the indoor environment through the PCM-enhanced wall was always lower than that of the standard plain insulation wall in the melting process. The opposite was true for the solidification process. These findings agree with the experimental results presented in Chapter 3. This can explain why and how part of the cooling loads was shifted.

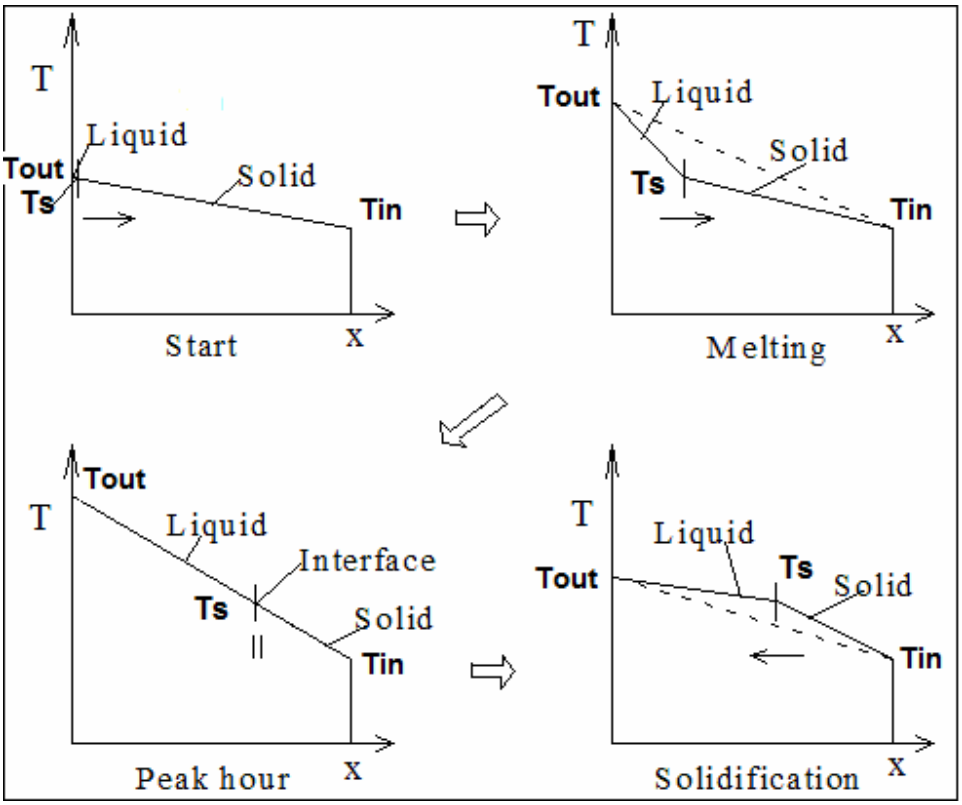

Figure 4.9 Temperature profiles in the insulation during phase change

4.4.2 Analysis of PCM phase change process in the PCM-enhanced insulation during the melting process - Mixing method

In the melting process, as the phase change interface moved from the outside (the hot side) towards the inside (the cold side), the heat flux transferred into the indoor environment would jump to higher values corresponding to the location of the phase change interface, as discussed in Section 4.2. Because it would take a certain amount of time for the PCM in the PCM-enhanced insulation to melt (i.e., the delay effect, or the "effective thermal mass" of the PCM), the heat flux of the PCM-enhanced wall would be later than that of the standard wall to increase to a certain value. In other words, there would be a "time delay" between the standard wall and

the PCM-enhanced wall for a certain heat flux value, as shown in Figure 4.10. And the time delays would add up and become larger over the time in the melting process. The heat flux curves for the PCM-enhanced wall (solid line) gradually deviated from that for the standard wall (dashed line) and followed different profiles, which depended mainly on the melting speed. As a result, the PCM-enhanced wall' heat flux curve (solid line) intersected that of the standard wall (dashed line) at a lower heat flux value than the peak of the standard wall, when the melting process stopped and the solidification process started.

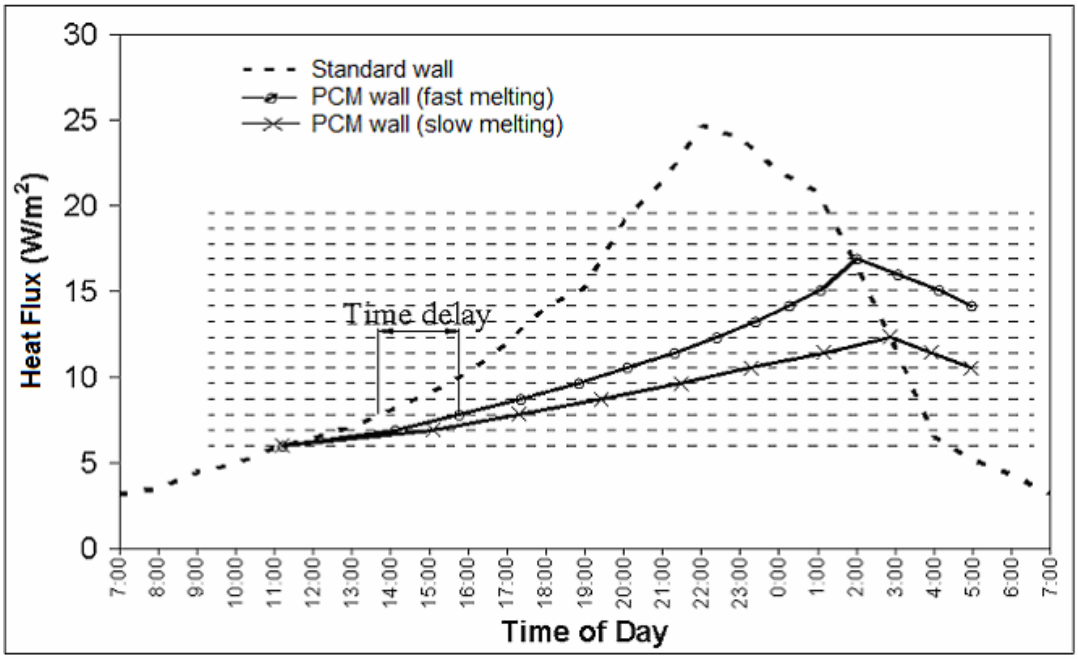

Figure 4.10 Comparison of heat fluxes across the standard wall and the PCM-enhanced wall during the melting process.

Figures 3.4 to 3.7, which represent experimental data, show the same behavior. When the outside environment was relatively hotter, the melting process

would take place at a faster speed and the phase change interface would also move faster. As a result, the “time delays” between the standard wall and PCM-enhanced wall became shorter. Under this scenario, the slope of the heat flux curve of the PCM-enhanced wall would be steeper and would intersect the heat flux curve of the standard wall earlier in time and at a higher value (depicted with the symbol “o” in Figure 4.10). Then a larger peak reduction would be produced.

4.4.3 Analysis of PCM phase change process in the PCM-enhanced insulation during the solidification process - Mixing method

During the solidification process, which coincided to the period when the wall was cooling down, the solid-liquid phase change interface moved away from the inside surface (cold side) and the heat flux followed a downward trend. Similar to the melting process, the heat flux curve of the PCM-enhanced wall would be later than that of the standard wall to drop to a certain heat flux value due to the PCM solidification process. As a result, the heat flux curves for the PCM-enhanced wall (solid line) gradually deviated from that for the standard wall (dashed line) and followed different profiles, which depended mainly on the solidification speed, as shown in Figures 4.11 and 4.12. With different nighttime outdoor environment temperatures and PCM solidification temperatures, the shape of heat flux curve varied.

4.4.3.1 Case one: The outdoor air temperature at night was equal to or higher than the PCM solidification temperature

The air conditioner would keep the indoor air temperature at a lower temperature than the PCM solidification temperature. When the lowest outdoor air temperature was higher than the PCM solidification temperature, the solidification process would only occur from the indoor side of the wall. When the outside environment was hotter, more heat would be transferred from outside to the PCM-enhanced insulation, which would slow the solidification process. As a result, the time delay became larger and heat flux curve for the PCM-enhanced wall (as shown by the line with symbol "o" in Figure 4.11) deviated from that for the standard wall further, when compared with that of a colder night (as shown by the line with symbol "x" in Figure 4.11).

For hotter nights, less PCM would solidify at night, which meant the phase change interface at the end of the solidification process would be closer to the cold environment, compared with the case of colder night. In other words, part of the latent thermal storage capacity was lost. As a result, the solid-liquid phase change interface would be closer to the indoor side at the end of the melting process and a larger peak heat flux was to be expected (i.e., the peak reduction would become smaller), if the weather conditions were assumed to be the same in the next day.

The above situation can be compared to a race. When the start line is moved forward. In the same amount of time, the runner can get somewhere further; When at the beginning of the second day's melting process the phase change interface is moved from the start location ("start line") of the first day towards inside surface of

the wall (cold side), the final location of the phase change interface at the end of the melting process for the second day is expected to be closer to inside surface than that of the first day.

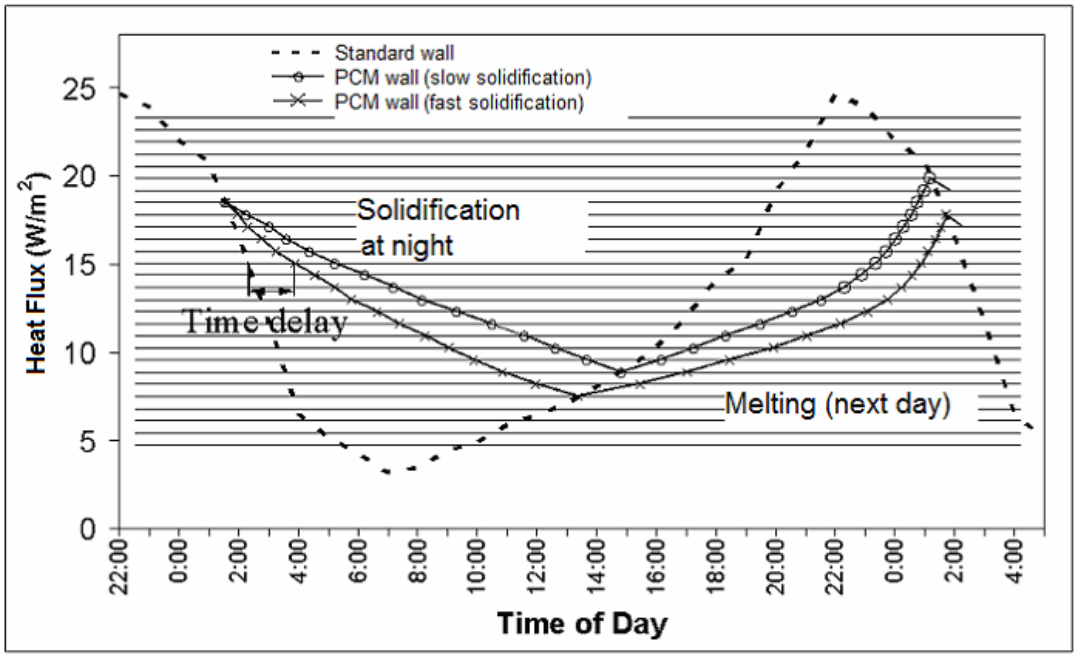

Figure 4.11 Comparison of heat fluxes across the standard wall and the PCM-enhanced wall during the solidification process – Case One.

4.4.3.2 Case two: The outdoor air temperature at night was lower than the PCM-solidification temperature

When the outdoor air temperature T_{out} could get lower than the PCM solidification temperature, the solidification process occurred from both the indoor side and outdoor side of the wall. When the outdoor environment was cold enough, the solidification process could complete before the beginning of next melting cycle. After that, because the specific heat of the insulation was neglected, the heat flux of the PCM-enhanced wall would follow the heat flux curve of the standard wall until

the PCM started to melt in the next cycle. The heat flux curve for the PCM-enhanced wall under the conditions described above is depicted by the line with the "x" symbols in Figure 4.12.

If the outdoor temperature was relatively milder, the PCM-solidification process would not be completed, when the melting process started. At that moment, there were two separated solid PCM layers in the PCM-enhanced insulation, as illustrated in Figure 4.14. In this case, the heat flux of the PCM-enhanced wall would continue to drop for some time, as shown by the line with the "o" symbol in Figure 4.12. This was the case because it would take time for the solid PCM layer close to the outside wall surface (hot side) to melt. That is, the outside PCM layer temporarily blocked the influence of the outside environment. As under this case the phase change interface close to the inside surface continued moving towards the outside as a result of the cool indoor environment, the heat flux of the PCM-enhanced wall would continue to drop until the outside PCM layer had completely. The length of that process depended on how fast the outside solid PCM layer melted and how thick that PCM layer was. Another situation would present itself when the outdoor temperature was in between those of the above two situations and the PCM would complete the solidification process at the exact moment when it was the time for it to start to melting process. This case is depicted by the line with the "Δ" symbol in Figure 4.12. The change of the liquid and solid PCM during the phase change processes are illustrated in Figures 4.13 and 4.14 for a "colder" outdoor air temperature and for a "milder" outdoor air temperature, respectively.

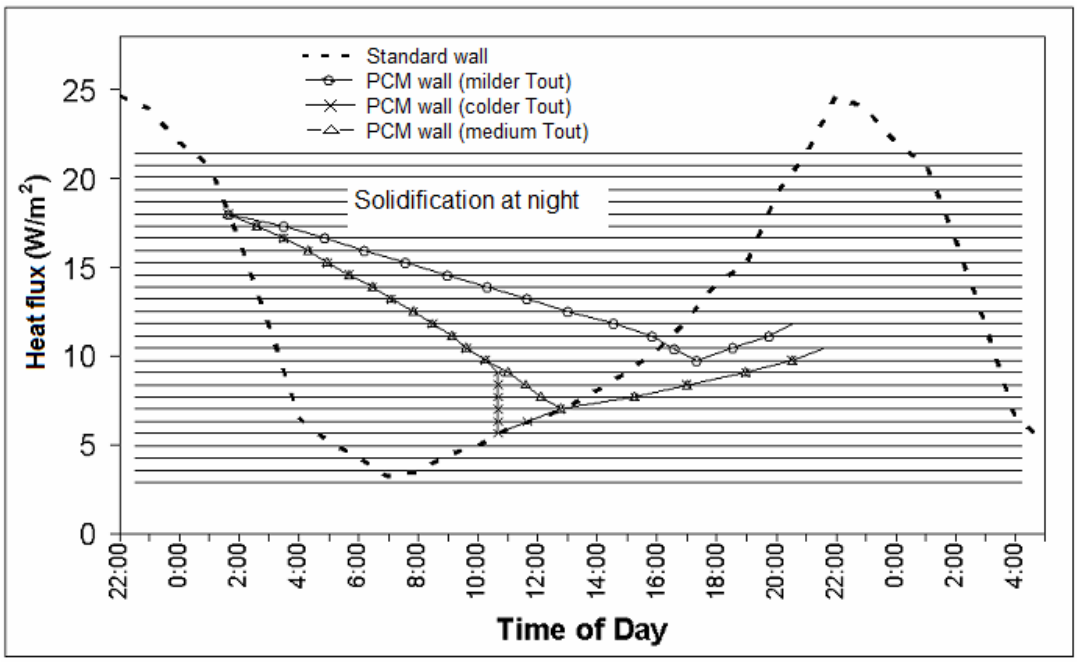

Figure 4.12 Comparison of heat fluxes across the standard wall and the PCM-enhanced wall during the solidification process – Case Two.

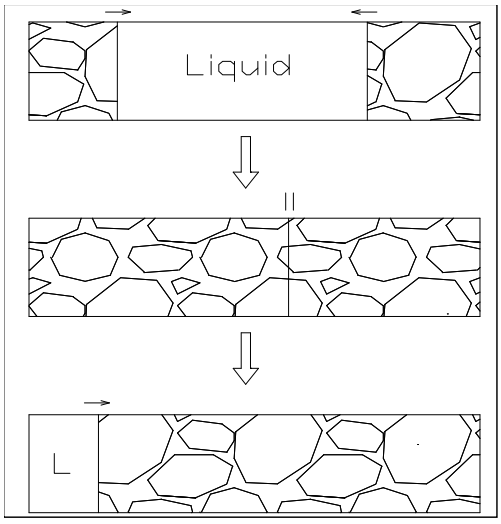

Figure 4.13 Phase change process for a “colder” outdoor air temperature

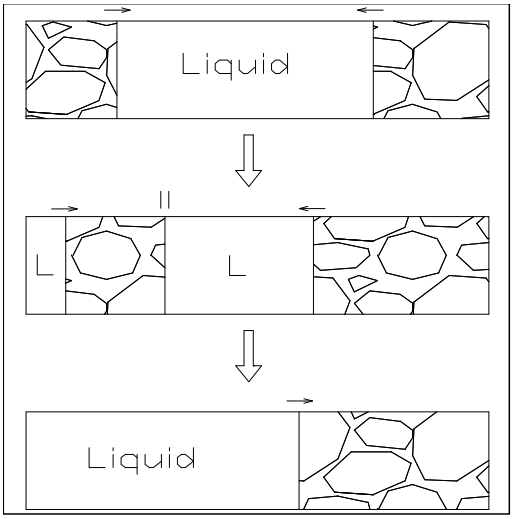

Figure 4.14 Phase change process for a “milder” outdoor air temperature

4.4.4 Suggestions for the mixing method

From the analysis above, the location of the solid-liquid phase change interface during the phase change was found to be the main variable that controled heat flux peak reduction. For larger peak heat flux reductions, the location of the phase change interface should be as far away from the indoor side of the wall as possible. This is accomplished when the PCM melting process proceeds as slow as possible.

Another important issue is that the indoor and outdoor environment at night should be cold enough to allow enough PCM to solidify. Otherwise, as discussed in section 4.4.3.1 above, because “start line is moved forward”, the peak heat flux of the following day will become larger accordingly. Thus, contrary to the PCM melting process, the PCM solidification process should proceed as fast as possible.

4.4.4.1 The influence of phase change temperature on peak heat flux reduction

Higher the phase change temperature creates a larger temperature difference between the phase change interface and the indoor environment. From section 4.2, the larger this temperature difference is, the larger the heat flux of the PCM-enhanced wall will be, which will result in a smaller peak heat flux reduction. In that sense, PCMs with lower phase change temperature is preferable for building applications.

But for the melting process, higher phase change temperature means smaller temperature difference between the phase change interface and the outside environment. The smaller this temperature difference is, the less heat will be transferred from hot outside environment to PCM-enhanced insulation. Because the heat flux from the hot outside environment is the main driving force for the melting process, higher phase change temperature will slow down the melting process, which is desirable for building applications.

In the solidification process, a larger temperature difference between the phase change interface and the inside surface translates to more heat released from the PCM. Under this case, the solidification process will proceed faster. Also if the phase change temperature is higher than the outdoor temperature, the solidification process can occur from the outside, which will further speed up the solidification process. Therefore, high phase change temperature is helpful for the solidification/recharging of the PCM at night.

As discussed above, it is difficult to tell an optimal phase change temperature. Also, the optimal value varies with different weather conditions and wall structures. Numerical simulation is needed to sort out the optimal phase change temperatures.

4.4.4.2 The influence of latent heat of fusion and PCM concentration on peak heat flux reduction

PCM with high latent heat of fusion will slow down the melting process, as more heat is needed for the melting process. Under this scenario the peak heat flux of the PCM-enhanced wall will be decreased. On the other hand, a higher latent heat of fusion would require more heat to be released during the PCM solidification process. In this case, the recharging/recovery of the PCM may become a problem in some applications. The influence of the PCM concentration is similar to that of the latent heat of fusion. Higher concentration is better for the peak reduction but it may also slow down the solidification process at night. Thus, like the phase change temperature, simulation is need for the selection of the optimal values.

4.5 Case study of the heat transfer in PCM -enhanced wall - layer method

As mentioned in Section 4.2, the layer method represents a more general situation of the mixing method. In this case, the phase change interface will move within the layer in the phase change process, just like in the mixing method case. Thus, the above analysis for the mixing method case would also apply for the layer method.

If the thickness of the layer is thin, the position of the phase change interface will not change significantly. Then its heat flux would be closer to the situation shown in Figure 4.8. When the layer is thick and heat of fusion is not too high, the phase change interface will move significantly in the PCM layer in daily cycles. Then the heat transfer and phase change process will be closer in results to the mixing methods case.

The mixing method represents a close average of the cases with PCM layers in different positions in the wall. From the experimental results from dynamic simulator tests (pipe test) in Chapter 3 and the simulation study in Chapter 6, it was found that there is an optimal location for the PCM layer. The peak reduction will decrease if the PCM layer is off that optimal location. Thus, the layer method will outperform the mixing method only if the layer location is optimized.

4.6 Summary

It was found that eliminating the spaces between the PCM pipes could improve the peak heat flux reduction of the PCM-enhanced wall. The layer method was presented as an alternative to the macro-encapsulation method and the direct mixing method. The layer method appears to be practical and convenient for mass production and installation.

By the case study of different situations and cases, the process in which PCMs reduce the peak heat flux of the residential building walls is presented. It was found that the position of the phase change interface was key to obtaining larger peak heat

flux reduction. As such, it was found that the melting process should be as slow as possible to keep the phase change interface away from the cold interior side. Contrary to the PCM melting process, the night time PCM solidification process should proceed as fast as possible. The influences of phase change temperature, heat of fusion and PCM concentration on the PCM wall's performance are complex. Further study with numerical simulation is needed.

The direct mixing method was found to be a special case of the layer method where its performance was close to an average of the cases with layers in different positions in the wall. If the location of the PCM layer in the wall was optimized, the layer method would outperform the direct mixing method.

Chapter V

Study of the Partially-Melted Phase Change Processes with a Differential Scanning Calorimeter (DSC)

In this chapter, the performance of PCMs during the phase change process, starting from partially-melted states was studied. From the experimental data, it was found that it would be very likely that the PCMs, once integrated into the walls, would 'start' the phase change process from partially-melted states. Currently-used simulation models, including the most widely accepted methods, the effective heat capacity method and the enthalpy method, come short when handling partially-melted processes. A DSC test method and its detailed steps, used to study the performance of PCMs from partially-melted states, are introduced. The results for a paraffin-based PCM were analyzed and are presented. Based on these DSC data, a modified PCM model for a paraffin-based PCM was developed.

5.1 Situations when partially-melted PCM problems may arise

In ideal situations, the PCMs in the wall of residential or commercial buildings would work in cycles. They would completely melt during the daytime, finish the melting process, and completely solidify during the nighttime and early morning. Both the melting and solidification processes would start from completely solid and completely liquid states. Under this scenario, all the thermal storage capacity of the PCMs would be used. From experimental results presented in

Chapters 2 and 3, it was found that there were three situations under which partially-melted problems might arise. These are described below.

5.1.1 PCM melting in the daytime

Let's picture the frame wall depicted in Figure 2.15 of Chapter 2. As mentioned in Chapter 2, the closer in distance to the inside wall (cold side), the lower the daily maximum temperature in that location would get. Thus, in these locations, it is likely that the maximum temperature would not rise above the upper limit of the phase change temperature range of some PCMs. Furthermore, when PCMs are added to the insulation, because of the heat storage in the PCMs, and subsequent delay in heat transfer, the maximum temperatures in the wall would be lower than those found in the case without PCMs. Under any of these case scenarios, at the time when the outside temperature would begin to drop (say, nighttime and early morning), the PCMs would begin the solidification process from a partially-melted state.

5.1.2 PCM solidification during colder times of the day (nighttime and early mornings)

Unlike the melting of the PCMs in the hotter times of the day (daytime), during the colder times of the day (nighttime and early morning) the driving force of the solidification process is the temperature difference between the PCMs and either the inside conditioned space or the outside environment. This driving force, a single digit temperature difference, is much smaller than the one found during the melting process, which is a 30-40 ^{o}C (54-72 ^{o}F) temperature difference. From test results, it was found that if the environment was not cold enough or the location of the PCMs in

the wall was not optimized, the PCMs would not completely solidify during nighttime and/or early morning. The “middle depth” pipe test in Chapter 3 is a good example. Because the pipe was placed in the middle of the insulation, the large thermal resistance of the insulation retarded the solidification process of the PCM. At the end of the testing cycle, the temperature of the PCM would not drop below the solidification temperature range of the PCM, and the solidification process was not completed. As a result, during the following cycle, a smaller peak heat flux reduction was achieved.

Because one of the important tasks of the numerical simulation under this study was to accurately predict the performance of PCM walls under different conditions, these kinds of “partially-melt” situations should be carefully considered.

5.1.3 Temperature fluctuations

Under real weather conditions, the exterior wall surface temperatures fluctuate often. For example, when clouds block the solar radiation, the exterior wall temperatures drop. After the clouds pass, the temperatures rise again, as shown in Figure 5.1. It is likely that during these periods, if a melting process is progressing, it would stop while solidification might commence from a partially-melted state. Accordingly, when the temperatures rise again, the PCM would start melting from a partially-solidified state.

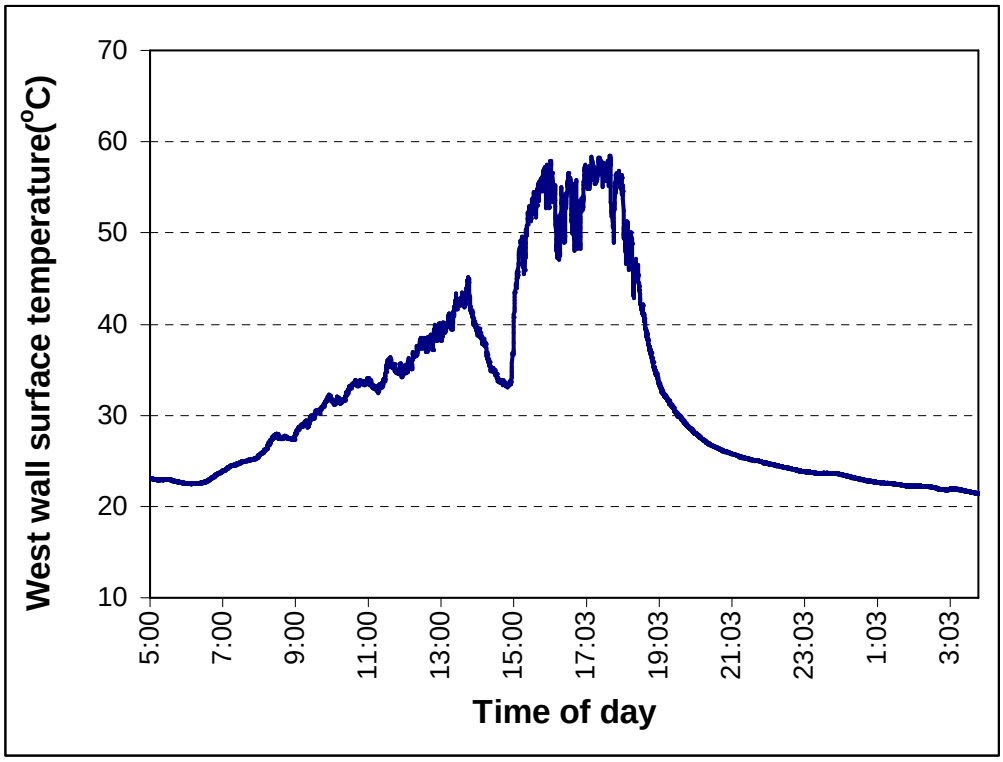

Figure 5.1 Example of exterior wall surface temperature fluctuations

5.2 Published PCM models and their shortcomings

As mentioned in the literature review, the enthalpy method and the effective heat capacity method are the two most commonly used models in PCM heat transfer modeling. Their main shortcoming arises from the assumptions made of the relationships between the effective heat capacity and temperatures. That is, their main shortcoming is how they handle the release and/or absorption of heat over the phase change temperature range during the phase change process. Improper assumption will lead to following two problems:

5.2.1 Over/underestimation of the thermal storage capacity

From DSC test results, it was found that during the phase change process of the PCMs, the heat was not evenly absorbed or released along the phase change temperature range. In fact, it was observed that there was always a single large heat flow peak that occurred at certain temperature in the phase change temperature range. Therefore, it was likely that the heat absorbed or released in the phase change process could be overestimated or underestimated, if incorrect heat absorption/release distribution assumption were made. For example, as illustrated in Figure 5.2 the total heat absorbed or released in the entire phase change temperature range, T_{solid} to T_{liquid}, under the evenly distributed heat absorption/release assumption (the area under the rectangle) would be the same as that of the actual heat absorbed/released in the actual situation (the area under the triangle). However, if the phase change process, for some reason, was not completed and stopped at *Ta*, the area under the assumed curve (rectangle) would be larger than that of an actual situation. As a result, the thermal storage capacity of this partially-melted PCM would be overestimated if an evenly distributed heat released/absorption were assumed. This problem would also happen if other distributions assumptions (for example, linear or normal distribution) were adopted.

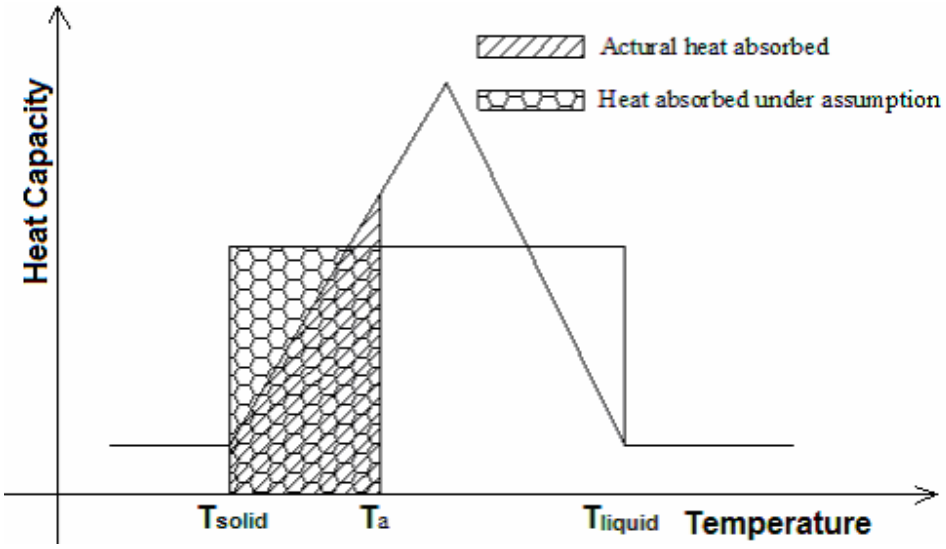

Figure 5.2 Comparison of the thermal storage capacity between the "even distribution" assumption and the actual situation

5.2.2 Incorrect prediction of the temperature in the phase change process

Inaccurate temperature predictions would be produced if incorrect heat absorption/release distributions were assumed. That is, if the heat of fusion at certain temperature were to be overestimated, the temperature produced by the simulation would rise slower than that of the actual (real) situation. The opposite would be the case if the heat of fusion were underestimated. When the phase change process takes place at a faster rate, however, these details are less relevant. But, as mentioned in Chapter 2, for the proposed applications for which the heat transfer models were developed, the phase change process is slow. It would take a relatively long time (in the hours range) for the PCM to complete the phase change process, especially when the PCM was located closer to the indoor cool environment of the building. Incorrect temperature predictions will, therefore, bring about large errors in temperature and wall heat flux predictions.

5.3 Differential scanning calorimeter (DSC) tests

As stated before, a DSC can measure the thermal properties of PCM samples, such as melting temperature, solidification temperature, and heat of fusion. In the effort to study the performance of a paraffin-based PCM from partially-melted states, a series of DSC tests were performed. The proposed testing method presented in this chapter can be applied to PCMs with different phase change temperature ranges.

5.3.1 DSC study of the performance of PCMs from partially melted states (Test I)

In Test I, the performance of a paraffin-based PCM (RT27) with a melting temperature around 27 ^{o}C (80.6 ^{o}F) was evaluated.

5.3.1.1 Study of the melting process from partially-solidified states:

Step 1) A paraffin sample (about 5mg) was first cooled to a temperature (the start temperature) and then kept at that temperature for 15 minutes to let the PCM have enough time to solidify. As shown in Figure 5.3, soon after the temperature was kept constant, the heat flow dropped to zero, which meant the no more PCM was being solidified (i.e., all the paraffin that could solidify at that temperature had solidified).

Step 2) After the stabilization, the PCM was heated at a rate of 0.1^{o}C/min (0.18 ^{o}F/min) until the PCM was completely melted, at which point the heat flow curve became flat again.

Step 3) The sample was cooled to another temperature where steps 1-2 above were repeated again. In this way, the performance of PCM melting from different starting temperatures (i.e., different percentages of solidified PCM) could be obtained.

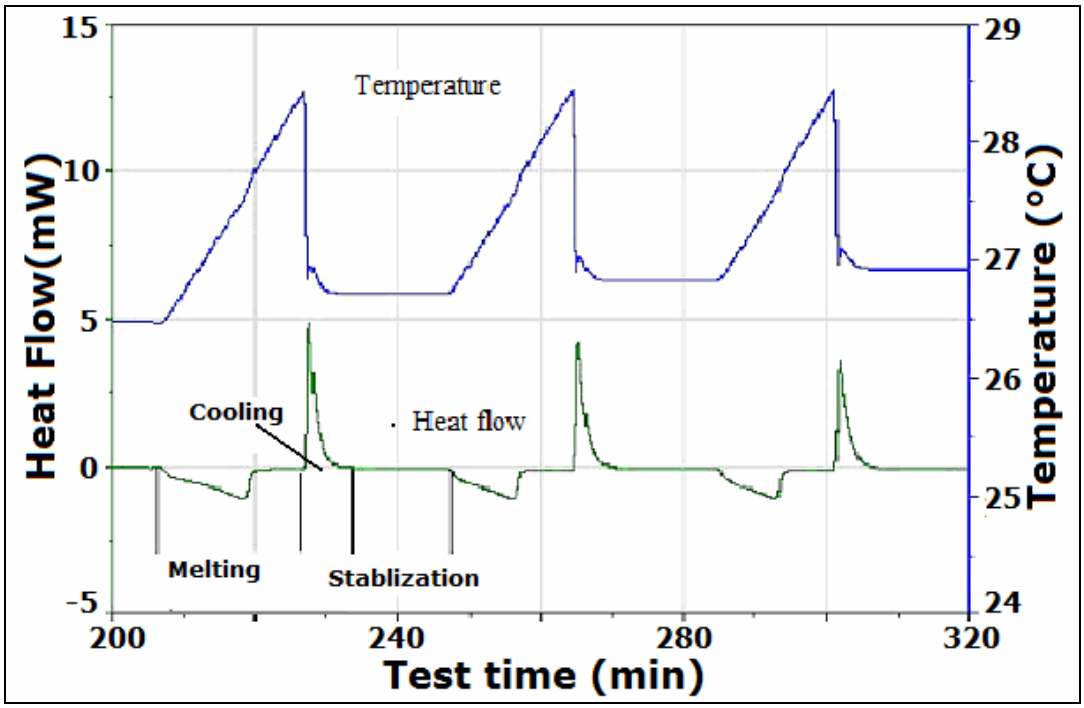

Figure 5.3 DSC temperature and heat flow curves for the study of PCM melting process from partially-solidified states

5.3.1.2 Study of the solidification process from partially-melted states:

For the study of the solidification process of the PCMs, a similar scheme was used, but instead of the samples being cooled, the samples were heated to several 'starting' temperatures from where the phase change process would start (i.e., from partially-melted states). That is, after the 15 minutes designated for the stabilization of the samples, the samples were cooled at a rate of 0.1 ^{o}C/min (0.18 ^{o}F/min) to a low

temperature. The DSC temperatures and heat flux curves over time are shown in Figure 5.4.

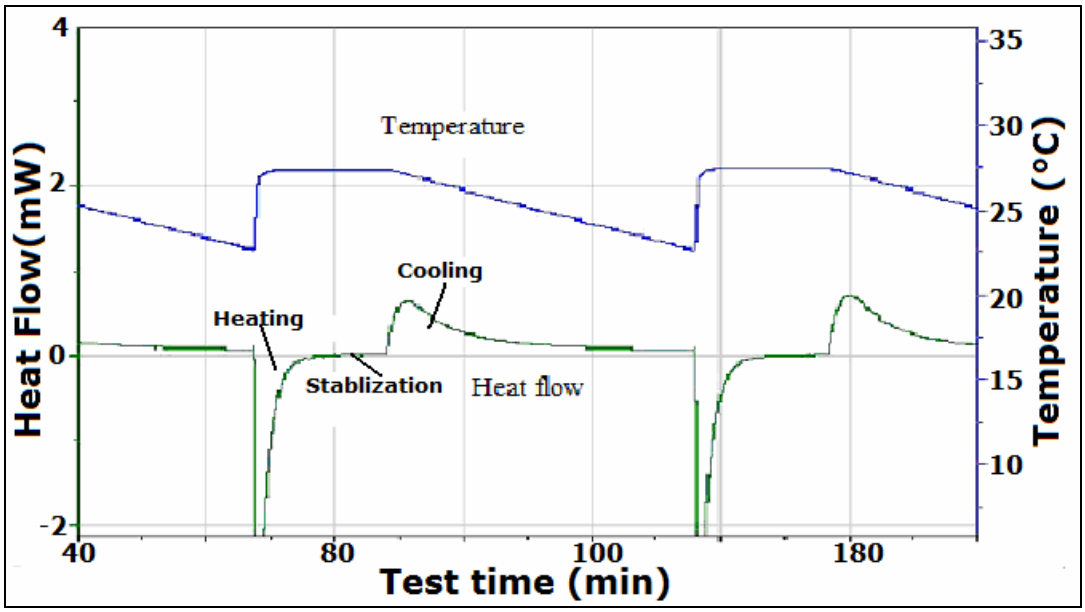

Figure 5.4 DSC temperature and heat flow curves for the study of PCM solidification process from partially-melted states

5.3.1.3 Results

The melting and solidification heat flow curves for different starting temperatures are shown in Figures 5.5 and 5.6. The heat flow curves from different tests were adjusted to get a common baseline (i.e., the baseline drift was eliminated by shifting the curve up/down. As a result, the heat flow values at the end of stabilization were exactly zero.). Endothermic process curves are depicted downwards.

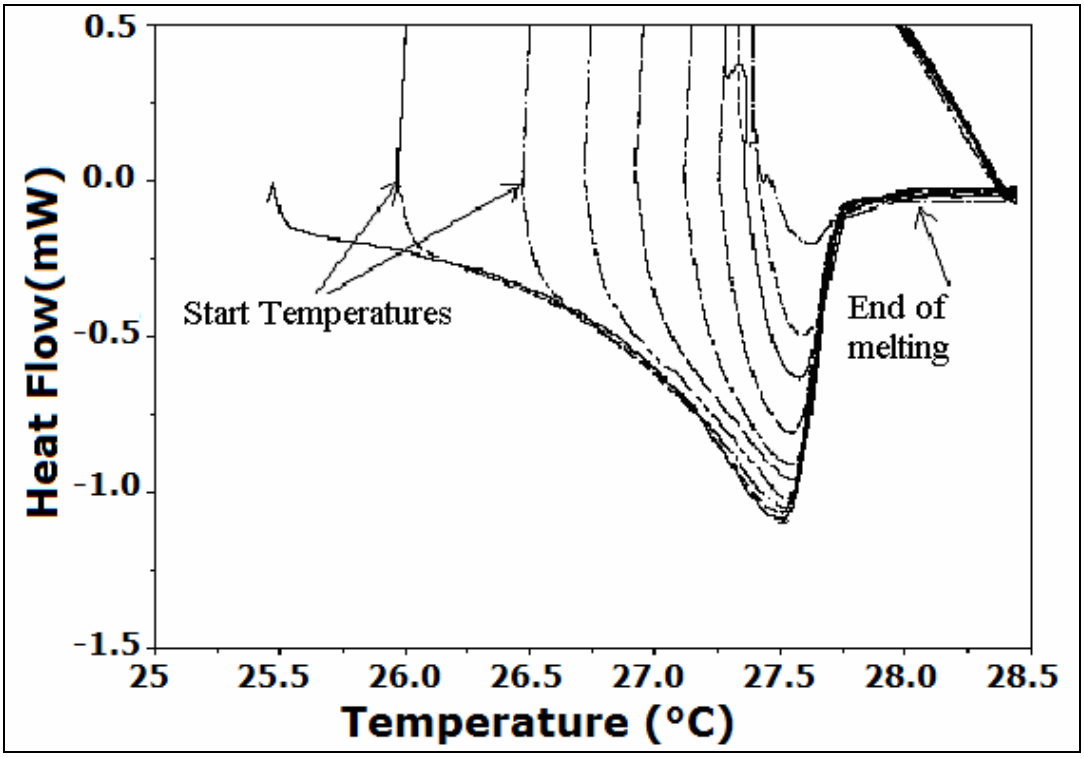

Figure 5.5 DSC melting curves of a paraffin-based PCM for different partially-solidified states

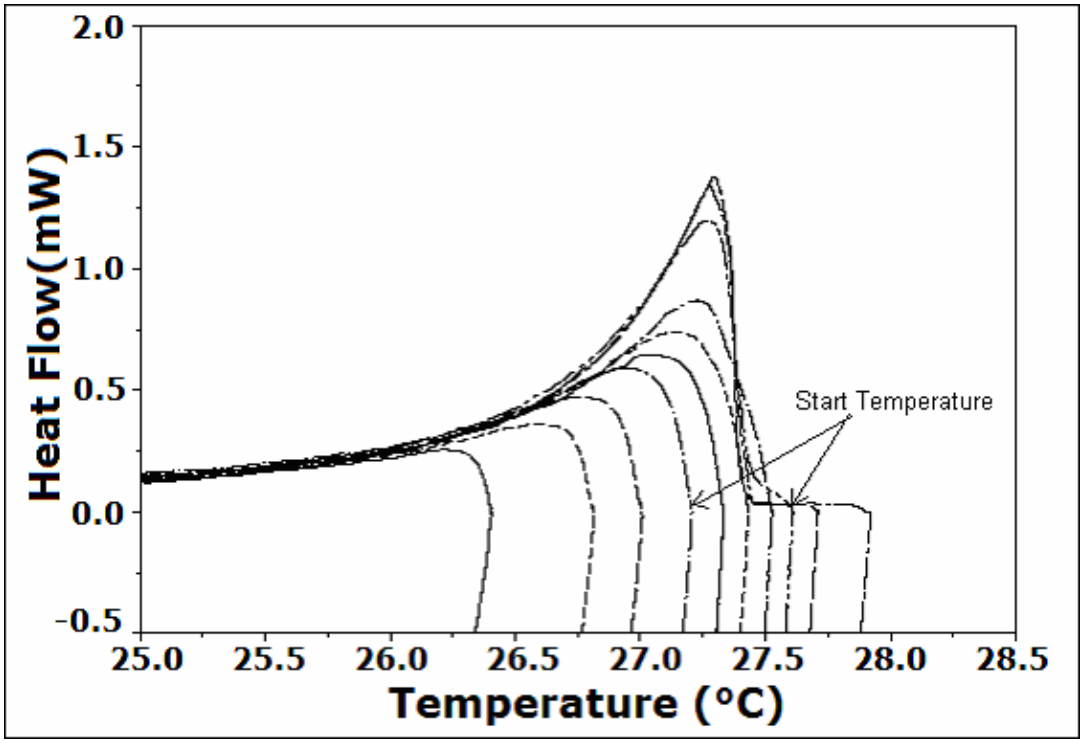

Figure 5.6 DSC solidification curves of a paraffin-based PCM for different partially-melted states

From the results shown in Figures 5.5 and 5.6, it was found that there existed a peak heat flow for all melting or solidification processes. For the melting process, though the melting process started from different temperatures (i.e., different percentage of the PCM solidified in the previous cooling cycle), the peak temperatures were within the narrow range of 27.5 ^{o}C to 27.6 ^{o}C (81.5 ^{o}F to 81.7 ^{o}F). After the peaks, the heat flow value dropped quickly. In the melting process, when the starting temperature was low, which meant more PCM had solidified in the previous solidification process, more heat (the area under the curve) was absorbed in the following melting process of the phase change cycle. Similarly, in the

solidification process, more heat was released when the starting solidification temperature was higher, which meant the PCM was closer to a completely melted state.

5.3.1.4 Characteristics of the heat of fusion distribution from theoretical analysis

In Figure 5.7, the PCM is assumed to go through a cycle between two very close temperatures where no work interactions took place. Theoretically, the heat released and the heat absorbed should be the same in one cycle in order to keep the net energy change at zero. Thus, the absolute value of the heat of fusion per unit temperature (i.e., the effective heat capacity value) at any temperature should be the same for both the melting and the solidification processes. Otherwise, the energy will not be balanced. Thus, the effective heat capacity curves for the melting and solidification should be “symmetrical.”

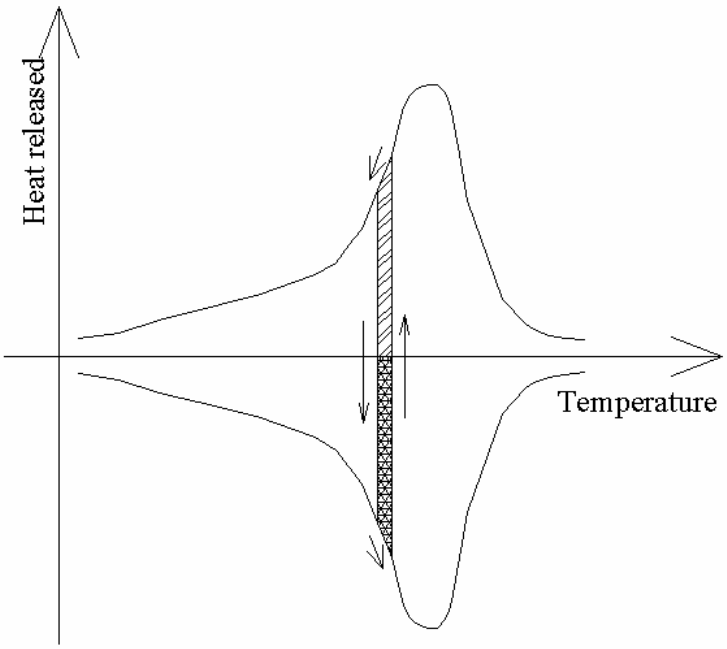

Figure 5.7 Illustration of the “energy balance” between the melting and solidification processes

In modeling, it is recommended to assume that the heat absorbed or released at certain temperature (effective heat capacity) in the phase change process is only a function of temperature. That is, the heat absorbed or released is assumed to be independent of the temperature change rate or the thermal history of the PCM that may have some influence on the crystal structure and the heat absorbed or released. Under these scenarios, for the partially-melted phase change processes, even though the melting or solidification processes start from different partially-melted states, their heat flow curves should jump to and follow the same heat flow curve as the continuous melting or solidification process, as illustrated in Figure 5.8.

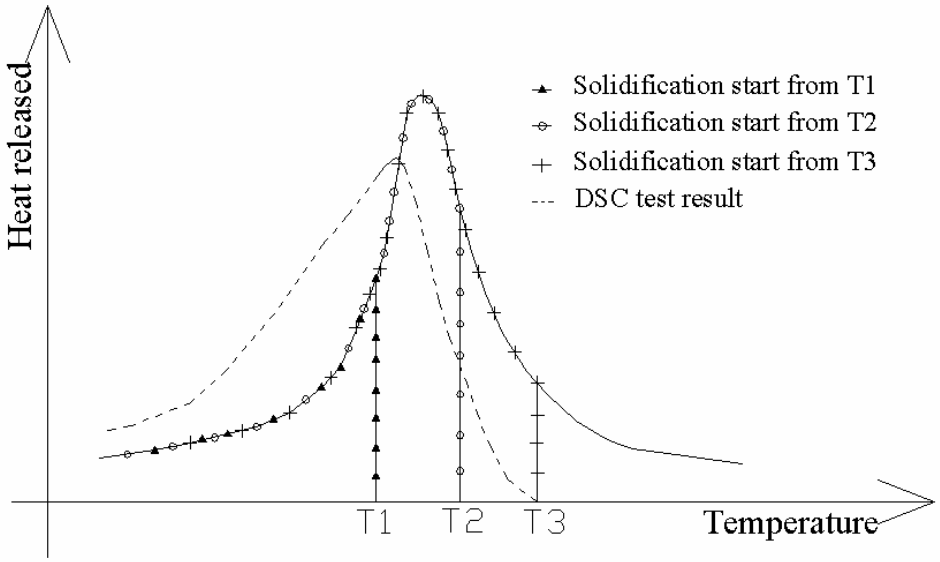

Figure 5.8 Illustration of heat released during phase change (solidification) from three starting temperatures

5.3.1.5 Inherent problems related to the DSC unit

As shown in Figures 5.5 and 5.6, the heat flow curves were different from the predictions shown in Figure 5.8. When the melting/solidification processes started from a certain temperature, the heat flow values always rose from zero, instead of immediately jumping to a certain value as in Figure 5.8. The heat flow values at specific temperatures were different for the cycles with different starting temperatures. Thus, the heat flow results from Test I showed some discrepancy. The reasons for this problem could be explored by a detailed study of the functioning principles of the DSC.

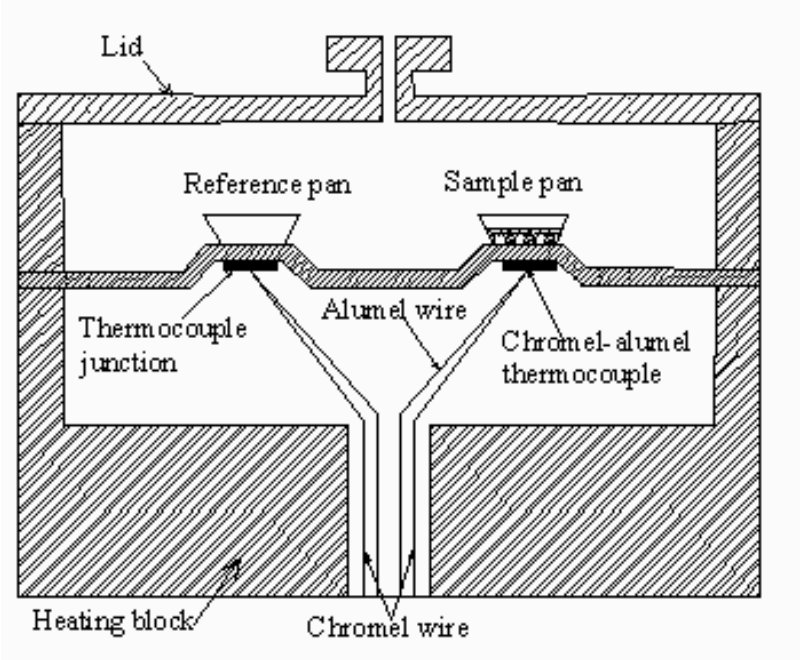

Figure 5.9 Cross-sectional diagram of the DSC testing cell

A cross-sectional diagram of the DSC testing cell is shown in Figure 5.9. In this unit, the sample temperature was measured by a Chromel-Alumel thermocouple located beneath the sample pan (not inside the sample pan). As a result, it is possible that a difference between the temperature reading of the PCM sample and the real temperature of the PCM sample existed. Also, although the PCM sample was a thin film, its temperature may not have been uniform. This was concluded because it took some time for a certain percentage of the PCM to melt/solidify corresponding to the temperature change. As a result, there was always a delay in response time between the sample temperature signal and the heat flow signal. In the heating DSC curve, the temperature signal led the heat flow signal (i.e., the peak of the curve was distorted towards the high temperature direction). While in the cooling period, the situation

was reversed. By studying different DSC test results, it was found that, when either the temperature change rate or the sample mass was larger, the heat flow peaks became wider. This could be explained by the larger time delays as a result of higher heat rate and larger sample mass. Thus, there were errors in the measurements of heat flows over the temperature range (i.e., the shapes of the curves were not 100% correct). The readings of the parameters that were obtained directly from the shape of the heat flow curve (for example, peak temperatures and the heat absorbed/released at specific temperatures) deviated from the true values. They might still be useful in qualitative analysis, but not accurate enough for the quantitative study, such as, numerical modeling. From the results from DSC tests using various settings, it was found that the measurement of heat absorbed or released in the phase change process (the area under the heat flow peak curve) remained the same even when the shape of the curve was distorted. Thus, the time delay problem would not affect its accuracy. This conclusion was verified by the DSC results from various tests using various settings.

5.3.2 DSC study of the performance of the PCM from partially melted states based on heat of fusion (Test II)

For this quantitative research and later modeling work, the accurate heat of fusion distribution (i.e., how the heat is absorbed/released during the phase change process) was critical. From the analysis above, only the absorbed/released heat was reliable in the DSC test. A new series of DSC tests based on the heat of fusion

measurement was set up to investigate the heat of fusion distribution within the phase change temperature range.

Similar to the Test I, the temperature of the PCM sample was first raised by 0.1 ^{o}C (0.18 ^{o}F) in the heating period at 0.1 ^{o}C/min (0.18 ^{o}F/min) heating rate. After this, the temperature of the sample was held constant to let the PCM to continue melting (because of the time delay mentioned above), until all the PCM that should melt at that temperature was able to melt. This process is shown in Figure 5.10. The heat absorbed could be obtained by integrating the area under the heat flow curve. Then the temperature was raised again and started another testing cycle. By step heating, the large heat flow peak for the entire phase change process was divided into many small peaks. By measuring the heat absorbed within these 0.1 ^{o}C (0.18 ^{o}F) temperature intervals (the area under these individual small peaks), the distribution of the heat of fusion over the phase change temperature range could be obtained. The results are shown in Figure 5.10. It should be noted that in the test results there was a shift of the baseline (i.e., the value of the heat flow was not zero when there was no heat absorbed/released). Because only the area under the curves was the concern of this research, this kind of shift would not affect the accuracy of the tests. For the solidification process, a similar scheme was used. The only difference is that a cooling process was used, instead of a heating process. This process is shown in Figure 5.11.

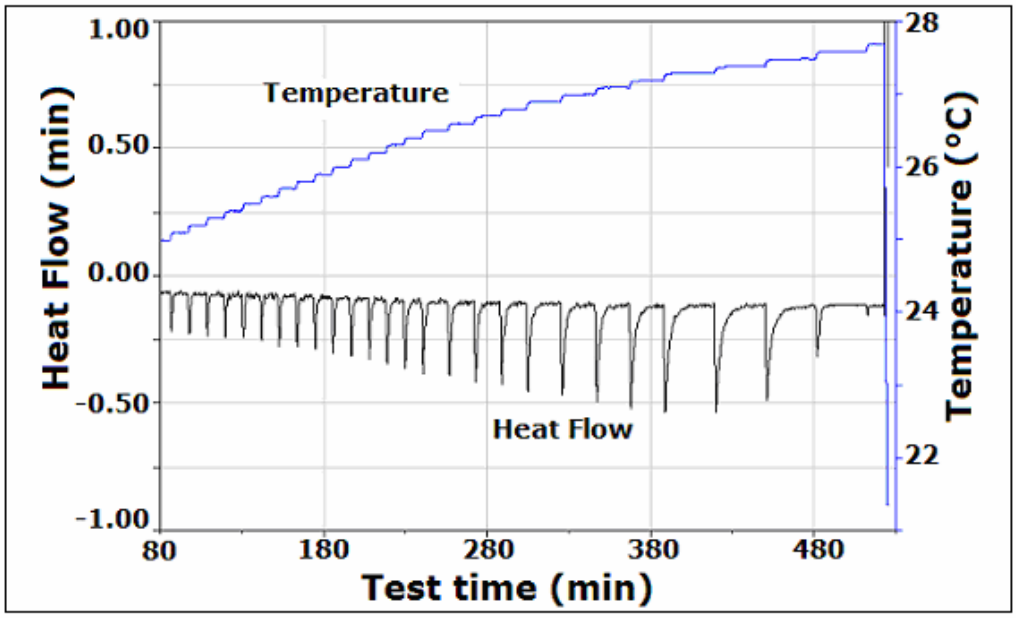

Figure 5.10 DSC heat flow and temperature curves of a paraffin-based PCM at 0.1 ^{o}C/min (0.18 ^{o}F/min) heating rate

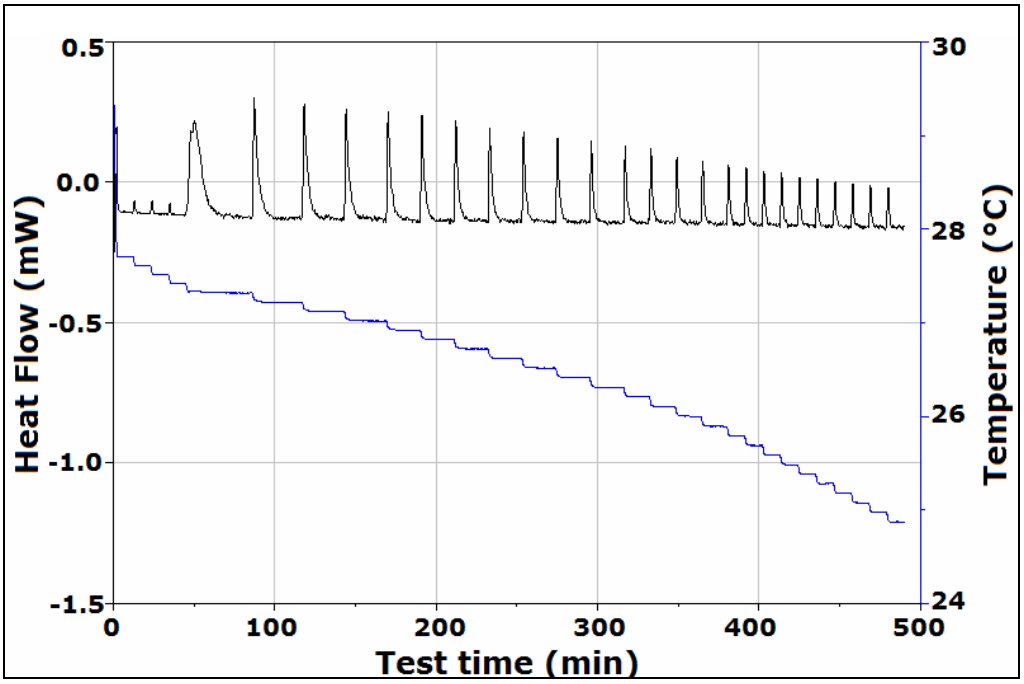

Figure 5.11 DSC heat flow and temperature curves of a paraffin-based PCM at 0.1 ^{o}C/min (0.18 ^{o}F/min) cooling rate

The detailed DSC heat flow and temperature curves over time are shown in Figures 5.12 and 5.13. As shown in the figures, when the temperature stopped rising and was held constant, the heat flow did not drop to zero immediately. The PCM kept releasing heat for some time. From the test results, it was found that at larger peaks it took longer before the heat flow curve became flat, which was the point when no more heat was released. This could be explained by the delay effect in the DSC testing. By integrating the area under the heat flow curve, the heat of fusion within that small temperature range could be obtained.

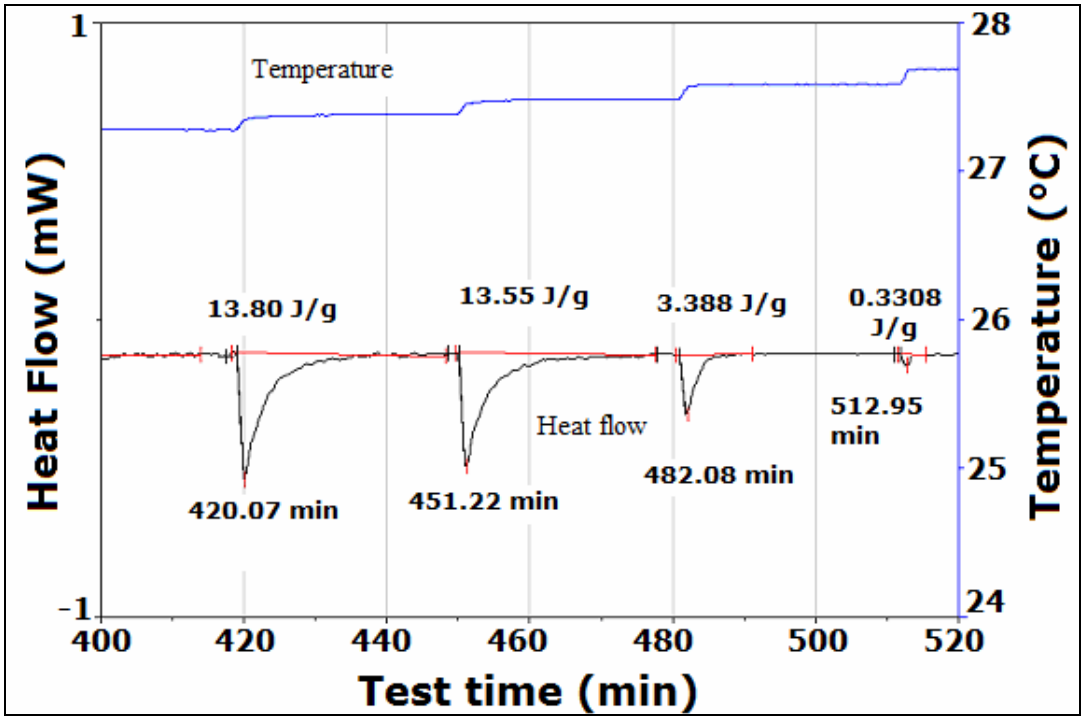

Figure 5.12 Detailed DSC heat flow and temperature curves of a paraffin-based PCM at 0.1 ^{o}C/min (0.18 ^{o}F/min) heating rate

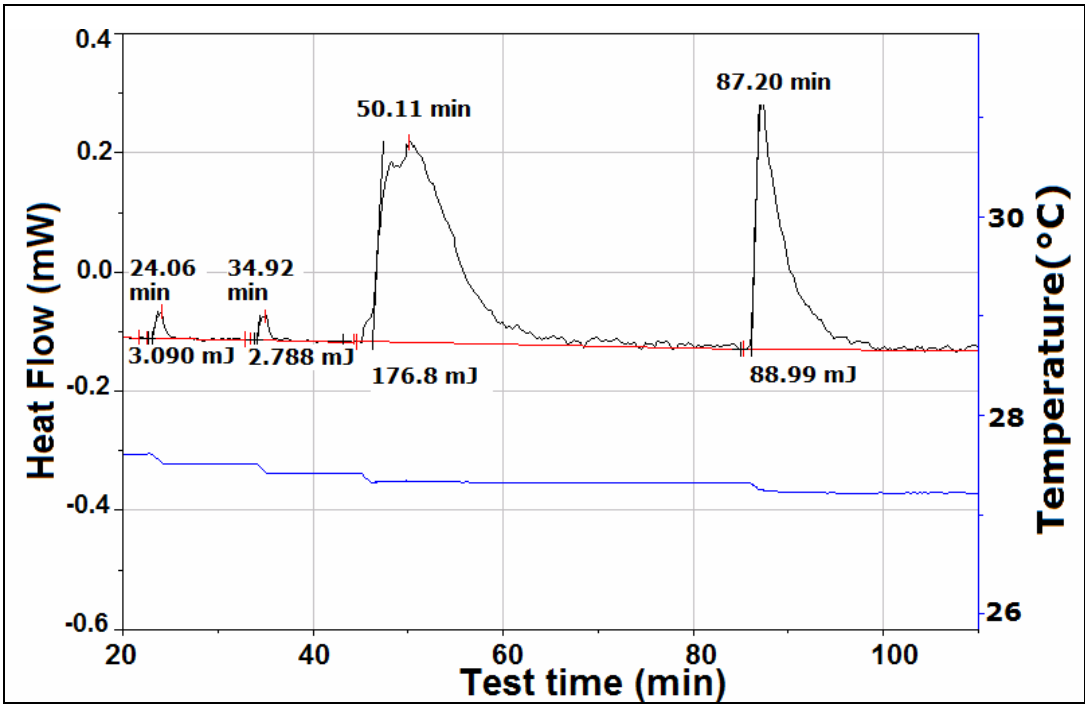

Figure 5.13 Detailed DSC heat flow and temperature curves of a paraffin-based PCM at 0.1 ^{o}C/min (0.18 ^{o}F/min) cooling rate

The heat absorbed/released in each temperature interval was calculated. This is shown in Figure 5.14. From the figure, it was found that, except for one data point at the beginning of the solidification process, the heat absorbed and the heat released in the heating process and the cooling process, respectively, were close to one another. This also confirms the previous analysis related to the energy balance.

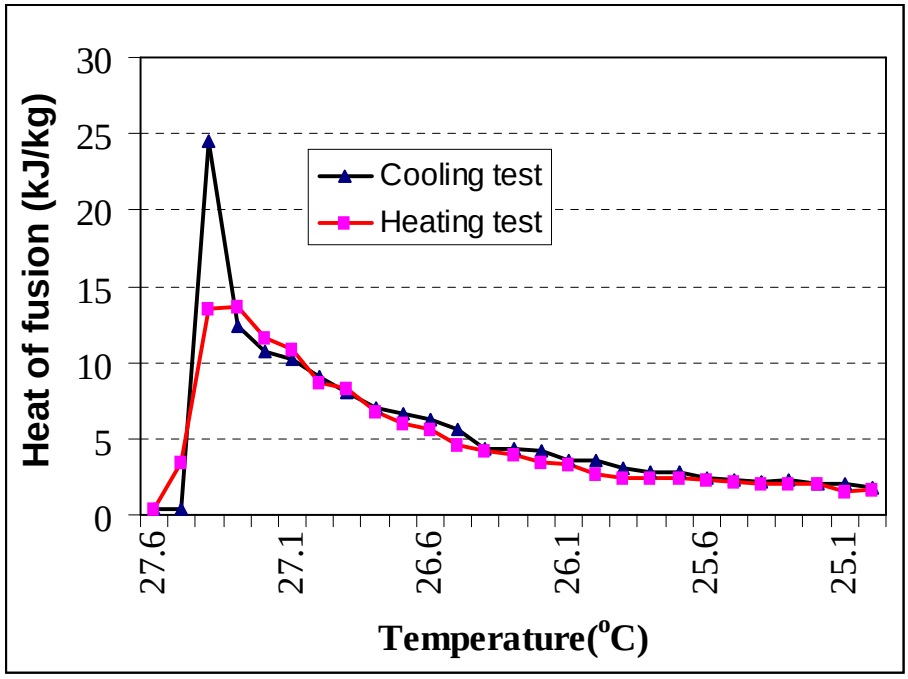

Figure 5.14 Comparison of the heat absorbed and heat released during the heating process and the cooling process, respectively

5.3.3 Supercooling problems during solidification

In reference to the outlier point in Figure 5.14 (highest peak in the cooling test), Figure 5.15 is presented. In the figure the heat flow curve of the data points around the 27.32 ^{o}C in the cooling test is of particular importance. It was found that when the temperature was lowered to 27.32 ^{o}C, the shape of the heat flow curve during that cooling period was different from those obtained for other start temperatures. Instead of decreasing, the temperature increased during the solidification process, which might be the result of supercooling. Supercooling means the PCM does not solidify until its temperature reaches several degrees below the theoretical solidification temperature, which is the ending temperature of the melting

process. When the temperature gets low enough, the PCMs solidification process is suddenly triggered by some disturbance. The temperature raise at around 27.32 ^{o}C in Figure 5.15 resulted because a large amount of heat was suddenly released, which exceeded the cooling capability of the DSC unit. This abnormal heat flow shape was also observed in the DSC test of hydrated salts, which are known for their supercooling problems. Paraffin products are not known for severe supercooling problems. For simplicity, this kind of small 0.1-0.2 ^{o}C (0.18-0.36 ^{o}F) supercooling problem was neglected in the modeling.

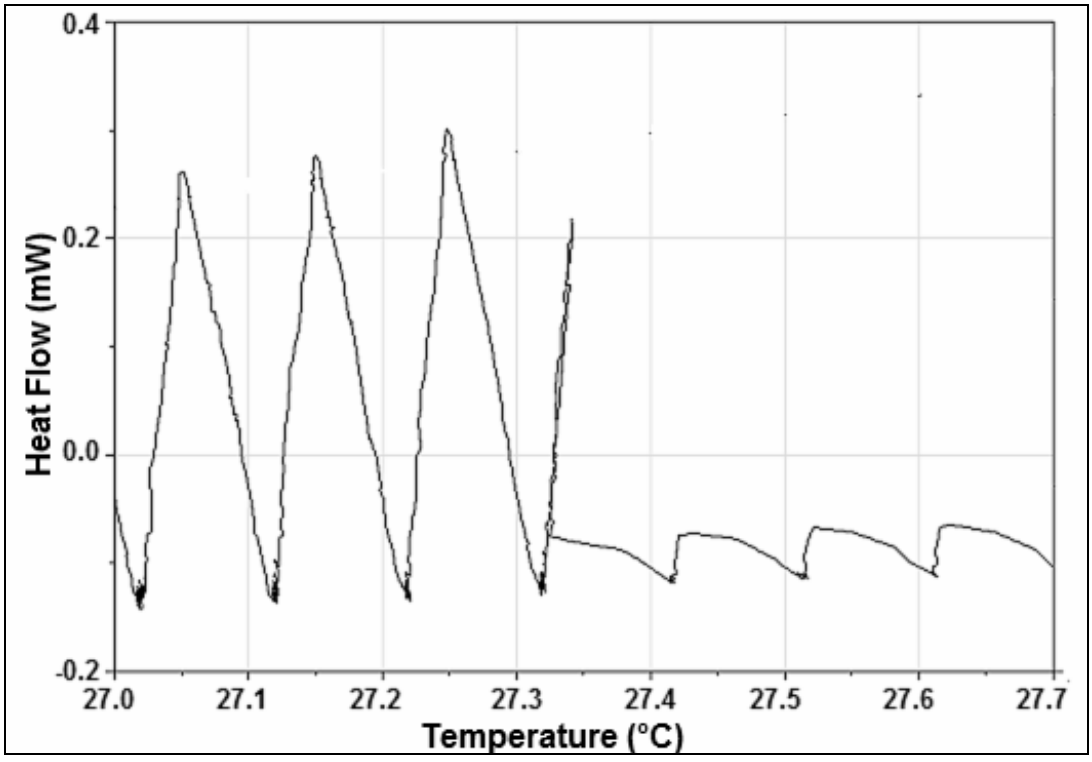

Figure 5.15 DSC curves of a paraffin-based PCM showing supercooling at around 27.32 ^{o}C (81.2 ^{o}F)

According to the assumptions of the heat flow measurement of the DSC, the temperatures of the furnace (the heat exchange surface) at the sample and the reference point should be equal. At the time when supercooling ended, a large amount of heat exceeded the cooling capability of the DSC unit and the temperatures of the furnace at the sample and at the reference point temperature became not equal. Therefore, the heat flow measurement was not considered accurate at this point. This explains the outlier point of Figure 5.14. It was decided to discard this outlier.

To verify the above results, a continuous DSC test was conducted at the same 0.1^{o}C/min (0.18^{o}F/min) heating/cooling rates. The results are shown in Figure 5.16. Comparing the sum of peaks in Figures 5.10 and 5.11 and that from the continuous test , it was found that the total heat absorbed in the melting process in the step tests was 131.8 kJ/kg (56.7 Btu/lbm). The heat released in the solidification process in the step test was 145.4 kJ/kg (62.5 Btu/lbm). The heat absorbed in the continuous test was 134.9 kJ/kg (58.0 Btu/lbm) and the heat released in the continuous test was 129.9 kJ/kg (55.8 Btu/lbm). By comparing the results, it was found that the heat absorbed in the step test and the heat absorbed in the continuous test were close. There was a difference between the results during the solidification for the step test and the continuous test. However, after accounting for the supercooling problem, as discussed above, and replacing the outlier of Figure 5.14 with the value of the peak value of the melting process, the sums of the heat released from the step and continuous tests became closer. Therefore, this provides the proof that the results from the step test

were accurate and reliable. These data would be deemed accurate and therefore be used to derive the proposed PCM model.

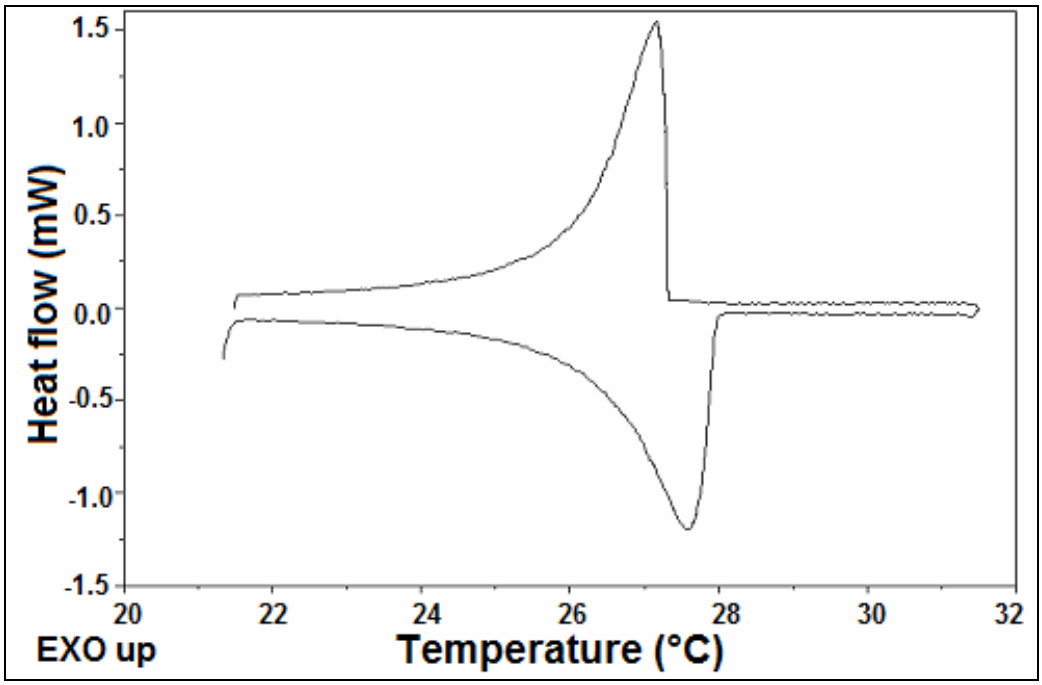

Figure 5.16 DSC curve of a paraffin-based PCM at 0.1 ^{o}C/min heating/cooling rate

5.4 A modified model for a paraffin-based PCM

The proposed modified model was based on the effective heat capacity (specific heat) method. The effective heat capacity could be calculated from experimental results by dividing the amount of heat absorbed in the temperature interval (kJ/kg, Btu/lb) by the width of the temperature interval (K, ^{o}F). Thus, the resulting effective heat capacity would have the same unit as the specific heat, kJ/(kg·K), Btu/(lbm·^{o}F). From the analysis above, the melting and solidification process were symmetrical. The heat of fusion distribution (i.e., the effective heat

capacity values over temperature) was the same for both processes. Melting test data were used to derive the new model.

As seen in Figure 5.16, the melting process heat flow curve gradually tailed off when the temperature became low. When compared with that of the peak values portion in the graphs, the thermal storage density in the tail part was very low. Also, it is safe to underestimate storage capacity values in real applications. Thus, for the applications in which PCMs will completely or mostly melt, the phase change temperature ranges for both melting and solidification process can be limited to the 24.98-27.48 ^{o}C (77.96– 81.46 ^{o}F) range. This truncation would not introduce a large error.

In situations when the temperature would not get high enough, like in the case when the PCMs are close to cold surface of the wall, the information about the tail part would be of interest. Direct measurements were not conducted by DSC test on the tail part in this research. This is because the heat released in that part was low and the areas of the peaks became smaller and smaller when the temperature decreased and the error in the measurement and integration became large. In addition, there was a limit on the numbers of cycles setting on the DSC unit.

From the DSC curve in Figure 5.16, it was found that the curve was relatively flat in the tail part. Thus, if the tail part should be considered, the specific heat could be calculated by linear interpolation.

Based on the study of daily maximum west exterior wall surface temperatures and corresponding minimum exterior wall surface temperatures in Chapter 2, it was

found that, for the top 20% of hot days, the minimum exterior wall surface temperatures were mostly above 20 ^{o}C (68 ^{o}F). The design indoor air temperature was usually 24 ^{o}C (75.2 ^{o}F) for the summer. Thus, the temperature in the insulation and that of the PCM would not get below 20 ^{o}C (68 ^{o}F). In the modeling, the phase change temperature range was assumed to be between 20 and 27.5 ^{o}C (68 and 81.5 ^{o}F).

Based on the data of the heating tests in Figure 5.14 and the above assumptions of the phase change temperature range, the mathematical expression of the effective heat capacity for the present paraffin-based PCM (in kJ/(kg·k)) and the corresponding temperatures were obtained. From the theoretical analysis above, the heat absorbed or released during the phase change process was only a function of temperature. Thus, the following model can be applied to the phase change processes from either complete-melted or partially-melted states.

$$Cp' = \begin{cases} 1.8^{*} & \text{for } T<20 \\ 2.2177 \times (T-20) + 1.8 & \text{for } 20 \leq T<24.98 \\ 7.945 \times 10^{-10} e^{0.941\,T} & \text{for } 24.98 \leq T<26.99 \\ 173.66T - 4601.9 & \text{for } 26.99 \leq T<27.28 \\ 135 & \text{for } 27.28 \leq T<27.48 \\ 2.4^{*} & \text{for } 27.48 \leq T \end{cases}$$

*Values from manufacturer data

The effective Cp' calculated from the above model is shown in Figure 5.17.

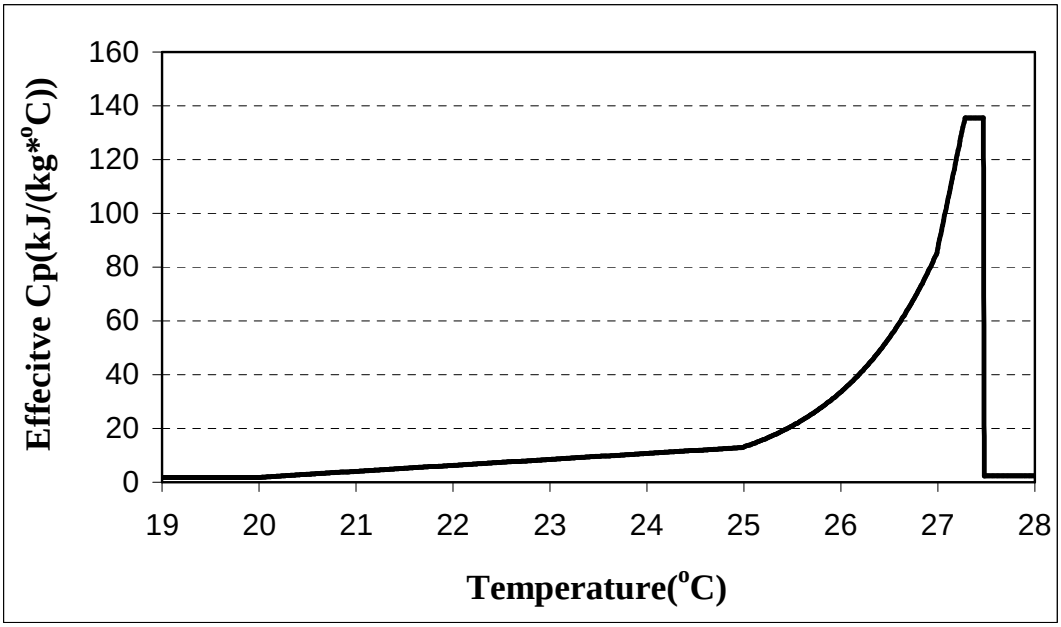

Figure 5.17 Effective Cp' values

Using the above model, the heat released in the same temperature intervals as those in the DSC heating test was calculated. The comparison of the calculated heat released to those from the DSC experimental data is shown in Figure 5.18. It was found that the two curves agreed with each other well. Therefore, the proposed model could be considered a good approximation of the real performance of the paraffin-based PCM (RT27). In Chapter 6, the accuracy of the model would be verified by comparison between the experimental data and the results of numerical simulation where the PCM model was incorporated.

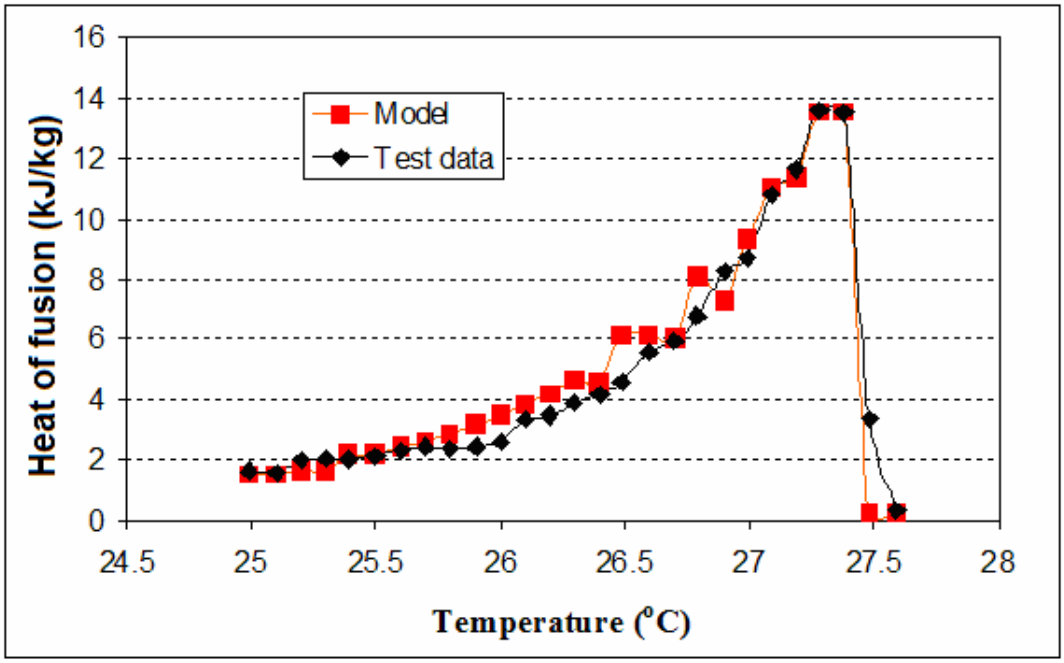

Figure 5.18 Comparison of the proposed model with experimental data

5.5 Summary

From the analysis of the experimental data, it was found that the possibility existed that the PCMs installed in walls of residential and small commercial buildings would not completely melt or solidify in the phase change processes and that PCMs would melt or solidify starting from partially-melted states. Incorrect heat absorption/release distributions would overestimate or underestimate the thermal storage capacity of the PCMs and would produce inaccurate temperature predictions. As a result of the limitations of the DSC test, there were inherent errors in the measurement of the heat flow curves (i.e., the shape of the curve was not 100% correct). The readings of the parameters that were obtained directly from the shape of the heat flow curves (for example, peak temperatures and the heat absorbed/released

at certain temperature) were not accurate enough for quantitative research. A DSC test method based on the heat of fusion measurement and its detailed steps, used to study the performance of PCMs from partially-melted states, were developed. The results for a paraffin-based PCM (RT27) were analyzed and based on these data a modified model for paraffin-based PCM was developed. The proposed method could also be applied to any other PCMs with any phase change temperature range.

Chapter VI

Numerical Simulation of PCM-enhanced Building Walls

In order to verify the accuracy of the new PCM model developed in Chapter 5, numerical simulation was conducted for the PCM-enhanced wall. The results of the simulation where actual experimental wall surface temperature data were used as boundary conditions, were compared with the experimental data for different cases. The reasons for the difference in the performance for the 1.27 cm(1/2 in) and 1.9 cm (3/4 in) pipe experiments were analyzed. A parametric study was performed using the verified model to investigate the influence of different variables on the performance of the PCM-enhanced building wall and find the optimal settings for real application. The performance of the PCM-enhanced wall (layer method with optimal settings) in several U.S. climate zones was studied.

6.1 Verification of the PCM model

Numerical simulations were conducted for the heat transfer across PCM-enhanced walls retrofitted with the macro-encapsulation method (simulator “pipe tests” in Section 3.2), where actual experimental wall surface temperature data were used as boundary conditions. The simulation results were compared with the experimental data to verify the accuracy of the new PCM model.

6.1.1 Model used in the simulation of macro-encapsulation method

The computational domain used in the simulation is shown in Figure 6.1. The length of the PCM-encapsulating pipe was assumed to be infinitely long. Thus, the heat transfer in the wall was considered two-dimensional. Because of the geometric symmetry, only half of the PCM-encapsulating pipe and half of the insulation were used in the simulation. A structured mesh was used. The mesh size was uniformly 0.001 m (0.039") in both the x and y directions.

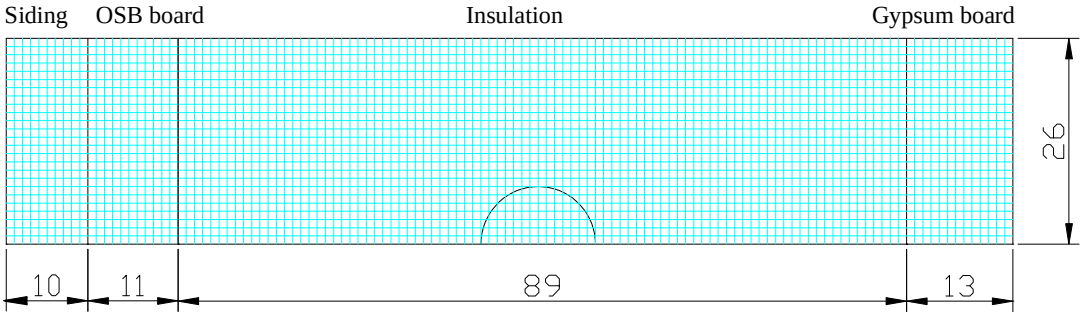

Figure 6.1 Computational domain (numbers indicate the number of nodes)

The top and bottom edges of the computational domain were set as symmetry boundary condition. The left and right ends were set as third-type boundary condition. "Dummy" or "ghost" node method was applied to the four boundaries to maintain the second order difference for all the nodes in the computational domain.

In the simulation, the convection in the PCM was neglected for simplification purposes. Thus, only conduction was considered in the heat transfer. The equation of conduction is:

$$\rho c \frac{\partial t}{\partial \tau} = K \nabla^2 t \tag{6-1}$$

Where

t = temperature (^oC, ^oF)

ρ = density (kg/m^3, lb/ft^3)

c = specific heat (kJ/kg·K, Btu/lbm·^oR)

K = conductivity (W/(m·^oC) , Btu/(ft·hr·^oF))

τ = Time (s)

Central difference was applied in space and the implicit method (backwards difference) was applied in time. Though it took more computational time, the program was stable and did not have the limitation on the time step interval.

Thus, for the nodes in the computational domain, the difference equation is:

$$\frac{t_i^k - t_i^{k-1}}{\Delta \tau} \rho c \Delta X \Delta Y = K_{Ei} \frac{t_E^k - t_i^k}{\Delta X} \Delta Y + K_{wi} \frac{t_w^k - t_i^k}{\Delta X} \Delta Y + K_{Ni} \frac{t_N^k - t_i^k}{\Delta Y} \Delta X + K_{Si} \frac{t_S^k - t_i^k}{\Delta Y} \Delta X$$

(6-2)

where

ΔX = x direction mesh size (m,ft)

ΔY = y direction mesh size (m,ft)

$\Delta\tau$ = time step (s)

^{k} = the current time step

$^{k-1}$ = the last time step

$_{i}$ = the current node

$_{E,W,N,S}$ = the four neighboring nodes of the current node (E,W in horizontal direction and N,S in vertival direction)

K_{xi} = the conductivity between the current and the neighboring node, $x \in \{E,W,N,S\}$ (W/(m·^{o}C) , Btu/(ft·hr·^{o}F))

At the interface of two materials, for example K_i and K_w (the conductivity of insulation and wallboard, respectively), the conductivity for the heat transfer between these two nodes are calculated by:

$$K_{iw}=\frac{2K_iK_w}{K_i+K_w} \qquad (6\text{-}3)$$

where

K_{iw} = the conductivity used in the calculation in the interface (W/(m·^{o}C), Btu/(ft·hr·^{o}F))

K_i = the conductivity of the insulation (W/(m·^{o}C) , Btu/(ft·hr·^{o}F))

K_w = the conductivity of the wallboard (W/(m·^{o}C) , Btu/(ft·hr·^{o}F))

In the simulation, the distance from the center of the pipe was used to determine whether the node was inside or outside the pipe. In other words, this distance indicated whether the node was insulation or PCM. The new PCM model developed in Chapter 5 was used to handle the phase change process in the simulation.

All the boundary condition data were prepared and saved in several .txt files in advance. The data was read before each time step. The simulation result, the averaged heat transfer rate per unit area across the wall, was written into a .txt file at the end of each time step. The alternating direction implicit (ADI) method was used in the iterations. If the maximum difference of all the nodes between iterations was under 10^{-7}, the iteration was considered converged.

The layout of the wall used in the simulations is shown in Figure 6.2. As mentioned in section 3.2, two layers of fiberglass insulation were installed in the wall cavity, the insulation batt was compressed to some extent. Thus, the R-value of the insulation in the testing wall panel was unknown.

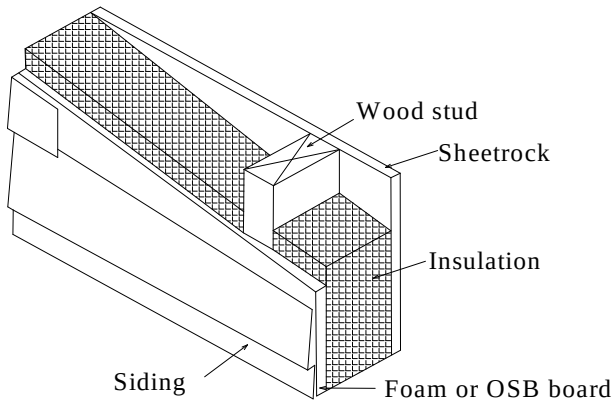

Figure 6.2 Layout of the wall used in the simulations

The experimental results of the control wall, in which only two layers of plain fiberglass insulation was installed, were used to determine the conductivity (R-value) of the insulation in the test. The conductivity value of the insulation used in the program was adjusted until the heat fluxes of both the simulation results and experimental data were nearly identical. The conductivity of the insulation in the simulator tests (pipe tests) was found to be 0.045 W/(m·^{o}C) (0.026 Btu/(ft·hr·^{o}F)), which is close to the published value of "R11" fiberglass insulation of 0.04 W/(m·^{o}C), 0.023 Btu/(ft·hr·^{o}F) (2005 ASHRAE handbook: Fundamentals). As shown in Figures 6.2, for the other tests, the simulation results also matched well with the experimental data when the value of 0.045 W/(m·^{o}C) (0.026 Btu/(ft·hr·^{o}F)) was used in the simulation, which provided the proof that 0.045 W/(m·^{o}C) (0.026 Btu/(ft·hr·^{o}F)) was a good estimation of the conductivity of the insulation used in the macro-encapsulation tests (PCM pipe tests) where two R11 fiberglass batts were installed in the wall cavity. The properties of the building materials used in the simulation are shown in Table 6.1.

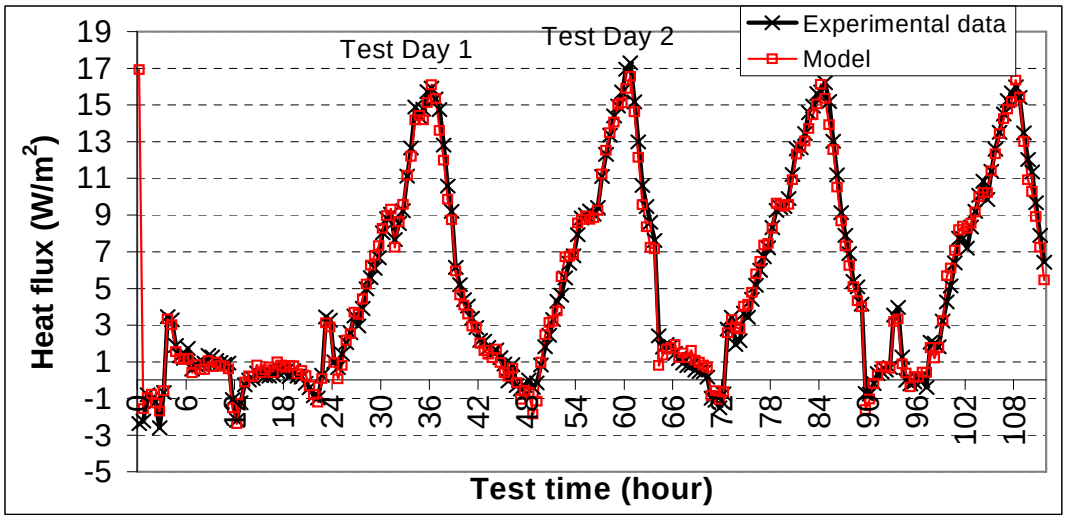

Figure 6.3 Heat fluxes across the wall panels - model vs. experimental data comparisons for control wall (no PCM)

Table 6.1 Properties of the building materials used in the simulation

Material	Density (kg/m^3)/(lbm/ft^3)	Conductivity (W/m·°C)/(Btu/hr·ft·°F)	Specific heat (kJ/(kg·K))/(Btu/lbm°F)
Gypsum board 12.7 mm (1/2 in)	800/50	0.16/0.092	1.09/0.26
OSB board 11.1 mm (7/16 in)	650/40.6	0.13/0.075	1.21/0.29
OSB Siding 9.5 mm (3/8 in)	650/40.6	0.13/0.075	1.21/0.29
Fiberglass insulation 88.9 mm (3.5 in)	12.71/0.79	0.045/0.026	0.84/0.2

6.1.2 Simulation results and analysis

6.1.2.1 PCM-enhanced wall ("Middle depth" configuration)

Several simulations were conducted representative of previous experiments and under different temperature cycles. The simulation results and experimental data for different the various cases are shown in Figures 6.4 through 6.11. The predictions

of the heat fluxes across the walls and the experimental data were significantly close for the configuration using the 1.27 cm (1/2 in) diameter pipes. For the data in the figures, the averaged percentage difference in the peak heat fluxes between the experimental data and model predictions was approximately 3.5%. For the configuration using the 1.90 cm (3/4 in) diameter pipes, the differences between the simulated heat fluxes and experimental data were larger, especially for the first couple of days. The averaged percentage difference in the peak heat fluxes was approximately 10%.

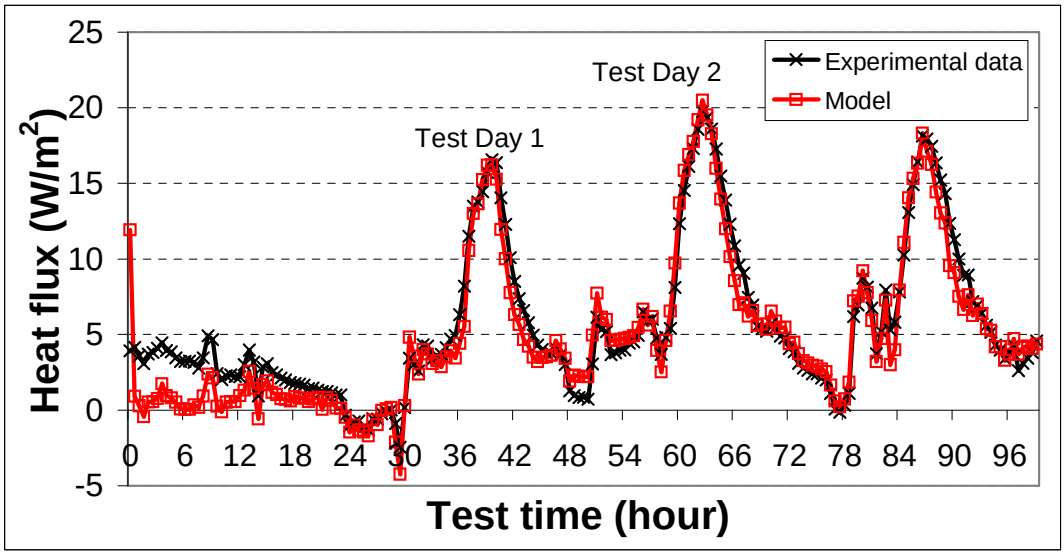

Figure 6.4 Heat fluxes across the wall panels – model vs. experimental data comparisons for PCM-enhanced walls ("middle depth" configuration, 1.27 cm (1/2 in) diameter pipes, maximum wall temperature of 69 ^{o}C(156.2 ^{o}F))

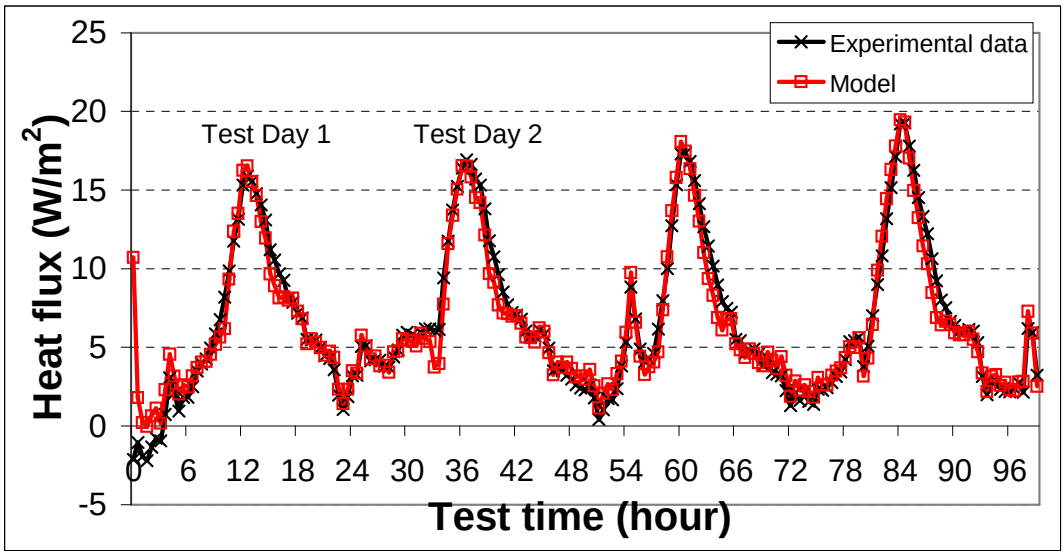

Figure 6.5 Heat fluxes across the wall panels – model vs. experimental data comparisons for PCM-enhanced walls ("middle depth" configuration, 1.27 cm (1/2 in) diameter pipes, maximum wall temperature of 65 ^{o}C(149 ^{o}F))

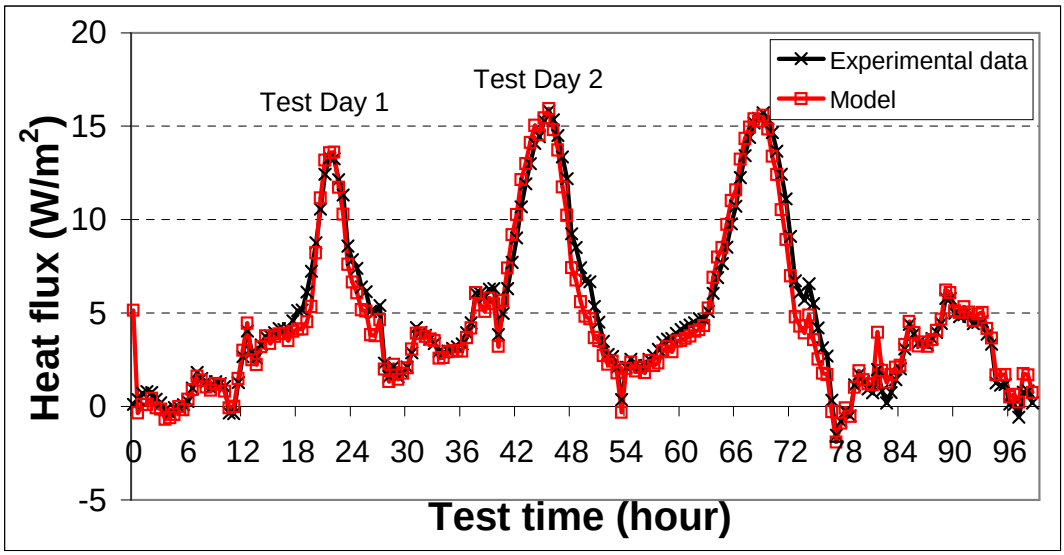

Figure 6.6 Heat fluxes across the wall panels – model vs. experimental data comparisons for PCM-enhanced walls ("middle depth" configuration, 1.27 cm (1/2 in) diameter pipes, maximum wall temperature of 61 ^{o}C(141.8 ^{o}F))

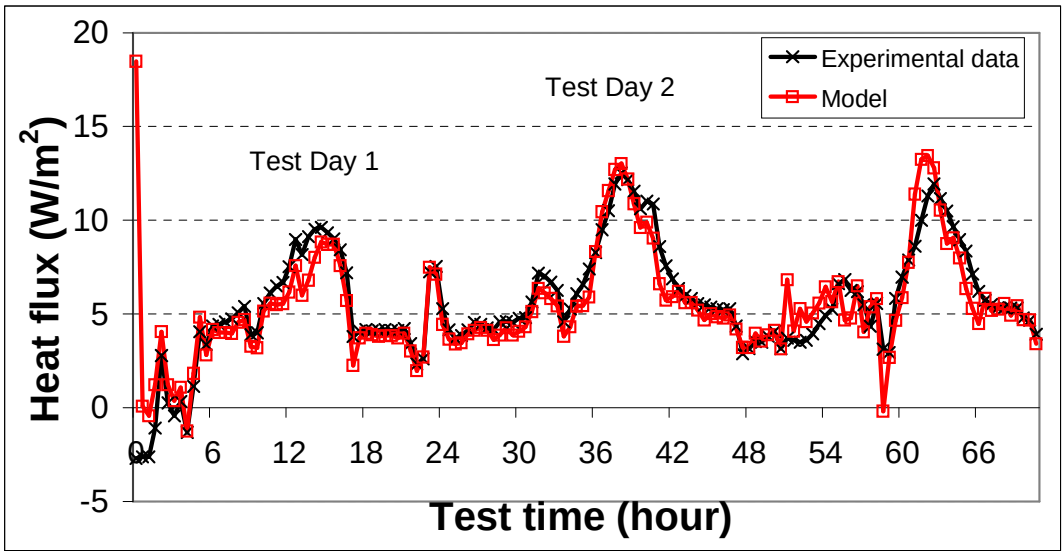

Figure 6.7 Heat fluxes across the wall panels – model vs. experimental data comparisons for PCM-enhanced walls ("middle depth" configuration, 1.27 cm (1/2 in) diameter pipes, maximum wall temperature of 55 ^{o}C(131 ^{o}F))

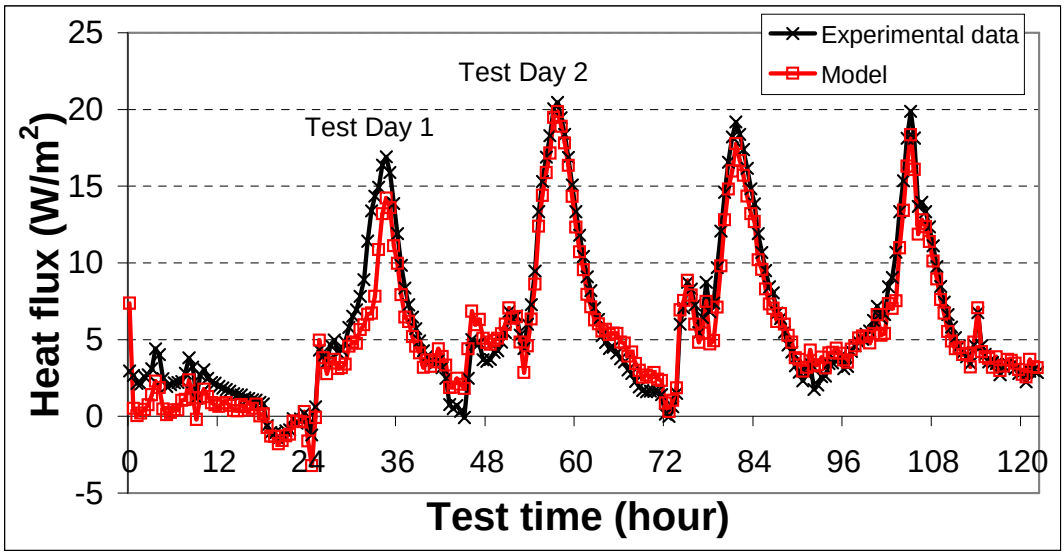

Figure 6.8 Heat fluxes across the wall panels – model vs. experimental data comparisons for PCM-enhanced walls ("middle depth" configuration, 1.9 cm (3/4 in) diameter pipes, maximum wall temperature of 69 ^{o}C(156.2 ^{o}F))

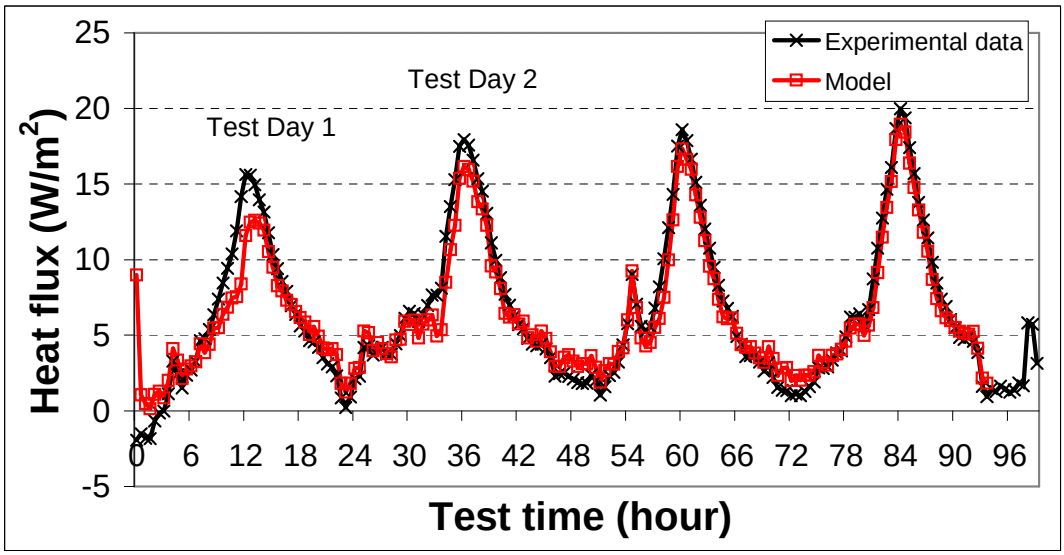

Figure 6.9 Heat fluxes across the wall panels – model vs. experimental data comparisons for PCM-enhanced walls ("middle depth" configuration, 1.9 cm (3/4 in) diameter pipes, maximum wall temperature of 65 ^{o}C(149 ^{o}F))

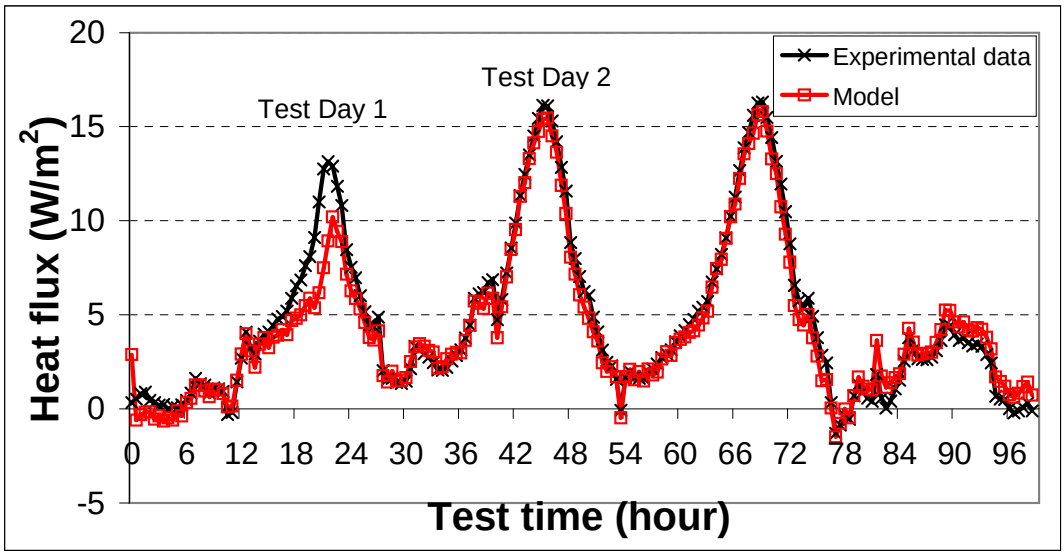

Figure 6.10 Heat fluxes across the wall panels – model vs. experimental data comparisons for PCM-enhanced walls ("middle depth" configuration, 1.9 cm (3/4 in) diameter pipes, maximum wall temperature of 61 ^{o}C(141.8 ^{o}F))

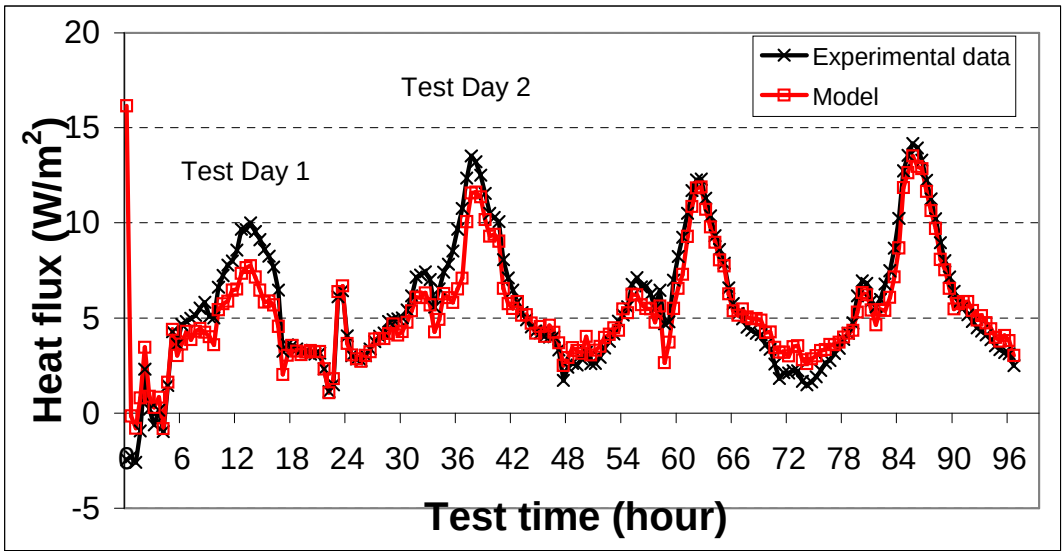

Figure 6.11 Heat fluxes across the wall panels – model vs. experimental data comparisons for PCM-enhanced walls ("middle depth" configuration, 1.9 cm (3/4 in) diameter pipes, maximum wall temperature of 55 ^{o}C(131 ^{o}F))

6.1.2.2 PCM-enhanced wall ("next to wallboard" configuration)

Simulation results for the "next to wallboard" configuration are shown in Figures 6.12 through 6.17. Similar to the results of "middle depth" configuration, the simulation for the "next to wallboard" configuration gave good predictions for the 1.27 cm (1/2 in) diameter pipe experiments. For the data in the figures, the averaged percentage difference in the peak heat fluxes between the experimental data and model prediction was approximately 7.9%. The predictions for the 1.9 cm (3/4 in) diameter pipe experiments were not as close. The simulation predictions produced lower heat flux values for the PCM-enhanced wall. The percent difference between model predictions and experimental data was 19.6%.

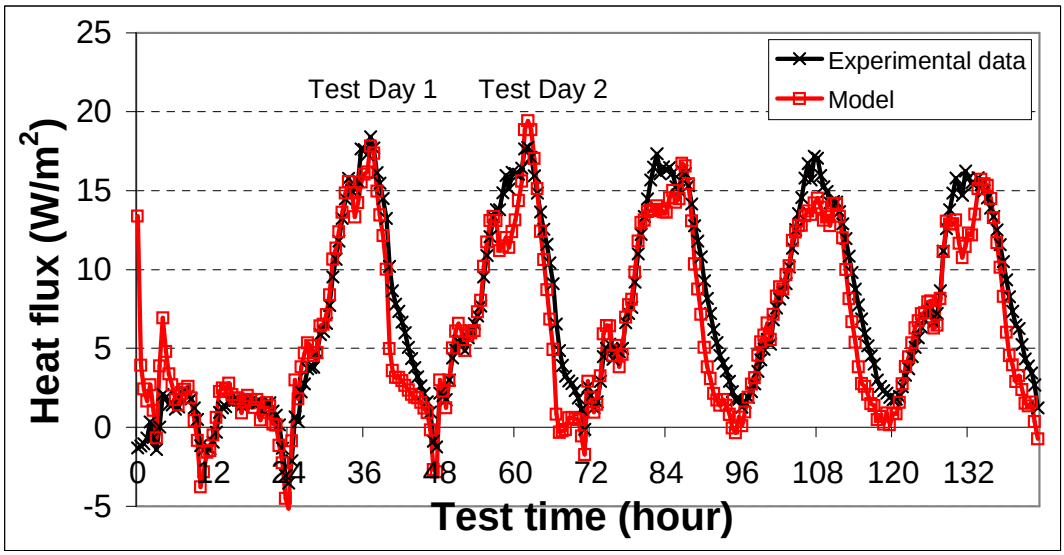

Figure 6.12 Heat fluxes across the wall panels – model vs. experimental data comparisons for PCM-enhanced walls ("next to wall board" configuration, 1.27 cm (1/2 in) diameter pipes, maximum wall temperature of 70 ^{o}C(158 ^{o}F))

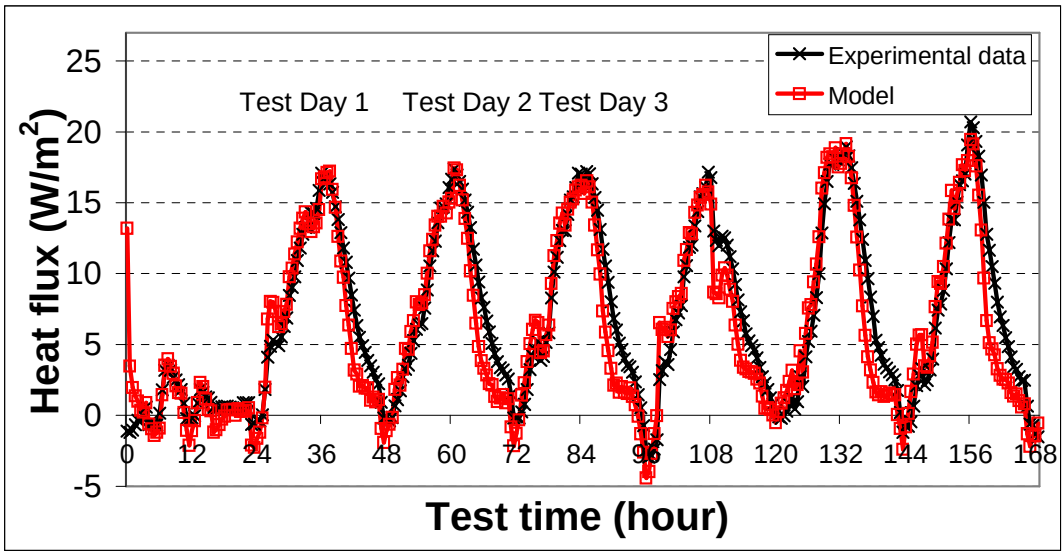

Figure 6.13 Heat fluxes across the wall panels – model vs. experimental data comparisons for PCM-enhanced walls ("next to wall board" configuration, 1.27 cm (1/2 in) diameter pipes, maximum wall temperature of 65 ^{o}C(149 ^{o}F))

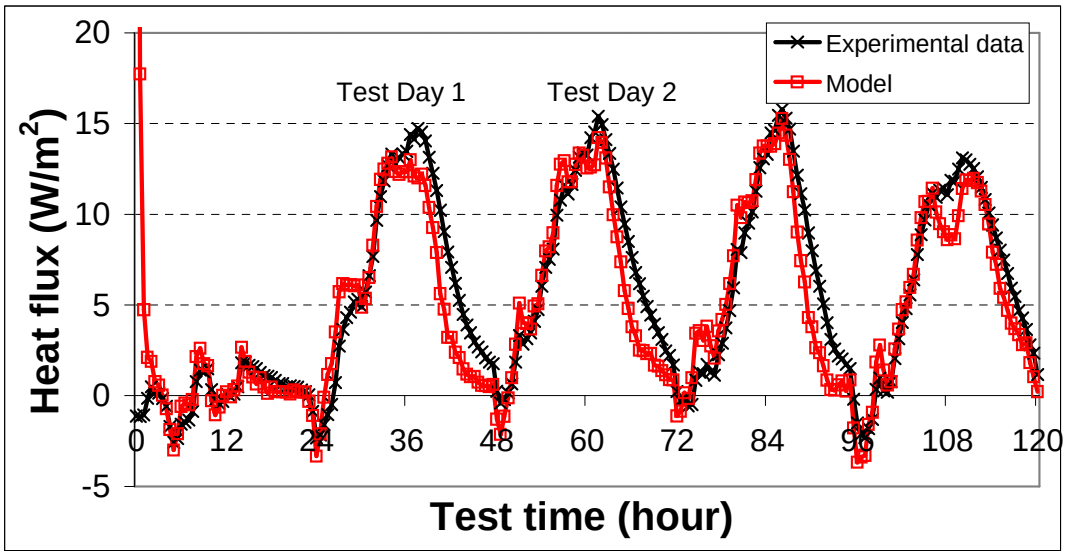

Figure 6.14 Heat fluxes across the wall panels – model vs. experimental data comparisons for PCM-enhanced walls ("next to wall board" configuration, 1.27 cm (1/2 in) diameter pipes, maximum wall temperature of 58 ^{o}C(136.4 ^{o}F))

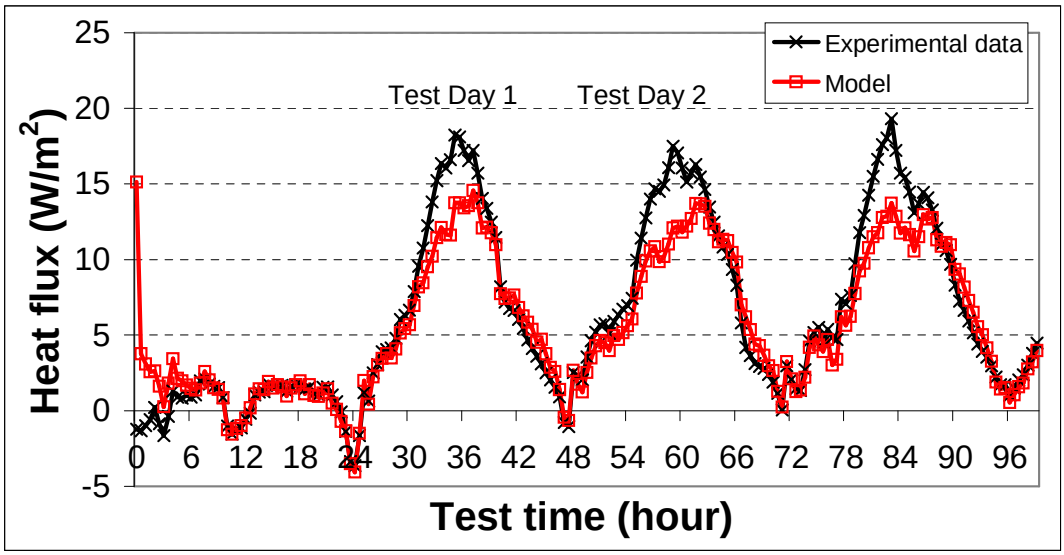

Figure 6.15 Heat fluxes across the wall panels – model vs. experimental data comparisons for PCM-enhanced walls ("next to wall board" configuration, 1.9 cm (3/4 in) diameter pipes, maximum wall temperature of 70 ^{o}C(158 ^{o}F))

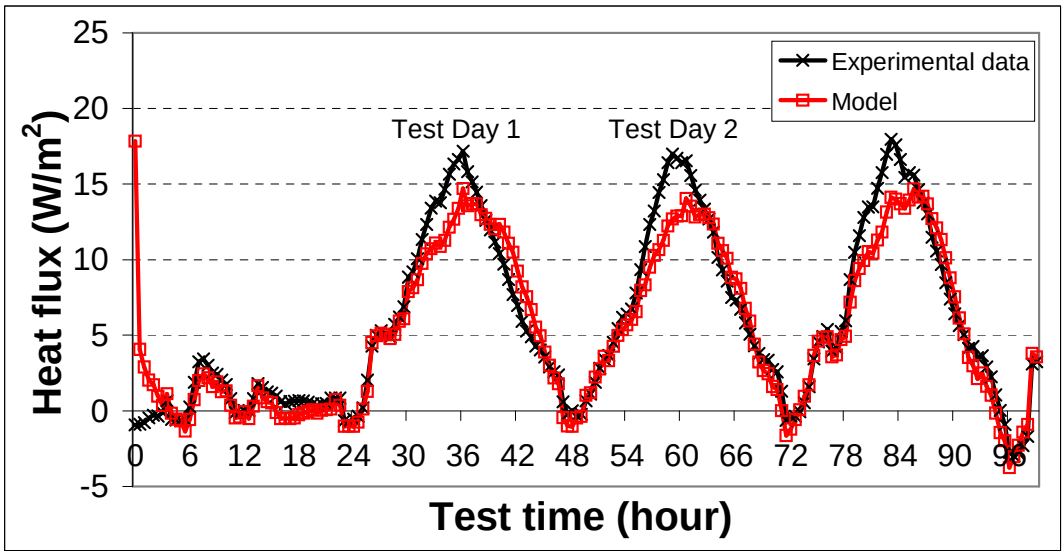

Figure 6.16 Heat fluxes across the wall panels – model vs. experimental data comparisons for PCM-enhanced walls ("next to wall board" configuration, 1.9 cm (3/4 in) diameter pipes, maximum wall temperature of 65 ^{o}C(149 ^{o}F))

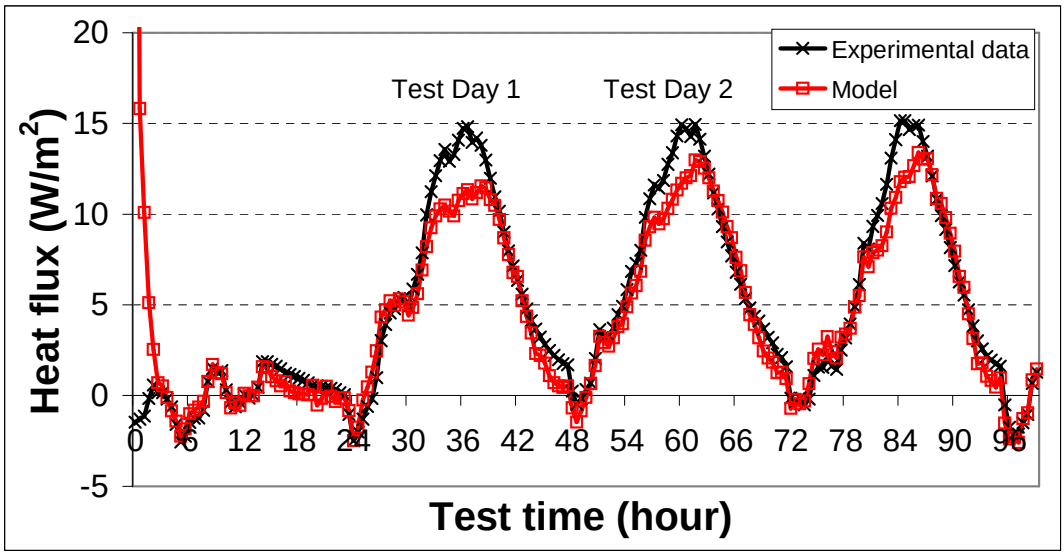

Figure 6.17 Heat fluxes across the wall panels – model vs. experimental data comparisons for PCM-enhanced walls ("next to wall board" configuration, 1.9 cm (3/4 in) diameter pipes, maximum wall temperature of 58 ^{o}C(140 ^{o}F))

6.1.2.3 Analysis of the results

The natural convection within the pipe in the two-phase mixture of the PCM in the phase change process might be one possible reason for the difference between the simulation results and experimental data. In the simulation, the natural convection was neglected. As a result, the heat transfer inside the PCM-encapsulating pipe was under-predicted. The under-predicted heat transfer in the simulation slowed down the melting process of the PCM. Larger heat flux peak reductions were predicted as a result.

In smaller pipes, the effect of the natural convection on the heat transfer was not as significant as that in the larger pipes. Consequently, the model performed better in smaller pipe cases. Also, when the temperatures inside the pipes were relatively higher, the natural convection was more pronounced. This is verified in the figures, as the simulated results deviated more from the experimental data in higher temperature experiment. Therefore, it was concluded that the present heat transfer model, including the modified PCM model for RT27 and the “no natural convection” assumption, could be used for the simulation of cases in which the PCM is contained in small space (i.e., small pipe or thin lay with a characteristic length of 14mm - 0.55”- or smaller), where the natural convection is not as pronounced.

6.2 Parametric study

As mentioned in Chapter 4, if the position of the PCM layer in the wall was optimized, the layer method would outperform both the direct mixing and macro-encapsulation method. In addition, the PCM layer method would overcome the

problems associated with macro-encapsulation method and direct mixing method, and make the process of integrating PCM into wall systems more practical. Therefore the PCM layer method is considered for real application. Because the thickness of the PCM layer is small, a parametric study, using the above verified heat transfer model, was conducted to investigate the influence of different factors on the performance of the PCM-enhanced building walls retrofitted with a layer of PCM and find the optimal settings for real application.

The dimensions and properties of the building materials used in the parametric study are shown in Table 6.1. Because the thickness of the PCM layer was small compared with the other two dimensions and the properties of the insulation were assumed to be homogeneous, the heat transfer across the wall could be considered to be one-dimensional, which made the simulation much easier compared with the two-dimensional cases in Section 6.1. A computer program was written in FORTRAN. The mesh size was set as 0.0005 m (0.02 in). The time step was 10 seconds. A backward difference (in time) and a central difference (in space) scheme was used to discretize the heat transfer equation. A tri-diagonal matrix algorithm (TDMA) was applied to solve the algebraic equations. The PCM model for a paraffin-based PCM (RT27) outlined in Chapter 5 was incorporated into the program.

In the simulation, the indoor room air temperature was assumed to be 24^{o}C (75.2^{o}F) and used as the boundary condition for the cold side of the wall. The wall surface temperature changes from the dynamic simulator tests, which were good approximations of the west wall surface temperatures under full weather conditions,

were used as the boundary conditions of the hot side of the wall. In the analysis that follows and in the graphs, $T_{max}=X^{o}C$ means the maximum wall surface temperature in the daily cycle was $X^{o}C$.

In the parametric study, one sixteenth of the thickness of the wall cavity (i.e., 1/16 of the thickness of the insulation) was the minimum change of the location of the PCM layer. In the analysis that follows and in the graphs, "(n/16)L" means the center of the PCM layer was n/16 of the depth of the wall (thickness of the insulation) to the gypsum wall board. Therefore, 0 means the layer was directly next to wallboard.

6.2.1 The influence of the PCM layer locations and indoor air temperatures on the performance of PCM-enhanced insulation – "Layer method"

Figure 6.18 presents the percent reduction in peak heat flux through the wall as a function of changing the location of the PCM layer for several maximum outdoor surface temperatures. The horizontal axis should be interpreted as though the PCM layer were moving from the wallboard towards the outside surface (i.e., the distance between the PCM layer and wall board increasing from 0/16L to 8/16L). For the hotter days with the maximum outside wall surface temperatures of 65 ^{o}C and 70 ^{o}C (149 ^{o}F and 158 ^{o}F) the peak heat flux reductions increased from about 40% when the PCM layer was next to the wallboard to about 62% when the PCM layer was located at a distance of about (3/16)L from the wallboard. Any further distance beyond this point produced percent reductions of less than 62%, which continued to decrease until a value of 20% was reached when the PCM layer was placed in the middle of the wall. For an outdoor surface temperature of 61 ^{o}C (141.8 ^{o}F) the percent reductions

increased from about 37% (PCM layer next to the wallboard) to about 64% at a distance of about (4/16)L from the wallboard. The values dropped until the percent reduction reached approximately 22% at a distance of (1/2)L (middle of the wall cavity). For the lowest outdoor surface temperature of 55 ^{o}C (131 ^{o}F) the maximum percentage in heat flux reduction was approximately 60% that was reached at a distance of about (4/16)L. In summary, there was always a maximum reduction for different situations, even though its position varied from case to case. These results agree with those presented in Chapter 4, where it was discovered that the PCM could not melt (i.e., the latent thermal storage capacity was not used) when the PCM layer was placed closer to the indoor wallboard. As a result, the peak reduction was low. On the other hand, when PCM layers was placed too close to the outdoor environment (hot side), the PCM would experience solidification problems.

The design air temperature for summer air conditioning is usually assumed to be 24 ^{o}C (75.2 ^{o}F) (2005 ASHRAE handbook: Fundamentals). To investigate the influence of the indoor air temperature on the performance of the PCM application, the indoor air temperature was lowered to 22 and 20 ^{o}C (71.6 and 68 ^{o}F). The insulation with a thermal resistance level of 2.29 m^2K/W (R13) and 7 mm (0.28 in PCM layer were used in the simulation. The peak reduction graphs are shown in Figures 6.19 and 6.20.

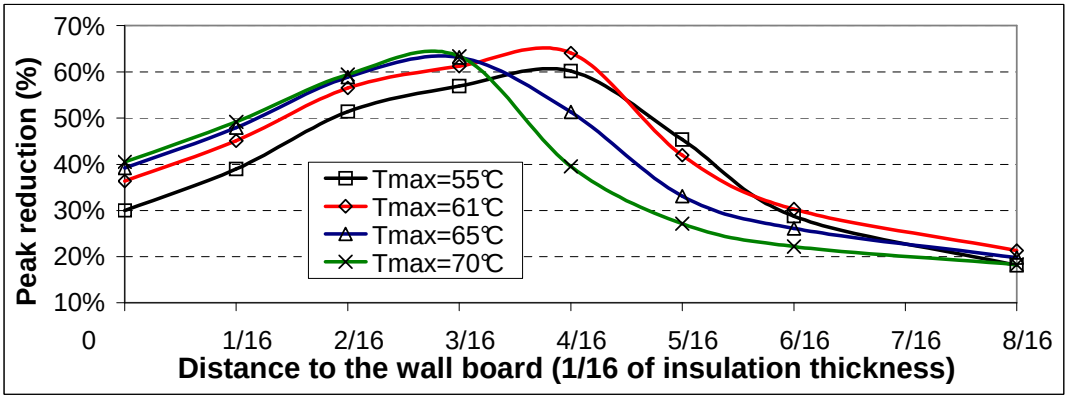

Figure 6.18 Peak heat flux reductions as a function of PCM layer distance from the interior wallboard for an indoor air temperature of 24 ^{o}C (75.2 ^{o}F) for various outdoor surface temperatures.

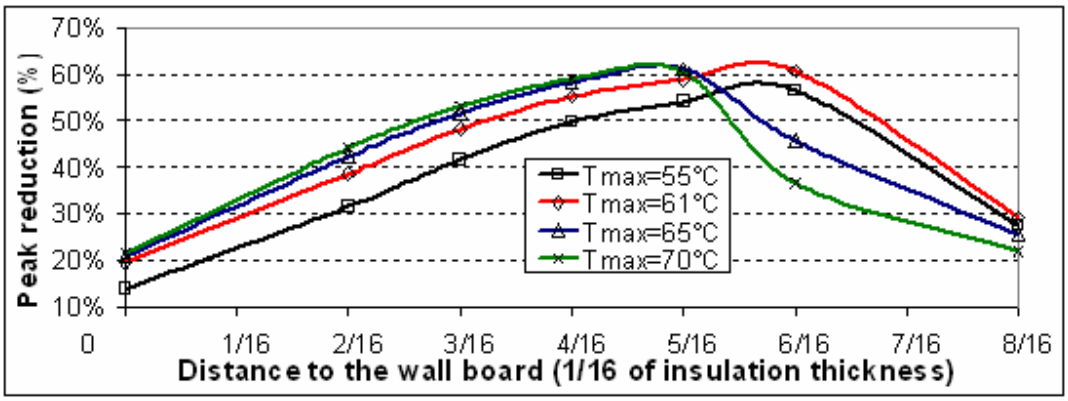

Figure 6.19 Peak heat flux reductions as a function of PCM layer distance from the interior wallboard for an indoor air temperature of 22 ^{o}C (71.6 ^{o}F) for various outdoor surface temperatures.

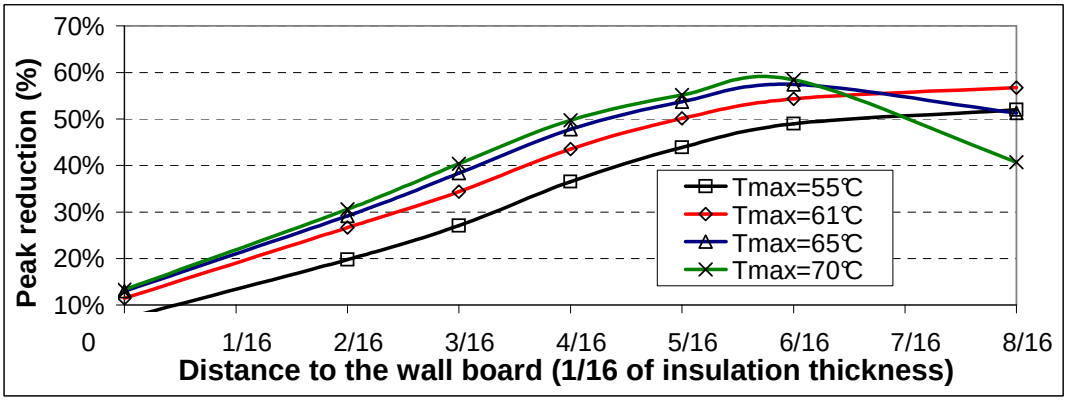

Figure 6.20 Peak heat flux reductions as a function of PCM layer distance from the interior wallboard for an indoor air temperature of 20 ^{o}C (68 ^{o}F) for various outdoor surface temperatures.

The results are explained based on the fact that the decrease in indoor temperature changed the temperature distribution inside the insulation. At lower indoor air temperatures, previous optimum PCM layer locations (as in the 24 ^{o}C/75.2 ^{o}F indoor temperature case) became too cold for the PCM melting temperature; and therefore, the maximum peak heat flux reduction would have to occur farther away from the wallboard (cold side). Furthermore, compared with the 24 ^{o}C (75.2 ^{o}F) case, the maximum peak reductions for the other two cases decreased slightly.

The detailed performances for different PCM layer locations as a function of maximum outdoor surface temperatures are shown in Figure 6.21 to 6.23. For 24 ^{o}C (75.2 ^{o}F) indoor air temperature, only the curves for position (3/16)L and (4/16)L were above the 50% reduction line for all the outside temperature conditions. For 22 ^{o}C (71.6 ^{o}F), only (4/16)L and (5/16)L were above the 50% line. For 20 ^{o}C (68 ^{o}F), only (6/16)L was above the 50% line. With the decrease of the indoor air temperature, the positions for large peak reductions moved towards outside and the width of the

optimal positions became narrow, which meant less tolerance for the deviation of the layer from the designed position in the installation. From the figures, it was found that the reduction values for the above optimal positions also decreased a little bit with lower indoor temperature. Thus, 24 ^{o}C (75.2 ^{o}F) was recommended for the application.

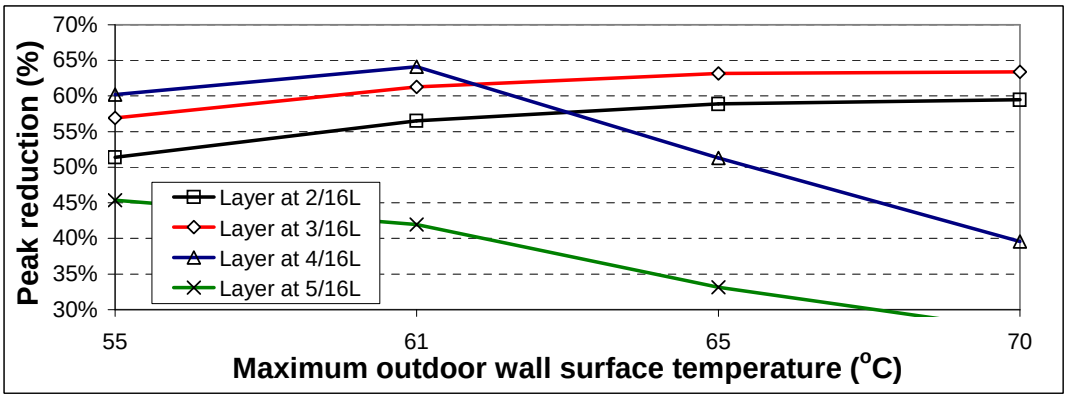

Figure 6.21 Peak heat flux reductions as a function of outdoor surface temperature for an indoor air temperature of 24^{o}C (75.2^{o}F) for various PCM layer locations.

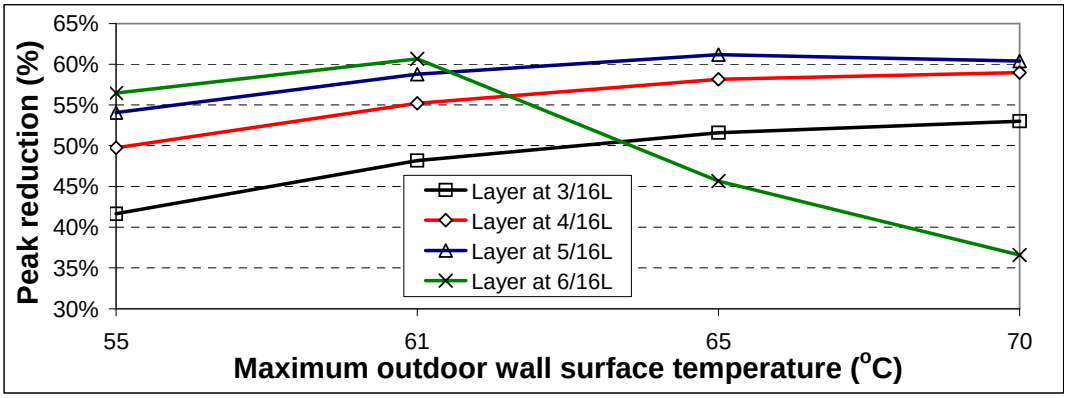

Figure 6.22 Peak heat flux reductions as a function of outdoor surface temperature for an indoor air temperature of 22 ^{o}C (71.6 ^{o}F) for various PCM layer locations

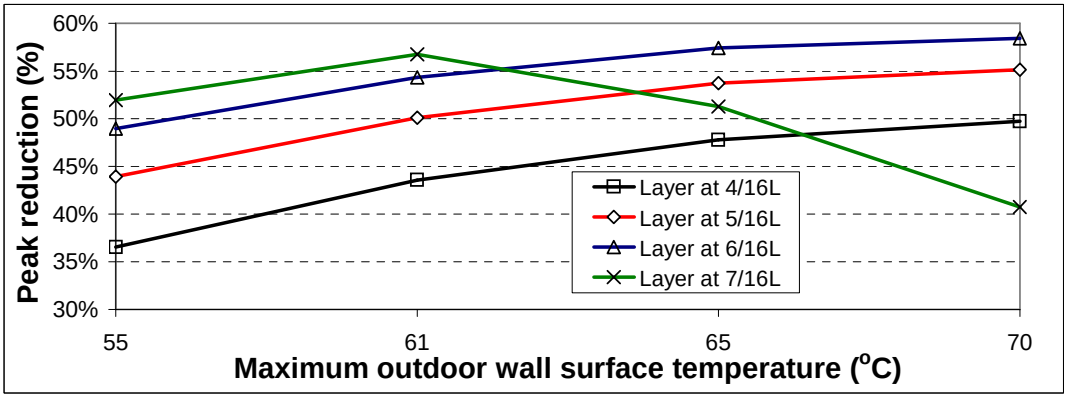

Figure 6.23 Peak heat flux reductions as a function of outdoor surface temperature for an indoor air temperature of 20 °C (68 °F) for various PCM layer locations

6.2.2 The influence of the thermal resistance value of the insulation on the performance of PCM-enhanced insulation – "layer method"

To investigate the influence of the thermal resistance of the insulation on the performance of PCM-enhanced insulation, insulation with thermal resistance values of 2.29 m^2 K/W (R13), 3.35 m^2 K/W (R19) and 6.70 m^2 K/W (R38)(an imaginary insulation material that had twice the thermal resistance of R19 insulation for the same thickness), were considered in the study. The thickness of the PCM layer was 7 mm (0.28in) and the indoor air temperature was 24 °C (75.2 °F). The peak heat flux reduction graphs are shown in Figure 6.24 through 6.26. The results indicate that with the increase in insulation thermal resistance (R-value), the locations for the maximum reduction in heat flux moved slightly towards the outside. This was the case because of the small temperature distribution change along the insulation. The maximum reductions in peak heat flux did not change significantly. The detailed performances for different layer positions under different outdoor surface temperatures are shown in Figures 6.27 through 6.29. For 2.29 m^2 K/W (R13) case, only the (3/16)L and (4/16)L

curves were above the 50% reduction line. For 3.35 m^2 K/W (R19), only the (2/16)L and (3/16)L curves were above the 50% line and the (4/16)L curve was above 50% line for most temperatures. For 6.70 m^2 K/W (R38), the (2/16)L, (3/16)L and (4/16)L curves were all above the 50% line. And as depicted, with the increase in resistance value of the insulation (R-value), the maximum heat flux reduction increased but only slightly. Thus, in conclusion, the larger the resistance value of the insulation (R-value) would widen the range of optimal locations. However, the 6.70 m^2 K/W (R38) insulation is imaginary and not available on the market. In real application, R13 and R19 are the two most commonly used types of wall insulation. As shown in the results, the difference between these two was not large. Thus, it is not necessary to change the local type of wall insulation.

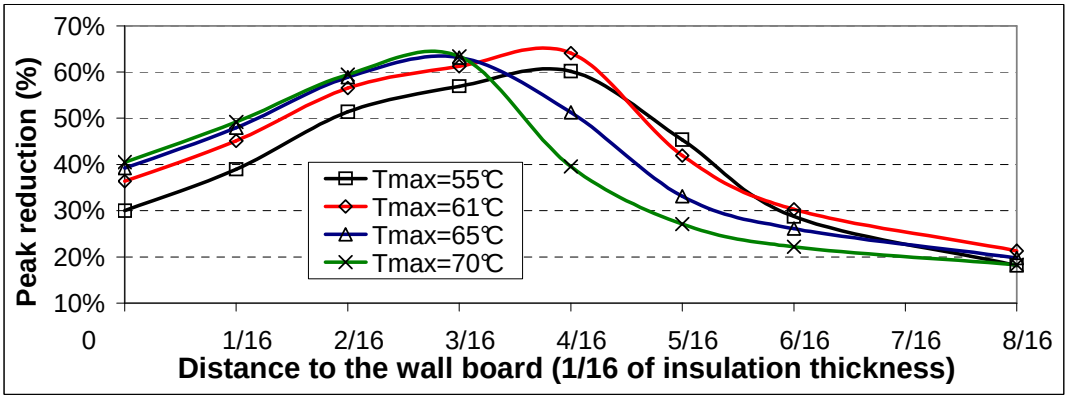

Figure 6.24 Peak heat flux reductions as a function of PCM layer distance from the interior wallboard for an indoor air temperature of 24 ^oC (75.2 ^oF) and insulation level of 2.29 m^2 K/W (R13) for various outdoor surface temperatures.

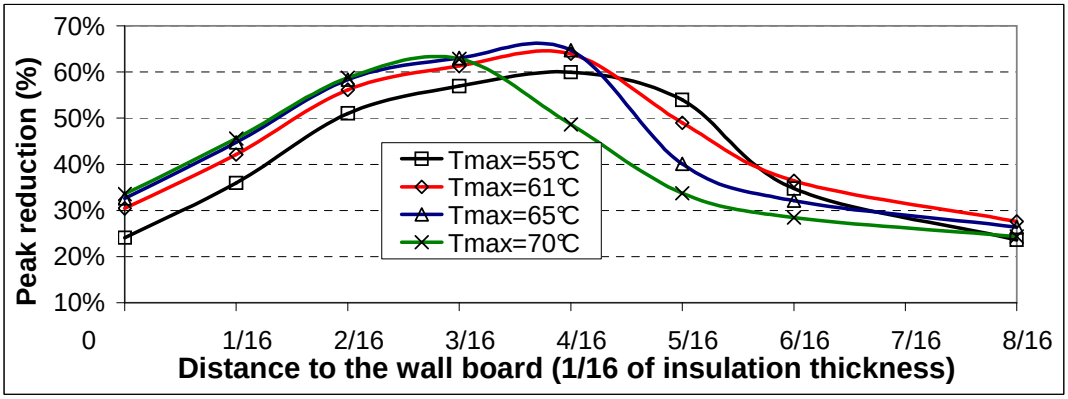

Figure 6.25 Peak heat flux reductions as a function of PCM layer distance from the interior wallboard for an indoor air temperature of 24 ^{o}C (75.2 ^{o}F) and insulation level of 3.35 m^2 K/W (R19) for various outdoor surface temperatures.

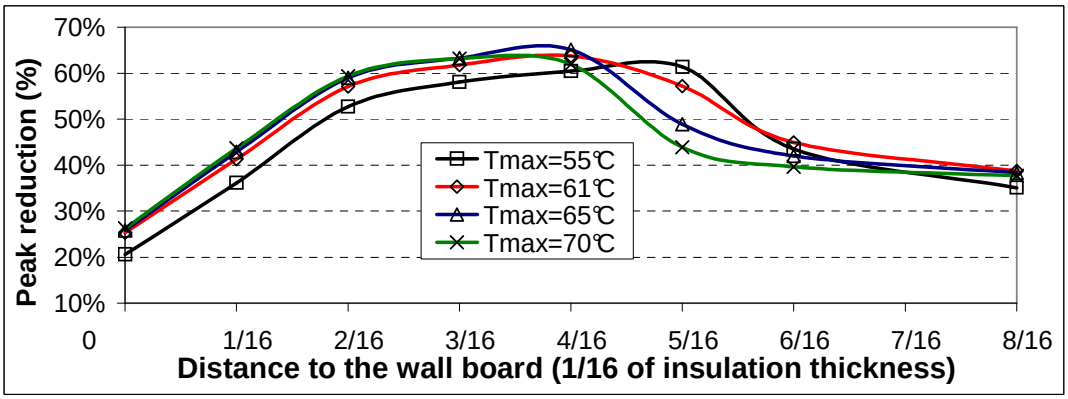

Figure 6.26 Peak heat flux reductions as a function of PCM layer distance from the interior wallboard for an indoor air temperature of 24 ^{o}C (75.2 ^{o}F) and insulation level of 6.70 m^2 K/W (R38) for various outdoor surface temperatures.

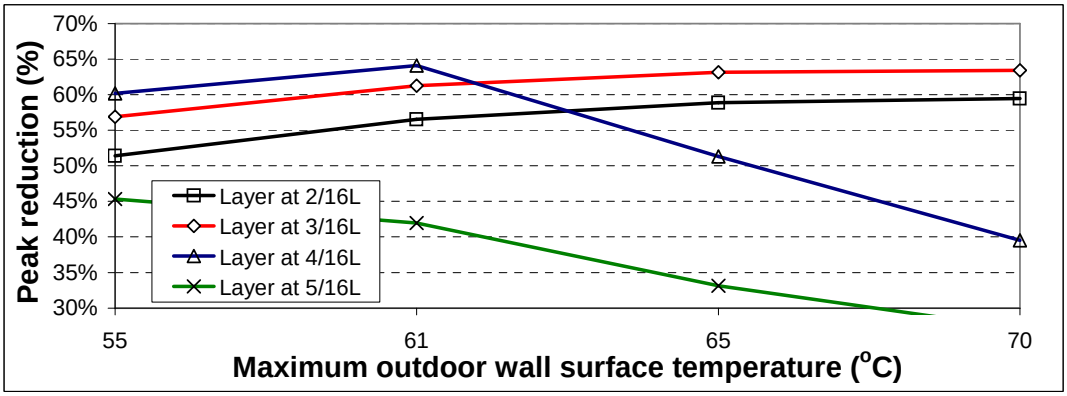

Figure 6.27 Peak heat flux reductions as a function of outdoor surface temperature for an indoor air temperature of 24 °C (75.2 °F) and insulation level of 2.29 m^2 K/W (R13) for various PCM layer locations.

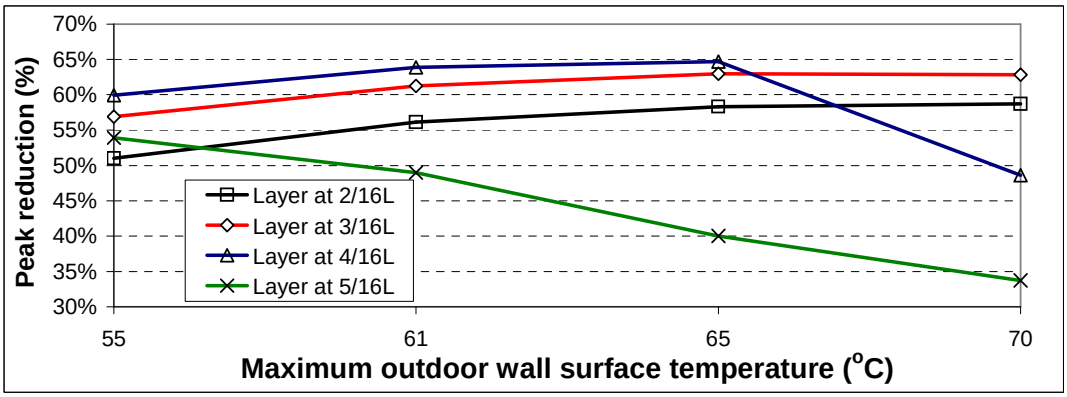

Figure 6.28 Peak heat flux reductions as a function of outdoor surface temperature for an indoor air temperature of 24 °C (75.2 °F) and insulation level of 3.35 m^2 K/W (R19) for various PCM layer locations.

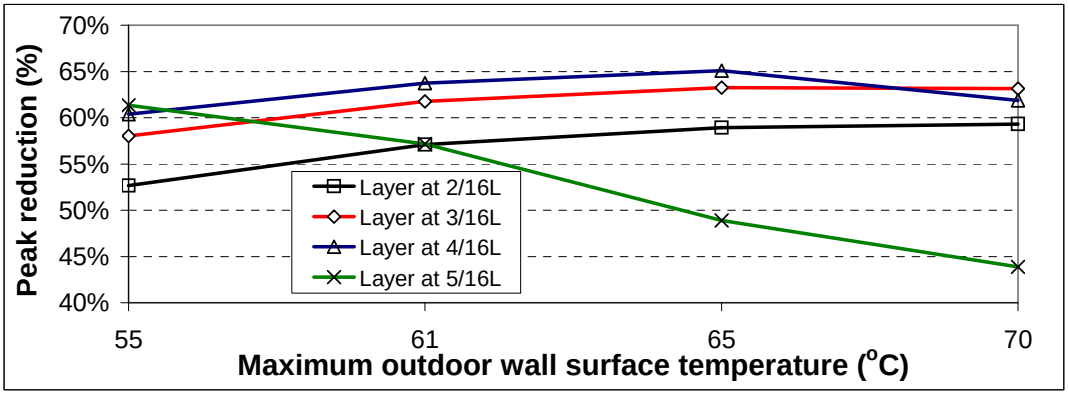

Figure 6.29 Peak heat flux reductions as a function of outdoor surface temperature for an indoor air temperature of 24 °C (75.2 °F) and insulation level of 6.70 m^2 K/W (R38) for various PCM layer locations.

6.2.3 PCM layer thickness influence on the performance of PCM-enhanced insulation – "Layer method"

To investigate the influence of the thickness of the PCM layer on the performance of PCM-enhanced insulation, 3 mm (0.12 in), 7 mm (0.28 in) and 10 mm (0.39 in) thick PCM layers were considered in the study. 2.29 m^2 K/W (R13) insulation and 24°C (75.2°F) indoor air temperature were used in the simulation. The peak reduction curves are shown in Figures 6.30 through 6.32. As shown, the maximum peak heat flux locations for the 3 mm (0.12 in) case were closer to the cold side than those for the 7 mm (0.28 in) and 10 mm (0.39 in) cases. The maximum peak reduction value for the 3 mm (0.12 in) case was lower than those of the 7 mm (0.28 in) and 10 mm (0.39 in) cases.

The detailed performances for different layer positions under different weather conditions are shown in Figures 6.33 through 6.35. For the 3-mm (0.12 in) layer case, no curve was entirely above 50% reduction. Only the (2/16)L and (3/16)L

curves were close to 50%. The (2/16)L location did not perform well in the low temperature range and the (3/16)L did not perform well in high temperature range. For the 7 mm (0.28 in) layer, the (2/16)L and the (3/16)L curves were above the 50% line. For the 10 mm (0.39 in) layer thickness, the (2/16)L and the (3/16)L curves were above the 50% line. The peak heat flux reduction values for the 3 mm (0.12 in) layer were lower than those of the 7 mm (0.28 in) and 10mm (0.39 in) cases. As expected, thicker PCM layers provided more latent thermal storage capacity for the hot days. In cool days, the unmelted PCM in the thick layer during the day would not become a burden on the solidification process. Thus, a thick PCM layer would be desirable for the application. However, when thermal storage capacity of the PCM layer is enough for a hot day, the benefit from the growth of thickness was limited. As shown in the figures, the performances of the 7 mm (0.28 in) and 10 mm (0.39 in) cases were close to each other. Thicker PCM layers would make the PCM-enhanced insulation less flexible and more PCM would be needed. Thus, 7 mm (0.28 in) would be recommended for real applications.

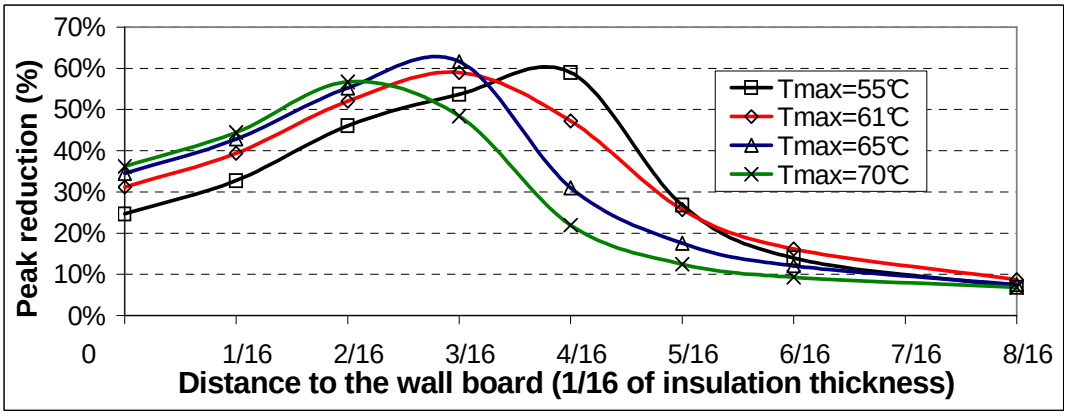

Figure 6.30 Peak heat flux reductions as a function of PCM layer distance from the interior wallboard for 3 mm (0.12 in) PCM layer, an indoor air temperature of 24 ^{o}C (75.2 ^{o}F) and insulation level of 2.29 m^{2} K/W (R13) for various outdoor surface temperatures.

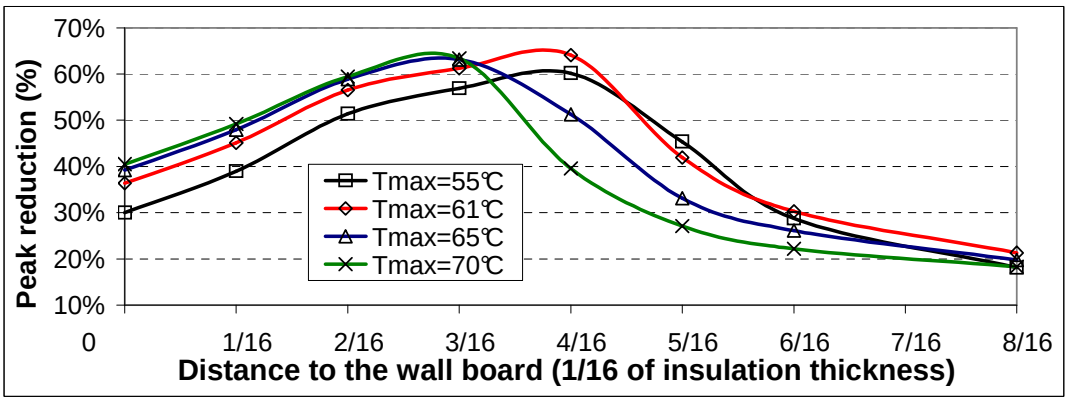

Figure 6.31 Peak heat flux reductions as a function of PCM layer distance from the interior wallboard for 7 mm (0.28 in) PCM layer, an indoor air temperature of 24 ^{o}C (75.2 ^{o}F) and insulation level of 2.29 m^{2} K/W (R13) for various outdoor surface temperatures.

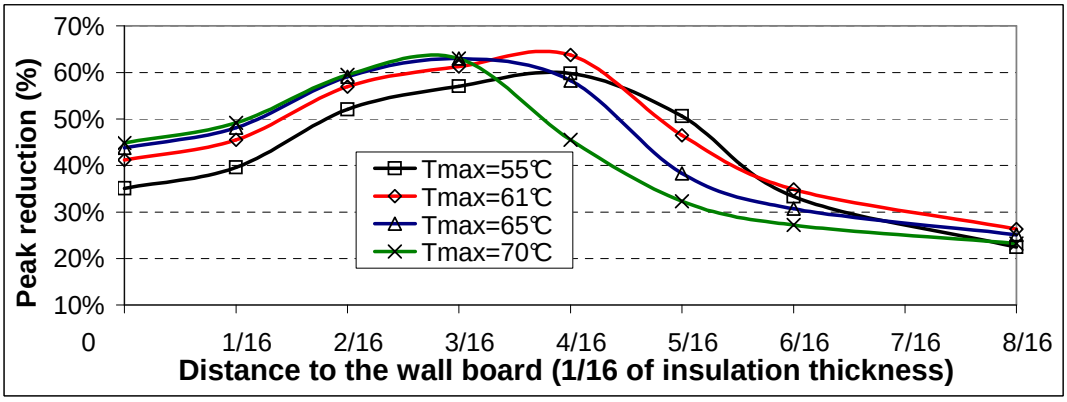

Figure 6.32 Peak heat flux reductions as a function of PCM layer distance from the interior wallboard for 10 mm (0.39 in) PCM layer, an indoor air temperature of 24 ^{o}C (75.2 ^{o}F) and insulation level of 2.29 m^{2} K/W (R13) for various outdoor surface temperatures.

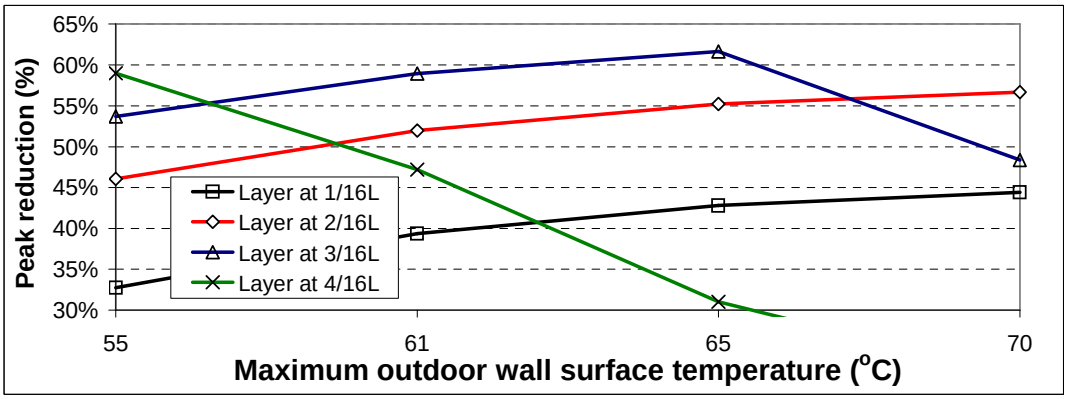

Figure 6.33 Peak heat flux reductions as a function of outdoor surface temperature for 3 mm (0.12 in) PCM layer, an indoor air temperature of 24 ^{o}C (75.2 ^{o}F) and insulation level of 2.29 m^{2} K/W (R13) for various PCM layer locations.

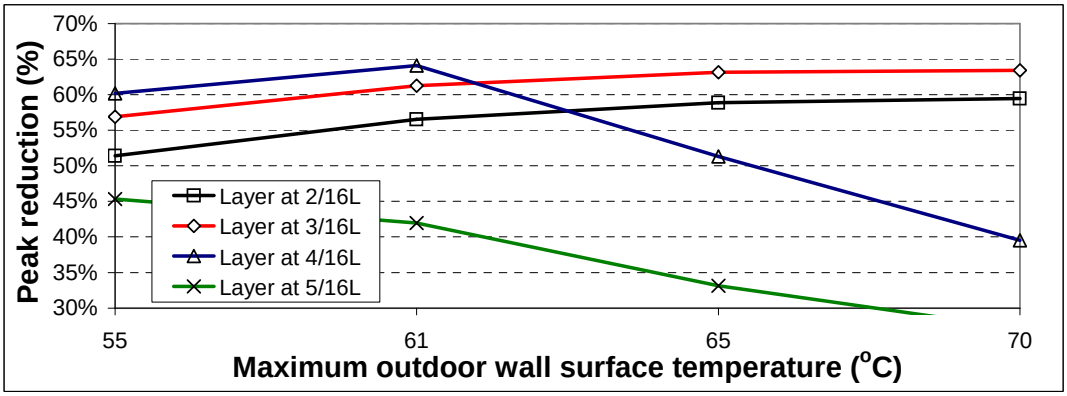

Figure 6.34 Peak heat flux reductions as a function of outdoor surface temperature for 7 mm (0.28 in) layer, an indoor air temperature of 24 °C (75.2 °F) and insulation level of 2.29 m^2 K/W (R13) for various PCM layer locations.

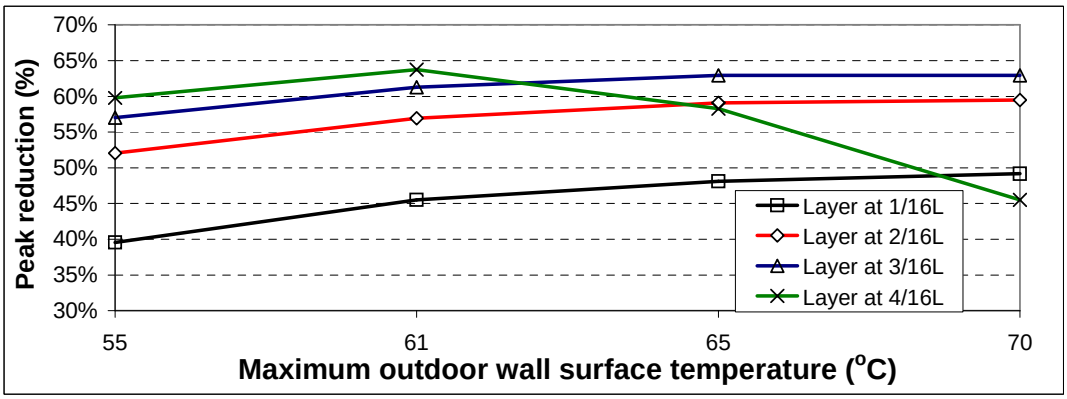

Figure 6.35 Peak heat flux reductions as a function of outdoor surface temperature for 10 mm (0.39 in) layer, an indoor air temperature of 24 °C (75.2 °F) and insulation level of 2.29 m^2 K/W (R13) for various PCM layer locations.

6.2.4 PCM phase change temperature on the performance of PCM-enhanced insulation – "Layer method"

For comparison, the shape of the effective Cp' curve, obtained in Chapter 5, was used for different phase change temperature cases. The maximum peak heat flux reductions for several PCM layer thicknesses and phase change temperatures were

studied. 2.29 m^2 K/W (R13) insulation, 70 ^oC (158 ^oF) maximum outside surface temperature, and 24 ^oC (75.2 ^oF) indoor air temperature were set constant for the simulation. The results are shown in Figure 6.36. For all PCM layer thicknesses, the maximum peak heat flux reductions decreased with increasing phase change temperature, except between 27 ^oC and 31 ^oC (80.6 ^oF and 87.8 ^oF). Based on these results, it appears that the phase change temperature of the PCM should be under 31^oC (87.8^oF).

Maximum peak heat flux reductions for a PCM layer thickness of 3 mm (0.12 in) were lower than those for the other three thickness cases. Therefore, for larger peak heat flux reductions, a thicker PCM layer should be used. From Figure 6.36, it was found that the heat flux reductions of the 7 mm and the 10 mm (0.28 in and 0.39 in) layers were very close. This suggests that beyond a certain thickness, say 7 mm (0.28 in), the benefit from the growth of thickness was limited. A similar trend had been observed in section 6.2.3.

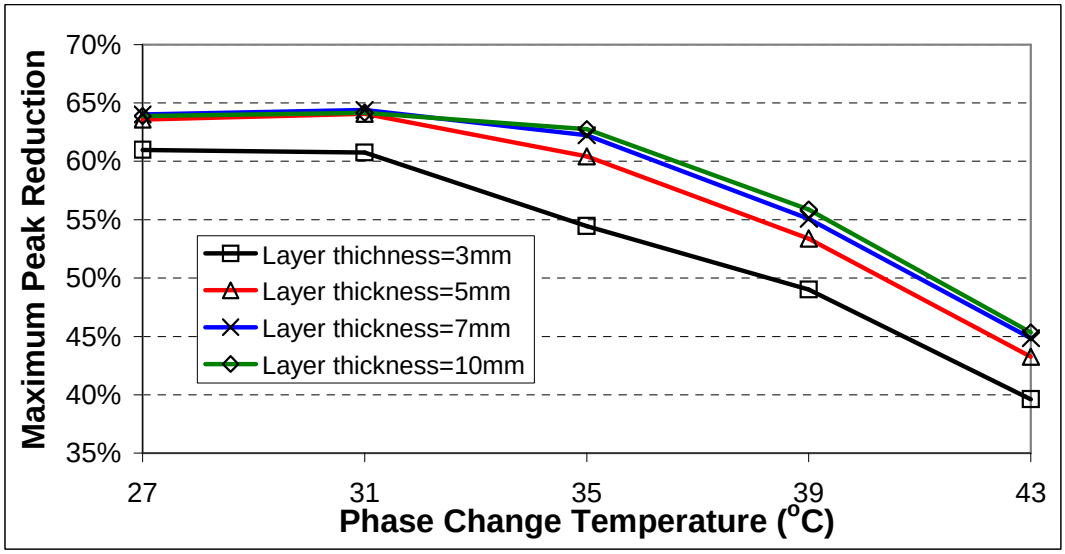

Figure 6.36 Maximum peak heat flux reductions as a function of PCM phase change temperature for several PCM layer thickness and maximum outdoor surface temperature of 70 ^{o}C(158 ^{o}F)

6.3 The performance of the PCM-enhanced building wall under several climates

The research above was based on the weather conditions for Lawrence, Kansas, U.S.. PCM-enhanced insulation's performance in different climate zones is important to the overall evaluation of this technology. The performance of the PCM-enhanced building wall retrofitted with layer method, using the optimal settings obtained from the parametric study, was investigated with numerical simulation.

Based on the parametric study results, the thickness of the layer was assumed to be 7 mm (0.28 in), the center of which was located (3/16)L from the interior wallboard. The indoor air temperature was assumed to be 24 ^{o}C (75.2 ^{o}F).

The one-dimensional heat transfer model used here was the same as the one outlined in Section 6.2. Unlike the parametric study, where the outdoor surface

temperature was used in the simulation, in this case the radiation incident on the exterior wall and the outside air temperature were coupled as the boundary condition of the outdoor side of the wall. The convective heat transfer coefficient of the exterior wall was calculated using published correlations (Yazdania and Klems, 1994; ASHRAE Handbook: Fundamentals, 1993; Energy Plus Engineering Reference, 2005) based on outside wind speeds and the temperature difference of the wall surface temperature and the outside air temperature.

6.3.1 Model inputs

The inputs to the model were obtained and calculated from Typical Meteorological Year 2 (TMY2) data. TMY2 data was derived from the National Solar Radiation Data Base (NSRDB) 1961-1990 by the National Renewable Energy Laboratory's Analytic Studies Division (William Marion and Ken Urban, 1995). The database includes a total of 239 locations across USA. The weather data, for example, outdoor air try bulb temperature, wet bulb temperature, direct normal radiation, diffuse radiation, wind speed and wind direction, are available hourly for the 8760 hours in a year.

6.3.1.1 Air temperature, wind speed, and wind direction

For the meteorological data like air temperature and wind speed, the hourly values are readily available from the database. Because the time step in the simulation program was 10 seconds, the climate data of air temperature and wind speed used in

the simulation were estimated using linear interpolation. For the wind direction; however, no interpolation was necessary because of the low variation of the dominant wind direction. For wind direction, hourly values were used.

6.3.1.2 Solar radiation incident on the outer walls

The solar radiation incident on vertical walls was not available from TMY2 data files. Therefore, this variable was calculated as follows (detailed derivation is available in [Duffie and Beckman, 1991]):

1) Get the direct and diffuse radiation data

The direct normal radiation and diffuse horizontal solar radiation were obtained directly from TMY data.

2) Calculate the angle of incidence

The angle of incidence, θ, is the angle between the direct radiation on a surface and the normal to that surface. It was calculated by

$$\begin{aligned}\cos\theta = {} & \sin\delta\sin\phi\cos\beta - \sin\delta\cos\phi\sin\beta\cos\gamma \\ & + \cos\delta\cos\phi\cos\beta\cos\omega + \cos\delta\sin\phi\sin\beta\cos\gamma\cos\omega \\ & + \cos\delta\sin\beta\sin\gamma\sin\omega\end{aligned} \qquad (6\text{-}4)$$

where,

δ = declination angle (the angular position of the sun at solar noon with respect to the plane of the equator, north is assumed to be positive, $-23.45^\circ \le \delta \le 23.45^\circ$). The declination angle was calculated by

$$\delta = 23.45 \sin(360 \frac{284 + n}{365}) \quad (6\text{-}5)$$

where

n = day number ($1 \le n \le 365$).

ϕ = local latitude (the angular location north or south of the equator, north is assumed to be positive, $-90^\circ \le \phi \le 90^\circ$).

β = slope (the angle between the plane surface and the horizontal $0 \le \beta \le 180^\circ$ -- if $\beta > 90^\circ$ then it meant that the surface was in a downward facing position).

γ = surface azimuth angle (the deviation of the projection on a horizontal plane of the normal to the surface from the local meridian, south was assumed to be 0^o; north 180^o; east -90^o; west 90^o, $-180^\circ \le \gamma \le 180^\circ$).

ω = hour angle (the angular displacement of the sun east or west of the local meridian due to rotation of earth on its axis at 15^o per hour, morning is assumed to be negative and afternoon positive, solar time 12:00 am is zero).

The Solar time, which is the time based on the apparent angular motion of the sun across the sky and which is different from the local clock time, was calculated using

$$\text{Solar time} = \text{local time} + 4(L_{st} - L_{loc}) + e \quad (6\text{-}6)$$

(The local time in the middle of two hours in the TMY2 data was used in the calculation.)

where

L_{st} = longitude for the standard meridian for the local time zone, ^{o}

L_{loc} = local longitude, ^{o}

e = equation of time, which was calculated by

$$e=9.87\sin 2B-7.53\cos B-1.5\sin B \tag{6-7}$$

where

$$B=\frac{360(n-81)}{364} \tag{6-8}$$

3) Calculate the total solar radiation incident on the wall

The total solar radiation on the wall was calculated by:

$$Rad_{total}=Rad_{direct} \times \cos\theta + Rad_{diffuse} \tag{6-9}$$

where

Rad_{direct} = direct radiation (W/m^2, Btu/hr ft^2)

$Rad_{diffuse}$= diffusive radiation (W/m^2, Btu/hr ft^2)

The hours immediately before the sunset and after sunrise should be paid more attention. In part of the time in those hours, there was no solar radiation, which was not indicated in the TMY2 data. The sunrise and sunset time was calculated for each day and the fraction of sun light time in those hours was obtained. Because the solar radiation values from the TMY2 data were the energy received in that hour, the real average radiation intensity for those periods should be the radiation values from TMY2 data divided by the fraction of sun light time in that hour, which was a smaller

than one number for the sunrise and sunset hours and one for the rest hours. In addition, the time of the angle of incidence calculation was updated.

For several days used in the simulation, the fraction of sun light time in the sunrise or sunset hour was small because the hour was close to the sunrise and sunset time. As a result, the solar radiation calculated using the model was unreasonably large. To solve this problem, a filter was set up to solve this problem: if the fraction of sun light time in the hour was smaller than 0.25 (i.e. the sun light time was shorter than 15 min in that hour), the solar radiation for that hour was omitted. From the study of the data from the days without the above problem, the magnitude of the solar radiation in the above hours was usually small. Thus, this assumption would not introduce large errors to the model.

4) Interpolate the total solar radiation within the hour

In the TMY2 data, the solar data, both direct and diffusive radiation, was the sum of the radiation received in the 60 minutes before the time indicated. That value could be viewed as the averaged radiation intensity within that hour. The radiation incidence on the wall within the hour was obtained by the interpolation of the data in the middle of the hours, as shown in Figure 6.37. As the areas of the two shades, as illustrated in the figure, were the same, the sum of the radiation incidence on the wall in a day would remain the same. For the hours close to sunrise and sunset, some radiation would be lost in the interpolation. Because the values in those two hours were relatively small, no large errors would be introduced.

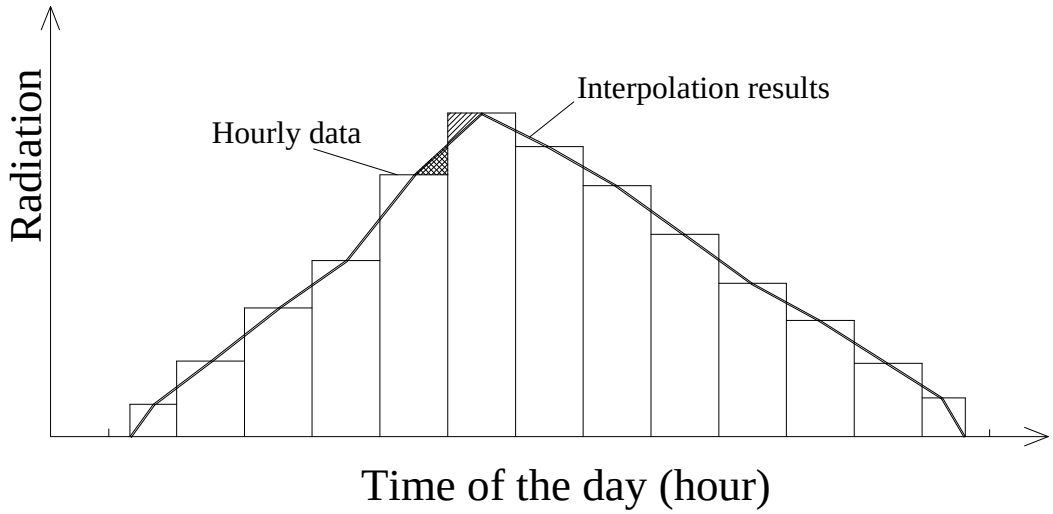

Figure 6.37 Illustration of the interpolation method used for the solar radiation data

6.3.1.3 Exterior wall solar absorptance

From (Siegel and Howell, 1992), the absorptances for incident solar radiation for different building materials were listed as follows: white paint 0.3; light green 0.5; light grey 0.75; black 0.9. For the light color wood siding, a 0.6 value was chosen for the simulation.

6.3.1.4 Exterior wall convective heat transfer coefficient

The MoWitt model (Yazdania and Klems, 1994) was based on the experimental data from Mobile Window Thermal Test (MoWiTT) facility on low-rise buildings under realistic conditions, which is close to the application presented in this research. Also in this model, the definition of wind speed is the 10-meter (32.8 ft) height wind speed, which is readily available from weather data files. In this case, the

problem of the estimating local wind speed from the wind profile can be by-passed. Because the MoWitt model is for window glass, which has a smooth surface, ASHRAE detailed models (1993 ASHRAE Handbook: Fundamentals), which are used in EnergyPlus, was combined to overcome this problem.

In the calculation, the MoWitt model was adopted for the forced convection part. The forced convective heat transfer coefficient was calculated by (Yazdania and Klems, 1994):

$$h_f = aV^b \tag{6-10}$$

The values of a and b are shown in Table 6.2.

Table 6.2 Coefficients in Equation 6-10 (Yazdania and Klems, 1994)

Wind direction	a	b
Windward	2.38	0.89
Leeward	2.86	0.617

The natural convection was calculated by (1993 ASHRAE Handbook: Fundamentals)

$$h_n = 9.482\frac{(|T_{surf} - Tair|)^{1/3}}{7.238 - |\cos\phi|} \quad \text{if heat flow is upward} \tag{6-11a}$$

$$h_n = 1.810\frac{(|T_{surf} - Tair|)^{1/3}}{1.382 + |\cos\phi|} \quad \text{if heat flow is downward} \tag{6-11b}$$

In which

ϕ = the tilt of the surface (rad)

T_{surf} = exterior wall surface temperature (^oC, ^oF)

T_{air} = the outdoor air temperature (^oC, ^oF)

The total convective heat transfer coefficient for smooth surfaces was calculated by (Energy Plus Engineering Reference, 2005):

$$h_{smooth} = \sqrt{h_n^2 + \left[aV^b\right]^2} \tag{6-12}$$

For a rough surface like the wall siding in the present research, the total convective heat transfer coefficient was (Energy Plus Engineering Reference, 2005):

$$h = h_n + R_f\,(h_{smooth} - h_n) \tag{6-13}$$

where,

h_n = Natural convection heat transfer coefficient ($W/(m^2 \cdot K)$, $BTU/(hr \cdot ft^2 \cdot ^oF)$)
R_f = Surface Roughness Multiplier, which was assumed as 1.67 from Table 6.3

Table 6.3 Surface Roughness Multiplier (Energy Plus Engineering Reference, 2005)

ASHRAE roughness number	Example surfaces with this roughness number	R_f
6.00	Glass, paint on pine	1.00
5.00	Smooth plaster	1.11
4.00	Clear pine	1.13
3.00	Concrete	1.52
2.00	Brick, rough plaster	1.67
1.00	Stucco	2.10

6.3.2 U.S. climate zones and representative cities

Based on analysis of the 4775 National Oceanic and Atmospheric Administration (NOAA) weather sites and statistical analysis of regional information, Briggs els. (2003) developed new climate zones, which was adopted by many organizations including ASHRAE 90.1, ASHRAE 90.2, Building America, and ENERGY STAR.

The map of the U.S. for the climate zone assignment under the classification is shown in Figure 6.38. The detailed information about each climate zone and one representative city are shown in Table 6.4.

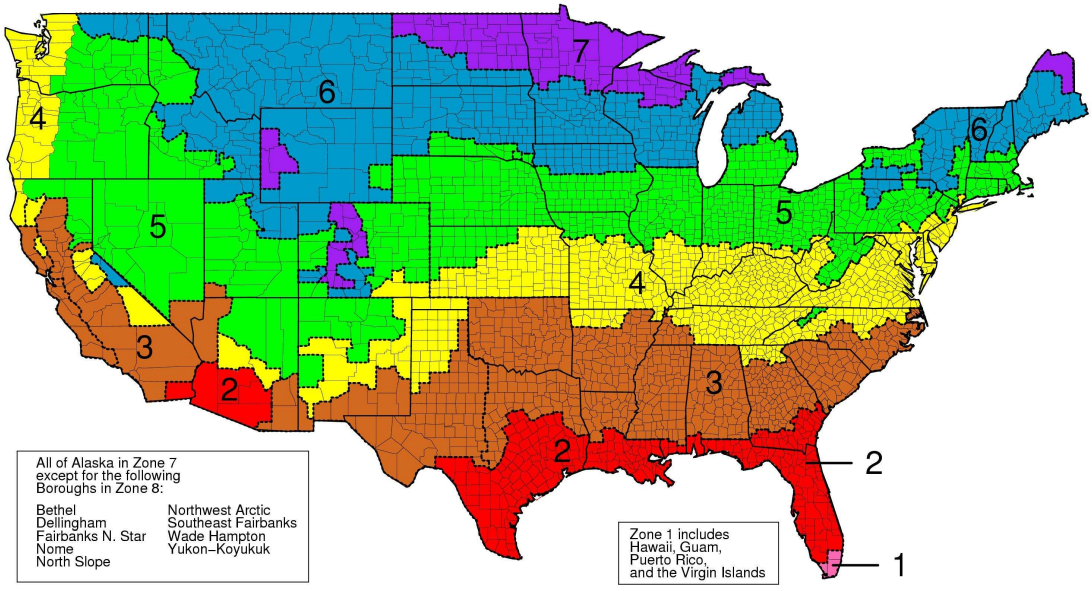

Figure 6.38 Map of the United States showing climate zones

Table 6.4 Climate zones and their representative cities (Briggs els.,2003)

Zone No.	Climate zone name and type	Thermal criteria	Representative U.S. city
1A	Very hot-humid	5000<CDD10°C	Miami, FL
1B	Very hot-dry	5000<CDD10°C	----
2A	Hot-humid	3500<CDD10°C<5000	Houston, TX
2B	Hot-dry	3500<CDD10°C<5000	Phoenix, AZ
3A	Warm-humid	2500<CDD10°C<3500	Memphis, TN
3B	Warm-dry	2500<CDD10°C<3500	El Paso, TX
3C	Warm-marine	HDD18°C>2000	San Francisco, CA
4A	Mixed-humid	CDD10°C<2500 and HDD10°C<3000	Baltimore, MD
4B	Mixed-dry	CDD10°C<2500 and HDD10°C<3000	Albuquerque, NM
4C	Mixed-marine	2000<HDD18°C<3000	Salem, OR
5A	Cool-humid	3000<HDD18°C<4000	Chicago, IL
5B	Cool-dry	3000<HDD18°C<4000	Boise, ID
5C	Cool-marine	3000<HDD18°C<4000	----
6A	Cold-humid	4000<HDD18°C<5000	Burlington, VT
6B	Cold-dry	4000<HDD18°C<5000	Helena, MT
7	Very cold	5000<HDD18°C<7000	Duluth, MN
8	Subarctic	7000<HDD18°C	Fairbanks, AK

Zones 6A, 6B, 7 and 8 have relatively cool summers. Therefore, these were not considered in the simulations. For the same reason, air conditioning is not usually required in zones 3C and 4C. In this research, the performance of PCM wall in those two zones was studied.

According to the International Energy Conservation Code (IECC) 2006, the requirement for the wood frame wall insulation is 2.29 m^2 K/W (R13) for Zones 1A-4B and 3.35 m^2 K/W (R19) for Zones 4C-5C. In the simulation, the correct type of insulation was installed according to the above zone requirement.

6.3.3 Simulation results

Simulations were performed for the representative cities for zones 1A-5C. The two hottest months of the year, July and August, were studied. The last 7 days in June (6/24-6/30) was also calculated in the simulation as "warm up" days for the program.

If radiation heat transfer between the surfaces in the room was neglected, the sum of the heat fluxes of four walls was the total space cooling load through the walls. As mentioned in Chapter 3, the weighs for the four walls could be assumed to be equal for all walls. Then, the sums of the heat fluxes through four walls (wall space cooling load) for different cities were calculated and the complete results are shown in the Figures A.1 to A.33 in the Appendix. The results for Houston are shown in Figures 6.39 to 6.41, as an example.

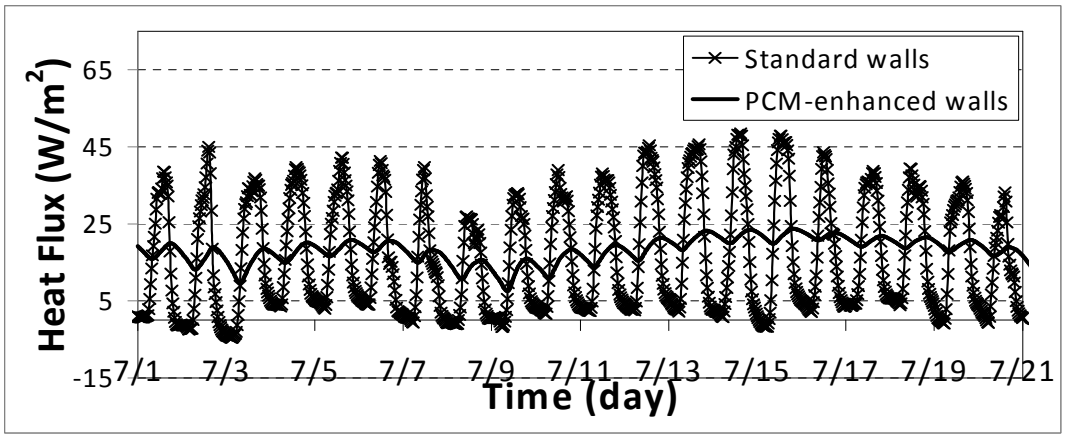

Figure 6.39 Wall space cooling load-7/1-7/21-(Houston 2A)

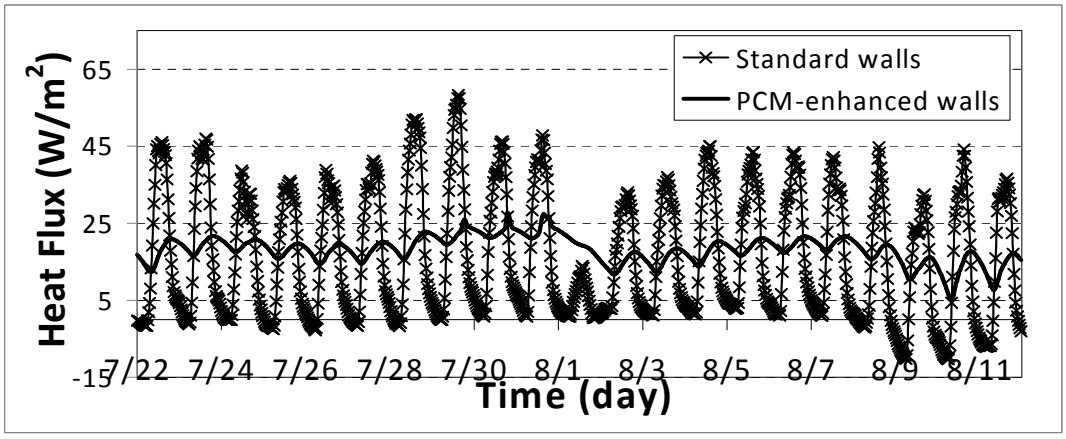

Figure 6.40 Wall space cooling load-7/22-8/11-(Houston 2A)

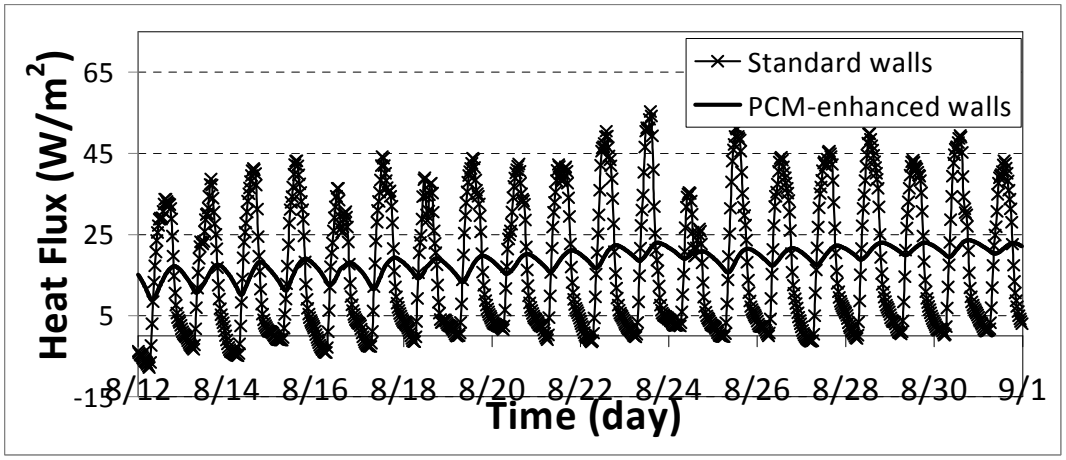

Figure 6.41 Wall space cooling load-8/12-8/31-(Houston 2A)

As shown in every graph, the PCM-enhanced wall retrofitted with PCM layer reduced the peak space cooling load across the walls significantly. The daily heat flux fluctuations of the PCM-enhanced wall were small. This would translate to more constant indoor surface temperatures, which would result in enhanced occupant comfort and longer air conditioning equipment life. For every city, the peak heat fluxes did not vary much from day to day. As a result, for hotter days, which is when the burden on the electric grid is larger, and in some cases problematic, the reductions were relatively larger, which would be a desirable feature of this technology. The averaged peak heat flux reductions of the sum of the four walls for the various cities are presented in Figure 6.42.

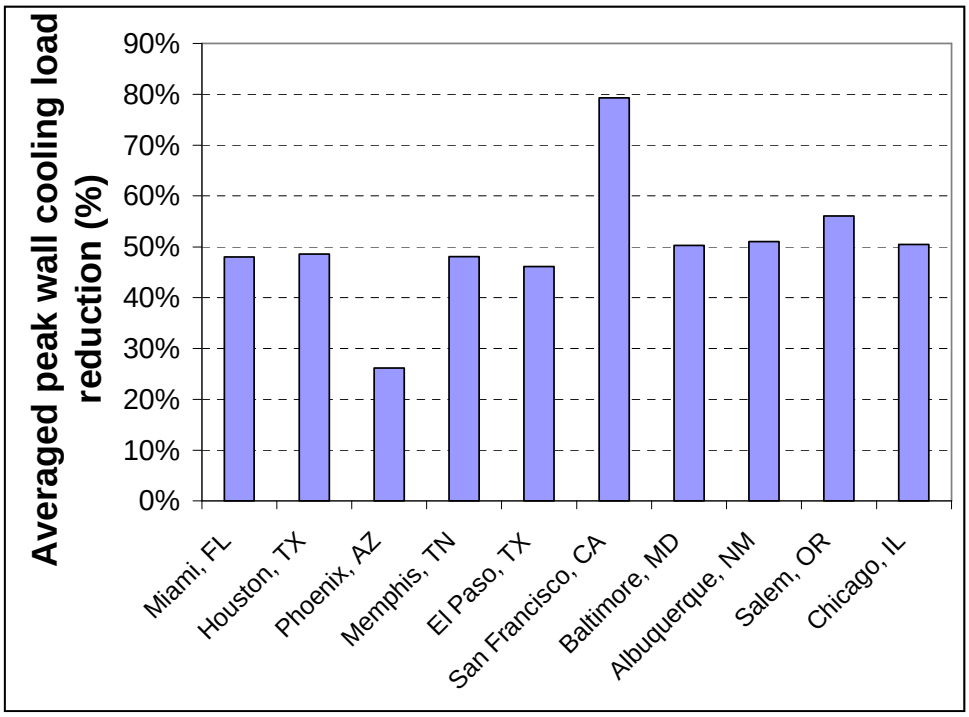

Figure 6.42 Averaged peak heat flux reductions for the various cities in percentages (7 mm (0.28 in), RT27, (3/16)L)

From the Figure 6.42, it was found that the peak reductions for Phoenix, AZ were small. This happened because it is believed that the PCM melted completely in the daytime and the heat fluxes would increase rapidly as shown in Figure 6.43.

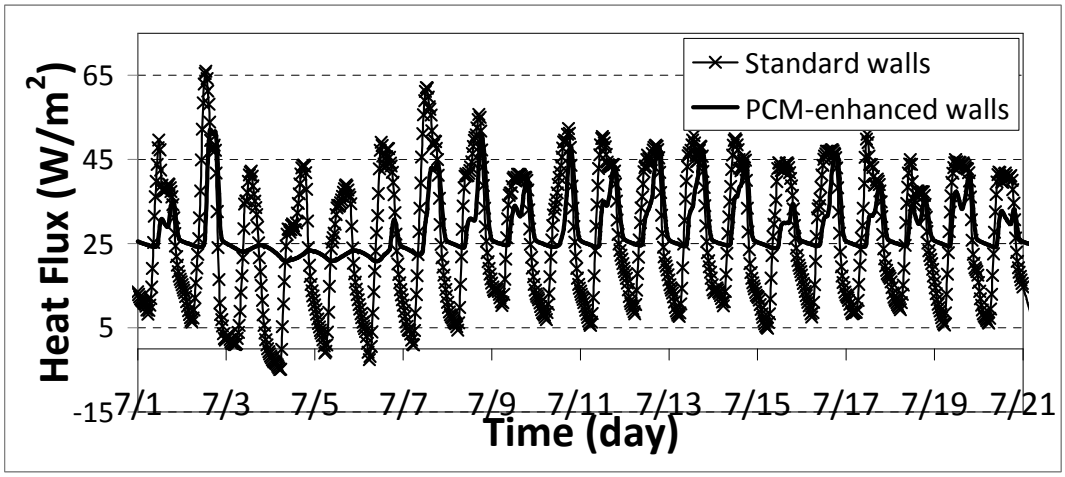

Figure 6.43 Wall space cooling load-7/1-7/21-(Phoenix 2B)

The above problem could be solved by adjusting the location of the PCM layer, moving it towards the wallboard (cold side). For Phoenix, that is, the PCM layer in south and north walls was moved by 5 mm (0.2 in) and the PCM layer in east and west walls was moved by 7 mm (0.28 in). After these modifications, the wall space cooling loads for Phoenix (7/1-7/21) are shown in Figures 6.44. Compared with the graphs of Figures 6.43, the peak reduction performance of the PCM-enhanced walls was improved. The averaged peak heat flux reduction increased from 26.2% to 37.8% and for the eight hottest days (55 W/m^2 (17.4 $BTU/(hr \cdot ft^2)$) or higher) the averaged reduction was 48.1%. Thus, for all the climate zones, the PCM-enhanced wall retrofitted with the layer method could lower the peak space cooling load through the walls by about 50%.

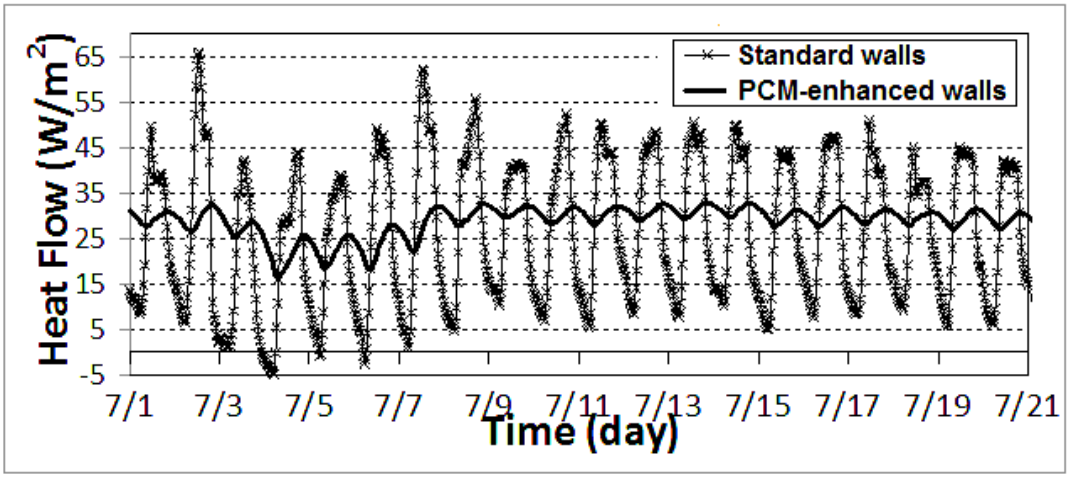

Figure 6.44 Wall space cooling load after layer location adjustion-7/1-7/21-(Phoenix 2B)

6.3.4 Discussion

6.3.4.1 Discussion on the placement of PCM-enhanced insulation in individual wall

As discussed in Section 3.1, the PCM in the PCM-enhanced insulation will not always be helpful in the peak reduction of the sum of the four wall heat fluxes. To see the variations in the sum of the heat fluxes, heat fluxes for the cases with one wall where PCM-enhanced insulation was not installed were calculated and some typical results are shown in Figure 6.45. In the figures, “East w/o PCM”, for example, means that the west, south and north walls were outfitted with PCM-enhanced insulation, but the east wall was not. In the corresponding simulations, the east PCM wall’s simulation results were simply replaced by the values of a standard wall facing east. This procedure was also done for the other three cases. As depicted, when a wall was not outfitted with PCM-enhanced insulation, the peak heat flux across the standard

wall was higher than those of the PCM-enhanced walls. As a result, that wall dominated in the sum and its peak hour became the peak hour of the new sum (e.g., morning for " East w/o PCM" and late afternoon for "West w/o PCM "). From the study of Figure 6.45 and the results for other days, it was found that the peak value for the case when the four walls were all outfitted with PCM-enhanced insulation was always lower than those of the other four cases. When two walls were not outfitted with the PCM-enhanced insulation, the situation would be even worse. Thus, the PCM layer should be installed in all the four walls.

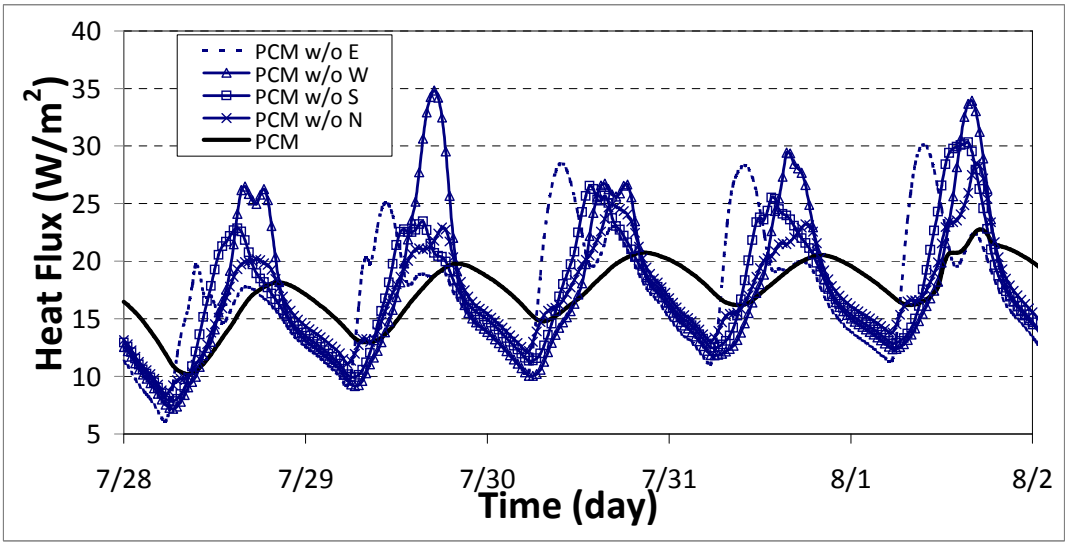

Figure 6.45 Heat fluxes for the cases with one wall not installed with PCM

6.3.4.2 The total heat transferred into the room through walls

As explained in Chapter 3, the application of PCM-enhanced insulation would not reduce the space cooling load on a daily basis. For the representative cities (1A-5B), the total heat transferred into the room through walls in July and August is shown in Figure 6.46. It was found that, except San Francisco, the total seasonal

cooling loads of the PCM walls were always larger than the case where plain insulation was used in the walls. Thus, the previous conclusion was confirmed for different climates.

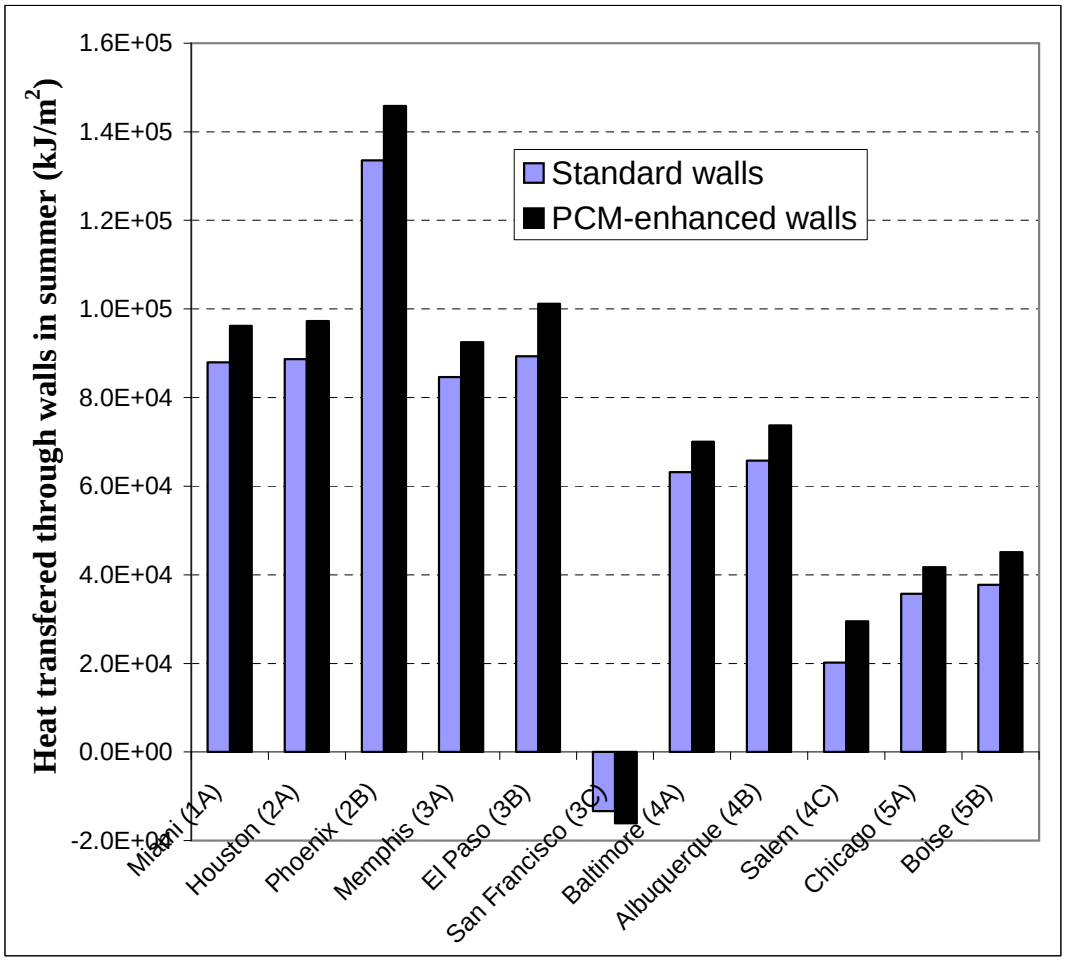

Figure 6.46 The total heat transferred into the conditioned space across the walls in July and August

6.4 Summary

In order to validate the new PCM model developed in Chapter 5, numerical simulation was conducted. The simulation results and the test data showed good

agreement for the 1.27 cm(1/2 in) diameter pipe experiments with PCM pipes in two different locations. The reasons for the difference in the performance for the 1.27 cm(1/2 in) and 1.9 cm (3/4 in) pipe experiments were analyzed. The present heat transfer model, including the modified PCM model for RT27 and the "no natural convection" assumption, could be used for the simulation of cases in which the PCM is contained in small spaces (i.e., small pipe or thin lay with a characteristic length of 14mm - 0.55"- or smaller), where the natural convection is not as pronounced.

From the parametric study, it was found that there was always an optimal location for the PCM layer for obtaining a maximum heat flux peak reduction. By comparing the performance of different cases, it was found that there was no need to change the indoor air temperature and the R-value of the insulation for the PCM application. A thicker PCM layer performed better than a thin layer. But after certain thickness, the benefit from the growth of thickness was limited. A 7 mm (0.28 in) layer would be recommended for RT27 PCM and 2.29 m^2 K/W (R13) insulation. With the increase of the phase change temperature, the maximum peak reduction would decrease. The phase change temperature should be under 31 ^oC (87.8 ^oF).

The numerical simulations for different representative cities for different climate zones were conducted. The details about the solar model, convective heat transfer coefficient, and climate zones are presented. The simulation results for the representative cities showed that the 7 mm (0.28 in) thick PCM layer placed at (3/16)L from the wallboard would produce large peak reductions for most climate zone. For the cities that have hot climates, like Phoenix, the PCM layer needed to be

adjusted towards the cold side. For all the climate zones, the PCM-enhanced wall retrofitted with the layer method could lower the peak space cooling load through the walls by about 50%.

Based on the simulation results, it was found that it would be necessary to install the PCM layer in all the walls. By summing up the heat transferred through the four walls in the summer, it was found that the PCM-enhanced wall would increase the total heat transferred in the summer, though the heat flux peaks would be reduced significantly.

Chapter VII

Conclusions and Recommendations

7.1 Conclusions

From the experimental data, the local typical maximum exterior wall surface temperature could be assumed to be 62.3 ^{o}C (144.1 ^{o}F) for the east facing wall, 67.8 ^{o}C (154.0 ^{o}F) for the west wall, 55.9 ^{o}C (132.6 ^{o}F) for the south wall, and 39.5 ^{o}C (103.1 ^{o}F) for the north wall. The typical minimum exterior wall surface temperature for the four walls could be assumed to be 23.6 ^{o}C (74.5 ^{o}F). The temperature change rate for the insulation was low. The influence of PCMs' properties on the phase change process could not be neglected and should be incorporated into the PCM heat transfer modeling for the proposed application.

From Differential Scanning Calorimeter (DSC) tests, the mixing of the PCMs with cellulose insulation did not change the heat of fusion of the PCMs in the mixture significantly. The mixture still showed a capacity to absorb and release heat during the phase change processes.

From the mass change experiments, hydrated salt-based PCMs, both pure hydrated salt (TH29) and hydrated salt mixed with paraffin (SP25), absorbed moisture at about 50% of their weight and lost their heat storage capability in a short time (about eight days in the tests). Paraffin-based PCM, both pure paraffin (RT27) and paraffin SiO_2 powder (PX27), would lose mass by oxidation when exposed to air. For high temperatures (40^{o}C, 104^{o}F), the process would proceed much faster. In one

test, the pure paraffin sample almost completely oxidized in about 20 days. Like the hydrated salt-based PCMs, paraffin-based PCMs would not be suitable to be directly mixed with insulation unless some airtight coating or encapsulation was developed to prevent oxidization.

From the experimental results related to the direct mixing of a concentration of 30% PCM with cellulose insulation, it was found that the PCM-enhanced insulation could reduce the heat peak heat transfer load and shift the load to later parts of the day. On average, the absolute sum peak space cooling load through the walls could be reduced by 21%, which was lower than average of the reductions of the four walls. From analyses of the details, it was found that this was the case because the various walls peaked at different times of the day. Based on the experimental data, it was recommended that the west wall be outfitted with PCM to lower the overall peak as low as possible. In cases when low concentrations of PCM were used, the PCM should not be installed in the east, south, or north walls. When higher concentrations of PCM are used, the PCM-enhanced insulation placed in east, south and north walls may help reduce the total peak heat flux. This was later confirmed by numerical simulations.

A PCM integration method, referred to as the “layer” method, was proposed to overcome problems associated with other integration and PCM holding methods, such as the macro-encapsulation method (via PCM pipes) and the direct mixing method. In addition, the “layer” method would make the application of PCM a practical and economical one.

By studying several case scenarios of PCM-enhanced insulation, the way in which PCMs reduce the peak heat flow was better understood. In the "layer" method and the mixing method, the location of the phase change interface (e.g., where the solid phase and the liquid co-exist) was found to be a key parameter in terms of peak heat flux reduction. It was discovered that during the melting process, the process should proceed as slow as possible to keep the phase change interface away from the cold side of the wall. Contrary to the PCM melting process, the PCM solidification process should proceed as fast as possible.

From the experimental data, it was found that it would be very likely that the PCMs, once integrated into the walls, would 'start' the phase change process from partially-melted states. Incorrect heat absorption/release distributions would overestimate or underestimate the thermal storage capacity of the PCMs and would produce inaccurate temperature predictions. A DSC test method based on the heat of fusion measurement and its detailed steps, used to study the performance of PCMs from partially-melted states, was developed. The results for a paraffin-based PCM (RT27) were analyzed, and based on these data, a modified model for paraffin-based PCM was developed.

A numerical simulation model was created to verify the accuracy of the new PCM model developed as part of this research. A heat transfer model with phase change was developed based on the observations and discoveries mentioned above. The results of the model, when compared with experimental data showed good agreement. This model could be used to simulate the cases in which the PCM was

contained in small spaces (i.e., small pipe or thin layer within the insulation). From parametric studies, it was found that there was always an optimal location for the PCM layer for obtaining a maximum heat flux peak reduction. By comparing the performance of the PCM-enhanced walls, it was found that there was no need to change the indoor air temperature or the R-value of the insulation during the PCM application. A thicker PCM layer performed better than a thin layer. But after certain thickness, the benefit of the larger thickness was limited. A 7-mm (0.28 in) layer of PCM is recommended when using for RT27 PCM and 2.29 m^2 K/W (R13) insulation. With the increase of the phase change temperature, the maximum peak reduction in heat fluxes would decrease. The phase change temperature of the PCM for the application in building walls should be under 31 ^oC (87.8 ^oF).

Numerical simulations for various representative cities for different climate zones were conducted. Details about solar model, convective heat transfer coefficient, and climate zones are presented. The simulation results for the representative cities showed that the 7 mm (0.28 in) thick PCM layer placed at (3/16)L from the wallboard would produce large peak reductions for most climate zones. For the cities located in places with hot climates, such as Phoenix, AZ, the PCM layer would need to be moved towards the colder side of the wall. For all the climate zones, the PCM-enhanced wall retrofitted with the layer method could lower the peak space cooling load through the walls by about 50%.

Based on the simulation results, it was found that it would be recommended to install PCM-enhanced insulation in all the walls. By summing up the heat transferred

through the four walls in the summer, it was found that the PCM-enhanced wall would increase the total heat transferred into the indoor environment during the summer, though the heat flux peaks would be reduced significantly.

7.2 Recommendations for future work

There are several recommendations for future work to further this research:

1. With the improvement of DSC testing technology, the test temperature range should be lowered to a range between 20-24.5 ^{o}C, (68-76.1 ^{o}F) for RT27, which was not tested due to the limitations of present available testing equipment.

2. The PCM integration via the "layer" method should be developed in more detail. The performance of the "layer" method should be tested experimentally, in both the test house and the dynamic simulator.

3. Using the dynamic wall simulator, the performance of the PCM-enhanced wall simulating the temperature changes in the east, south, and north walls should be investigated.

4. For organic phase change materials, like paraffin, some fire retardant formulation should be developed and added to the PCM to prevent fire hazards.

5. Various other phase change materials, especially hydrated salt PCM, with a high latent thermal storage capacity, should be considered in the research.

References

Arampatizis, G. and Assimacopoulos, D.,1998, Numerical modeling of convection-diffusion phase change problems, *Computational Mechanics*, Vol. 21:409-415.

Aziz, A. and Na, T., 1984, Perturbation methods in heat transfer, Hemisphere Publishing Corp, Washington, DC.

ASHRAE, ASHRAE Handbook: Fundamentals, 1993,ASHRAE Inc., Atlanta, GA.

ASHRAE, ASHRAE Handbook: Fundamentals, 2005,ASHRAE Inc., Atlanta, GA.

Banu, D., Feldman, D., Haghighat, F., Paris, J., and Hawes, D., 1998, Energy-storing wallboard: flammability tests, *Journal of Materials in Civil Engineering*, May:98-105.

Benard, C., Body, Y., and Zanoli, A., 1985, Experimental comparison of latent and sensible heat thermal walls, *Solar Energy*, Vol.34, No.6:475-487.

Bradley, R. S. , Shellard, A. D., The Rate of Evaporation of Droplets. III. Vapour Pressures and Rates of Evaporation of Straight-Chain Paraffin Hydrocarbons. Proceedings of the Royal Society of London. Series A, Mathematical and Physical Sciences, 1949

Briggs, R.S., Lucas, R.G., and Taylor, T.; Climate Classification for Building Energy Codes and Standards: Part 1 - Development Process, Technical and Symposium Papers, ASHRAE Winter Meeting, Chicago, IL, January, 2003

Briggs, R.S., Lucas, R.G., and Taylor, T.; Climate Classification for Building Energy Codes and Standards: Part 2 - Zone Definitions, Maps and Comparisons, Technical and Symposium Papers, ASHRAE Winter Meeting, Chicago, IL, January, 2003

Cabeza, L., Castellon, C., Nogues, M, Medrano, M., Leppers, R., and Zubillaga O., 2007, Use of microencapsulated PCM in concrete walls for energy savings, *Energy and Buildings*, Vol. 39:113-119.

Cabeza, L., Roca, J., Nogues, M., Mehling, H., and Hiebler, S., 2005, Long term immersion corrosion tests on metal-PCM pairs used for latent heat storage in the 24 to 29 °C temperature range, *Materials and Corrosion*, Vol. 56, no.1:33-38.

Charach, Ch., Zarmi, Y., and Zemel, A.,1987, New perturbation method for planar phase-change processes with time-dependent boundary conditions, *J. Appl. Phys*. 62:4375-4381

Carslaw, H.S. and Jaeger J.C., 1959, Conduction of Heat in Solids, Oxford University Press, Oxford.

Casella, E. and Giangi M., 2001, An analytical and numerical study of the Stefan problem with convection by means of an enthalpy method, *Mathematical Methods in the Applied Sciences*, Vol. 24:623-639.

Darkwa, K., O'Callaghan, P., and Tetlow, D., 2006, Phase-change drywall in a passive-solar building, *Applied Energy*, 83:425-435

Duffie, J. and Beckman, W., 1980, Solar engineering of thermal process, Wiley-Interscience, New York.

EIA, Residential Energy Consumption Survey 2001, Forms EIA-757-A-C, E and H (http://www.eia.doe.gov/emeu/recs/recs2001/enduse2001/enduse2001.html)

EIA, 2006, International Energy Annual 2005

EIA, 2007, U.S. Carbon Dioxide Emissions from Energy Sources 2006 Flash Estimate

El-Genk, M. S., and Cronenberg, A.W., 1979, Solidification in a semi-infinite region with boundary condition of the second kind: an exact solution, Letters in Heat Mass transfer, 6: 321-327.

EnergyPlus (2007) Engineering Reference, 71-72

Feldman, D., Banu, D., Hawes, D., and Ghanbari, E., 1991, Obtaining an energy storing building material by direct incorporation of an organic phase change material in gypsum wallboard, *Solar Energy Materials*, Vol. 22: 231-242.

Feldman, D. and Banu, D., 1996, DSC analysis for the evaluation of an energy storing wallboard. *Thermochimica Acta*, Vol. 272, January: 243-251.

Freund, M., Cikos, R., Keszthelti, S., and Mozes G., 1982, Paraffin Products. Elsevier Science Publishing Company, Inc.: New York.

Giangi, M., Stella, F., and Kowalewski T., 1999, Phase change problems with free convection: fixed grid numerical simulation, *Computing and Visualization in Science*, Vol. 2, Numbers 2-3 / December: 123-130.

Goodman, T., 1964, Integral methods for nonlinear heat transfer, *Advances in Heat Transfer*, Vol.1:51-122.

Hawlader, M..., Uddin, M., and Zhu, H., 2000, Preparation and evaluation of a novel solar storage material: microencapsulated paraffin, *Int. J. of Solar Energy*, Vol.20:227-238.

Hawlader, M..., Uddin, M., and Khin, M., 2003, Microencapsulated PCM thermal energy storage system, *Applied Energy*, 74:195-202.

Heim, D. and Clarke, J., 2004, Numerical modeling and thermal simulation of PCM–gypsum composites with ESP-r. *Energy and Buildings*. Vol. 36, Issue 8, August: 795-805.

Ismail, K. and Castro, J., 1997, PCM thermal insulation in buildings, *International Journal of Energy Research*, Vol. 21:1281-1296.

Joishi, C., Goswmi, D., and Tomlinson, J., 1992, Solar thermal energy storage in phase change materials, *Proceedings of the 1992 Conference on Solar Energy* (Solar '92), American Solar Energy Society Annual Conference:174.

Kedl, R. and Stovall, T., 1989, Activities in support of the wax-impregnated wallboard concept, Thermal Energy Storage Research Activities Review, U.S. Dept. of Energy, New Orleans, LA, March.

Kośny, J., Yarbrough, D., Miller, W., Petrie, T., Childs, P., Syed, A., and Leuthold D., 2008, PCM-Enhanced Building Envelopes in Current ORNL Research Projects. Oak Ridge National Laboratory website. (http://www.ornl.gov/sci/roofs+walls/AWT/ComputerSimulations/Kosny_PCM%20overviewl.pdf).

Lv, S., Zhu, N., and Feng, G., 2006, Impact of phase change wall room on indoor thermal environment in winter, *Energy and Buildings*, Vol. 38, Issue 1, January:18-24.

Medina, M.A., King, J.B., and Zhang, M., 2008, On the Heat Transfer Rate Reduction of Structural Insulated Panels Outfitted with Phase-change Materials, *Energy - The International Journal*. Vol. 33, Issue 4:667-678.

Medina, M.A., and Stewart, R., Phase-Change Frame Walls (PCFWs) for Peak Demand Reduction, Load Shifting, Energy Conservation and Comfort, *Sixteenth Symposium on Improving Building Systems in Hot and Humid Climates*, December 16-17, 2008, Plano, TX.

Medina, M.A. and Zhu, D., A Comparative Heat Transfer Examination of Structural Insulated Panels (SIPs) With and Without Phase Change Materials (PCMs) Using a Dynamic Wall Simulator, *Sixteenth Symposium on Improving Building Systems in Hot and Humid Climates*, December 16-17, 2008, Plano, TX.

Neeper, D., 2000, Thermal dynamics of wallboard with latent heat storage. *Solar Energy*, Vol. 68, Issue 5: 393-403.

Petrie, T., Childs, K., Childs, P. , Christian, J., and Shramo, D., 1995, A thermal behavior of mixtures of perlite and phase change material in a simulated climate, Insulation Materials, Oak Ridge National Laboratory Technical Report ORNL/M-6639.

Pham, Q., 1985, A fast, unconditionally stable finite–difference scheme for heat conduction with phase change, *Int. J. Heat Mass Transfer*, 28: 2079-2084.

Porisini, F., 1988, Salt hydrates used for latent heat storage: corrosion of metals and reliability of thermal performance, *Solar Energy*, Vol.41, No.2:193-197.

Robert Siegel and John R. Howell, Thermal Radiation Heat Transfer third edition, Hemisphere Publishing Corp., 1992 Washington ,DC

Salyer, I. and Sircar, A., 1990, Phase change materials for heating and cooling of residential buildings and other applications, *Proceedings of the Intersociety Energy Conversion Engineering Conference*, Vol.4:236-243.

Scalat, S., Banu, D., Hawes, D., Paris, J., Haghighata, F., and Feldman D., 1996, Full scale thermal testing of latent heat storage in wallboard, *Solar Energy Material and Solar Cells*, Vol. 44:49-61.

Schossig, P., Henning, H., Gschwander, S., and Haussmann T., 2005, Micro-encapsulated phase change materials integrated into construction materials", *Solar Energy Materials and Solar Cells*, Vol. 89: 297-306.

Song, Y, 1981, On the Solution of heat conduction in a cylindrical body undergoing solidification by the method of singular perturbation, *Journal of Engineering Thermophysics*, 2(4):359-365 (in Chinese).

Stetiu, C. and Feustel, H., 1998, Phase-change wallboard and mechanical night ventilation in commercial buildings. Lawrence Berkeley National Laboratory website.

Telkes, M., 1980, Thermal Storage in Salt-hydrates, Solar Materials Science, Academic Press:337-404

Voller, V. and Prakash C., 1987, A fixed-grid numerical modeling methodology for convection- diffusion mushy region phase-change problems. *Int. J. Heat Mass Transfer*, 30:1709-1720.
William Marion and Ken Urban, 1995, User's Manual for TMY2s, National Renewable Energy Laboratory.

Yao, L. and Prusa, J., 1989, Melting and freezing, *Advances in Heat Transfer*, Vol.19:1-79 .

Yazdanian, M. and Klems, J., 1994, Measurement of exterior convective film coefficient for windows in low rise buildings. *ASHRAE Transactions*: 100(1).

Zhang, M., Medina, M., and King, J., 2005, Development of a thermally enhanced frame wall with phase-change materials for on-peak air conditioning demand reduction and energy savings in residential buildings. *International Journal of Energy Research.* Vol. 29, No. 9: 795-809.

Zhang, M., 2004, Performance evaluation of a phase change frame wall, Master's thesis, Department of Civil, Environmental, and Architectural Engineering, University of Kansas.

Zhu, D., 2005, A comparative heat transfer examination of structural insulated panels (SIPs) with and without phase change materials (PCMs) using a dynamic wall simulator, Master's thesis, Department of Civil, Environmental, and Architectural Engineering, University of Kansas.

Appendix

A. PCM-enhanced wall simulation results for all the representative cities

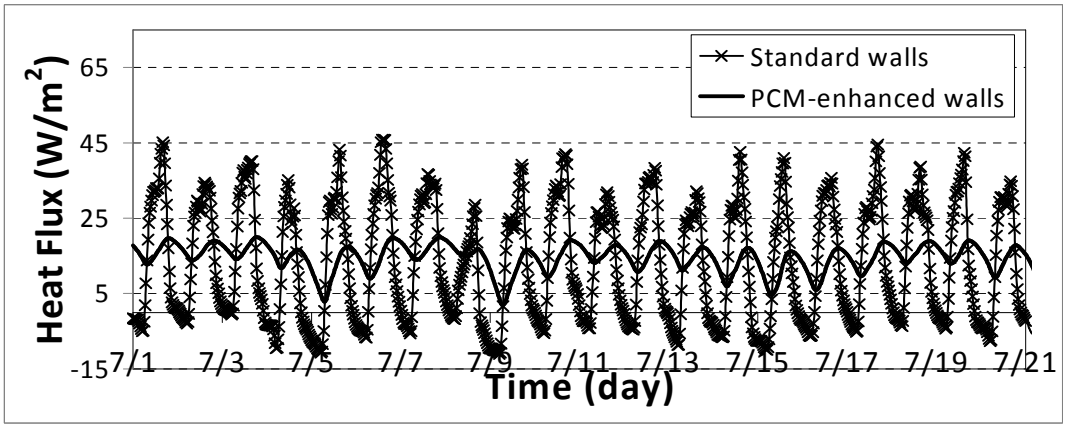

Figure A.1 Wall space cooling load-7/1-7/21-(Miami 1A)

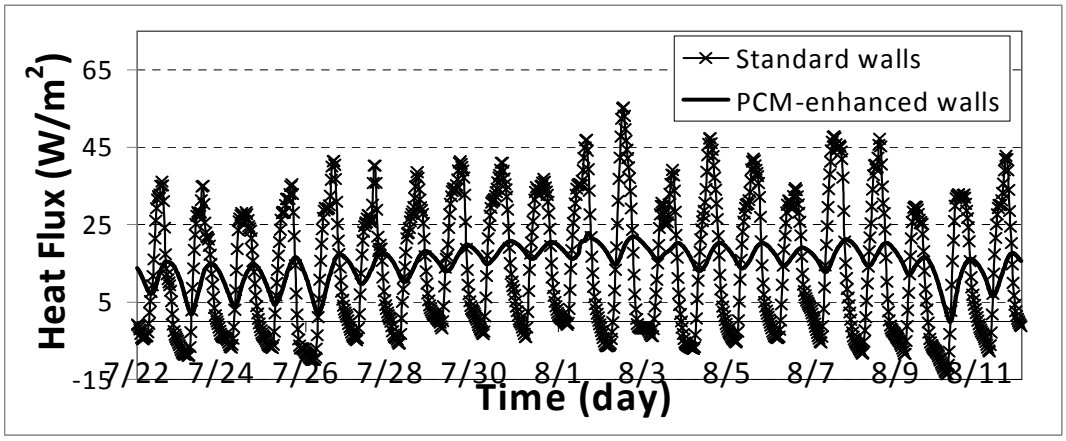

Figure A.2 Wall space cooling load-7/22-8/11-(Miami 1A)

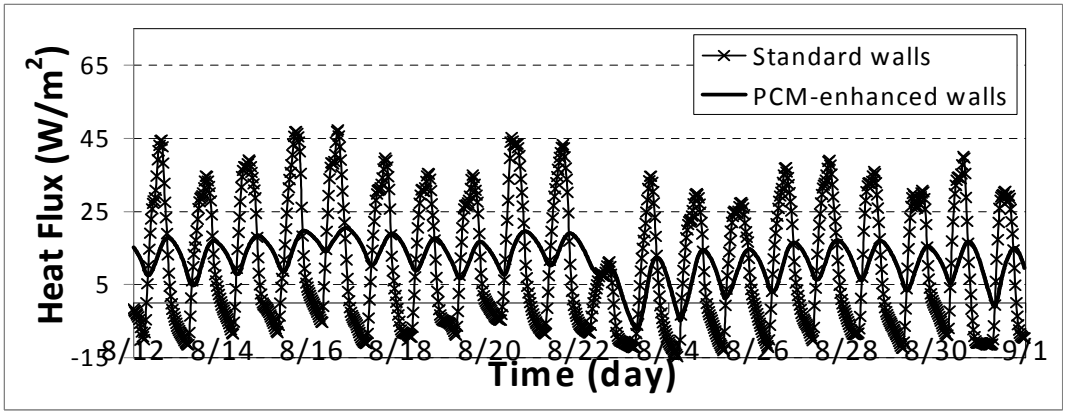

Figure A.3 Wall space cooling load-8/12-8/31-(Miami 1A)

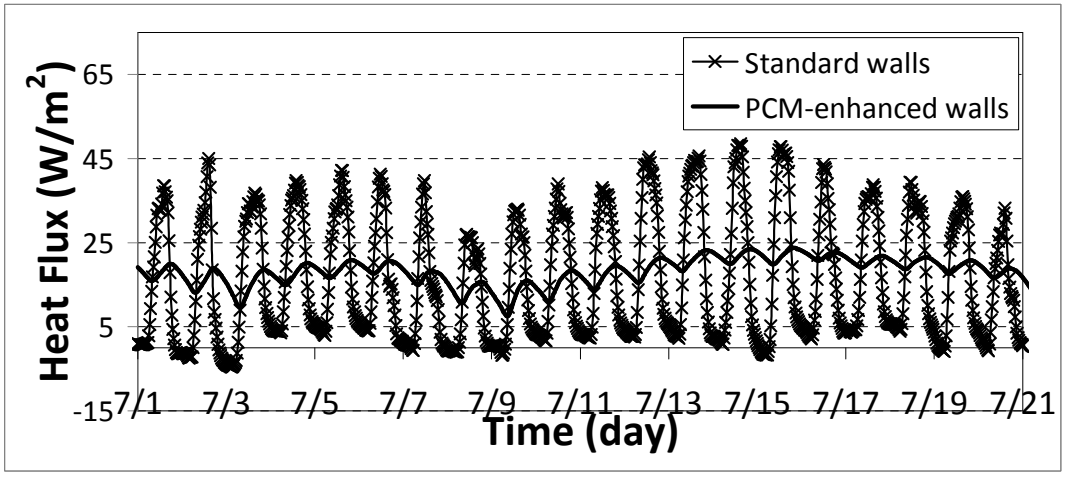

Figure A.4 Wall space cooling load-7/1-7/21-(Houston 2A)

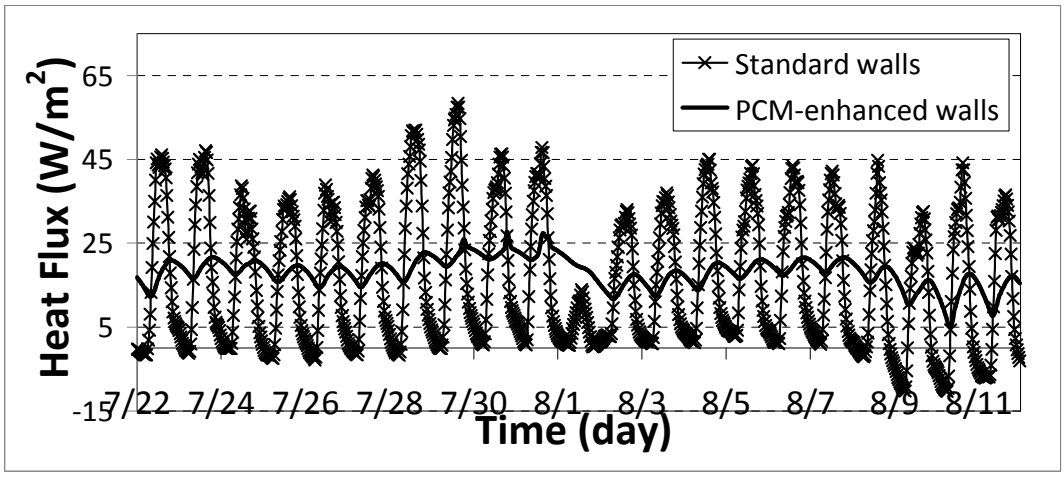

Figure A.5 Wall space cooling load-7/22-8/11-(Houston 2A)

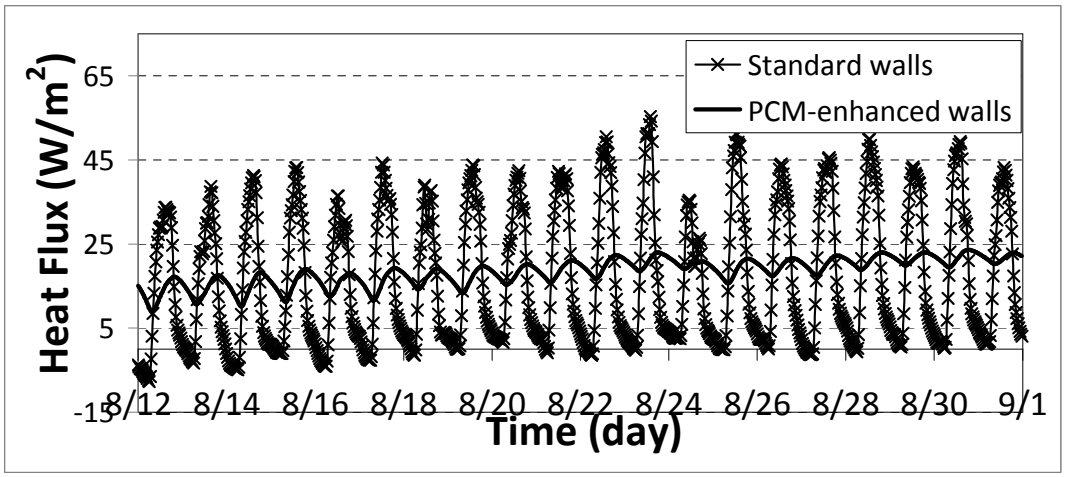

Figure A.6 Wall space cooling load-8/12-8/31-(Houston 2A)

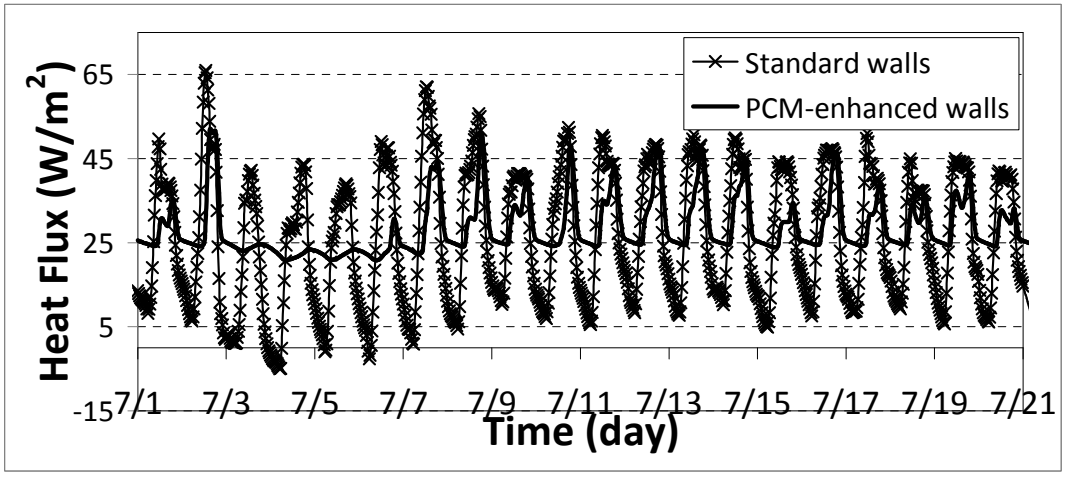

Figure A.7 Wall space cooling load-7/1-7/21-(Phoenix 2B)

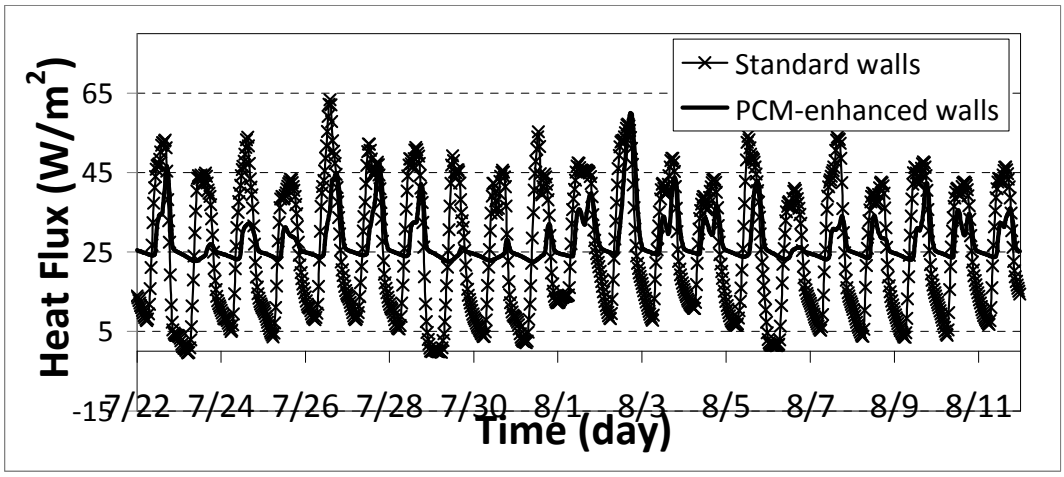

Figure A.8 Wall space cooling load-7/22-8/11-(Phoenix 2B)

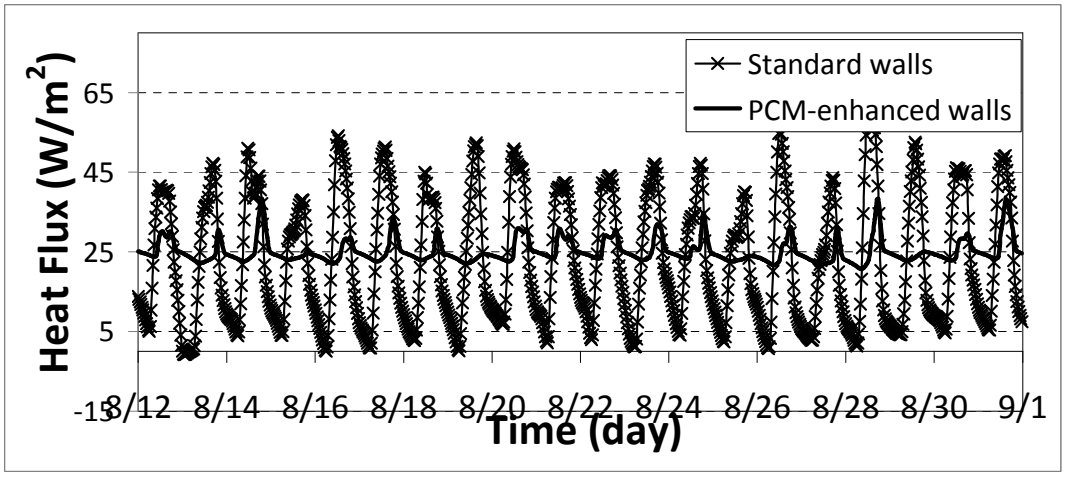

Figure A.9 Wall space cooling load-8/12-8/31-(Phoenix 2B)

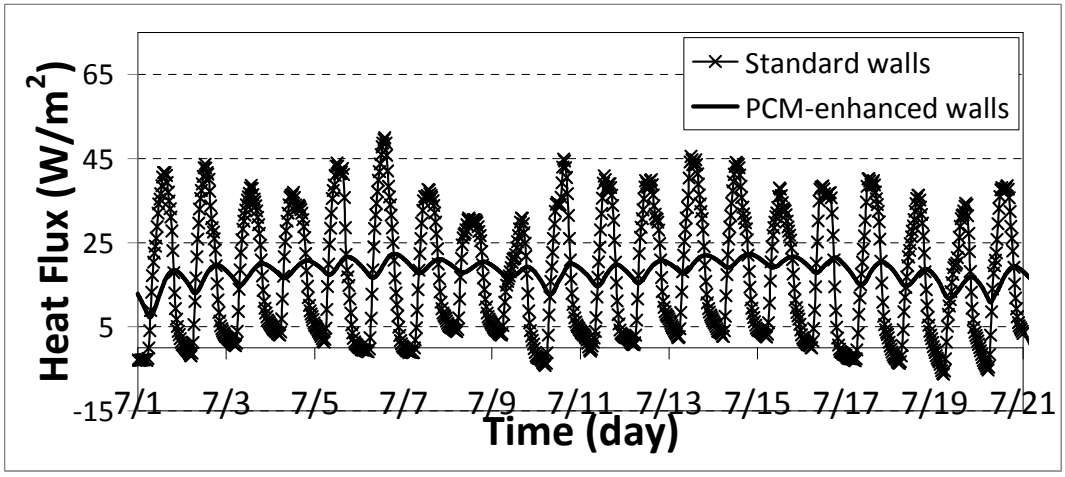

Figure A.10 Wall space cooling load-7/1-7/21-(Memphis 3A)

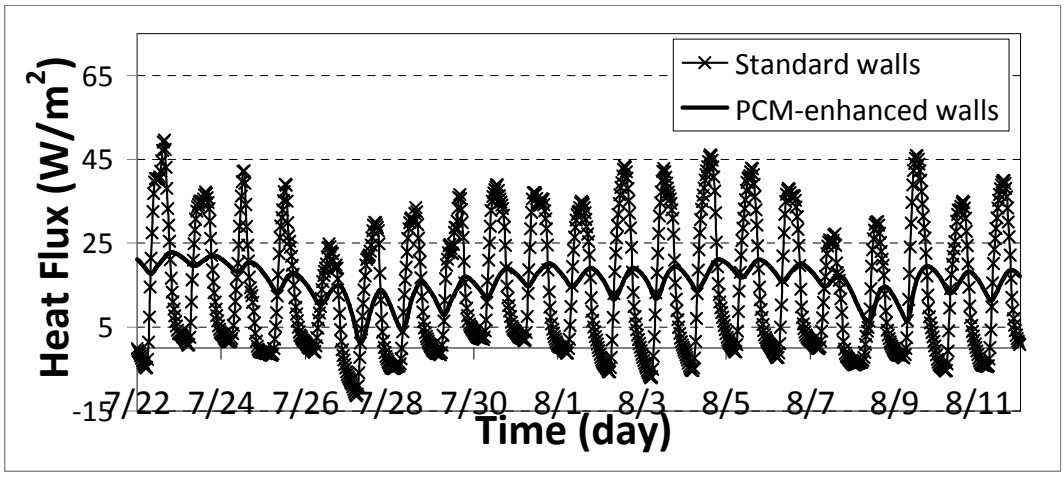

Figure A.11 Wall space cooling load-7/22-8/11-(Memphis 3A)

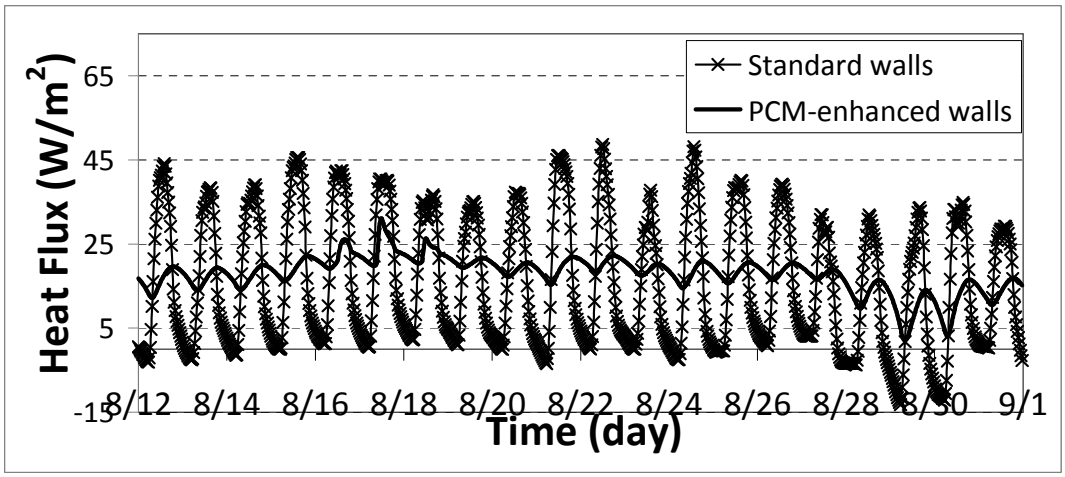

Figure A.12 Wall space cooling load-8/12-8/31-(Memphis 3A)

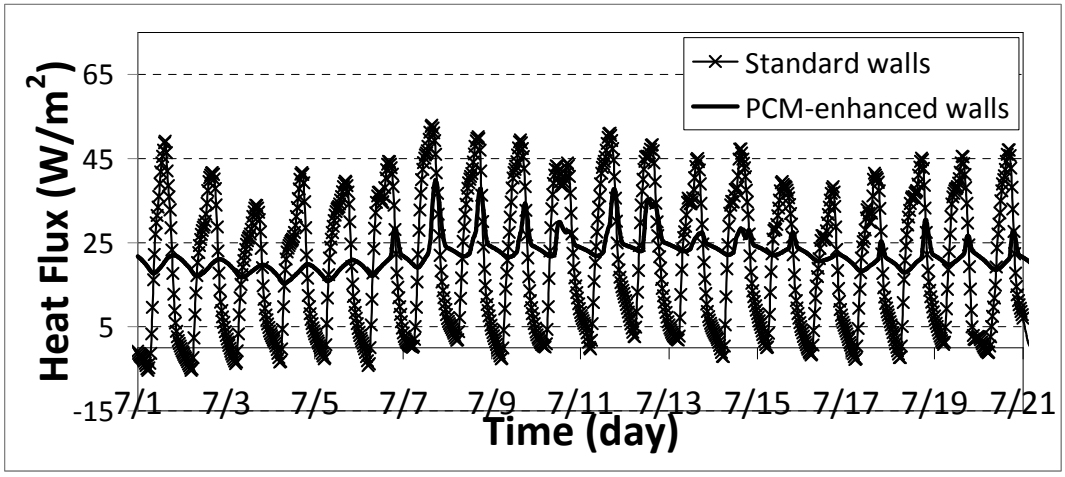

Figure A.13 Wall space cooling load-7/1-7/21-(El Paso 3B)

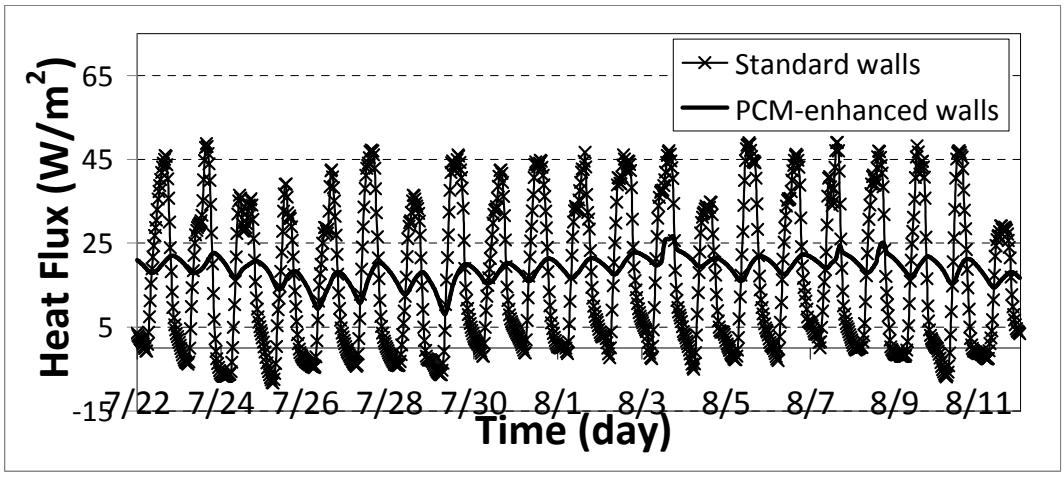

Figure A.14 Wall space cooling load-7/22-8/11-(El Paso 3B)

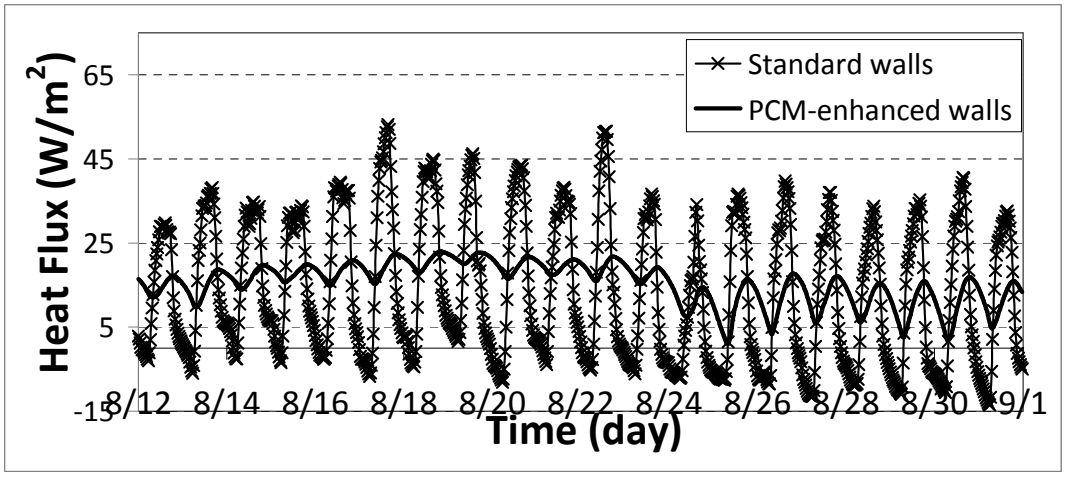

Figure A.15 Wall space cooling load-8/12-8/31-(El Paso 3B)

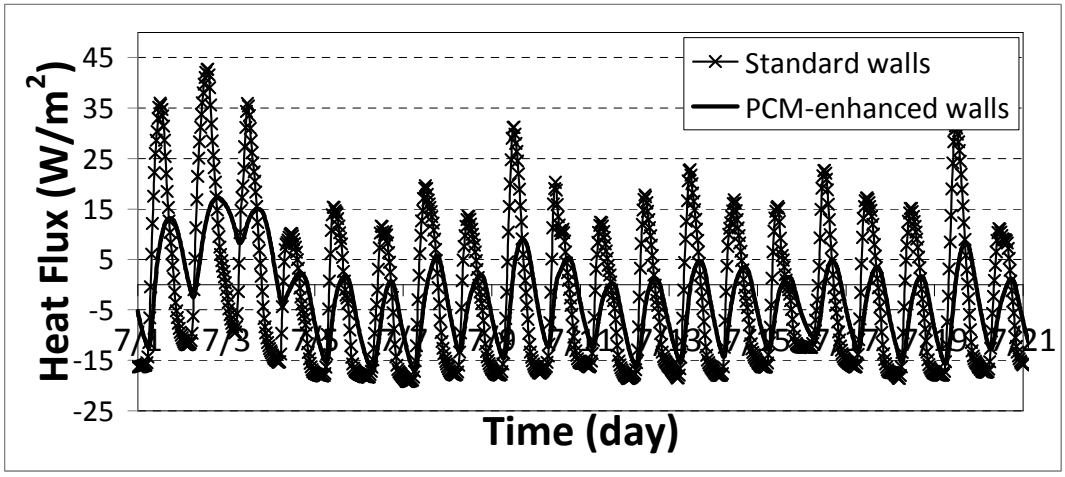

Figure A.16 Wall space cooling load-7/1-7/21-(San Francisco 3C)

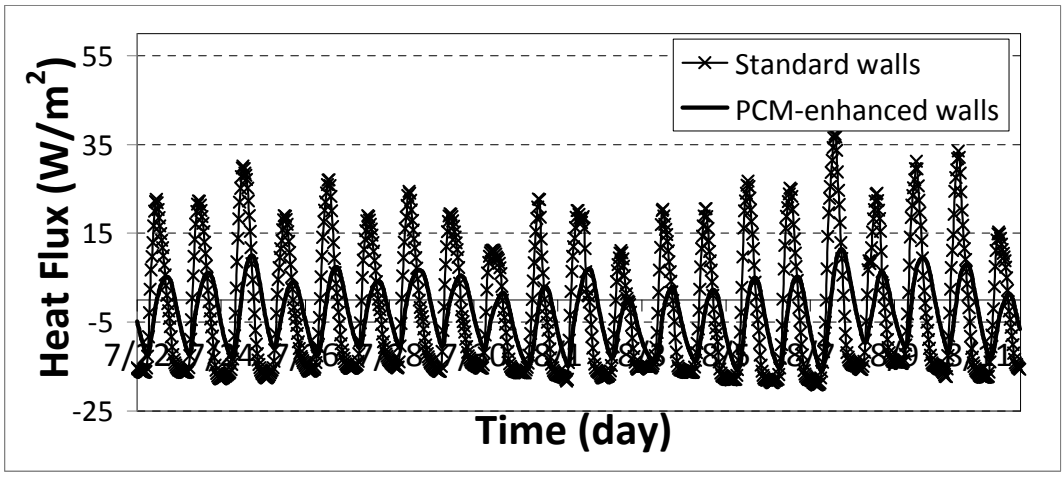

Figure A.17 Wall space cooling load-7/22-8/11-(San Francisco 3C)

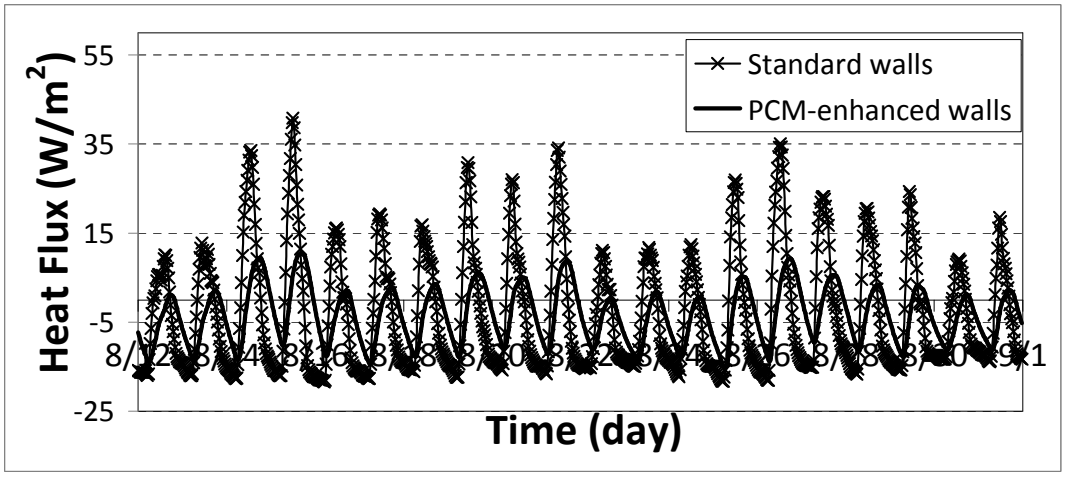

Figure A.18 Wall space cooling load-8/12-8/31-(San Francisco 3C)

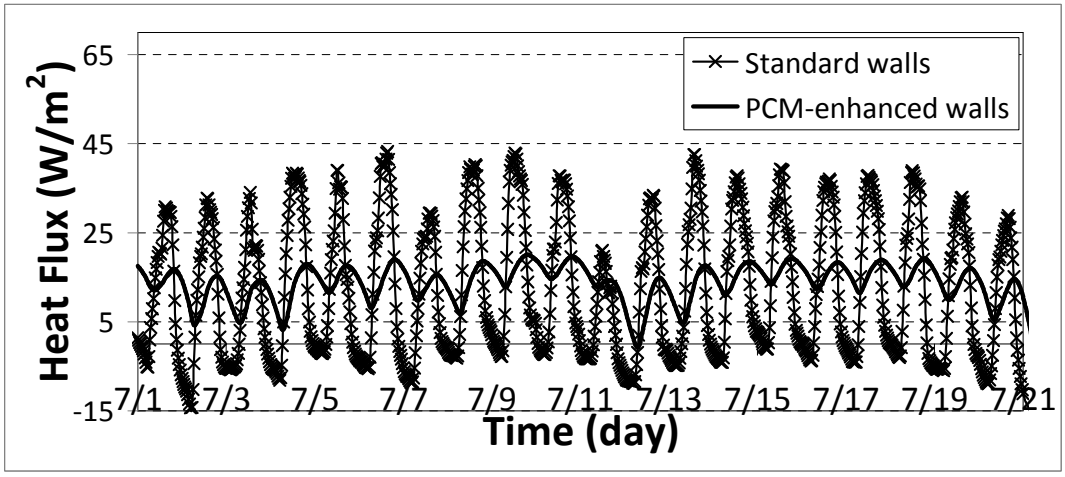

Figure A.19 Wall space cooling load-7/1-7/21-(Baltimore 4A)

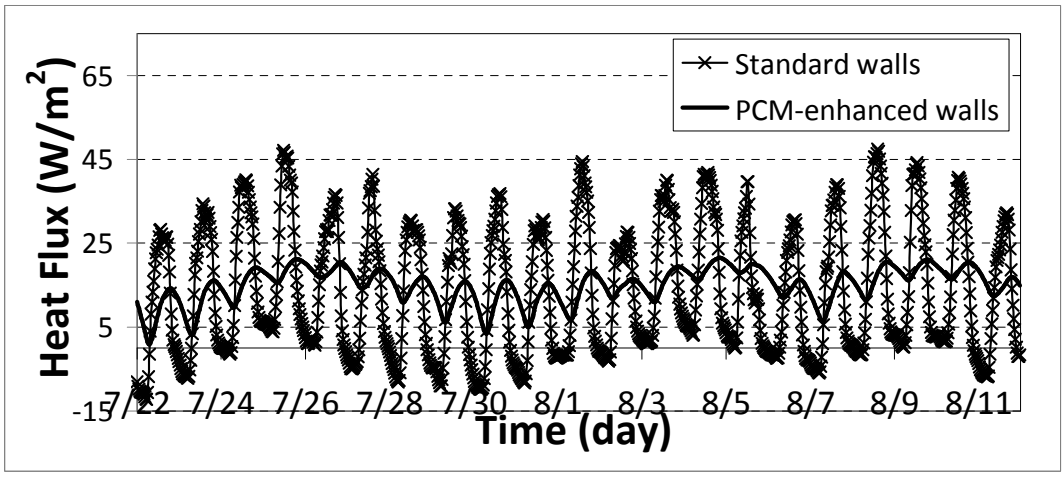

Figure A.20 Wall space cooling load-7/22-8/11-(Baltimore 4A)

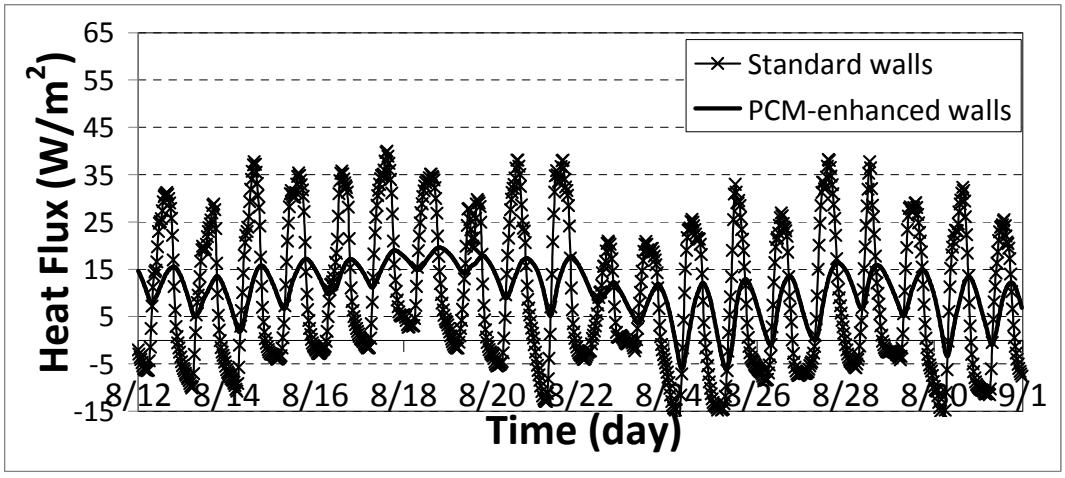

Figure A.21 Wall space cooling load-8/12-8/31-(Baltimore 4A)

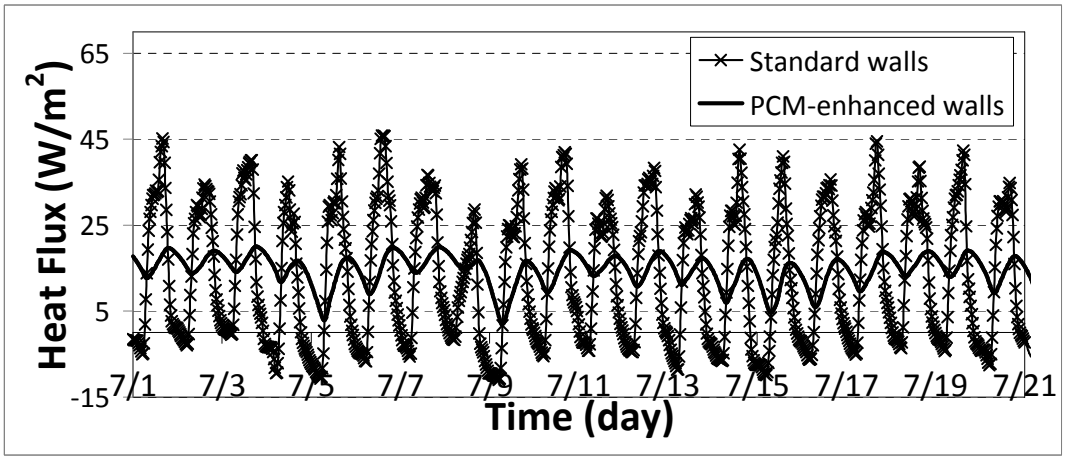

Figure A.22 Wall space cooling load-7/1-7/21-(Albuquerque 4B)

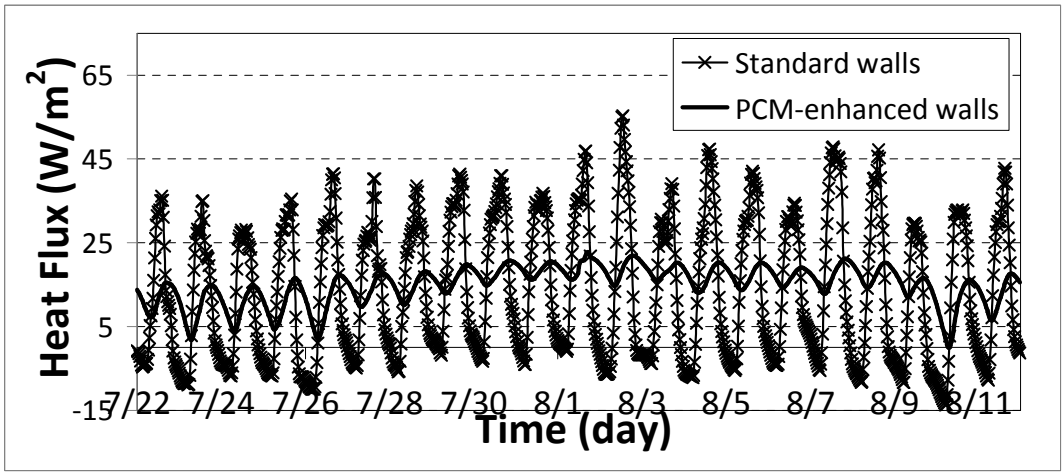

Figure A.23 Wall space cooling load-7/22-8/11-(Albuquerque 4B)

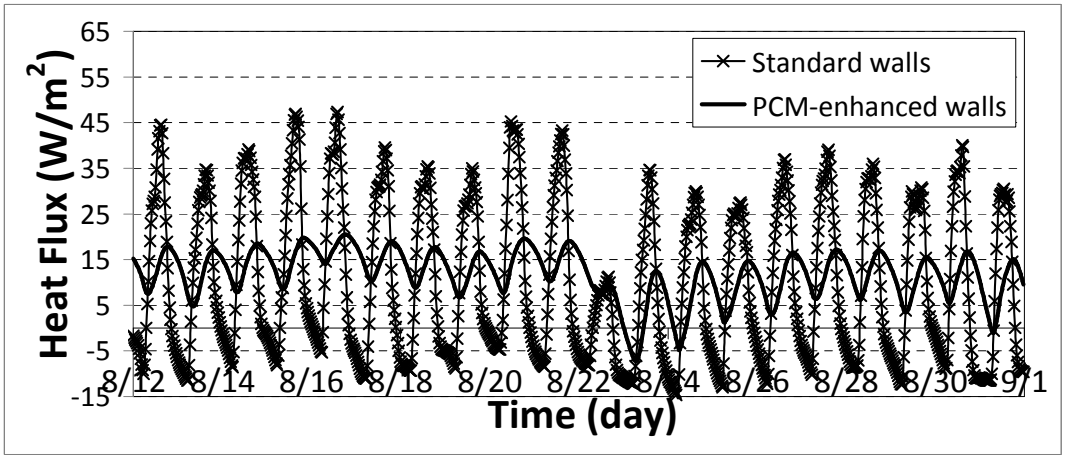

Figure A.24 Wall space cooling load-8/12-8/31-(Albuquerque 4B)

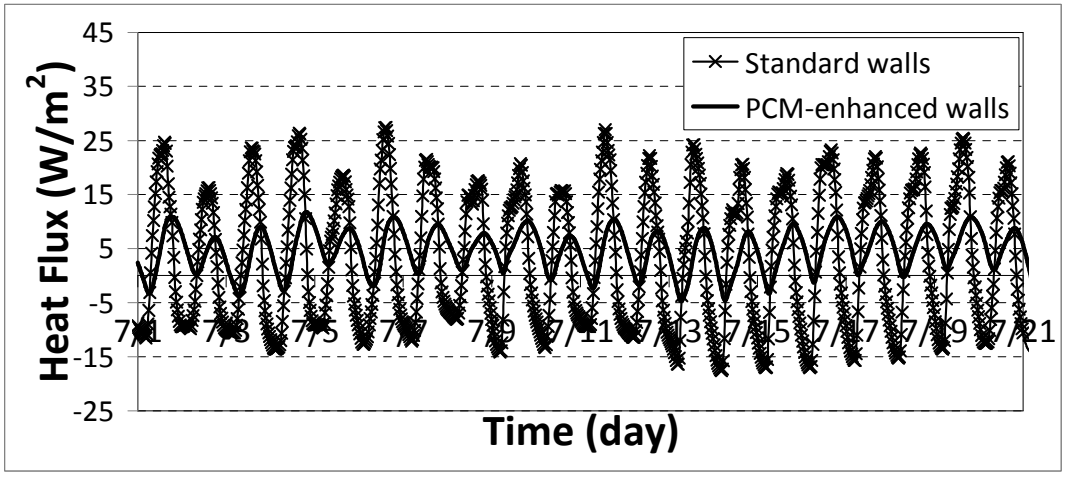

Figure A.25 Wall space cooling load-7/1-7/21-(Salem 4C)

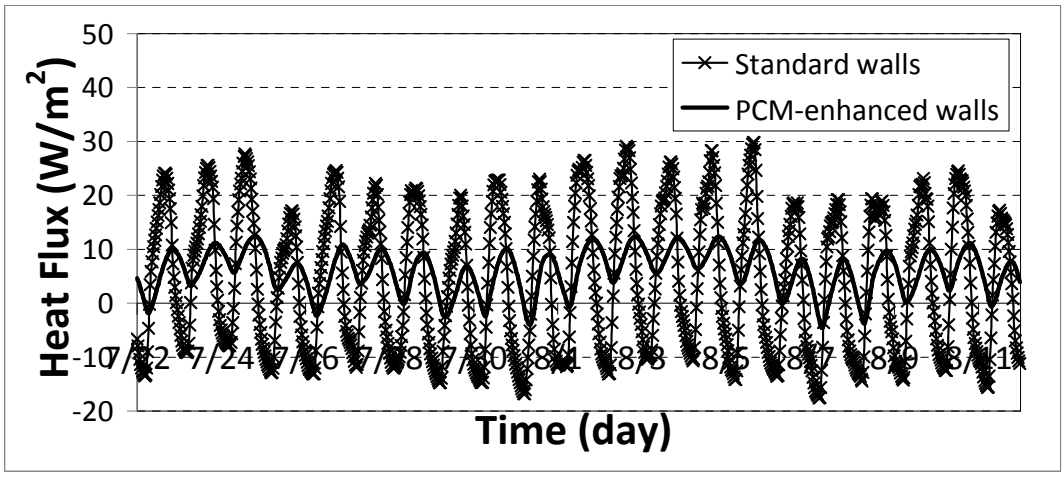

Figure A.26 Wall space cooling load-7/22-8/11-(Salem 4C)

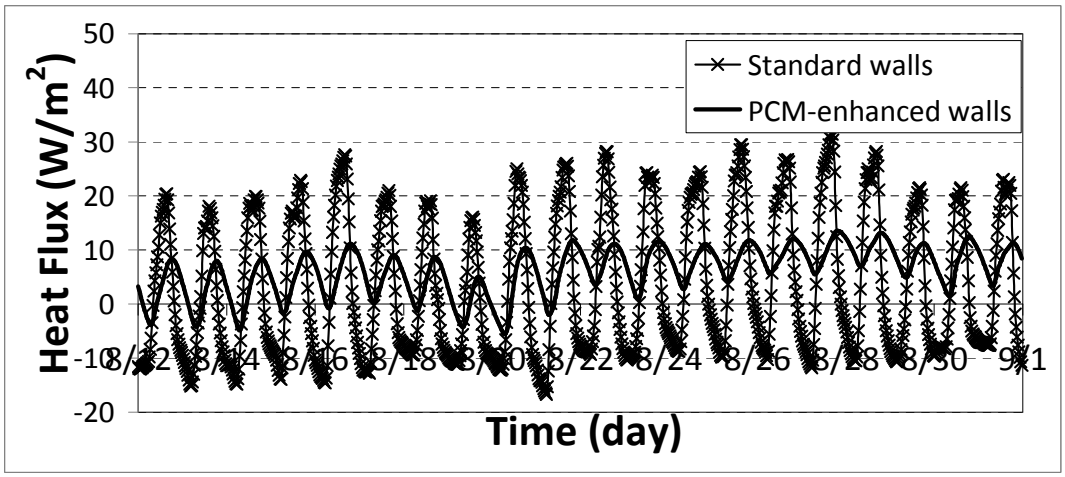

Figure A.27 Wall space cooling load-8/12-8/31-(Salem 4C)

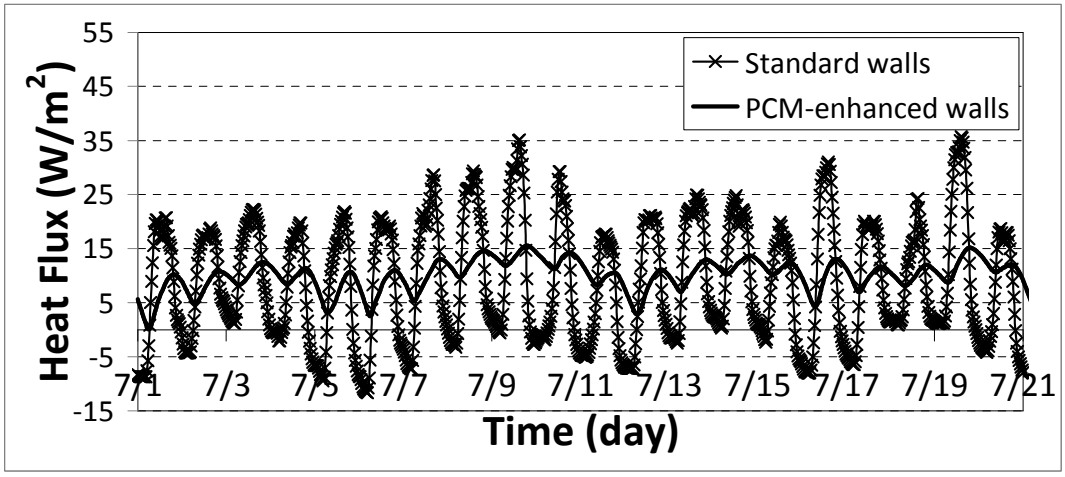

Figure A.28 Wall space cooling load-7/1-7/21-(Chicago 5A)

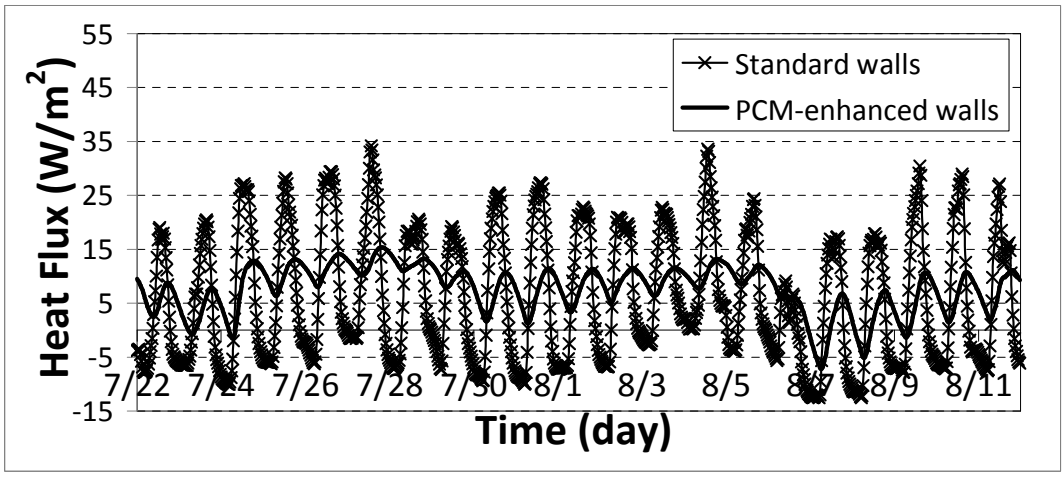

Figure A.29 Wall space cooling load-7/22-8/11-(Chicago 5A)

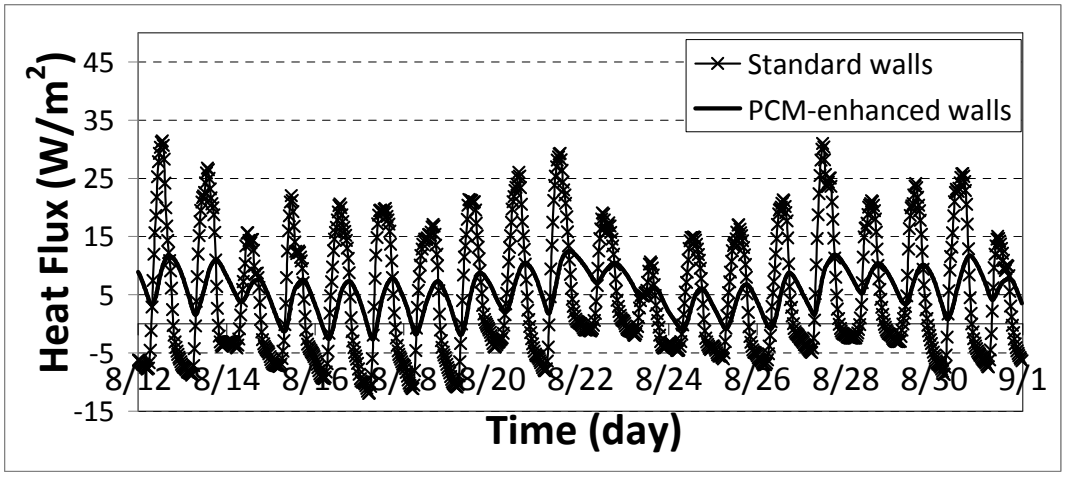

Figure A.30 Wall space cooling load-8/12-8/31-(Chicago 5A)

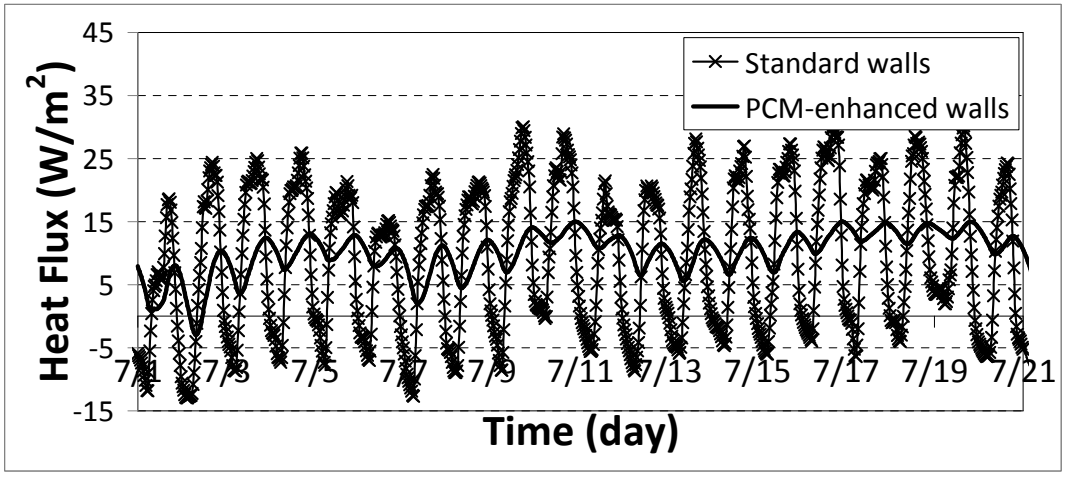

Figure A.31 Wall space cooling load-7/1-7/21-(Boise 5B)

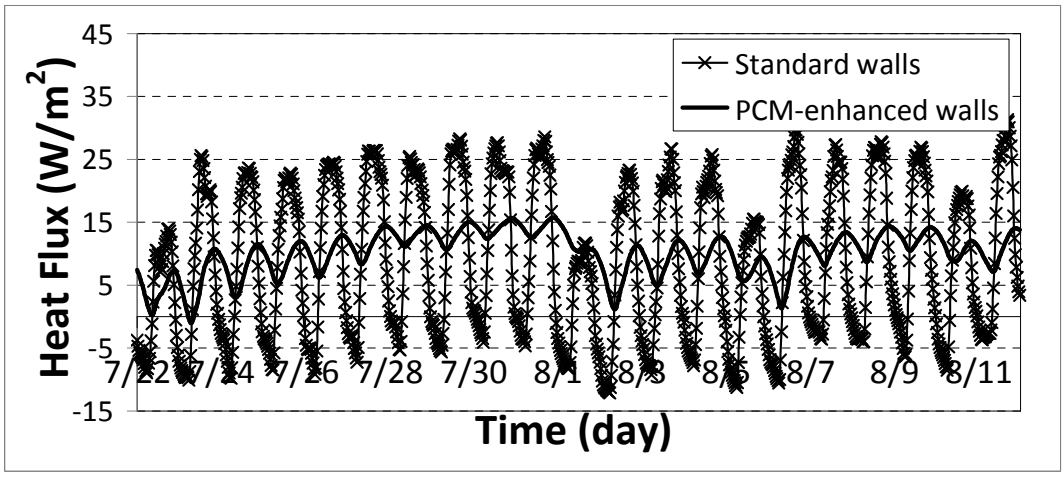

Figure A.32 Wall space cooling load-7/22-8/11-(Boise 5B)

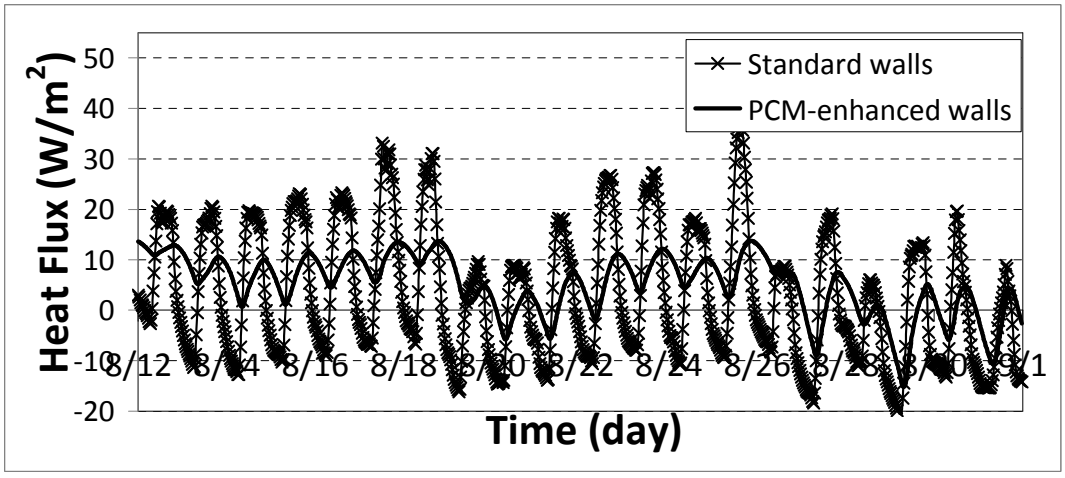

Figure A.33 Wall space cooling load-8/12-8/31-(Boise 5B)